ASTEROSEISMOLOGY

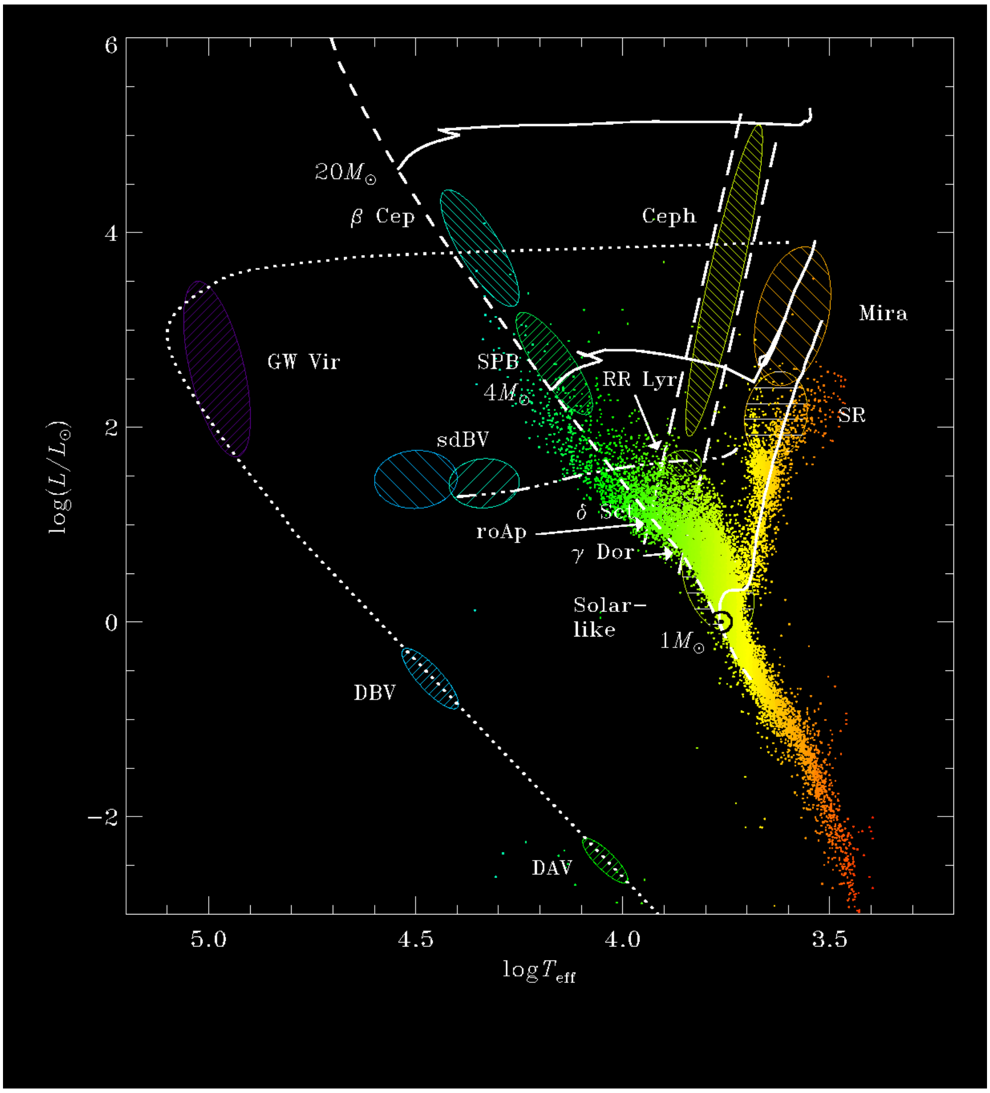

Figure kindly provided by Professor Jørgen Christensen-Dalsgaard, Aarhus University, Denmark

Lecture notes by Conny Aerts

Universities of Leuven and Nijmegen

Academic year 2007 – 2008

Contents

Preface

The purpose of this 6 ECTS course is to introduce students into the research domain of asteroseismology, which has become a very popular topic within stellar astrophysics the last decade. The main goal of the lecturer is to learn the students how to interprete data of non-radially oscillating stars. In order to achieve this the students will be provided with state-of-the-art analysis methods and with recent data of stars.

During the lectures, a large emphasis will be put on observational aspects of stellar oscillations. There are several reasons for that. First of all, this orientation corresponds to the lecturer's expertise. Second, the students of Leuven University have the opportunity to follow a parallel 30-hour course on the "Theory of stellar oscillations". Third, complete lecture notes including the technical theoretical background of stellar oscillations written by specialists in that field are available on the internet and in books (references are provided in the current notes in Chapter 3) while we believe this is less so for the observational studies, perhaps because they change and improve rapidly.

The current notes are a revision of those written eight years ago. The first edition, only available in Dutch, was limited to observational asteroseismology of stars with opacity-driven modes. The current lectures have been extended to stars with stochastically driven modes. The previous version did not include any theoretical aspects for reasons outlined above. However, it was felt that a basic introduction into the theory of stellar oscillations was desirable, because some students did not follow the parallel course. Also, the lecturer preferred to put more and more emphasis on seismic interpretations of the data in the recent years and this requires some insight into the mathematical properties of the oscillations. For this reason, a brief chapter containing the basic theoretical treatment of non-radial oscillations has been added in the current version.

The current lecture notes are divided into three parts. The first part constitutes an overview of the general properties of stellar oscillations and their occurrence across the Hertzsprung-Russell diagram. All the currently known types of non-radial oscillators are introduced. The current text is only meant as *printed lecture notes* for students, not as a book or any official document. As such it does often not contain the references to the original sources of information, or if references are quoted, they are not given explicitly. This is due to the current notes being part of a book on asteroseismology that is being prepared by the Lecturer and Professors Jørgen Christensen-Dalsgaard and Don Kurtz. The book, including the full references, is not yet finished. For this reason, this current text is **NOT** meant to be copied or distributed to other parties but only for your personal study. The students know how to use modern astronomical databases and libraries available from the internet to find the full references to the cited papers.

The second part of the notes, consisting of two chapters, describes the analysis methods needed to derive the basic properties of the observed stellar oscillations. One chapter deals with the time aspect of the oscillations and is devoted to time series analysis of data of oscillating stars. The following chapter concerns the identification of the wavenumbers of the observed non-radial oscillations, once frequencies have been determined.

The final part of the notes is composed of several chapters devoted to recent applications of asteroseismology to selected stars. It concerns stars of quite different type and/or evolutionary state. The text of these chapters consists of selected refereed papers taken from the international literature on asteroseismology. A first chapter is devoted to helioseismology and solar-like oscillations. Another chapter consists of seismic studies of compact oscillators, such as white dwarfs and sub-dwarf B stars. Finally, the last chapter highlights some detailed seismic analyses of stars considerably more massive than the Sun.

These lecture notes, as well as additional ones and state-of-the-art asteroseismic datasets, can be retrieved from the Word Wide Web, at URL `http://www.eneas.info`.

Conny Aerts,

Leuven, September 2007

Evaluation procedure

The students following this course will be evaluated on a quasi-permanent basis, i.e. during the course. The students can either work individually or can work in groups of two persons (with at most one group of three for an odd number of students). They will have to make two main exam projects and will be given additional tasks during the course as well.

The first exam project concerns time series analysis and mode identification based upon datasets provided by the lecturer. They are expected to make a written report of maximum 10 pages (in Dutch or in English), describing their results of the analyses. Additionally, they must present their results during a 10-minutes oral presentation (in Dutch or in English) attended by all the students following this course, followed by a round of questions on their presentation from the audience.

For the second exam project, each (group of) student(s) is assigned (one of the) papers from the recent literature available in Part III of the current lecture notes. It concerns a seismic analysis of a particular star or a group of stars. The students must make a literature study of that/these object(s) and summarize the results of the seismic study by giving an oral presentation, again of 10 minutes, in front of their class mates, followed by a round of questions.

All students of each group must give parts of the two presentations. The written report must be handed over to the lecturer a few days in advance of the oral presentation (practical arrangement to be discussed with the lecturer during the courses). The use of the lecture notes is admitted during each part of the exam. The data set and the paper(s) they must study will be handed over to them well in advance of the deadline for the written report.

The course will end with a discussion between students and lecturer with the goal to give each other feedback on all aspects of these lectures. At the end of the course, successful students will have learnt to analyse modern data of oscillating stars, to report on such analyses before an audience, to summarize the highlights of recent international papers on stellar oscillations, to collaborate and discuss among each other, and to formulate relevant questions on papers in a clear and concise way so that persons not having read the paper understand the issue of the question.

Good luck to all of you !!

Part I

General properties of stellar oscillations

Chapter 1

Introducing asteroseismology

The research field of asteroseismology will be introduced to you by means of a computerpresentation, which contains many graphical illustrations. These illustrations are not suitable to be copied on paper, so we refer you to that introductory presentation in addition to the text of the current chapter.

The subject of this course is situated in the research domain of stellar astrophysics. More particularly, it concerns the topic of *oscillations* that occur inside stars. The recent research domain of *asteroseismology* refers to the study of the internal structure of stars through the interpretation of their oscillation frequency spectra. For one of the early reviews on the topic, we refer to Brown & Gilliland (1994)[1]. Essentially, asteroseismologists try to make use of the oscillations to probe the stellar interior, which is not directly observable. The basic principles of asteroseismology are, to a certain extent, similar to those developed and employed by earth seismologists. Asteroseismology relies on advanced mathematical descriptions of oscillations in a three-dimensional body and numerical modelling. It is therefore a prominent example of interdisciplinary science, more precisely of “integrated” physics.

The interiors of the stars are among the most difficult parts of the Universe to observe. The reason why stellar interiors can be probed from the oscillations is that the behaviour of the oscillations is determined uniquely by the properties of the overall stellar structure. More particularly, the different oscillation modes of a star penetrate to different depths inside that star and so one is able to study the internal layers from the frequency differences of the modes. Asteroseismology is the only available method to derive in a quasi-direct way the internal structure of the stars with high precision.

The ultimate goal of asteroseismology is to improve the evolutionary models of the stars. The theory of stellar evolution is reasonably well established in a global sense. We know that stars are born out of giant

---

[1] We remind the students that they have to search for the complete reference and the paper themselves through electronic libraries as explained further in the text

clouds of dust and that they burn hydrogen into helium in their core during 95% of their life. As soon as the central fuel is exhausted, they become red giants and expell their outer layers. Depending on their mass, they end their lifes as white dwarfs or supernovae. This broad picture is derived from, and in agreement with, the observations of many different kinds of stars of different ages. However, the current observations do not allow a very detailed confrontation between the theoretical models and real physical properties of the stellar material in the deepest internal layers. Asteroseismology will lead to significant contributions in this context.

1.1 Basic properties of non-radial oscillations

On the frontcover of these lecture notes, you find a schematic representation of the different classes of oscillating stars in the Hertzsprung-Russell (HR) diagram (in which the stellar luminosity, i.e. the energy released at the stellar surface, is plotted against the surface temperature of the stars) known up to the present day. The dashed line indicates the “main sequence”. All stars in this stage of evolution are relatively young and burn hydrogen in their core. Along the main sequence many different classes of non-radial oscillators occur, from the low-mass solar-like stars up to the massive β Cep stars. To the right, we find classes of oscillating stars along the horizontal and red-giant branch. These stars burn helium in their core. All classes of non-radial oscillators to the lower left of the main sequence are evolved stars that have reached the stadium of (pre-)white dwarfs. They no longer have nuclear burning and are condemned to cool. The full lines in the figure are the evolutionary tracks for stars with different initial masses. It is very fortunate that oscillations are excited in almost all types of stars and in many stages of stellar evolution.

The simplest oscillation a star can undergo is a *radial* one. In that case, the star expands and contracts radially and spherical symmetry is preserved during the oscillation cycle. From a mathematical point of view, the differential equation describing the radial displacement is of the Sturm-Liouville type and thus allows eigensolutions that correspond to an infinitely countable amount of eigenfrequencies. The smallest frequency corresponds to the fundamental radial oscillation mode. The period of this mode is inversely proportional to the square root of the mean density of the star. Radial oscillations are characterised by the radial wavenumber n: the number of nodes of the eigenfunction between the center and the surface of the star. Well-known radial oscillators are the Cepheids, RR Lyrae stars and Red Giants.

If transverse motions occur in addition to radial motions, one uses the term *non-radial oscillations*. The oscillation modes are then not only characterised by a radial wavenumber n, but also by non-radial wavenumbers l and m. The latter numbers correspond to the degree and the azimuthal number of the spherical harmonic $Y_l^m(\theta,\varphi)$ that represents the dependence of the mode on the angular variables θ and φ for a star with a spherically symmetric equilibrium configuration. The degree l represents the number of surface nodal lines, while the azimuthal number m denotes the number of such lines that pass through the rotation axis of the star. The surface pattern of some non-radial oscillations is graphically depicted in Figure 1.1. These *Doppler maps* show the radial velocity structure at the stellar surface of a non-radial oscillator at one particular phase of the oscillation cycle. The red parts are moving inwards and cause a redshift in the observed stellar spectrum while the blue parts move simultaneously outwards and give rise to a blueshifted spectrum. Half an oscillation cycle later, the red parts have become blue and vice versa. The

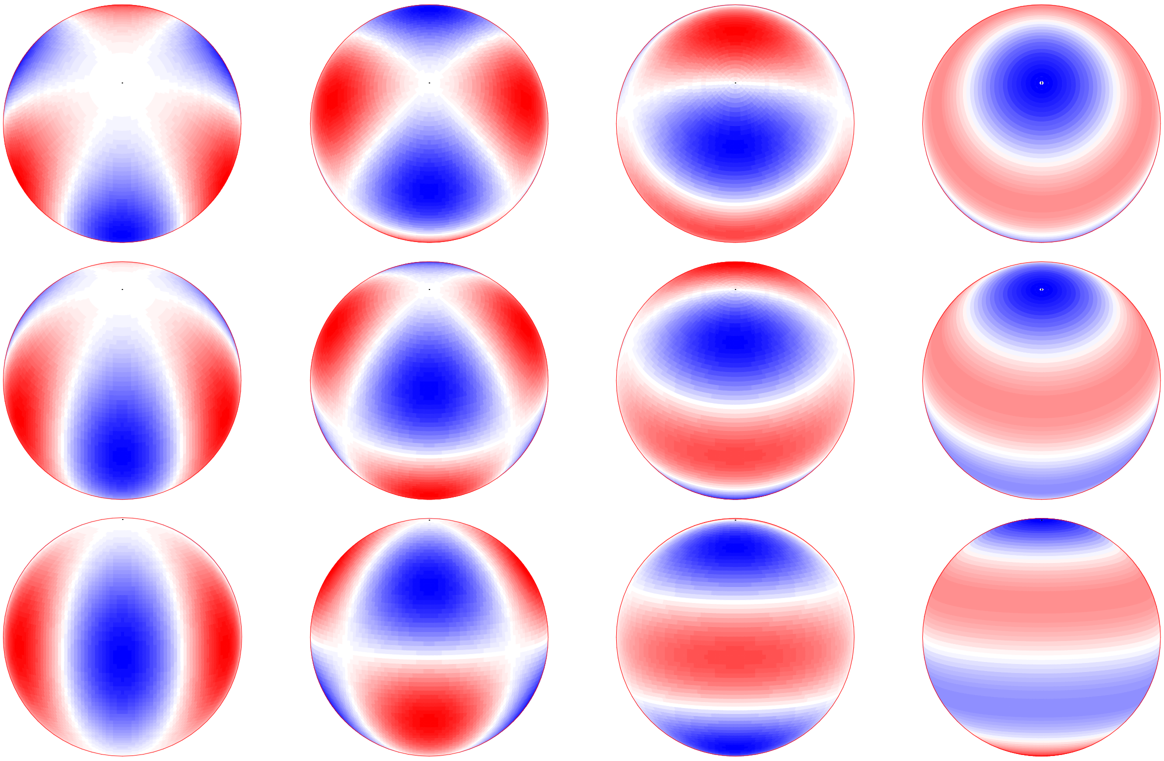

Figure 1.1: Different examples of non-radial oscillations, seen from a different inclination angle: $i = 30°$ (top row), $i = 60°$ (middle row), $i = 90°$ (bottom row). The velocity field of a non-radial oscillator is represented by a spherical harmonic Y_l^m. The meaning of the spherical wavenumbers (l, m) is visualised. In these examples $l = 3$ and m takes values from 0 (right) to 3 (left). The dot indicates the symmetry axis of the oscillation, which corresponds to the rotation axis of the star. The colouring denotes the Doppler shift in an observed spectrum due to the oscillation, i.e. at this particular instance in the oscillation cycle, the red parts are moving towards the stellar center (thus away from the observer) and therefore shift the spectrum to longer wavelengths (redshift) while the blue parts are moving outwards (towards the observer) and result in a shift to shorter wavelengths (blueshift).

white lines in Figure 1.1 represent the l *nodal lines*. The mass elements on these lines do not move during the oscillation cycle.

The modes with $m = 0$ are standing waves. They are called axisymmetric or zonal modes. Non-zonal modes are running waves. We take the following convention with respect to the rotation: positive $m-$values denote modes that move opposite to the rotation (retrograde modes) while negative $m-$values are associated to motion in the direction of the rotation (prograde modes). The modes with $l = |m|$ are called *sectoral* and those with $0 \neq |m| < l$ are *tesseral* (see Figure 1.1).

Non-radial oscillations can penetrate deeply inside a star. For each oscillation the surface pattern is a continuation of the internal oscillatory behaviour and so the latter can, to a certain extent, be derived from measuring the surface variability. For each surface pattern, a whole series of oscillations with different internal behaviour is possible. This series is characterised by the radial wavenumber n, which represents the number of nodal surfaces inside the star in the case of a non-radial oscillation. The latter is thus characterised by three numbers (n, l, m) and its frequency ω_{nlm}.

1.2 Why do stars oscillate ?

The basic properties of oscillation modes are explained in the previous section. However, one needs to have a mechanism that *excites* the modes in the stars. Three types of excitation mechanisms exist.

The Sun oscillates in millions of acoustic modes with extremely low velocity amplitudes which are of the order of cm/s. These modes are caused by the motions of the outer convective cells and have lifetimes of the order of days to weeks. One speaks of *stochastically excited modes*. Such oscillations are expected in all stars having convective outer layers.

For most of the classes of pulsating stars indicated in the frontcover plot, however, the modes are *self-excited*. This self-excitation is possible because some layers in the stars turn out to have the potential to act as a heat engine. Such layers are able to trap the energy radiated outwards by the stellar core in a very efficient way during a small contraction of the star, and to release the trapped energy during the subsequent expansion. For this so-called κ *mechanism* to work, i.e. for it to be able to make the whole star oscillate, the pertinent layer has to be situated at a suitable position in the star. As a result, oscillations can only be excited when a suitable combination of stellar luminosity, temperature, and chemical composition occurs. For this reason, non-radial oscillations are excited in so-called *instability strips* in the Hertzsprung-Russell diagram.

Whenever two components of a close binary interact significantly, dynamic tides will result. Such tides can give rise to oscillations of one or both components. One speaks of *forced oscillations*, contrary to the two types of *free* oscillations mentioned above. Theory predicts that forced oscillations are characterised by degree $l = 2$.

1.3 Brief description of the mathematics of non-radial oscillations

In the framework of these lectures we consider a self-gravitating gaseous spherically symmetric star in the absense of external forces (i.e. no visceous effects nor magnetic fields). We assume that the axis of symmetry of the oscillations coincides with the rotation axis of the star. Moreover, we assume that the rotation of the star is so slow that it has no effect on the oscillations. This approximation is valid as long as the deformation of the star due to the centrifugal force can be neglected and when the ratio of the pulsational periods to the rotational period remains small (typically well below 10%). In other words, we assume that several oscillation cycles have taken place on the time span that the star needs to turn around its rotation axis.

In the theory of stellar oscillations, which is outlined in more detail in Chapter 3, one studies the reaction of the star to small perturbations which cause deviations from the spherical symmetry. The equations which have to be fulfilled form a system of non-linear partial differential equations: the perturbed equation of motion, the perturbed continuity equation, the perturbed energy equation and the perturbed Poisson equation. Assuming that all physical quantities undergo only small deviations from their equilibrium value allows one to linearise the perturbed equations. The equations are invariant with respect to a translation in time whenever the evolution of the star is to a good approximation a succession of quasi-static states of hydrostatic and thermal equilibrium. In that case, solutions with a time dependence $\sim \exp(\mathrm{i}\omega t)$, with ω the pulsation frequency, can be found. The unknowns in the system of equations are the components of the Lagrangian displacement vector, the perturbed pressure, the perturbed temperature and the perturbed density, among others.

We consider a system of cartesian coordinates (x, y, z) of which the $z-$axis coincides with the rotation axis of the star. In this system, we introduce spherical coordinates (r, θ, φ) whose polar axis coincides with the z-axis. It is convenient to describe any scalar function $X(r, \theta, \varphi)$ in terms of spherical harmonics, which are a complete orthogonal set of functions, for any physical problem with spherical symmetry:

$$X(r,\theta,\varphi) = \sum_{l=0}^{+\infty} \sum_{m=-l}^{l} X_{lm}(r) Y_l^m(\theta,\varphi), \tag{1.1}$$

in which the spherical harmonic Y_l^m is defined as

$$Y_l^m(\theta,\varphi) \equiv \sqrt{\frac{2l+1}{4\pi}\frac{(l-m)!}{(l+m)!}} P_l^m(\cos\theta)\exp(\mathrm{i}\, m\varphi), \tag{1.2}$$

with $P_l^m(\cos\theta)$ the *associated Legendre function* which is defined as

$$P_l^m(x) \equiv \frac{(-1)^m}{2^l l!}\left(1-x^2\right)^{m/2} \frac{d^{l+m}}{dx^{l+m}}\left(x^2-1\right)^l . \tag{1.3}$$

We are only interested in time-dependent solutions, which we call spheroidal modes. In terms of spherical harmonics we write the components of the Lagrangian displacement vector as:

$$\begin{cases} \xi_r(r,\theta,\varphi,t) = a(r) Y_l^m(\theta,\varphi)\exp(-\mathrm{i}\,\omega t), \\ \xi_\theta(r,\theta,\varphi,t) = b(r)\dfrac{\partial Y_l^m(\theta,\varphi)}{\partial\theta}\exp(-\mathrm{i}\,\omega t), \\ \xi_\varphi(r,\theta,\varphi,t) = \dfrac{b(r)}{\sin\theta}\dfrac{\partial Y_l^m(\theta,\varphi)}{\partial\varphi}\exp(-\mathrm{i}\,\omega t). \end{cases} \tag{1.4}$$

The functions $a(r)$ and $b(r)$ are eigensolutions of an eigenvalue-problem of fourth order. This eigenvalue problem is degenerate with respect to the azimuthal number m (see Chapter 3).

Radial modes are a special case of non-radial modes for which $l = 0$. The system of equations reduces to one of second order for radial modes. This system is of Sturm-Liouville type and so gives rise to an infinite number of eigenvalues ω_n^2, each of which corresponding to one particular eigenvector. The eigenvector belonging to ω_n^2 has one zero point less than the one of ω_{n+1}^2. Each of the eigenvalues is real because the operator is self-adjoint. We hence obtain two types of solutions. A first series for which $\omega_n^2 > 0$. In that case ω_n is real and the eigenvectors have an oscillatory behaviour through the $\exp(\mathrm{i}\,\omega_n t)$ dependence. Whenever $\omega_n^2 < 0$ we are dealing with pure imaginary numbers ω_n and the oscillations grow or damp exponentially (we do not consider such solutions in this course). The hermiticity of the operator also ensures a minimal eigenvalue ω_0^2, which corresponds to the longest oscillation period $P = 2\pi/\omega_0$. Its corresponding eigenvector is called the *radial fundamental mode*. All the eigenvalues are ordered according $\omega_0 < \omega_1 < \omega_2, \ldots$, which corresponds to oscillation periods $P_0 > P_1 > P_2 > \ldots$. The eigenvector with the eigenfrequency ω_1 is called the first harmonic, the one with ω_2 the second harmonic and so on. Each of these modes are standing acoustic modes, i.e. sound waves and so the oscillations of a star are quite similar to those of musical instruments. The star passes through her equilibrium position twice per oscillation cycle.

An important mathematical difference with the non-radial modes is that the system of differential equations to be solved is no longer of Sturm-Liouville type, the operator is only Hermitic. Hence, the eigenvalues ω_n^2 are still real numbers, but they can no longer be ordered as for radial oscillations and the existence of a smallest eigenvalue is no longer garantueed. However, one can show (beyond our scope) that the system of equations evolves towards a Sturm-Liouville problem whenever $\omega_n^2 \to 0$ for $n \to +\infty$ or when $\omega_n^2 \to +\infty$ for $n \to +\infty$. In the latter case we recover again an ordered sequence $\omega_1 < \omega_2 < \omega_3 < \ldots$ with corresponding $P_1 > P_2 > P_3 > \ldots$. Such modes are called $p_1, p_2, p_3, \ldots$ and one speaks of pressure (acoustic) or p-modes. The subscript denotes again the number of nodes of the radial component of the eigenvector. The restoring force for p-modes is the perturbed pressure force. In the case $\omega_n^2 \to 0$ for $n \to +\infty$ an ordering also occurs, this time

$$0 < \frac{1}{\omega_1} < \frac{1}{\omega_2} < \frac{1}{\omega_3} < \ldots$$

and such modes are called $g_1^+, g_2^+, g_3^+, \ldots$ or gravity modes (g-modes). The buyancy force is the main restoring force for such non-radial modes. Gravity modes hence have periods that are longer than the period of the radial fundamental mode. Finally, the limit case of $\omega = 0$ belongs to an eigenvector that has no nodes in the radial direction.This modes is called the non-radial fundamental, or f-mode.

The p-modes mainly attain a large amplitude in the outer layers of the star while g-modes have a large amplitude in the deep layers of the star. Therefore, g-modes are by far the most interesting from an asteroseismological point of view. However, the corresponding periods of g-modes are one order of magnitude longer than those of p-modes.

1.4 Contents of this course

We now highlight very briefly the different topics that will be touched upon in the framework of this course. Detailed studies will be presented in the subsequent chapters and are also listed in the references given at the end of these lecture notes.

1.4.1 Helioseismology

Although very succesful applications of asteroseismology were already obtained from ground-based data of the 3-15 minutes oscillations of the Sun, the breakthrough in *helioseismology* came from the space data of the Sun obtained with the ESA/NASA satellite SoHO which was launched in 1995 (for more information, see `http://sohowww.nascom.nasa.gov/`). The solar frequency spectrum (for a definition, see Chapter 4) derived from SoHO data is shown in Figure 1.2, while an enlargment for the highest-amplitude region is shown in Figure 1.3. The regular pattern in the peaks is clearly visible. One defines two important quantities derived from such a spectrum: the *large frequency separations* $\triangle\nu_l$, which occur between the frequency peaks belonging to modes with wavenumbers (n, l) and $(n-1, l)$, and the *small frequency separations* $\delta\nu_l$ which represent the frequency differences between modes with wavenumbers (n, l) and $(n-1, l+2)$. The large frequency separation is dependent on the average stellar density while the small separation is determined by sharp features in the sound speed, such as those caused by the core of the star. It is possible to infer the mass of the star, and also the age since the core composition changes as more hydrogen is turned into helium by the nuclear burning. The small frequency separation is, therefore, a measure of the evolutionary state of the star.

The diagnostic properties of solar-like oscillations have been derived in great detail. The seismic studies based on the SoHO data have revealed for the first time the detailed properties of the outer convective layers of the Sun. The outer convection zone of the Sun turns out to be 50% more extended than previously thought. Moreover, the internal differential rotation and mixing in the Sun could be mapped in full detail at the level of 0.1%. Finally, the age of the Sun can be derived from the large and small separations. It turns out that these quantities lead to an age estimate better than 0.1% (we can quantify this because we know the age of the Sun from meteorites). We refer to Chapter 6 for more details.

1.4.2 Solar-like stars

The successes of helioseismology have of course led to huge efforts to obtain the same level of precision in other oscillators over the whole mass range. As far as the search of oscillations in other solar-like stars is

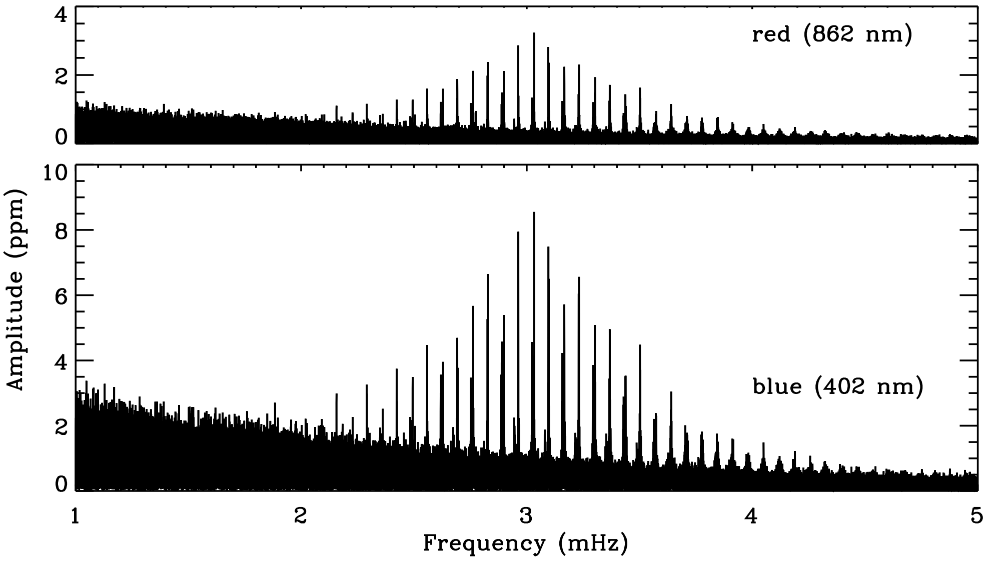

Figure 1.2: The oscillation spectrum of the Sun derived from the experiment VIRGO onboard SoHO. The amplitude of the oscillations, expressed in ppm (parts per million), is drawn as a function of frequency, for both blue and red solar light. The highest frequency peaks have amplitudes of a few ppm, which means that the relative change of the luminosity of the Sun due to the oscillations is only a few parts per million.

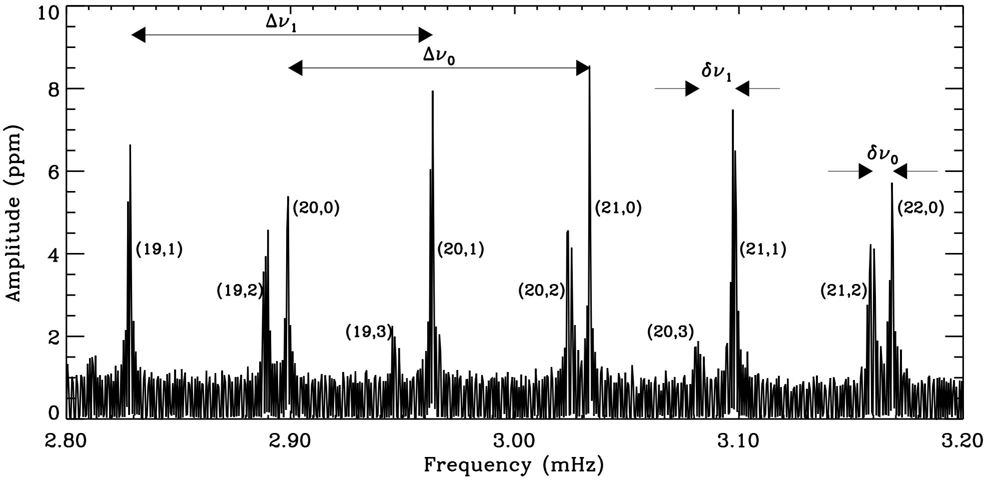

Figure 1.3: Enlargment of the oscillation spectrum of the Sun shown in Figure 1.2 for the frequency range with the highest amplitudes.

concerned, clear detections of stochastically excited p-modes were recently found (see Chapter 6), after more than 10 years of efforts. For stars with solar-like oscillations, many of the techniques of helioseismology are immediately applicable once the frequency spectrum is well determined, and so we expect quite a bit of progress in the derivation of the internal structure parameters of these types of stars in the near future now that firm evidence of acoustic modes exists for a number of objects.

1.4.3 Compact stars

Other concrete in-depth asteroseismological results, in the sense of probing the internal structure, were obtained for the g-modes in white dwarfs since the early 1990s already. White dwarfs are the compact end-products of stars with initial masses below 9 solar masses. The white dwarfs oscillate multiperiodically, in g-modes with periods around 10 minutes. In order to cover the overall beat-period of all the excited modes, a network of telescopes around the Earth equator was set up in the late 1980s: the WET, which stands for Whole Earth Telescope. A WET campaign on the DOV PG 1159-035 implied a breakthrough in white-dwarf seismology and allowed to derive the mass, rotation rate, and internal stratification of this object with unforeseen precision (see Chapter 7). Other succesful campaigns on white dwarfs followed later, up to the present day.

Oscillation modes were recently found in another group of compact evolved stars, B-type subdwarfs (sdB stars). These objects are situated at or just beyond the extreme blue end of the horizontal branch and are core-helium burning stars surrounded by a thin hydrogen envelope developped during the giant branch. This envelope is too thin to sustain hydrogen-shell burning. Therefore, sdB stars will not follow a path to the Asymptotic Giant Branch (AGB) after core-helium exhaustion, but will turn immediately left in the HR diagram, becoming low-mass white dwarfs. Both p-mode and g-mode pulsating sdB stars have been discovered. These sdB oscillators were, almost simultaneously with their observational discovery, understood theoretically in terms of the κ mechanism. The exploitation of the asteroseismological potential of the sdB stars is currently ongoing (Chapter 7) and receives a lot of attention, as the evolution and structure of the sdB stars is relatively poorly known.

1.4.4 Massive stars

While the seismological studies of evolved stars have fine-tuned the evolutionary cooling tracks of such objects, they do not help us to confine the early phases of the evolution of the progenitors of these stars. Such studies thus cannot help us to constrain the internal structure at the main-sequence stage of the stars that will eventually become sdBs and white dwarfs, nor of those that will explode as a supernova. The current status of asteroseismology of non-solar-like main-sequence stars (i.e. of stars with at least twice the mass of the Sun) is not yet so evolved because the application of asteroseismology for such objects is not straightforward. A prerequisite for such an application is of course the detection of many oscillation modes and their mode identification, i.e. the knowledge of their wavenumbers (n, l, m). The modes in these stars are not in the asymptotic frequency regime, only a limited number of modes is detected and the selection mechanism of their excited modes is not known. Hence, mode identification is a serious problem for seismic applications.

The best candidates according to the number of modes detected are the δ Scuti stars, which are situated in the classical instability strip and which pulsate in p-modes. For some of these stars, more than 30 oscillation frequencies have been detected from multisite campaigns, such as WET and the DSN: Delta Scuti Network. While early attempts of seismology of such stars were very promising, it has become clear that unexplained amplitude and period changes occur in these stars. Moreover the lack of accurate mode identifications, due to the incomplete observed frequency spectra, limits seismic applications.

The rapidly oscillating Ap (roAp) stars are chemically peculiar stars in the δ Scuti instability strip with a strong magnetic field. Because of this, their oscillation symmetry axis is probably not aligned with the rotation axis, but rather with the magnetic axis or even with yet another axis. Their oscillations are explained in terms of the so-called modified oblique pulsator model. They oscillate in p-modes with periods of the order of minutes. Seismic applications will be discussed in Chapter 8.

For the massive B-type main-sequence oscillators, as well as for the recently discovered γ Doradus stars, the problem of detecting multiple modes and of identifying them is even more severe, since their oscillation periods are considerably longer. The only way to make progress in asteroseismology of stars with masses higher than twice that of the Sun is to obtain uninterrupted time series that cover the overal beat-periods of the oscillations and to develop better mode identification methods (see Chapter 5). The current state of seismic applications to massive stars is presented in Chapter 8.

In the following two chapters we give respectively an overview of the occurrence of stellar oscillations in the HR diagram for the different evolutionary states and a concise description of the theory of non-radial oscillations. Subsequent chapters contain methodological approaches to disentangle and interprete observations of non-radial oscillations as well as applications of asteroseismology to different types of stars.

Asteroseismology is a research field that is undergoing very rapid changes and progress is considerable on a short time scale (e.g. the current notes are a revision of those written 5 years ago, which were very much out of date). This rapid progress will even increase the coming decade as several worldwide networks and space missions dedicated to this topic will be in operation during the coming 5 years. We therefore advise the interested student to keep up-to-date by checking regularly the two most important astronomical databases accessible at:

`http://adsabs.harvard.edu/abstract_service.html`
`http://cdsweb.u-strasbg.fr/Simbad.html`

The first one of these internet addresses brings you to the ADS abstract service that allows you to search for scientific papers by queries, e.g. author names, title words, stellar objects, etc. The second address is the one of the astronomical database held at Strassbourg, in which numerous measurements of stars are available, as well as basic stellar parameters and references to papers. Whenever appropriate we also list interesting internet sites. Detailed searches on the internet starting from these mentioned web addresses will lead you to the most appropriate and up-to-date information.

Chapter 2

Observations of Stellar Oscillations across the Hertzsprung-Russell Diagram

This chapter is a journey through the Hertzsprung-Russell (HR) Diagram with stops at all the ellipses shown in Fig. 2.1. We discuss briefly each of the currently known classes of oscillating stars, outlining their most important properties, such as their fundamental stellar parameters and the general character of their oscillations, but skipping many of the details. For each class, we provide a recent overview paper and/or book to which we refer for additional information and deeper discussion. We provide one prototypical time series of a class member and sometimes its Fourier transform, in order to give the reader a first impression of the frequency range and the behaviour of the oscillations. We further restrict ourselves to a description of the basic properties of the stars; details on asteroseismic applications are postponed to the later chapters in this book specifically dedicated to them.

An evident conclusion from Fig. 2.1 is that stellar oscillations occur in almost all phases of stellar evolution. However, there clearly exists a particular region in the HR diagram in which the density of pulsating stars is greater than elsewhere. This region is situated between the two slanted dashed lines in Fig. 2.1 and is called the *classical instability strip*. The oscillations in the stars situated in this strip are caused by the heat mechanism primarily acting in the second partial ionization zone of helium, *i.e.*, the zone in which both He II and He III occur. The Cepheids, RR Lyrae stars, δ Sct stars and rapidly oscillating Ap stars are all situated in this strip, along with pre-main-sequence pulsators. On the other hand, the first partial ionization zones of hydrogen and helium, combined with strong and efficient convection, are responsible for the heat-driven oscillations in cool red giants and supergiants, such as the Mira stars and semiregular variables; hence they are situated along the cool, that is, red, side of the classical instability strip. Finally, opacity features associated with the iron-group elements are responsible for oscillations in the hottest stars, such as β Cep stars, slowly pulsating B stars, B supergiants, and also in the evolved subdwarf B stars. Stochastically excited oscillations are expected in all stars with an outer convective envelope, *i.e.*, along the main sequence up to masses of about $1.5\,\mathrm{M}_\odot$ and anywhere from the end of the main sequence up to the giant and asymptotic giant branch. The hottest pulsators among the compact stars are grouped together in a class termed GW Vir stars. They are dominantly driven by the heat mechanism acting in the partial

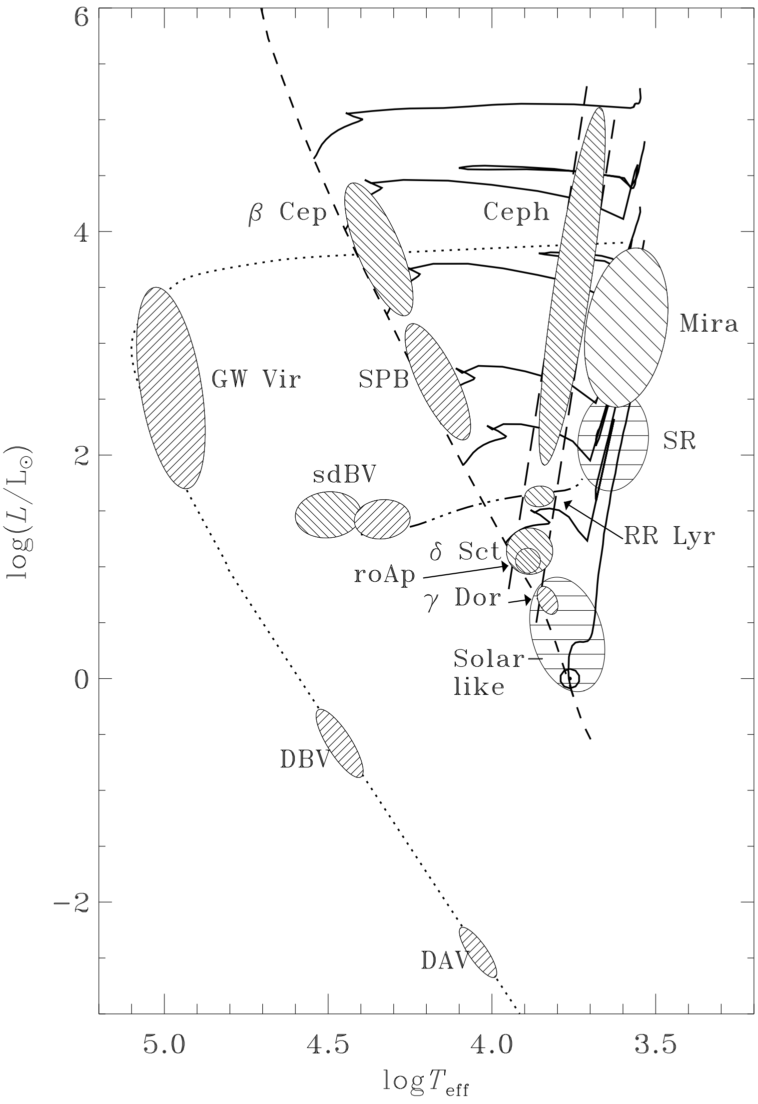

Figure 2.1: Hertzsprung-Russell Diagram showing different classes of pulsating stars. Some of these are named after a particular member of the class. Others are acronyms, standing, respectively, for: rapidly oscillating Ap (roAp); Slowly Pulsating B (SPB); subdwarf B variables (sdBV). The group labelled GW Vir includes what has formerly been known as the PNNV stars (for Planetary Nebulae Nuclei Variables), and the variable hot DO white dwarfs (DOV); the DBV and DAV stars are variable DB (helium-rich) and DA (hydrogen-rich) white dwarfs. The parallel long-dashed lines indicate the Cepheid instability strip. Figure courtesy of Jørgen Christensen-Dalsgaard.

ionization zones of carbon and oxygen at their surface. It was only recently realized that there is a common cause of the oscillations for stars in this part of the HR diagram, which includes the DOV and DBV stars, as well as the central stars of planetary nebulae and Wolf-Rayet stars (Quirion *et al.* 2006). The cooler DAV stars, on the other hand, are compact pulsators driven by a phenomenon termed convective driving by Brickhill (1991). A convection-related mechanism, convective blocking, also operates in the γ Dor stars along the main sequence.

Adopting a philosophy similar to the one in the review by Gautschy & Saio (1996), we organize the journey with five main stopping areas to discuss pulsations near the main sequence, in pre-main-sequence stars, in evolved stars of low mass, in evolved stars of high mass and in compact objects. Evolved stars of high mass (typically above $30\,\mathrm{M}_\odot$) are currently not yet the subject of seismic inference because the observational establishment of their oscillation frequencies is much harder than for the stars in all other categories, due to occurrence of several kinds of instabilities in their atmospheres. Moreover, our theoretical understanding of their oscillations is far less detailed than for lower-mass stars for which radiation-driven mass loss can be ignored. For this reason we are at present unable to make a detailed comparison between their overall observed variability and in-depth stellar structure and oscillation computations; hence we do not come back to these stars after this chapter. The same holds true for the pre-main-sequence pulsators. While oscillations have clearly been found in several of these, we lack good knowledge of their frequency spectra and mode identification for the moment. Gravitational-wave asteroseismology through nonradial oscillations of interacting white-dwarf binary stars, neutron stars and black holes is also a field still under development lacking strong observational constraints. We discuss it briefly in this chapter. Finally, the classical large-amplitude monoperiodic radial pulsators, such as RR Lyrae stars, Cepheids, RV Tauri stars, Mira stars and semi-regular variables, are not suitable for seismic modelling of interior physics. We discuss their pulsational characteristics in this chapter, including the seismic potential of double- and triple-mode classical pulsators, in the section on Cepheids and do not return to them further on in the book.

Before beginning our journey into asteroseismology, we first give a brief overview of stellar evolution and of the impact of large-scale surveys on pulsating star research.

2.1 Stellar Evolution in a Nutshell

Stars are born in groups, called clusters, when dense interstellar molecular clouds collapse under the effect of gravity. Any perturbation within the cloud, due to whatever origin, will result in a collapse whenever the mass of the cloud is above a certain threshold: $M > M_\mathrm{J} \sim T^{3/2}\rho^{-1/2}\mu^{-3/2}$, with T the temperature of the cloud, ρ its density and μ its molecular weight. This condition for free-fall collapse is known as the *Jeans criterion*. The process will continue as long as the collapse happens isothermally. As soon as the free-fall time becomes similar to the thermal relaxation time, however, an adiabatic contraction takes over, and the process comes to a natural end, leaving behind protostellar fragments with masses of the order of stellar masses. Owing to their initially rather low internal temperature and consequent high opacity, the entities that result from the process, called *protostars*, are initially fully convective and hence are located on the *Hayashi track*.

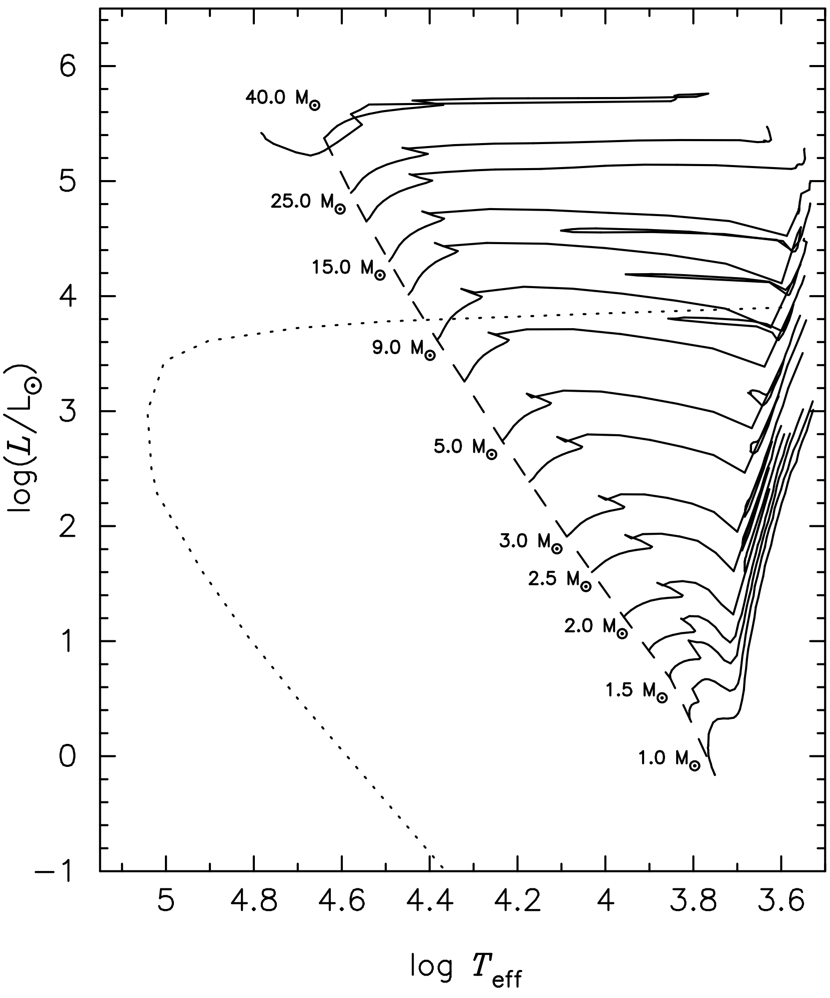

Figure 2.2: HR diagram showing the evolutionary tracks of stars with masses between 1 $M_\odot$ and 40 $M_\odot$ (full lines, Schaller *et al.* 1992). The dashed line is the zero-age main sequence and the dotted line symbolizes the transition phase from the Asymptotic Giant Branch to the white-dwarf cooling track.

After the rapid dynamical contraction, the protostar reaches hydrostatic equilibrium and is said to have entered its *pre-main-sequence phase*. The further contraction of the star implies that the star descends the Hayashi track, keeping essentially the same effective temperature and decreasing in luminosity. As the internal temperature gradually increases, the opacity decreases and the convective zone starts to recede from the center of the star. This implies that the star leaves its Hayashi track and starts radiative contraction along its *Henyey track*. As contraction proceeds in a more and more transparent matter, the star reverses its downward luminosity trend into a rising one.

The increasing core temperature initiates the proton-proton reaction, which converts H into ^{2}H, and this fresh deuterium is immediately burnt into ^{3}He. The less massive the pre-main sequence star, the closer to the Hayashi track occurs this first nuclear burning. The full proton-proton chain cannot be completed yet since ^{3}He has not yet reached its equilibrium value. As a consequence, the temperature sensitivity of the nuclear reactions is high (about three times the sensitivity of proton-proton chain operating at equilibrium) and this leads to the development of a convective core. In stars less massive than about $1.1\,M_\odot$, this convective core will disappear as soon as the proton-proton chain has all its intermediate chemical species at equilibrium. More massive stars, on the contrary, rapidly switch to hydrogen burning through CNO cycle, which is far more temperature sensitive than the proton-proton chain at equilibrium, and they keep their convective core during the whole central hydrogen burning phase.

The accretion continues during most of the pre-main-sequence phase, on a Kelvin-Helmholtz time scale. Consequently, protostars with masses above about $9\,M_\odot$ move so fast from their Hayashi track to the main sequence that they are unobservable in their pre-main-sequence phase as they keep on being embedded in a thick circumstellar shell of infalling material. Pre-main-sequence stars with masses between $\sim$1.6 and $9\,M_\odot$ end their accretion phase before they reach the main sequence. Such pre-main-sequence stars are termed *Herbig Ae/Be stars*. In pre-main-sequence stars with masses between some 0.8 and $1.6\,M_\odot$, as soon as the accretion process stops, the star lights up in the HR diagram as an optically bright source named *T Tauri star*. Observations of both Herbig Ae/Be stars and T Tauri stars suggest that they undergo active surface phenomena such as a stellar wind and differential rotation.

Once the hydrogen is burning in full equilibrium and completely dominates the energy production, the star reaches a state of thermal equilibrium and is said to be born on the *zero-age main sequence* (ZAMS). The circumstellar remnant material vanishes within a Kelvin-Helmholtz time and the star forgets its formation history. Protostars with a mass below some $0.08\,M_\odot$ never reach the ZAMS because they become degenerate before having reached a high enough central temperature to burn hydrogen in equilibrium. Such objects are called *brown dwarfs*. Since oscillations have not yet been found in brown dwarfs we will not discuss them further.

The stars spend about 95% of their life on the main sequence, burning H into He on a nuclear timescale. Depending on their mass, the interior structure in terms of radiative, convective, diffusive and rotational energy transport is quite different. The initial chemical composition is also a determining factor in the details of the evolution. Once the central hydrogen is exhausted, the star has reached the *terminal-age main sequence* (TAMS). At that time the hydrogen shell burning takes over as the energy source; the helium core starts contracting, while the outer parts of the star expand greatly, causing the star to move back to and up the Hayashi track as a red giant. The further evolution of the star is now again largely dependent on its mass. Evolutionary tracks for different masses are indicated in Fig. 2.2 and are briefly discussed below.

The gas in the cores of stars with $M \geq 9\,\mathrm{M}_{\odot}$ does not become degenerate before carbon burning, so these objects follow subsequent central burning and shell burning cycles, producing all elements up to iron and nickel. At that stage, the star encounters a major problem because ^{56}Fe and ^{62}Ni are the most tightly bound nuclei. Their fusion into heavier elements would result in less tightly bound nuclei and thus would require an input of energy. The inescapable core contraction is accompanied by photodissociation of its heavy nuclei, transforming them into He nuclei and then into neutrons, with a catastrophic loss of thermal energy and pressure causing the core to collapse. The stupendous release of gravitational potential energy implies that the rest of the star explodes as a supernova, blowing away a huge fraction of its processed material which thus enriches the interstellar medium in the surroundings, and leaving a neutron star or a black hole as a remnant. Rapid neutron capture operates for a brief period during supernova explosions, producing a substantial fraction of the heavy elements beyond iron.

The internal mixing processes acting in these stars while they evolve from the TAMS to the supernova stage are very uncertain, as are the details of their mass loss, which implies we are not able to make accurate predictions of the properties of the star just before the supernova explosion. Stars of such initial mass have typical lifetimes less than a few tens of million years.

The evolution of stars with masses above $25\,\mathrm{M}_{\odot}$ is subject to very strong radiatively-driven winds while on the main sequence and lose a huge amount of mass because of that, dramatically affecting their evolution. The radiation pressure is so strong that they are not very stable, resulting in complex phenomena such as instabilities and outbursts. Such stars are termed *luminous blue variables* and, after their hydrogen envelope has essentially been blown away, *Wolf-Rayet stars*. They live less than a few million years, also finishing their lives in supernovae explosions, and are likely progenitors of stellar black holes.

At the other end of the mass range, stars with masses below about $0.5\,\mathrm{M}_{\odot}$ have not yet had time to evolve off the main sequence, but when they do their core temperatures will not become high enough to initiate helium burning, so they will finish their lives as He white dwarfs. Stars with an initial mass in the range $0.5 \leq M \leq 2.3\,\mathrm{M}_{\odot}$, the precise cut-off depending on the metallicity, have a degenerate helium core after the main sequence. They reach the TAMS after a few to several gigayears, depending on the birth mass. The shell burning after the TAMS accompanies a shrinkage of the core until the latter reaches the temperature at which helium burning through the triple-α reaction starts. Since this happens in degenerate matter, a thermal runaway occurs and the star is said to undergo a *helium flash*. The helium flash lifts the degeneracy in the helium core, and the star settles down on the *horizontal branch* burning helium in its core and hydrogen in a shell. In case the metal abundance is less than about 10% that of the Sun, the horizontal branch is very extended, depending on the mass and the extent of the hydrogen-rich envelope (*e.g.*, Prialnik 2000, Chapter 8).

Stars with higher metallicity are redder because their opacity is higher, and they cluster near the red-giant branch in the *red clump*.

At that stage of evolution, the low-mass central helium burning objects join the stars with initial birth mass $2.3\,\mathrm{M}_{\odot} \leq M \leq 9\,\mathrm{M}_{\odot}$, which started helium burning calmly as their core at the end of the TAMS did not reach degeneracy. After the central helium exhaustion, the stars are forced to live on helium- and hydrogen-shell burning. They are said to ascend the *Asymptotic Giant Branch* (AGB). In this phase nuclear burning involves *thermal pulses* due to the extinction and re-ignition of the helium shell burning. This implies a large amount of internal mixing, leading to complex nuclear reactions. The slow-neutron capture process becomes active and leads to nuclear yields beyond the iron-peak elements. These products are dredged up for stars with $M \geq 4\,\mathrm{M}_\odot$. Stars with initial masses above some $6\,\mathrm{M}_\odot$ and below some $9\,\mathrm{M}_\odot$ may experience some stages of carbon burning, leading in the end to an O, Ne, Mg white dwarf. The lower limit mentioned of $6\,\mathrm{M}_\odot$ in birth mass for which this occurs is rather uncertain and depends heavily on the mass loss and rotational mixing since the TAMS. It may be that only the heaviest stars in this mass range effectively ignite carbon. Stars on the AGB lose a significant amount of their mass through a dust-driven wind in combination with large-amplitude pulsations. The outer layers are so loosely bound due to the envelope expansion accompanying the shell burning that they are easily removed by the radiation acting on dust particles. The dust-driven mass loss stops as soon as the hydrogen-burning shell is largely extinguished and the star enters its *post-Asymptotic Giant Branch* (post-AGB) phase. The remaining envelope is rapidly lost and the resulting circumstellar material shines for a few thousand years as a *planetary nebula*. This exposes the degenerate core as a *white dwarf*, which subsequently evolves down along the *white-dwarf cooling track* over a timescale of billions of years. The coolest, and hence oldest, white dwarfs in the solar neighbourhood have the same age as the Galaxy, around 10 Gyr.

Most of the post-AGB stars start cooling off directly as a white dwarf, *i.e.*, do not return to the AGB once they left it. About 25% of the post-AGB stars, however, undergo a so-called *born-again* episode. Such episodes are due to a late thermal pulse, re-igniting helium near the hot white-dwarf core, either when the hydrogen shell burning is still active or else shortly after the hydrogen burning has essentially stopped. In both cases, the star returns rapidly to the AGB and becomes a hydrogen-deficient helium-burning object, consisting of a CO core surrounded by surface layers rich in helium, carbon and oxygen (Werner & Herwig 2006). They traverse once more the HR diagram towards the white-dwarf phase in less than 200 years. Depending on the core mass and on the effective temperature, a strong or a weak radiation-driven wind occurs in that stage. The star thus shows up as a hydrogen-deficient compact central star of a planetary nebula. These stars are almost indistinguishable from the Wolf-Rayet central stars of planetary nebulae, usually denoted as [WCE], in the sense that their position in the HR diagram is the same. Their spectra look different, though, because the Wolf-Rayet stars have emission lines in their spectra due to a strong wind, while the luminosity of the post-AGB central stars of planetary nebulae is such that they have only a weak line-driven wind and thus absorption lines.

2.2 Variability studies from large-scale surveys

2.2.1 Hipparcos

One of the most important large surveys of variable stars was carried out by the satellite Hipparcos of the European Space Agency. The mission's name stands for **HI**gh **P**recision **PAR**allax **CO**llecting **S**atellite. It was launched in 1989 and has measured the parallax of some 120 000 bright stars in the solar neighbourhood. The satellite's name is not only an acronym but also refers to the Greek astronomer Hipparchus of Nicea, who was the first to compose a stellar catalogue with the position and brightness of many stars, based upon personal naked-eye observations. Therefore, Hipparchus is considered to be the father of astrometry.

The prime goal of the Hipparcos mission was to measure the distances of stars with unprecedented precision of 2 milli-arc-seconds for the parallax. The proper motions of the stars were measured with an accuracy of 2 milli-arc-seconds per year. This was achieved by measuring each star on average 100 times during the 3.3-year lifetime of the mission. The Hipparcos filter was a broad-band white-light filter sensitive to wavelengths between 4 000 Å and 8 000 Å. The Hipparcos data were further complemented with those of the Tycho experiment, which determined the parallax and proper motion of a million fainter stars with an accuracy of 30 milli-arc-seconds (per year).

A very important by-product of the Hipparcos mission was that it provided us for the first time with an unbiased view of variable stars with periods longer than approximately one hour in the solar neighbourhood. Indeed, for each star a unique time series was measured, with, on average, 100 time points that were quasi-randomly chosen during the 3.3 years. These are time series that are very different from those obtained with ground-based instruments. The input catalogue was completely unbiased in the sense that the pre-selection of the target stars did not take into account any knowledge of variability.

The Hipparcos mission led to the discovery of a few thousand new periodically variable stars and yet another few thousand variables without a clear dominant periodicity. These were made publicly available by means of two catalogues: the "Catalogue of Periodic Variables" and the "Catalogue of Unsolved Variables". The latter contains stars that are clearly variable but for which no obvious periodicity could be unravelled from the data for different types of reasons (long-term trends, very long uncovered periods, too low amplitude variability, *etc.*).

One of the more striking results derived from the mission was the discovery of numerous new variables with periods of the order of days. Such variables are indeed very hard to find from (single-site) ground-based data, which suffer from strong one-day aliasing (see Chapter 4 for a definition of this phenomenon). The Hipparcos mission particularly had a large impact on the study of slowly pulsating B stars and γ Dor stars. The number of such nonradial g-mode oscillators known was increased by a factor more than ten in both cases (Waelkens *et al.* 1998, Handler 1999), leading to about one hundred candidate class members for each of these two classes. As a result, extensive follow-up long-term ground-based photometric and spectroscopic campaigns were organized to study the pulsational behaviour of the brightest such class members (Aerts *et al.* 1999, Mathias *et al.* 2001, De Cat & Aerts 2002 and De Cat *et al.* 2006 for the slowly pulsating B stars and Eyer & Aerts 2002, Handler & Shobbrook 2002, Henry & Fekel 2004, 2005, Mathias *et al.* 2005 and Cuypers *et al.* 2006 for the γ Dor stars). These campaigns led to the general properties of the stars as discussed further on in this chapter.

It is also worth noting that the number of known eclipsing binaries was about doubled from Hipparcos, with the discovery of 343 new ones (*e.g.*, Sönderjhelm 2000).

Surveys of variable stars from space will come from the high time-resolution missions CoRoT[1] (Convection, Rotation and planetary Transits, launched on 27 December 2006) and Kepler[2], to be launched at the end of 2008) as well as from Gaia[3], scheduled for launch near the end of 2011). The numbers of new variables to be discovered from these missions will be outrageously large (certainly in the millions), requir-

---

[1] `http://corot.oamp.fr/`

[2] `http://www.kepler.arc.nasa.gov/`

[3] `http://www.rssd.esa.int/SA-general/Projects/GAIA/`

ing fully automated variability classification tools based on Artificial Intelligence methodology (Sarro *et al.* 2006, Debosscher *et al.* 2007).

2.2.2 Ground-based surveys

Significant progress on the group properties of large-amplitude oscillators, such as Cepheids, RR Lyrae stars, and red-giant and supergiant pulsators, was made by several large surveys that were initiated in the early nineties. These surveys were set up with the goal to search for **MA**ssive **C**ompact **H**alo **O**bjects or MACHOs. The idea was that such MACHOs, if discovered, could perhaps help explain some of the missing dark matter in the Universe. The primary aim of the surveys was therefore to test the hypothesis that a significant fraction of the dark matter in the halo of the Milky Way is made up of objects such as brown dwarfs and planets.

It was Paczynski (1986) who suggested that dark matter could be discovered from a microlensing effect. The idea is that, when a dark compact massive body (the lens) passes in between us and a background light source, the latter's apparent luminosity increases because the dark body acts as a gravitational lens, concentrating the light rays of the source in the line of sight due to light bending according to general relativity. This implies a magnification of the source luminosity which is independent of wavelength. One can therefore use this phenomenon to discover dark compact bodies within our galactic halo, *e.g.*, using the stars of the Magellanic Clouds or of the Galactic Bulge as light sources. The duration of the magnification depends on the speed, the position and the mass of the deflector and ranges from half an hour to about two months for dark masses ranging from a lunar mass to a solar mass. The magnification can reach values from a few to a thousand. The phenomenon is rare and non-repetitive, as it requires a good alignment of light source, lensing dark body and observer while the lens and observer move with respect to each other. Microlensing can also be used to discover exoplanets orbiting around the lens. In that case, the effect of the planet on the lensing gravitational field causes a brief increase in the magnification.

The detection of microlensing events thus requires long-term monitoring of a vast number of light sources with high precision photometry, since the events are rare. Several large observational initiatives to discover MACHOs were set up more than a decade ago and additional ones were started after 1995 to search for exoplanets. Important by-products of such surveys are huge inventories of accurate light curves of stars, among them Cepheids and RR Lyrae stars and long-period red variables, but also many other periodic variables.

The best known surveys are MACHO[4] itself and OGLE[5] which stands for **O**ptical **G**ravitational **L**ensing **E**xperiment. EROS[6] is another survey whose acronym stands for **E**xpérience pour la **R**echerche d'**O**bjets **S**ombres while MOA[7], which denotes **M**icrolensing **O**bservations in **A**strophysics, started somewhat later than the previous three surveys.

---

[4] `http://wwwmacho.mcmaster.ca/`

[5] `http://bulge.princeton.edu/∼ogle/`

[6] `http://eros.in2p3.fr/`

[7] `http://www3.vuw.ac.nz/scps/moa/`

These surveys, and others that can be found through links on the webpages mentioned, several of which specifically designed for exoplanet detection, have resulted in millions of stars in the Galactic Bulge and Magellanic Clouds being monitored and led to thousands of lensing events. Besides these events, tens of thousands of variable stars were discovered in the Galactic Bulge and Magellanic Clouds, among which are hundreds of Cepheids, RR Lyrae stars, eclipsing binaries and ellipsoidal variables.

In addition to the microlensing surveys, there are also all-sky surveys specifically designed to find variable stars. They have been carried out with small wide-field cameras since the mid-1990s. The best known and largest of thesed surveys is ASAS[8], the **A**ll-**S**ky **A**utomated **S**urvey (Pojmański 1997). A summary of the variables found by ASAS is provided in Pojmański & Maciejewski (2004, 2005 and references therein.) The **2 M**icron **A**ll **S**ky **S**urvey[9] (2MASS, Beichmann *et al.* 1998), on the other hand, is a catalogue of over 100 000 000 individual objects, the vast majority of which are stars of spectral type K and later. Its monitoring was carried out in three wavebands, J (1.25 μm), H (1.65 μm), and K (2.2 μm), with limiting sensitivity (10σ detection) of point sources with K less than 14. The all-sky coverage was selected primarily to support studies of the large-scale structure of the Milky Way and the Local Universe. Nevertheless, the catalogue is of much value for variable star research, particularly when combined with the microlensing surveys discussed above, *e.g.*, Fraser *et al.*'s (2005) study of long-period variables to which we will return later in this Chapter.

The **S**loan **D**igital **S**ky **S**urvey[10] (SDSS, Stoughton *et al.* 2002) is an imaging survey that covers one quarter of the celestial sphere while collecting also spectra of hundreds of thousands of targets. The imaging data are collected in five bandpasses (u, g, r, i, and z) and are complete until magnitudes 22.0, 22.2, 22.2, 21.3, and 20.5, respectively. The SDSS turned out to be a very important survey for faint (compact) objects that had been missed in previous surveys with brighter limits, such as Cataclysmic Variables (CVs, Szkody *et al.* 2002), cool dwarfs (Hawley *et al.* 2002), white dwarfs (Harris *et al.* 2003), and spectroscopic binaries (Pourbaix *et al.* 2005), and of course the pulsating ones among all these categories. Another important, more recent survey, specifically designed to find emission-line objects, is IPHAS, which stands for the **I**saac **N**ewton **T**elescope **P**hotometric **H**-**A**lpha **S**urvey[11] of the Northern Galactic Plane (Drew *et al.* 2005). It spans the latitude range $-5^\circ < b < +5^\circ$ and reaches down to $r' = 20$. The final catalogue of the IPHAS point sources is still awaited. It will contain photometry on about 80 million objects, making it a major future source for the study of stellar populations in the disk of the Milky Way.

The impact of large-scale surveys on pulsating-star research was summarized after about ten years of microlensing monitoring in Szabados & Kurtz (2000). We refer to the web pages of the consortia mentioned above for more up-to-date achievements and recent papers on variable star research, as well as on detected lenses and their interpretation. While the surveys mainly led to the discovery of new large-amplitude oscillators, some nonradial oscillators such as β Cep stars and δ Sct stars were also found (see, *e.g.*, Pigulski & Kołaczkowski 2002, Pigulski *et al.* 2003, Pigulski 2005), as well as numerous new compact oscillators (see below). As the surveys mainly observe faint members of the classes, and as they do not provide multicolour photometry of mmag level precision nor high-resolution, high S/N spectroscopy, these discoveries have not yet led to mode identification; hence asteroseismic modelling of the individual targets has so far not been

---

[8] `http://archive.princeton.edu/∼asas/`

[9] `http://www.ipac.caltech.edu/2mass/`

[10] `http://www.sdss.org/`

[11] `http://astro.ic.ac.uk/Research/Halpha/North/index.shtml`

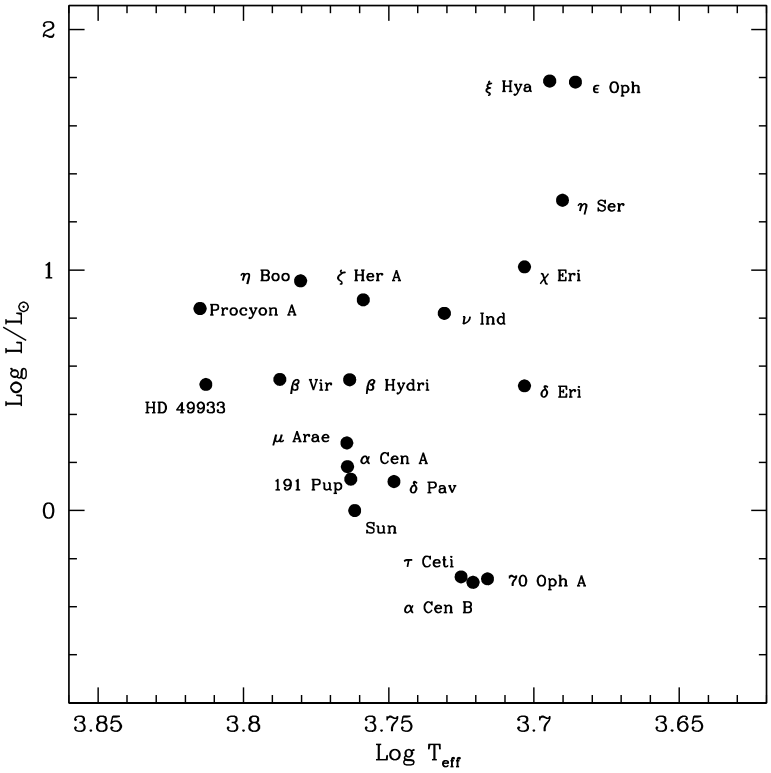

Figure 2.3: HR diagram showing the stars in which solar-like oscillations have been detected. Figure courtesy of Fabien Carrier.

possible. Thus massive follow-up projects are required specifically dedicated to this task.

2.3 Oscillations near the main sequence

2.3.1 Solar-like oscillations in solar-like stars

The best case of a solar-like star with the clearest solar-like oscillations is of course the Sun. Its oscillation frequency spectrum was already shown in Fig. 1.8 and reveals hundreds of peaks centred around 3 mHz with corresponding periods between 3 and 15 minutes. The brightness variations have amplitudes near 8 ppm for the strongest modes and down to the detection threshold of about 1 ppm. These variations correspond to velocity amplitudes of a few to tens of $\mathrm{cm\,s^{-1}}$.

As the oscillations of the Sun are caused by turbulent convective motions near its surface, we expect

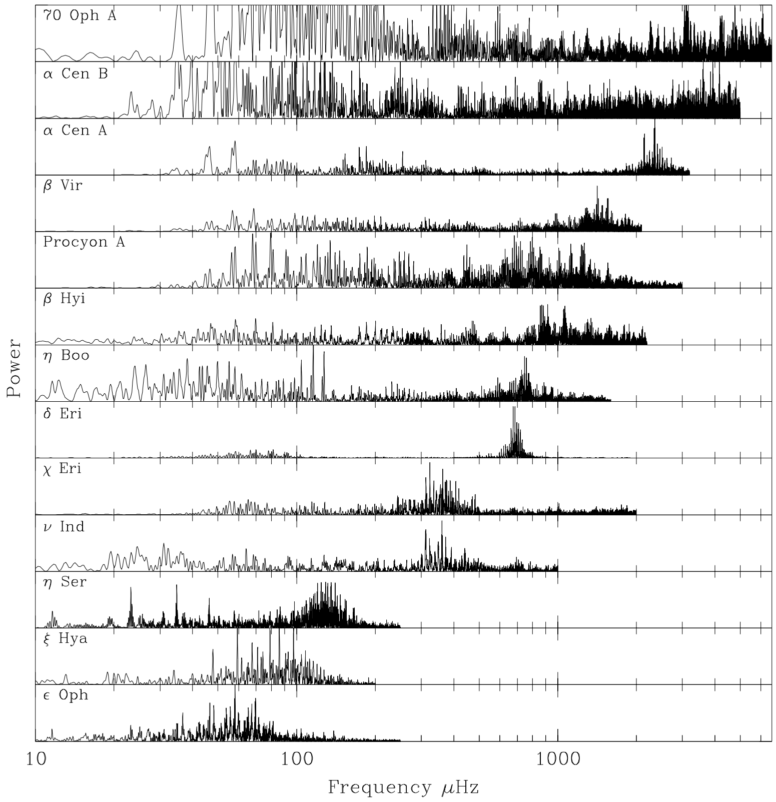

Figure 2.4: Frequency spectra of a sample of solar-like oscillators covering the entire range in spectral type. Figure courtesy of Fabien Carrier.

such oscillations to be excited in all stars with outer convection zones. Solar-like oscillations are indeed predicted for the lowest-mass main-sequence stars up to objects near the cool edge of the classical instability strip with masses near some 1.6 $M_\odot$ (*e.g.*, Christensen-Dalsgaard 1982; Christensen-Dalsgaard & Frandsen 1983; Houdek *et al.* 1999) as well as in red giants (Dziembowski *et al.* 2001). Such stochastically excited oscillations have very tiny amplitudes, which makes them hard to detect, particularly for the low-mass stars. The velocity amplitudes were predicted to scale roughly as L/M before the first firm discoveries of such oscillations in stars other than the Sun (Kjeldsen & Bedding 1995). This scaling law was later modified to $(L/M)^{0.8}$ from excitation predictions based on 3D computations of the outer atmosphere of the stars (Samadi *et al.* 2005), resulting in lower amplitudes compared with those found for 1D models.

The search for solar-like oscillations in stars in the solar neighbourhood has been ongoing since the early eighties. The first indication of stellar power with a frequency dependence similar to that of the Sun was obtained by Brown *et al.* (1991) in α CMi (Procyon, F5IV). The first detection of individual frequencies of solar-like oscillation was achieved from high-precision time-resolved spectroscopic measurements only in 1995 for the G5IV star η Boo (Kjeldsen *et al.* 1995); Brown *et al.* (1997) could not establish a confirmation of this detection from independent measurements, but it was subsequently confirmed by Carrier *et al.* (2003) and Kjeldsen *et al.* (2003). It took another four years before solar-like oscillations were definitely established in Procyon (Martić *et al.* 1999). Subsequently, such oscillations were found in two more stars: the G2IV star β Hyi (Bedding *et al.* 2001) and the solar twin α Cen A (Bouchy & Carrier 2001). These important discoveries opened the floodgates which led to several more discoveries, a summary of which was provided by Bedding & Kjeldsen (2003). Meanwhile, solar-like oscillations have been firmly established in numerous stars. Their position in the HR diagram is displayed in Fig. 2.3. Frequency spectra of a selected sample, covering the whole range in spectral type, is shown in Fig. 2.4. The detected frequencies and frequency separations for all stars behave as expected from theoretical predictions and scaling relations based on extrapolations from helioseismology.

Detailed seismic studies of stars with stochastically excited modes are currently still in their infancy compared with helioseismology. However, given the recent detections and the continuing efforts to improve them, we expect a real breakthrough in the seismic interpretation of the targets in the coming years.

The quest for solar-like oscillations in metal-poor stars considerably less massive than the Sun is an important goal of asteroseismic space missions. This is particularly so because asteroseismology has proven to be a very successful technique to probe interior stellar structure and derive a high-precision age estimate (Christensen-Dalsgaard 2002). Indeed, such low-mass stars are among the oldest in our Galaxy (and hence in the Universe) and accurate age estimates of such objects, which can in principle be achieved from measuring their large and small separations as in the Sun, can provide a good age determination of the Universe which would be completely independent of any method currently in use.

2.3.2 γ Dor stars

In 1995, a new group of Population I nonradially oscillating stars was established near the intersection of the red edge of the classical instability strip and the main sequence. This followed from the discovery of multiperiodic variability with amplitude near 0.1 mag in the F0V star 9 Aur and the realization that the three stars γ Doradus (F4III), HD 96008 (F0V), and HD 164515 (F2IV-V) have similar behaviour (Krisciunas *et al.* 1992). This group of stars have early-F spectral type and are called after the prototype, the star γ Doradus whose variability was first discovered by Cousins *et al.* (1989; Cousins 1992) and extensively studied by Balona *et al.* (1996).

As already mentioned in Sect. 2.2.1, the Hipparcos mission was very important for the discovery of new class members in view of the intrinsic periodicities near one day and the difficulty to study such variations from the ground. Some 50 confirmed members are established by now, while more than 100 additional candidates are being studied observationally (*e.g.*, Mathias *et al.* 2005; Henry *et al.* 2005; De Cat *et al.* 2006 and references therein), most of them originally found from mining the Hipparcos database. The stars have multiperiodic behaviour with individual periods between some 0.5 and 3 d, which is an order of magnitude longer than acoustic modes would have for such stars. Their variability is therefore interpreted in terms of multiperiodic high-order nonradial g modes.

There are very few long-term multicolour and/or high-resolution spectroscopic datasets available for γ Dor stars. Such datasets exist only for some selected stars (*e.g.*, Poretti *et al.* 2002; Aerts *et al.* 2004), besides 9 Aur and γ Dor. The particular case of g modes with long periods of the order of a day implies that the data sets of such oscillators consist of only a few points per night, and makes it difficult to illustrate the periodicity in the time domain. One therefore usually uses phase diagrams (see Chapter 4 for a formal definition). The periodograms of the ground-based Geneva data of HD 12901 (F2V) are shown as a representative example for the whole class in Fig. 2.5. Figure 2.6 shows the phase diagrams after identification of the frequencies. It can be seen from Fig. 2.6 that the variations have low amplitudes. The three frequencies indicated are trustworthy only because they occur in independent datasets (Hipparcos and/or radial-velocity data), a situation often encountered in frequency analysis as will be explained in Chapter 4. All existing data are in agreement with the interpretation in terms of multiperiodic g modes.

The observational properties of γ Dor stars were summarized by Kaye *et al.* (1999). The class members have masses between 1.5 and 1.8 $M_\odot$. Handler & Shobbrook (2002) made a careful observational study to understand the relationship between δ Sct oscillations (see below) and the behaviour of the γ Dor stars. They found a very clear separation in oscillatory behaviour between the two classes, except for the hybrid star HD 209295 which has both p and g modes, but this object is a member of a very close eccentric binary and its g modes seem to be tidally driven (Handler *et al.* 2002, see Sect. 2.8.2).

The earliest proposals for an excitation mechanism came from Guzik *et al.* (1998), who proposed driving by convective-flux blocking at the base of the convective envelope. This mechanism was treated in the frozen-convection approximation, in which the perturbation to the convective flux is ignored. The resulting instability strip was studied by Warner *et al.* (2003). As noted by, *e.g.*, Löffler (2000) and Dupret *et al.* (2005a) these calculations did not appropriately take into account the fact that since these stars have well-developed outer convection zones the pulsation–convection interaction must be taken into account in a detailed way in instability calculations. This was recently achieved by Dupret *et al.* (2005a) by means of a time-dependent treatment of the convection. It allowed them to interpret and predict the g-mode instabilities observed in the γ Dor stars and to quantify an appropriate value of the mixing length parameter between 1.8 and 2.2 local pressure scale heights for γ Dor stars. Their instability strip is shown in Fig. 2.7. Interestingly, they found that convective blocking was in fact the dominant instability mechanism. Moreover, Dupret *et al.* (2005b) applied their theory to interpret successfully the multicolour behaviour of the five best studied γ Dor

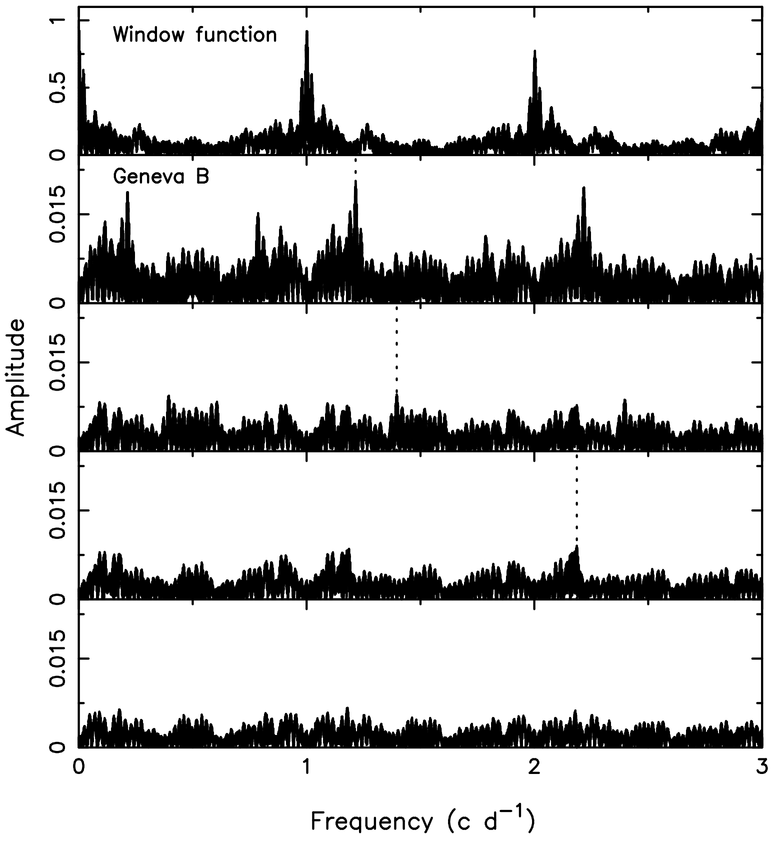

Figure 2.5: Spectral window (top) and frequency spectra after subsequent stages of prewhitening (second to fifth panel) for single-site ground-based Geneva B data of the γ Dor star HD 12901. The three detected frequencies which were derived from independent data sets are indicated as dotted lines. (From Aerts *et al.* 2004.)

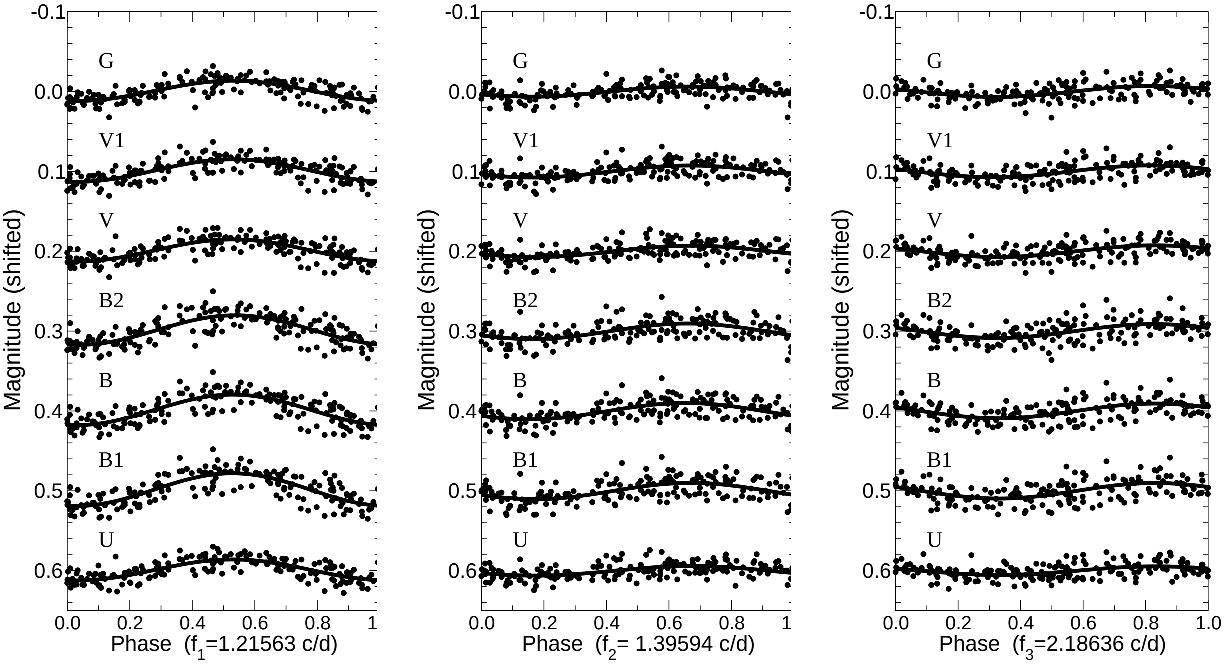

Figure 2.6: Phase diagrams of the γ Dor star HD 12901 for the three frequencies indicated as dotted lines in Fig. 2.5. (From Aerts *et al.* 2004.)

stars. A warning is needed, however, since these theoretical computations ignore the effects of the Coriolis and centrifugal forces, while most of the γ Dor stars are fast rotators, in the sense that their oscillation periods are of similar magnitude to their rotation period. The urgently required investigation of the rotational effects on current theoretical predictions remains to be carried out.

At present, very large observing efforts are being undertaken by several research teams, including long-term multicolour photometric monitoring and high-resolution spectroscopic campaigns (De Cat *et al.* 2006 and references therein). The γ Dor stars are very challenging objects in this respect, because beat periods up to years occur. Nevertheless, it seems worthwhile to undertake such endeavours, because these pulsators have the potential to undergo at the same time g modes and solar-like p modes. Indeed, they are situated at the high-mass end where solar-like oscillations are predicted (Fig. 1.11). The firm establishment of the occurrence of both these types of oscillations, which probe very different inner stellar regions, holds very large potential for high-precision seismic inference of their interior structure. For this reason, γ Dor stars are among the prime targets of the CoRoT space mission.

2.3.3 δ Sct stars

The δ Sct stars form a well-established group of Population I pulsating stars with masses in the range $1.5 - 2.5\,\mathrm{M}_\odot$. They are situated at the position where the classical instability strip crosses the main sequence (see

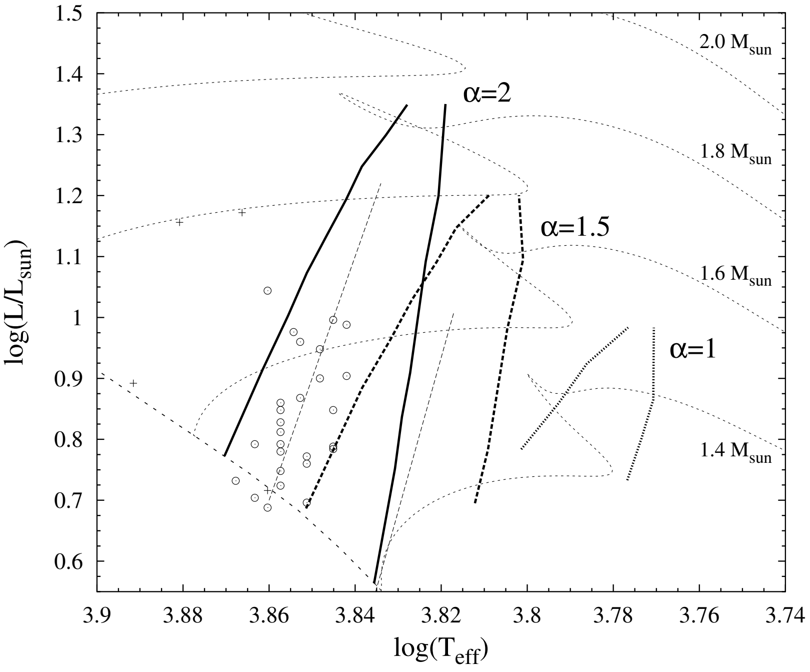

Figure 2.7: The instability strip for $l = 1$ modes of the γ Dor stars for three different values of the mixing length parameter $l = \alpha H_p$ based on the convective blocking mechanism for a time-dependent treatment of the convection (Dupret *et al.* 2005a). The results for the frozen-convection approximation with mixing length parameter $l = 1.87\,H_p$ obtained by Warner *et al.* (2003) are shown as thin dashed lines for comparison. The open circles are all of the bona fide γ Dor stars known up to 2005. The squares are binary γ Dor stars. The evolution tracks are for the masses indicated and were computed assuming overshoot from the convective core of 0.2 pressure scale height. (From Dupret *et al.* 2005a.)

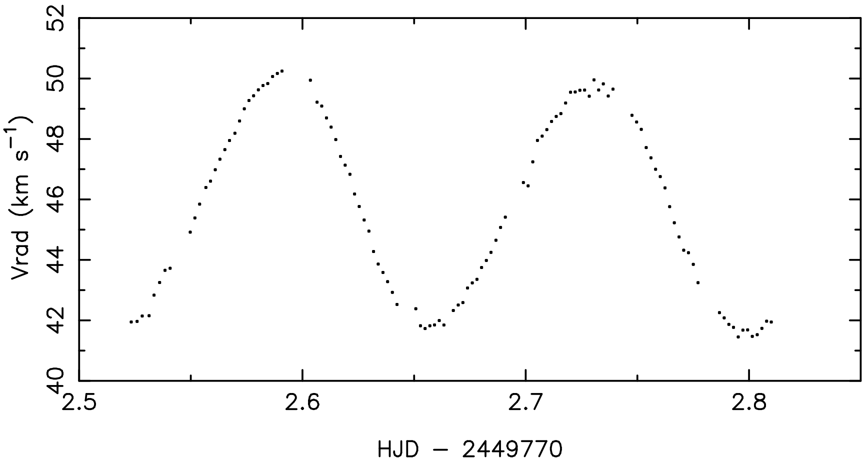

Figure 2.8: Radial-velocity curve of the high amplitude δ Scuti star ρ Pup derived from high-quality spectra of which some are shown in Fig. 5.16. Note the slight deviation from symmetry in this observed curve. Data taken from Mathias *et al.* (1997).

Fig. 1.11) and so are in a stage of central hydrogen or shell-hydrogen burning. The oscillations are driven by the heat mechanism active in the second partial ionization zone of helium.

Both radial and nonradial oscillations occur in δ Sct stars. Those are generally low-order p modes with periods in the range 18 min to 8 hr. The observed amplitudes have a large range, from mmag up to tenths of a magnitude. The highest-amplitude δ Sct stars (also called HADS, meaning high-amplitude δ Scuti stars) are usually monoperiodic radial fundamental mode oscillators and so, at first sight, of less interest for asteroseismology. Nevertheless, Mathias *et al.* (1997) have shown convincingly that the very precise radial velocity curve they obtained for the HADS ρ Puppis (Fig. 2.8) yielded the detection of low-amplitude nonradial modes besides the dominant radial one. Moreover, Poretti (2003) found nonradial modes in the light curves of some HADS. It may very well be that this is a property of all HADS. In several lower-amplitude δ Sct stars, many nonradial oscillations have been detected. The most up-to-date catalogue of δ Sct stars was provided by Rodríguez *et al.* (2000). It contains a summary of all the observational characteristics of more than 600 class members that had been studied up until 2000. A comprehensive analysis of the properties of all these class members was made by Rodríguez & Breger (2001). Montgomery & Breger (2000) and Zverko *et al.* (2004) present the proceedings of two international meetings on, respectively, δ Sct and related stars, and A stars in general, containing a wealth of information. A few δ Sct stars have been observed from space (*e.g.*, θ^2 Tau and Altair with the star-tracker on the WIRE satellite, Poretti *et al.* 2002 and Buzasi *et al.* 2005, respectively; and HD 263551 with the MOST[12] satellite).

Within the class of δ Sct stars one sometimes considers the subclasses of the pulsating λ Boo stars, and classical and evolved metallic-line A (Am) stars. These types of stars have been defined in general (*i.e.*, irrespective of their pulsational nature) as specific classes with anomalous surface abundances. The latter affect the oscillations and, therefore, these subclasses have slightly different behaviour compared with the δ Sct stars with normal abundances (Rodríguez & Breger 2001). Keeping this in mind, the pulsating λ Boo

---

[12] `http://www.astro.ubc.ca/MOST/index.html`

and Am stars are fully compatible with the normal δ Sct pulsators.

Numerous radial and nonradial modes have been detected in some selected δ Sct stars, such as FG Vir (79 frequencies, Breger *et al.* 2005, see Figs 2.9 and 2.10), 4 CVn (34 frequencies, Breger 2000, see Fig. 2.11) and XX Pyx (30 frequencies, Handler *et al.* 2000). These results were all obtained by the Delta Sct Network[13] (DSN), consisting of several telescopes around the globe and led by Michel Breger and his research team at Vienna University in Austria. The frequency spectra of these few, selected, well-studied stars show that the δ Sct stars have complex oscillation patterns, with variable amplitudes from season to season and non-linear resonant mode coupling (*e.g.*, the case of 4 CVn: Breger *et al.* 2000 and Fig. 2.11; V1162 Ori: Arentoft *et al.* 2001; FG Vir: Breger & Pamyatnykh 2006). This complexity turns out to lead to a problem in identifying the modes and hence hampers in-depth seismic interpretation, despite the large number of detected oscillations. An additional problem in identifying the modes is that mixed modes occur, particularly in the more evolved class members. These are modes that have a mixed character, *i.e.*, a g-mode character in the interior and a p-mode character in the outer layers of the star. Mixed modes occur in general in stars that have evolved off the main sequence and are undergoing hydrogen-shell burning.

Pamyatnykh (1999) provided an extensive overview of the history of instability computations in the upper HR diagram and presented his own computations based on progress in opacity determinations by Iglesias & Rogers (1996) and Seaton (1996). His work included the determination of the blue edge of the classical instability strip which is mainly determined by the helium opacity bump. The unstable modes in the hottest δ Sct ZAMS models are found near $\log L/\mathrm{L}_\odot \approx 2$, while instability in the radial fundamental mode occurs all the way up to $\log L/\mathrm{L}_\odot = 5$ for evolved stellar models. In practice, the δ Sct stars are found on the main sequence and near the TAMS, with luminosities ranging from $\log L/\mathrm{L}_\odot \approx 0.6$ up to $\log L/\mathrm{L}_\odot \approx 2$ (Rodriguez & Breger 2001). The heat mechanism is no longer effective for the coolest δ Sct star models. The red edge could therefore not be determined by Pamyatnykh (1999). For such cool stars, the damping and excitation are strongly affected by convection. Houdek (2000) included the time-dependent heat and momentum fluxes following the formulation by Gough (1977) in calculations of δ Sct models and found a return to stability at approximately the correct location of the red edge. The red edge of the instability strip was also computed by Dupret *et al.* (2005a, see Fig. 2.12), who included a time-dependent convection treatment also for δ Sct star models with different values of the mixing length parameter. They compared the results obtained from their time-dependent convection treatment with those resulting from a frozen-convection treatment and found much better agreement with observations. Both Houdek's and Dupret *et al.*'s treatments approximate the red edge in a satisfactory way (Fig. 2.12).

Main-sequence stars near $2\,\mathrm{M}_\odot$ are transition objects as far as the occurrence of a convective ($M < 2\,\mathrm{M}_\odot$) versus radiative ($M > 2\,\mathrm{M}_\odot$) outer zone is concerned. On the other hand, stars develop a convective core between $1\,\mathrm{M}_\odot$ and $2\,\mathrm{M}_\odot$. The class of δ Sct stars encompasses such transition objects and asteroseismology could in principle fine tune our knowledge of the detailed physics of these transitions from convective to radiative energy transport and mixing. Dziembowski & Pamyatnykh (1991) pointed out that the sensitivity of particular nonradial oscillation modes to the size of the mixed stellar core could provide a very valuable asteroseismic test of core overshooting in A- and B-type oscillators. At present, this stage is not yet reached for δ Sct stars, however. Another outlook for the future is the simultaneous detection of heat-driven and stochastically-excited acoustic modes. Indeed, Samadi *et al.* (2002) predicted the occurrence of

---

[13] `http://www.astro.univie.ac.at/~dsn/index.html`

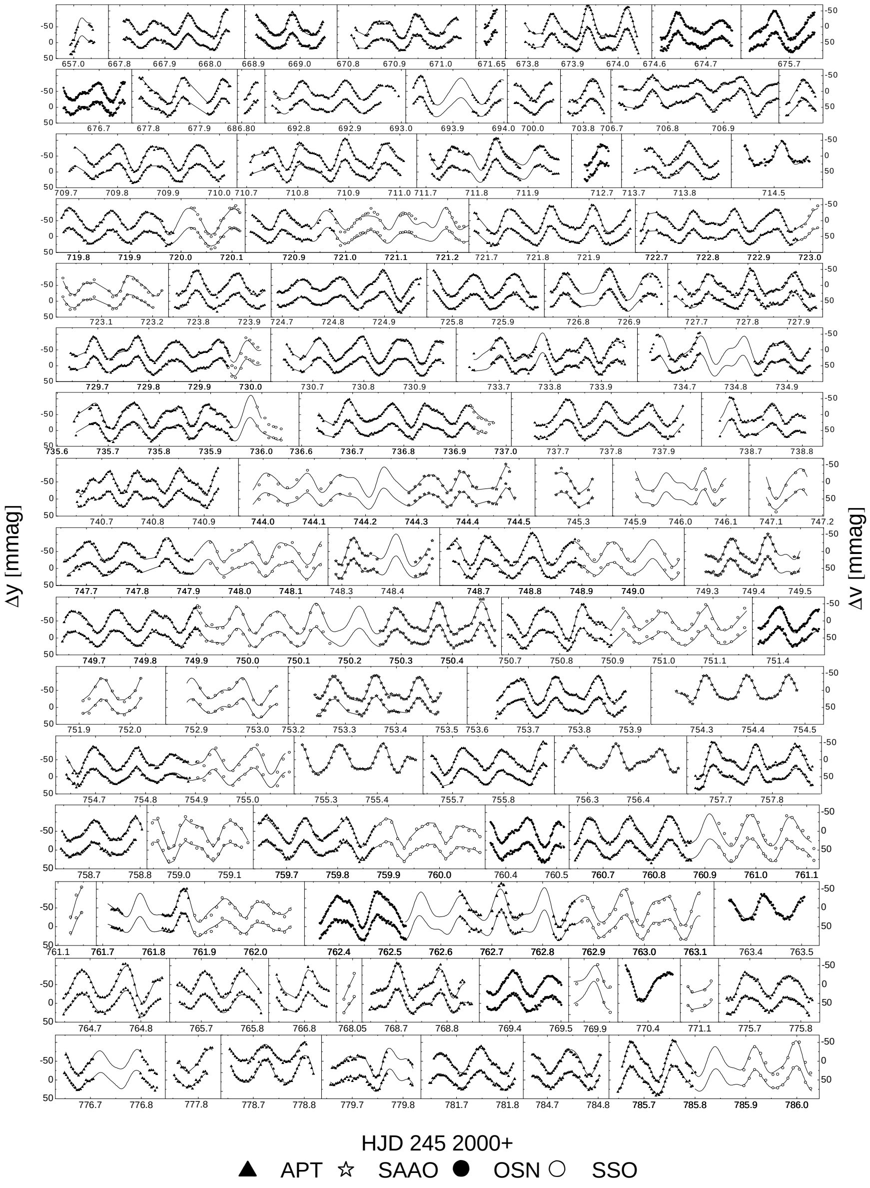

Figure 2.9: Some observed light curves for FG Vir obtained by the DSN (dots) and a fit including 79 significant frequencies (full line). (From Breger *et al.* 2005.)

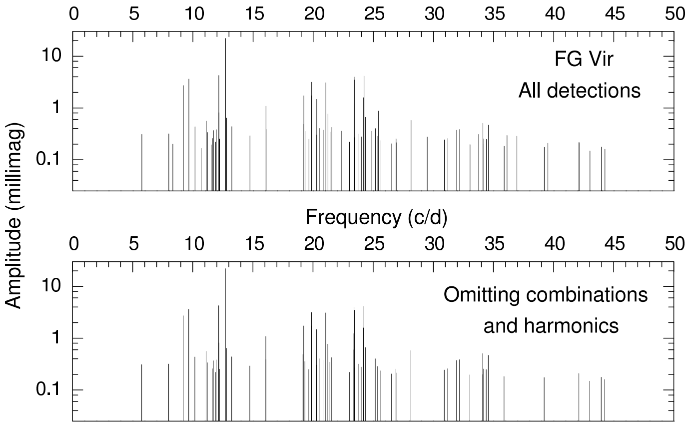

Figure 2.10: Schematic frequency diagram of the δ Sct star FG Vir deduced from DSN data, some of which is shown in Fig. 2.9. (From Breger *et al.* 2005.)

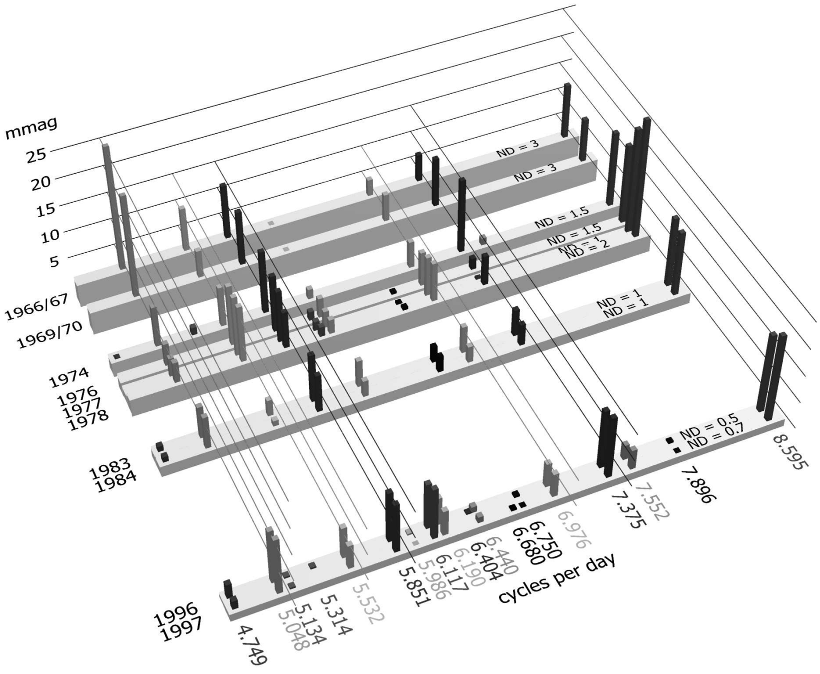

Figure 2.11: Amplitude variability found from season to season in DSN data of the δ Sct star 4 CVn. (From Breger *et al.* 2000.)

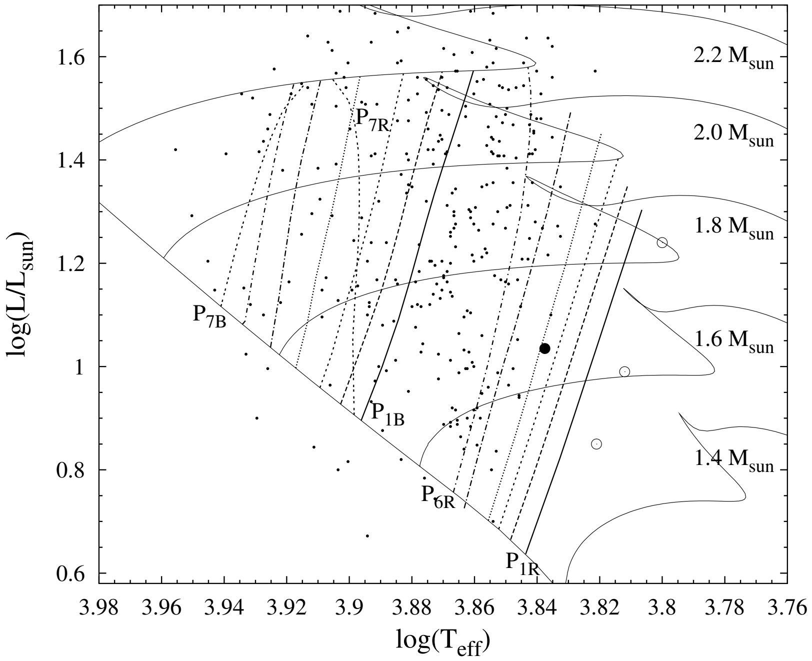

Figure 2.12: Blue and red edges of the instability strip of the δ Sct stars obtained by Dupret *et al.* (2005a). The lines are for radial modes p_1 to p_7 taking a mixing length parameter $l = 1.8\,H_P$. The red edge of the radial fundamental mode computed by Houdek (2000, $\bullet$) and by Xiong *et al.* (2001, $\odot$) are also indicated for comparison. The small dots correspond to all the δ Sct stars in the catalogue of Rodriguez *et al.* (2000). The evolution tracks are for the masses indicated and were computed assuming overshoot from the convective core of 0.2 pressure scale height. (From Dupret *et al.* 2005a.)

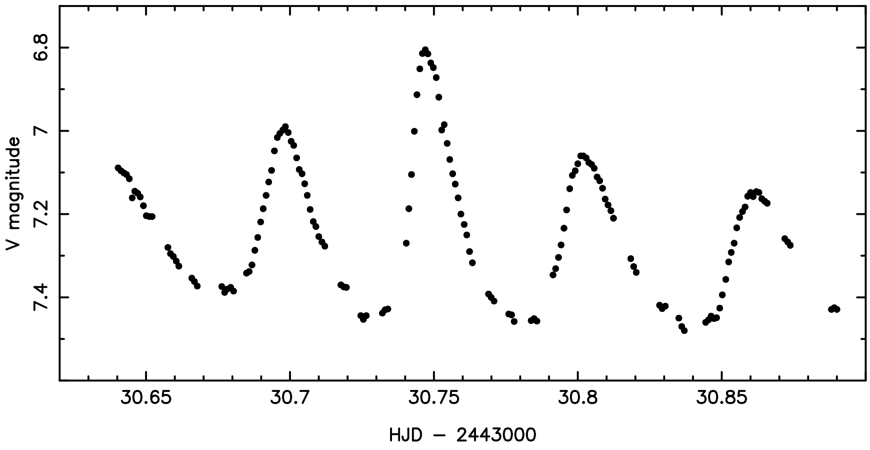

Figure 2.13: Part of the Strömgren y light curve of SX Phe produced from the data in Kim *et al.* (1993).

the latter type of oscillations in this area of the HR diagram. For all these reasons, δ Sct stars are *the* prime targets for CoRoT.

2.3.4 SX Phe stars

The SX Phe stars have variability behaviour which is very similar to the large-amplitude δ Sct stars known as HADS (see the previous section), but the SX Phe stars are old Population II stars, while the HADS are younger Population I stars. For this reason, the SX Phe stars were proposed as a separate class of pulsators by Frolov & Irkaev (1984) and have been regarded as such ever since. They can be recognized by their high amplitude, low metallicity and large spatial motion. Most of them are members of globular clusters, but some occur in galactic discs.

A part of the light curve of the prototype is shown in Fig. 2.13. This star exhibits variations with two distinct frequencies: 18.19 d^{-1} and 23.39 d^{-1} and their harmonics, along with sum and beat frequencies (Fig. 2.14 and Kim *et al.* 1993). The SX Phe stars indeed have a bimodal period distribution which is interpreted in terms of the fundamental and first radial overtone modes being excited. Those pulsating only in the first overtone have nearly symmetrical light curves with peak-to-peak amplitudes less than 0.15 in V. The fundamental pulsators, such as SX Phe itself (Fig. 2.13), have amplitudes above 0.15 in V and asymmetrical light curves. This period separation propagates into two distinct period-luminosity relations with an offset of 0.37 mag, in agreement with theoretical predictions (McNamara 1995).

Rodríguez & López-González (2000) presented the first catalogue of SX Phe stars containing 149 objects in 18 globular clusters of our galaxy and in the Carina and Sagittarius dwarf galaxies. From the observational characteristics of all these 149 members they deduced that the metal abundances and mean periods of these stars show that both parameters are correlated in the sense that the periods of the variables are longer as the metallicity is higher.

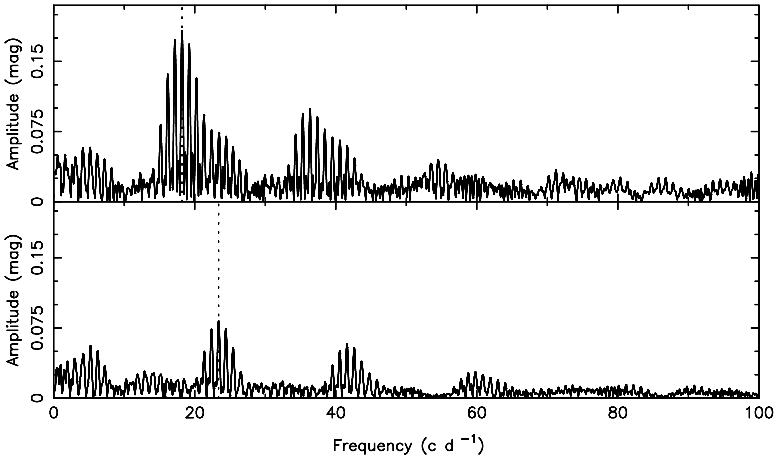

Figure 2.14: Frequency spectrum of SX Phe. The dotted lines indicate the significant frequencies. The bottom panel is for the residuals after prewhitening with 18.19 d^{-1} and its two harmonics. Data taken from Kim *et al.* (1993).

Olech *et al.* (2005) made a dedicated study of the oscillation spectra of 69 SX Phe stars with very diverse pulsational behaviour, all belonging to the globular cluster ω Centauri. The observations are interpreted in terms of multiperiodic oscillations with at least some of the excited modes being nonradial and with the occurrence of rotationally split triplets in some cases. The stellar parameters of the radial mode pulsators are found to be consistent with standard evolutionary models for stars with Z between 0.002 and 0.0002 and in the mass range 0.9 to 1.15 $M_\odot$, and the observed frequencies are in agreement with predictions for unstable modes.

A significant fraction of the SX Phe stars are believed to be blue stragglers. We come back to this issue in Sect. 2.8.3.

2.3.5 Rapidly oscillating Ap stars

Largely within the classical instability strip, close to the main sequence where the δ Sct stars are situated, one also encounters the rapidly-oscillating Ap (roAp) stars. These are Population I stars of spectral type A with a peculiar (hence Ap) chemical surface composition caused by atomic diffusion, and they are also strongly magnetic with global fields typically of kilogauss to many kG strengths. They were discovered as a separate group of pulsators by Kurtz (1982), who reported amplitudes up to about 0.01 mag peak-to-peak in blue wavelengths for five class members. The roAp stars, of which there are now 35 known (see Kurtz *et al.* 2006, Table 1, for a list), have multiperiodic variations with individual oscillation periods between 5.65 and 21 min, which correspond to high-order, low-degree p modes. Many of the modes show frequency multiplets interpreted as being caused by rotational amplitude modulation of modes with pulsation axes that are oblique to the rotation axes of the stars. For extensive overviews of the photometric observations and their interpretation see Kurtz (1990) and Kurtz & Martinez (2000).

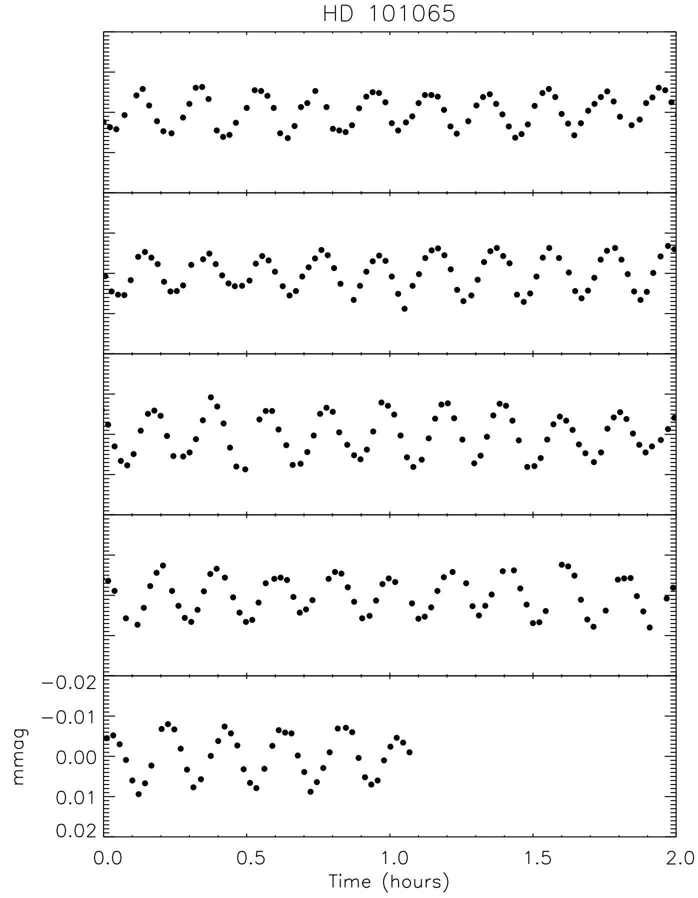

Figure 2.15: Part of the Johnson V light curve of the roAp star HD 101065 obtained by Kurtz *et al.* (1980).

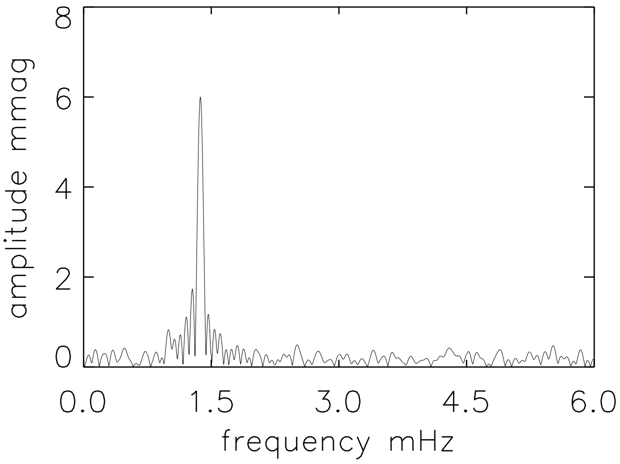

Figure 2.16: Frequency spectrum of the roAp star HD 101065. (From Kurtz *et al.* 1980.)

In Fig. 2.15 we show part of the light curve of HD 101065, the first discovered roAp star (Kurtz 1978, 1980). Its frequency spectrum is shown in Fig. 2.16 and reveals a principal frequency of 1.37 mHz, corresponding to a period of 12.14 min, with an amplitude of some 6 mmag. As more such stars were discovered, and extensive light curves were gathered, it became obvious that the observed amplitudes are modulated according to the time-dependent variation in the effective magnetic field strength. The timescale of the modulation is compatible with the rotation periods of the stars, which are of the order of days to decades. The average strength of the measured magnetic fields can reach tens of kG. It is therefore evident that the stellar oscillations must be strongly influenced by the magnetic field. In such a situation, we are dealing with magneto-acoustic oscillations.

During many years the roAp stars were thought to behave according to the so-called *oblique pulsator model*, in which the symmetry axis of the oscillations is aligned with the magnetic axis, which is inclined (oblique) to the rotation axis (Kurtz 1982; Dziembowski & Goode 1985; Kurtz & Shibahashi 1986). Such a configuration gives rise to rotationally-induced frequency splittings such as those observed. The value of the frequency splittings within a multiplet allows one to derive an accurate estimate of the magnetic field strength and also of the angles between the rotation and magnetic axes on the one hand and between the rotation axis and the line-of-sight on the other hand.

The matter of mode excitation in the roAp stars is difficult to solve due to the complexity of the computations caused by the inclusion of the magnetic field effects. The complete suppression of convection near the magnetic poles by the strong magnetic field turned out to result in mild net driving in the hydrogen ionization zone for high-order p modes (Balmforth *et al.* 2001). However, it is not yet clear if such a driving mechanism is fully compatible with the effect of diffusive forces, such as gravitational settling, regarding the existence and character of the surface abundance anomalies (Ryabchikova *et al.* 2004). Cunha (2002) attempted to understand the differences between roAp and noAp stars (*i.e.*, Ap stars that do not oscillate, at least not at the level of current detection thresholds) by the computation of a theoretical instability strip based on this instability mechanism and found good agreement with the observations, including the spectroscopic differences between roAp and noAp stars (Ryabchikova *et al.* 2004). Very recently, intermediate-period roAp stars were found using VLT data (Elkin *et al.* 2005), which will help to detail the instability computations further.

Over the last few years, the validity of the “classical” oblique pulsator model has been questioned because it remains unclear how an oblique oscillation can stabilize during such a long time. Moreover, some of the excited modes remain present during a long time, while others seem to disappear on relatively short timescales. This called for a new theoretical magnetic model. A first such model, which is valid for rapid rotators (in the sense that the ratio of the oscillation frequency to the rotation frequency is high) with a moderate magnetic field strength, was proposed by Bigot & Dziembowski (2002). In this model, the symmetry axis of the oscillations is not aligned with the rotation nor with the magnetic axis. Moreover, the effects of the centrifugal force are taken into account for the first time. This force seems to be the prime cause of rotational frequency shifts causing amplitude asymmetries, *i.e.*, peaks for m and $-m$ are unequal in amplitude. This new theoretical model seems to be very promising to explain the long-term properties present in the observations of some of the roAp stars, but it was so far not yet applied in full detail to data of any roAp star. A second model is the one presented by Saio (2005) and concerns axisymmetric nonradial oscillations including a strong magnetic dipole, ignoring rotation and envelope convection. The high-order dipole and quadrupole p modes are excited by the heat mechanism in the H ionization zone, while low-order p modes excited in the He II ionization zone are damped by the magnetic field when its strength raises above 1 kG.

From an observational viewpoint, the study of roAp stars has changed drastically over the past few years, with photometric studies being overtaken by time-resolved high-spectral-resolution spectroscopic studies. These are being vigorously carried out by several groups who are beginning to resolve the pulsation structure in roAp stars in 3 dimensions. These novel observations resolve the pulsation as a function of atmospheric depth, using the abundance stratification of certain ions to determine the pulsation amplitude and phase in the range $-5 \leq \tau_{5000} \leq 0$, and even higher into the atmosphere. Some examples are the high-resolution studies of 33 Lib by Mkrtichian *et al.* (2003) and of HD 166473 by Kurtz *et al.* (2005), the latter using very precise data from VLT/UVES. Finally, Kochukhov (2004) made an “image” of the pulsation velocity field from time series observations of spectra for HR 3831 and showed that the oscillations of this star *do* seem to be aligned with the axis of the global magnetic field, lending strong support to the oblique pulsator model. Clearly, further confrontation between these splendid new data and the oblique pulsator model as well as its alternatives, must be undertaken in the near future.

2.3.6 Slowly pulsating B stars

The term “slowly pulsating B stars” (SPB stars) was introduced by Waelkens (1991). With this term he pointed towards a group of seven young Population I variable mid-B stars with spectral type between B3 and B9, for which he had detected multiperiodic brightness and colour variations in photometric data spread over some 10 years. In Figs 2.17 and 2.18, the frequency spectra of the Geneva B and Hipparcos light, and radial-velocity variations of the brightest among the SPB stars, o Vel, and of a bright SB2 SPB star, HD 123515, are shown. De Cat & Aerts (2002) found respectively four and five independent frequencies for

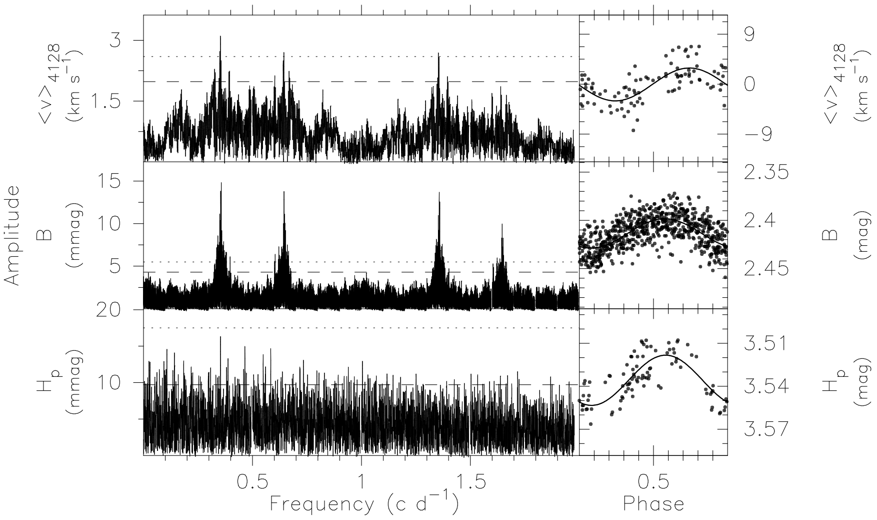

Figure 2.17: The frequency spectra of Geneva B, Hipparcos, and radial-velocity data derived from the Si II 4128 Å line of the single SPB star HD 74195. The horizontal dashed line indicates the 1% false-alarm probability and the dotted one the 3.7 S/N ratio level (see Chapter 4). (From De Cat & Aerts 2002.)

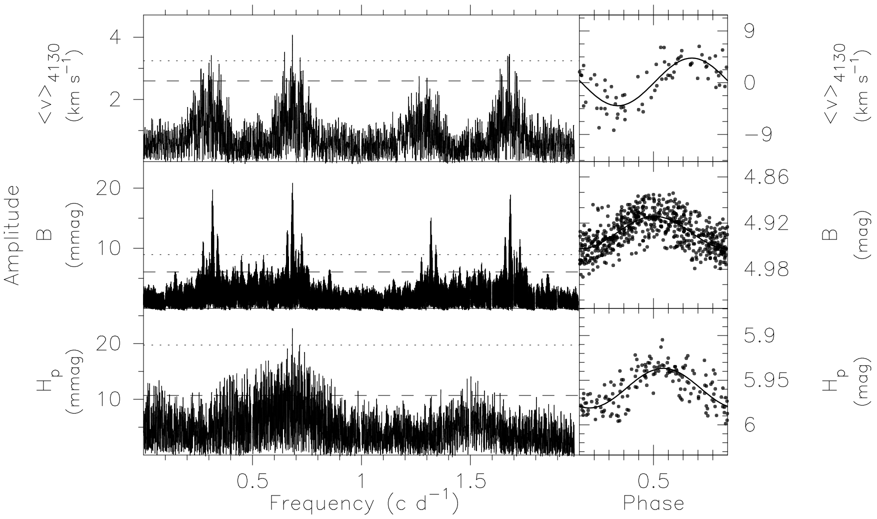

Figure 2.18: The frequency spectra of Geneva B, Hipparcos, and radial-velocity data derived from the Si II 4128 Å line of the SB2 SPB HD 123515. The horizontal dashed line indicates the 1% false-alarm probability and the dotted one the 3.7 S/N ratio level (see Chapter 4). (From De Cat & Aerts 2002.)

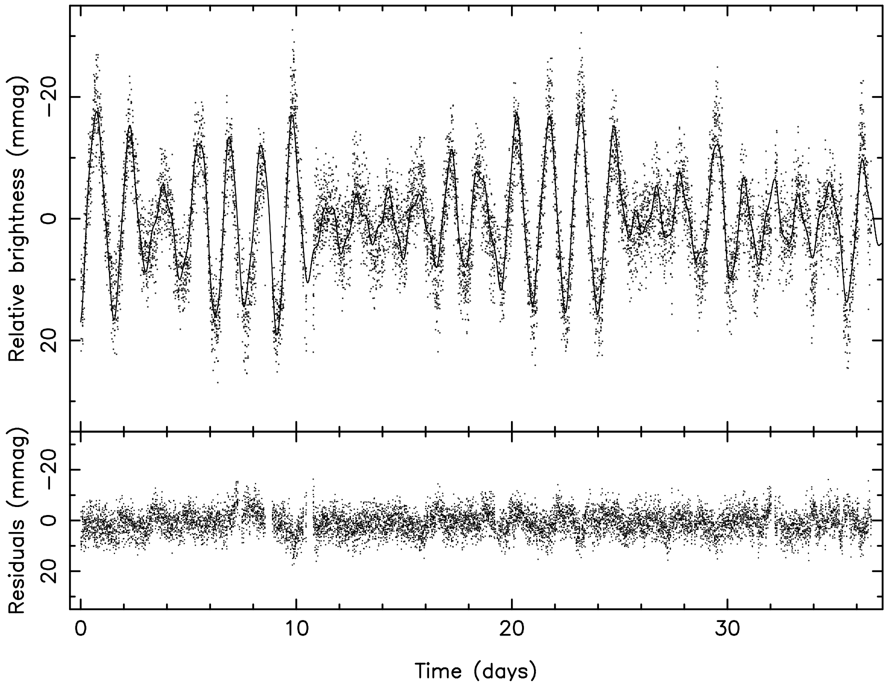

Figure 2.19: The MOST light curve of the SPB HD 163830 (upper panel, dots) and the best fit based on the 21 significant frequencies (upper panel, full line). The residuals after subtraction of the fit are shown in the lower panel. (From Aerts *et al.* 2006.)

these two SPB stars after subsequent prewhitening. The intrinsic periods of SPB stars are similar to those of the γ Dor stars except a bit longer because the stars are bigger, *i.e.*, roughly between 0.8 and 3 d. It is therefore extremely difficult to find such variables, as long-term planning is needed, just as for the γ Dor stars. This is readily visible in Figs 2.17 and 2.18 where the confusion between frequencies f and $1 - f$ is prominent. Only with multisite data, or with uninterrupted data from space, can one avoid such confusion, as shown by the MOST light curve of the SPB star HD 163830 reproduced in Fig. 2.19 (Aerts *et al.* 2006).

Line-profile variable counterparts of SPB stars were known prior to Waelkens' discovery of the SPB star class. Already in the late 1970s Myron Smith and his collaborators had done a search for line-profile variability in stars surrounding the β Cep stars (see below for a description of this group of pulsating stars). In this way they had discovered spectroscopic variables with spectral types between O9 and B5. Smith termed them 53 Per stars after his prototypical target. It has meanwhile become clear that the coolest among Smith's variables are SPB stars, but the explanation for the hotter stars in Smith's list is different. Indeed, the hottest among the 53 Per stars have p mode oscillations like the β Cep stars rather than high-order g modes. For this reason, the term SPB stars was finally chosen to indicate a class of stars with common pulsational properties in terms of g modes and one well-understood excitation mechanism, in contrast to the group of Smith's 53 Per stars. The masses of SPB stars range from 2 to 7 $M_\odot$, whereas some of the 53 Per stars have masses as high as 20 $M_\odot$.

As already emphasised, the Hipparcos mission led to a tenfold increase in the number of class members; huge long-term multicolour photometric and high-resolution spectroscopic follow-up campaigns were undertaken following this discovery (Aerts *et al.* 1999, Mathias *et al.* 2001). Those led to accurate frequency values and empirical mode identification for some selected targets (De Cat & Aerts 2002, De Cat *et al.* 2005) which are in excellent agreement with theoretical predictions of excited (mainly) $l = 1$ modes (Townsend 2003). All confirmed SPB stars are slow rotators (De Cat 2002).

As shown by Dziembowski *et al.* (1993) and Gautschy & Saio (1993), the explanation for the multi-periodic variations of SPB stars is the excitation of high-order g modes by the heat mechanism, associated with an opacity enhancement due to iron-group elements, also termed the *Z bump*. These features occur at a temperature near 200 000 K. This explanation for mode excitation in B stars, both for SPB stars and for β Cep stars (see below), had to await sufficiently accurate opacity computations of elements heavier than hydrogen and helium, such as those provided by Iglesias & Rogers (1996) in the OPAL[14] opacity project at Livermore and Seaton (1996) in the Opacity Project, OP[15]. Accurate opacity tables for elements heavier than hydrogen and helium are only available since the OPAL and OP projects were completed in 1992. Any previous opacity determinations for such elements were typically a factor three too low and so did not lead to mode excitation in B stars. The new opacity projects led to a natural explanation of the modes in SPB stars and in β Cep stars in terms of the heat mechanism at the position where the opacity bump occurs. We refer again to Pamyatnykh (1999) for a general overview of the properties of models with excited modes and their dependence on metallicity and core overshoot.

The agreement between theoretical predictions and observations is excellent in a statistical sense. The known SPB stars indeed lie entirely within and populate fully the computed theoretical instability strip. As parallaxes for isolated field B stars are very uncertain, one is not able to provide accurate luminosities either, which is the reason why in many seismic studies the model computations are represented in a $(\log T_{\rm eff}, \log g)$ diagram as in Fig. 2.20.

During the last half century, there has been significant confusion and debate in the literature about the existence of a specific group of variables with spectral types between B7 V–III and A2 V–II and periods between 2 and 8 h, baptized “Maia stars” by Struve (1955). At the time when Struve (1955) made his suggestion, SPB stars were still unknown. These hypothetical stars would be partly situated within the SPB instability strip, extending towards the δ Sct strip. There are no oscillations predicted by the classical heat mechanism in this part of the HR diagram (Pamyatnykh 1999) and indeed, despite large search campaigns (see, *e.g.*, Scholz *et al.* 1998 and references therein) unambiguous detection of short-period variability was achieved for only four out of fifteen stars. Each of these four has high rotational velocity (Aerts & Kolenberg 2005). In such a situation, the effects of the Coriolis force introduce significant frequency shifts for the low-frequency g modes (Townsend 2003) so that shorter periods must indeed be observed in an inertial frame. Such shifts may offer the correct explanation for the relatively high observed frequencies in these four stars. Another suggestion was made independently and almost simultaneously by Savonije (2005) and Townsend (2005), who found heat-driven retrograde mixed mode instability in B stars for spectral types B4 to A0 rotating faster than half of the critical rate. Both these interpretations lead to the conclusion that the “Maia stars” are simply rapidly rotating SPB stars.

---

[14] `http://www-phys.llnl.gov/Research/OPAL/opal.html`

[15] `http://vizier.u-strasbg.fr/topbase/op.html`

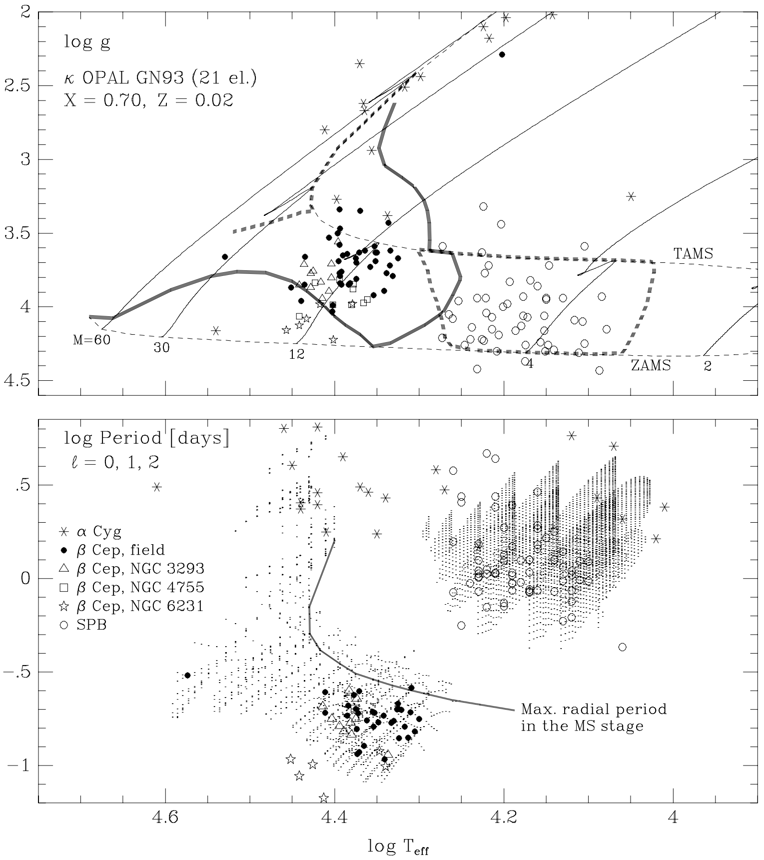

Figure 2.20: The theoretical instability domains predicted by the heat mechanism for B stars of metal abundance $Z = 0.02$ (thick lines, upper panel). The lower panel shows the oscillation periods as a function of effective temperature, pointing out the clear separation between the low-order p modes in the β Cep stars and the high-order g modes in the SPB stars. (From Pamyatnykh 1999.)

2.3.7 β Cep stars

The β Cep stars have been known as a group of young Population I near-main-sequence pulsating stars for more than a century. They have masses between 8 and about 18 $M_{\odot}$ and oscillate in low-order p and g modes with periods between about 2 and 8 h. More than 100 members of this group are known and the class contains dwarfs up to giants. A recent overview of the properties of the class was provided by Stankov & Handler (2005). Most of the β Cep stars show multiperiodic light and line-profile variations. Excluding the four stars BW Vulpeculae, ξ^1 CMa, HD180642 and σ Scorpii, which have exceptionally large velocity and/or light amplitudes, the phase diagrams for individual frequencies are nearly sinusoidal. The light variations clearly have larger amplitudes at blue than at red wavelengths and have a phase difference of about 0.25 with the radial-velocity variations. Such a phase lag is expected for adiabatic oscillations (Dupret *et al.* 2003). As for the SPB stars, the majority of the β Cep stars rotate at only a small fraction of their critical velocity, two of the exceptions being 19 Mon (Balona *et al.* 2000) and HD 203664 (Aerts *et al.* 2006) whose rotational velocities approach half of their critical value.

Until 2002, these stars were mainly observed during single-site photometric campaigns lasting typically one or two weeks. Some stars were monitored during different seasons, most often, unfortunately, with large gaps of several years in the data. An example is the star HD 129929 which was monitored during 21 years in 3-week campaigns from La Silla with one and the same high-precision photometer attached to the 0.70-m Swiss telescope (Aerts *et al.* 2003). This led to the detection of six independent oscillation modes, which was at that time the largest number of excited frequencies known in such type of star. The star 12 Lac was also known to have six oscillation modes from much earlier photometry (Jerzykiewicz 1978), and these modes turned out to have very stable amplitudes during many years as they were recovered in high-resolution spectroscopy more than a decade later (Mathias *et al.* 1994). Starting from the early 1990s, the β Cep stars were indeed also extensively studied from high-resolution spectroscopy (Aerts & De Cat 2003 and references therein).

A new era in β Cep star research was initiated after the international pulsation conference held at Leuven university (Aerts *et al.* 2002), where Mike Jerzykiewicz suggested the consideration of this type of star for multisite observing campaigns similar to those performed for the δ Sct stars. Handler & Aerts (2004) set up the largest such campaign ever performed for the star ν Eri, including not only multi-colour photometry but also simultaneous high-resolution spectroscopy during five months. This very rich dataset implied a significant step forward in the detection and interpretation of oscillation modes of a β Cep star. A subsequent campaign was carried out by Handler *et al.* (2006) on the star 12 Lac. Several additional modes, besides the six already detected by Jerzykiewicz (1978) and Mathias *et al.* (1994), were discovered. A part of the light curve of the campaign is shown in Fig. 2.21 and the frequency spectrum in Fig. 2.22. While aliasing still occurs, this figure illustrates the gain of multisite versus single-site data.

The nonradial oscillations in the β Cep stars are caused by the heat mechanism acting through opacity features associated with elements of the iron group (Dziembowski & Moskalik 1993), as discussed already for the SPB stars. The short periods of several hours are generally well explained in terms of heat-driven low-order p modes, but we stress that low-order g modes are also simultaneously excited and observed in several class members. There is a small overlap in the theoretical instability strips of the SPB stars and β Cep stars (see Fig. 2.20). This is observationally confirmed for only very few stars, among which is ν Eri.

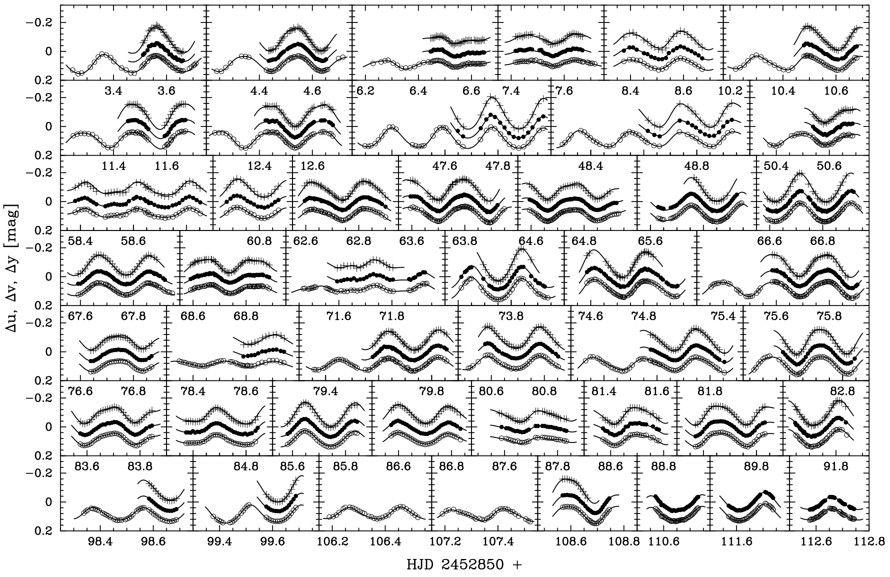

Figure 2.21: Strömgren photometry of the β Cep star 12 Lac from a multisite campaign. (From Handler *et al.* 2006.)

For this best-studied star, however, the most accurate seismic models do not predict all the observed modes to be excited. The extensive multisite campaign of ν Eri thus made it clear that not all the details of the mode excitation mechanism are well understood. Bourge *et al.* (2006) have recently shown that radiative diffusive processes, which have been ignored so far in such hot stars, may in fact enhance significantly the amount of iron in the driving region. Their computations followed the earlier suggestions by Pamyatnykh *et al.* (2004) and by Ausseloos *et al.* (2004) that a factor four higher iron abundance in the driving zone, or in the star as a whole, is necessary to solve ν Eri's excitation problem.

As can be seen on Fig. 2.20, the agreement between observed β Cep stars and the theoretical instability strip is very satisfactory for the class as a whole, although the blue part of the strip is not well populated. Numerous new candidate members were recently found from large-scale surveys, in the LMC and SMC (Kołaczkowski *et al.* 2006) as well as in our own Galaxy (Pigulski 2005, Narwid *et al.* 2006). Assuming that all these faint variable stars are indeed β Cep stars more than doubles the number of class members to over 200. The occurrence of so many β Cep stars in environments with very low metallicity demanded a new look upon the mode excitation, which relies heavily on the iron opacity. Miglio *et al.* (2007) have shown these results at low metallicity to be fully compatible with excitation predictions based on the OP opacities and the solar abundances by Asplund *et al.* (2005).

2.3.8 Pulsating Be stars

Be stars are Population I B stars close to the main sequence that show, or have shown in the past, Balmer line emission in their photospheric spectrum. This excess is attributed to the presence of a circumstellar

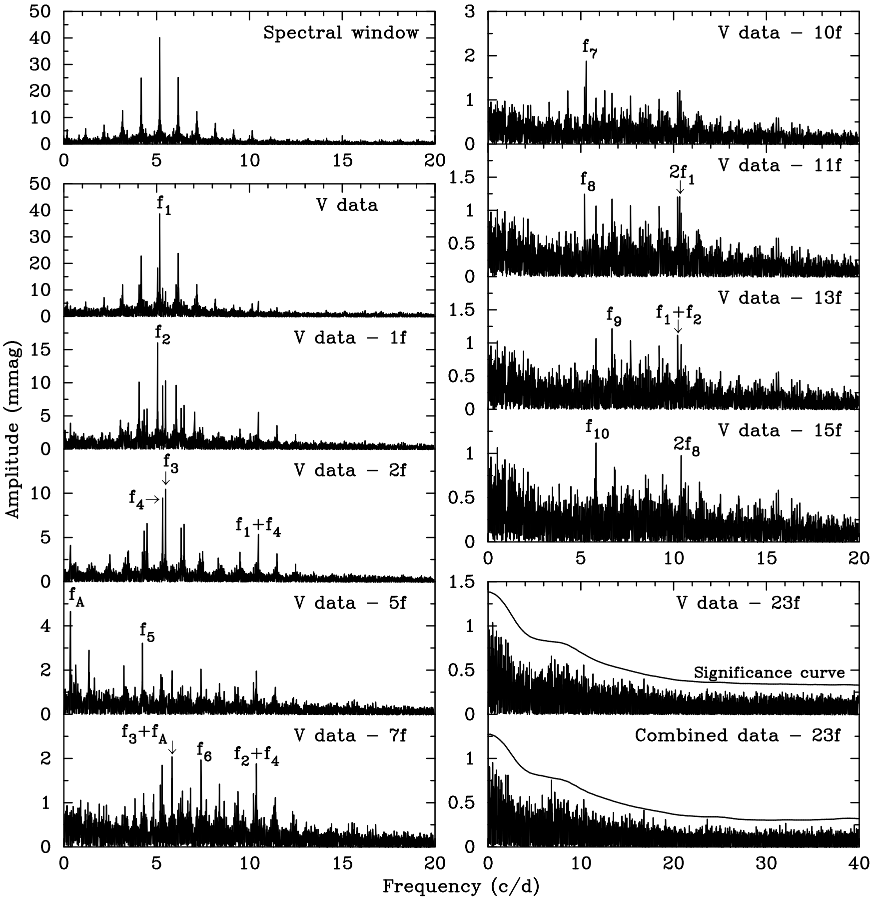

Figure 2.22: Frequency spectrum of the data for 12 Lac, some of which is shown in Fig. 2.21. (From Handler *et al.* 2006.)

equatorial disk. See the review on Be stars by Porter & Rivinius (2003) for general information on this rather inhomogeneous class of stars. Several different physical mechanisms are thought to be responsible for the disk. Numerous Be stars are members of close binary systems of very different kinds. Roche-lobe overflow or mass transfer in general may cause the disk in such cases. For single Be stars, rotation close to the critical velocity (Townsend *et al.* 2004), in addition to either multimode beating of oscillation modes (Rivinius *et al.* 2003) or mass loss along magnetic field lines (Townsend & Owocki 2005) could explain the disk. However, while magnetic fields (Neiner 2006) and nonradial oscillations (Rivinius *et al.* 2003) have been detected in some Be stars, it is not at all clear if these mechanisms suffice to explain a disk for the whole class of single Be stars. Also, it is at present unclear whether the occurrence of a disk around single Be stars can be attributed to a particular evolutionary state or not. The nature and evolution of disks around hot stars was recently summarized in the proceedings by Ignace & Gayley (2005) and by Stefl *et al.* (2006).

Single Be stars show variability on very different time scales and with a broad range of amplitudes. Balona (1995a) studied a subclass of the Be stars which show one dominant period between 0.5 and 2 d in their photometric variability, with amplitudes of a few tens of a mmag which he termed the λ Eri variables. He provided extensive evidence of a clear correlation between the photometric period and the rotational period of the λ Eri stars and interpreted that correlation in terms of rotational modulation. When observed spectroscopically, several of the λ Eri stars turn out to have complex line-profile variations with travelling sub-features similar to those observed in the rapidly rotating β Cep stars, except for the much longer periods (days versus hours). This rather seems to suggest oscillations as origin of this complex spectroscopic variability.

The first claim of nonradial oscillations in a Be star dates back from 1982, when Baade (1982) discovered complex line-profile variations for the star ω CMa, a star listed among the λ Eri variables in Balona's (1995a) list. The picture became even more complicated when Balona (1995b) introduced the class of ζ Oph variables. These are late-O type stars with clear complex multiperiodic line-profile variations which he attributed to high-degree nonradial oscillations. They are named after the prototypical O9.5V star ζ Oph, whose rotation is very close to critical and whose photometric variability was recently firmly established by the MOST space mission. Walker *et al.* (2005a) disentangled a dozen significant oscillation frequencies in the 24-d photometric light curve assembled from space. These frequencies range from 1 to 10 d^{-1} and clearly indicate the star's relationship to the β Cep stars.

An extensive summary of the detection of short-period line-profile variations due to oscillations in hot Be stars was provided by Rivinius *et al.* (2003). They monitored 27 early-type Be stars spectroscopically during six years and found 25 of them to be line-profile variables at some level. For several of their targets the variability was interpreted in terms of nonradial oscillations with $l = m = +2$. Almost all stars in the sample also show traces of outburst-like variability rather than a steady star-to-disk mass transfer. The authors interpreted the disk formation in terms of multimode beating in combination with fast rotation.

To make the picture complete, multiperiodic oscillations were recently reported in the rapidly rotating B5Ve star HD 163868 from a 37-d MOST light curve (see Figs 2.23 and 2.24). Walker *et al.* (2005b) derived a rich frequency spectrum, with more than 60 significant peaks, resembling that of an SPB star and termed the star an SPBe star in view of its Be nature. They interpreted the oscillation periods between 7 and 14 h as high-order prograde sectorial g modes and those of several days as Rossby modes (*e.g.*, Townsend 2005 for a recent description of such modes). There is remaining periodicity above 10 d which cannot be explained

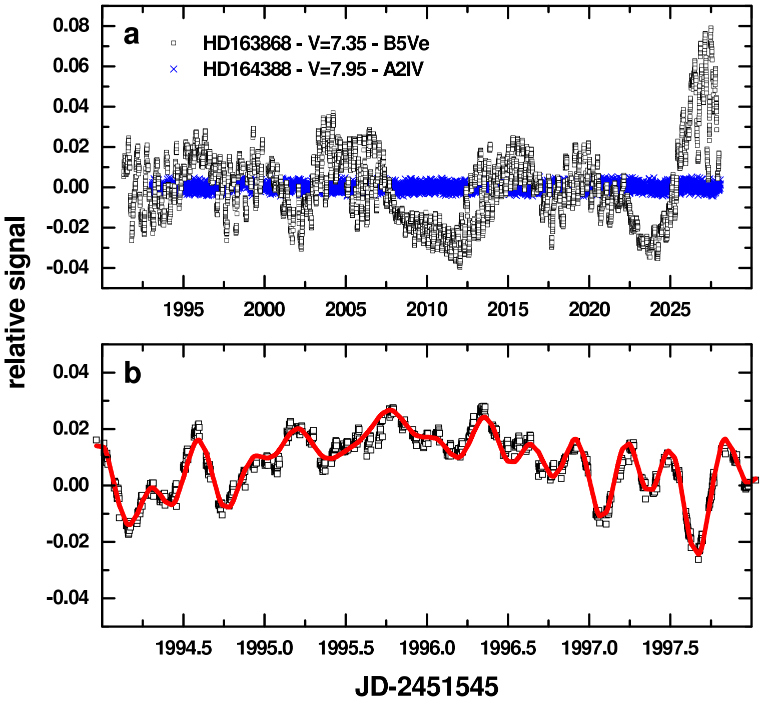

Figure 2.23: Space photometric light curve of the Be star HD 163868 observed by the MOST satellite. The lower panel shows a higher time resolution look at a 5-d portion of the light curve. (From Walker *et al.* 2005b.)

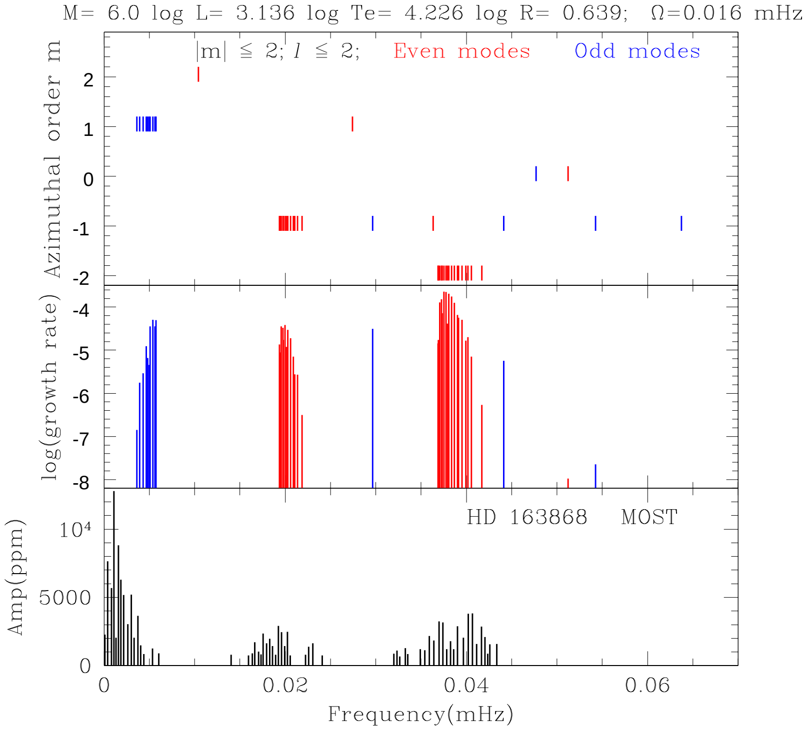

Figure 2.24: Model frequency spectrum resembling the observed one for the Be star HD 163868. (From Walker *et al.* 2005b.)

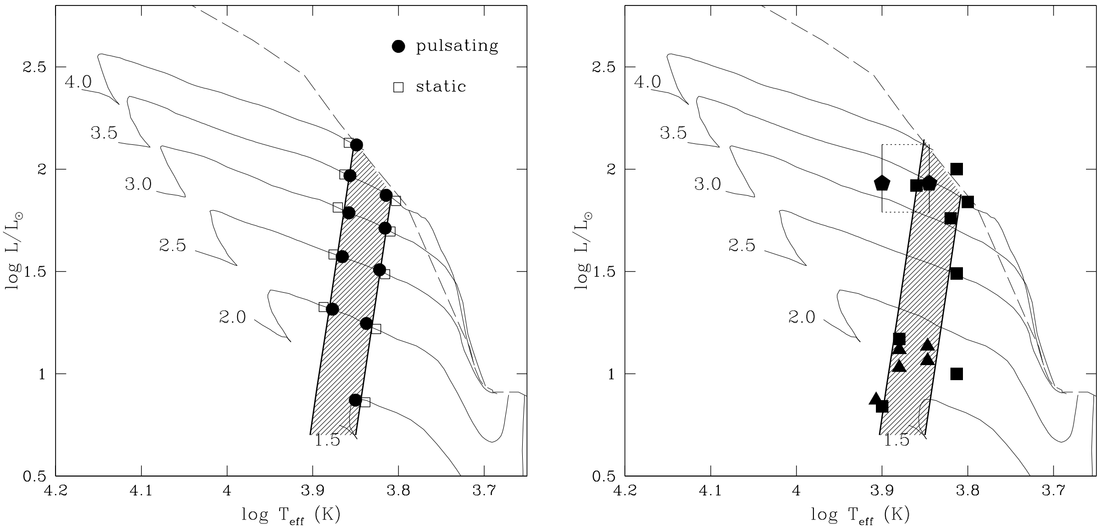

Figure 2.25: Left: location of the instability strip of the pre-main-sequence stars. Right: candidate pre-main-sequence pulsators known as of 1998. Triangles: UX Ori stars from Natta *et al.* (1997), squares: Herbig Ae/Be stars from Berrilli *et al.* (1992) and van den Anker *et al.* (1998), the error box is for HD 144668 (HR 5999: Kurtz & Marang 1995). (From Marconi & Palla 1998.)

at present. Finally, nonradial oscillations at low amplitude were also detected in the bright B8Ve star β CMi (Saio *et al.* 2006).

We come to the conclusion that the oscillations detected in Be stars show a multitude of different behaviour, which is in full accordance with those of β Cep stars and SPB stars. It seems that pulsating Be stars are complicated analogues of β Cep stars and SPB stars rotating typically above half of the critical velocity, and with some rotating very close to critical velocity. It remains to be studied what the role of the oscillations is in the disk formation for the class of Be stars as a whole.

2.4 Oscillations in pre-main-sequence stars

As newly born protostars contract towards the main sequence, either radiatively as the Herbig Ae/Be stars or convectively as the T Tauri stars, the higher-mass stars enter or cross the classical instability strip. Such pre-main-sequence stars tend to be highly variable, both in photometry and spectroscopy, on time scales of minutes to years. Part of this variability is surely due to activity and interaction with the circumstellar environment. On the other hand, part of the shorter-period variability may be due to oscillations. Since the interior structure of pre-main-sequence stars is different from that of evolved stars in the instability strip, their oscillation spectra may allow us to distinguish between the two evolutionary stages for stars with the same effective temperature and luminosity.

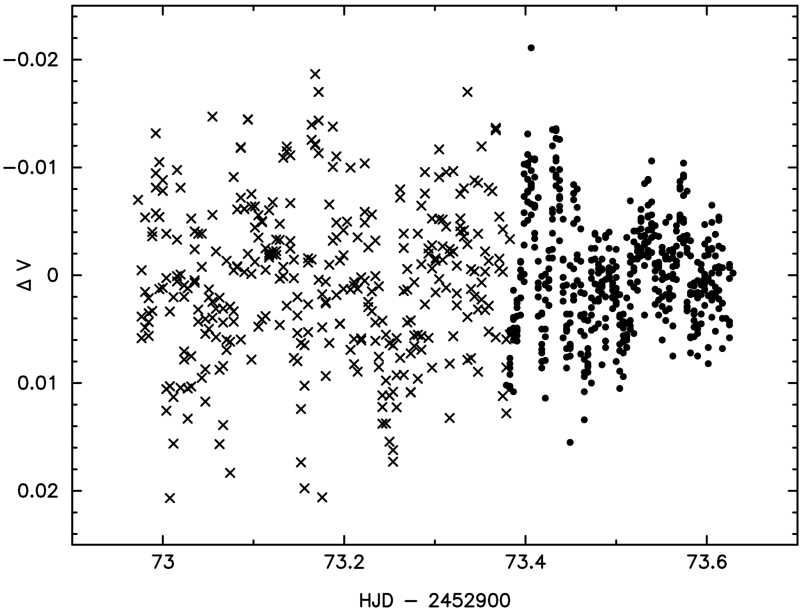

Figure 2.26: Part of the multisite campaign data obtained in 2003 by Ripepi *et al.* (2006) for the pre-main-sequence star IP Per. ΔV stands for $V_{\rm IP\,Per} - V_{\rm comp}$. Crosses and dots indicate data from two different sites.

Breger (1972) found the first two candidate pre-main-sequence δ Sct pulsators, while monitoring the young open cluster NGC 2264 photometrically. He also found 25% of the member stars of this cluster to be short-period variables and unravelled a clear correlation between the variability and shell characteristics. Some time later, Baade & Stahl (1989a,b) detected nonradial oscillations in two pre-main-sequence stars based on high-resolution spectroscopy. They found line-profile variability, but were unable to pinpoint clear periodicities from them. Kurtz & Marang (1995) made the next step and disentangled the low-amplitude (6 mmag) δ Sct pulsation with the first clear oscillation period of about 5 h from the long-term large-amplitude (0.35 mag) variations caused by variable dust obscuration in the disk of the Herbig Ae star HD 144668.

Marconi & Palla (1998) investigated the pulsational properties of pre-main-sequence stars with masses in the range 1 to 4 $M_\odot$ by means of linear and non-linear calculations and defined the instability strip for these stars in the HR diagram (see Fig. 2.25). They found periods ranging from 1.5 to 7.5 h for the fundamental mode. Delta Sct type oscillations have been suggested in about thirty pre-main-sequence stars so far. The reported periods are quite uncertain, and range from less than one hour to several hours, in agreement with theoretical predictions. For reviews on this topic see Catala (2003), Marconi & Palla (2004), Zwintz *et al.* (2004) and Ripepi *et al.* (2006a).

The most extensive dataset and interpretation of a pre-main-sequence δ Sct pulsator was achieved by Ripepi *et al.* (2006b, see Figs 2.26 and 2.27). They monitored the star IP Per photometrically in a multisite campaign involving ten sites. The total time span of their data is about 500 d. IP Per is a low-metallicity UX Ori type star, which is a class of precursors of the Herbig Ae/Be stars surrounded by self-shadowed disks (see

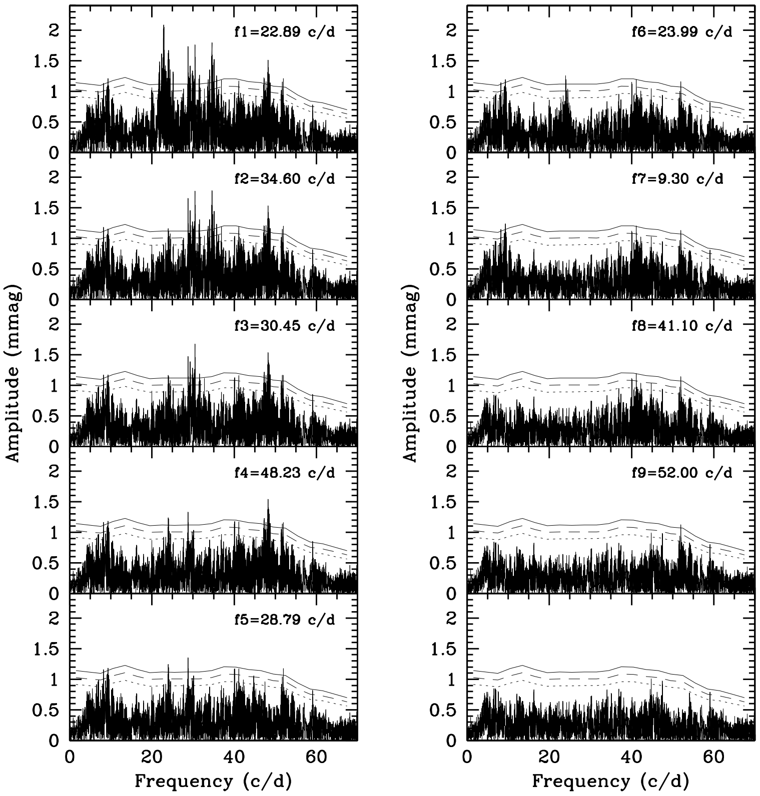

Figure 2.27: Frequency spectra for the V data of IP Per of which some were shown in Fig. 2.26. (From Ripepi *et al.* 2006.)

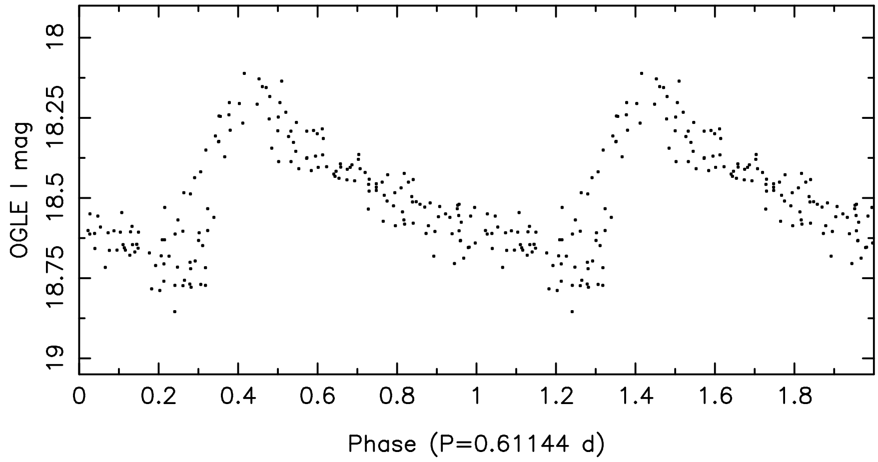

Figure 2.28: Light curve of an RRab star observed by OGLE folded according to the dominant oscillation period. Data taken from Soszynski *et al.* (2003).

Herbst & Shevchenko 1999 for a photometric catalogue and Dullemond *et al.* 2003 for a physical model). It has long-term variations with an amplitude of about 0.3 mag and a duration between 10 and 50 d onto which the oscillatory variability is superposed. The authors found nine frequencies for the star, ranging from 23 to 52 d^{-1}, and with an amplitude range from 1.1 to 3.3 mmag (see Fig. 2.27). A fit of theoretical frequencies to the observed ones indicates that a maximum five of the modes can be radial modes; thus nonradial modes occur as well. The frequency matching of the five radial modes led to an accurate mass, luminosity and temperature estimate of the star, in agreement with previous spectroscopic derivations. Unfortunately, the frequencies alone did not allow a discrimination between a pre- and post-main-sequence star.

2.5 Pulsations in evolved stars with $M \leq 9\,\mathbf{M}_{\odot}$

By evolved low-mass stars we mean objects with an initial mass below 9 $\mathrm{M}_{\odot}$, which have evolved off the main sequence. These stars may, at a certain phase in their life, start a burning cycle in degenerate matter in their core. This is surely the case for stars with a mass below 2.3 $\mathrm{M}_{\odot}$. They will undergo a helium flash at the tip of the red-giant branch. The more massive among the low-mass stars avoid ignition in a degenerate core. In any case, all of these stars are candidate oscillators during their post-main-sequence evolution. As discussed in Sect. 2.3.1, solar-like oscillations are found in subgiant stars in the hydrogen shell-burning phase which for stars of mass below around 1.7 $\mathrm{M}_{\odot}$ is relatively slow. However, only more massive stars cross the instability strips for heat-driven oscillations during this phase, and for such stars the phase is fast and the probability of catching a star before central helium burning is small. In the present section we therefore consider only the phases after central helium burning has started.

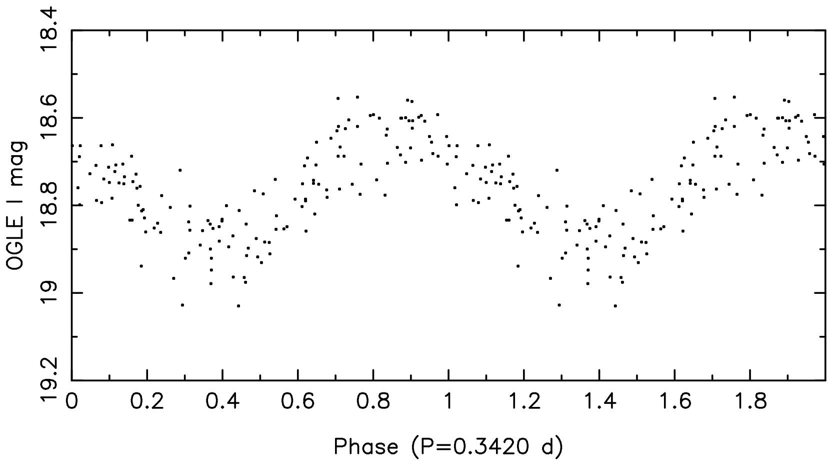

Figure 2.29: Light curve of an RRc star observed by OGLE folded according to the dominant oscillation period. Data taken from Soszynski *et al.* (2003).

2.5.1 RR Lyrae stars

Together with the Cepheids (see below), RR Lyrae stars are considered to be the *classical radial pulsators*. Most of them are monoperiodic stars with an oscillation period near half a day. While their monoperiodicity implies that they are not suitable for seismic studies, they are of great galactic and cosmological importance and we highlight some of their properties for this reason, referring to the monograph by Smith (1995) for more detailed information on their observational characteristics and to Catelan (2007) for an extensive overview of horizontal branch stars in general.

The first RR Lyrae stars were discovered in globular clusters by Bailey in 1895. Their spherical spatial distribution and kinematic properties (high velocities in all directions) imply that these stars must be extreme Population II stars. As they are low-mass stars, their observed abundances are, to a good approximation, those at their birth, *i.e.*, those of the interstellar cloud from which they were born. The abundances of elements heavier than hydrogen and helium, Z, ranges from 0.0001 to 0.01. RR Lyrae stars are also used to estimate the distance and the age of the clusters they belong to. For these reasons, they are considered to be standard candles of galactic evolution.

All stars with birth masses between $\simeq 0.5$ and $\simeq 2.2\,\mathrm{M}_\odot$ start helium burning in a degenerate helium core and undergo a helium flash, after which they settle on the horizontal branch. The stars with the thickest hydrogen envelope are at the red end of the branch and those with the thinnest at the blue end. The higher the envelope mass, the more the hydrogen shell contributes to the energy production and the larger the extent of the convective zone in the envelope. Blue horizontal branch stars have thin envelopes, weak hydrogen burning shells and develop a radiative outer zone (Prialnik 2000). As a consequence, the hydrogen envelope needs to have a particular mass to result in oscillations driven by the heat mechanism, which requires a radiative zone. It turns out that horizontal branch stars with masses between $\simeq 0.60$ and $0.80\,\mathrm{M}_\odot$ have the appropriate regions of hydrogen and helium ionization zones to become RR Lyrae stars (*e.g.*, de Santis & Casisi 1999), the precise mass limits depending on the metallicity and on the mass lost on the giant branch.

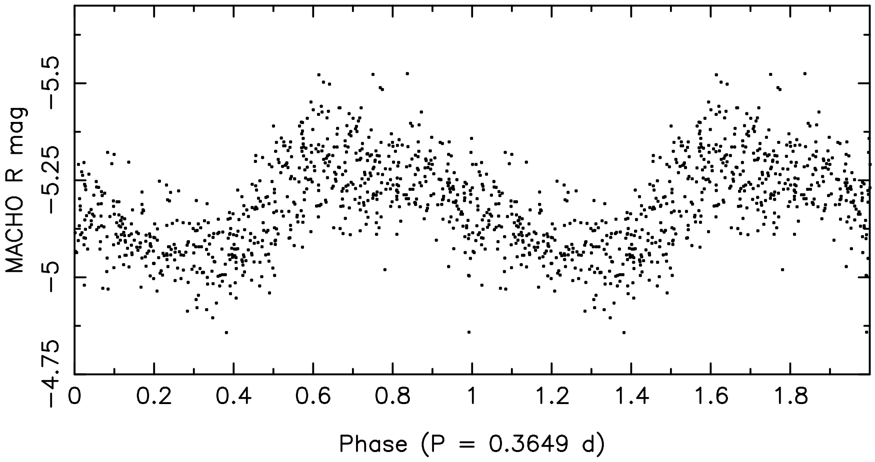

Figure 2.30: Light curve of an RRd star observed by MACHO folded according to the dominant oscillation period. Data taken from Kovacs (2000).

RR Lyrae stars either have settled immediately on the horizontal branch within the instability strip after the helium flash or they crossed the strip while evolving on the horizontal branch. The excitation mechanism of the RR Lyrae stars is well-known as the heat mechanism acting in the partial ionization zone of He II – He III (see, *e.g.*, Stellingwerf 1984 for an instability strip). Transient phenomena, such as mode switching, are also predicted. Bono *et al.* (1995) made a thorough analysis of the different details of the mode excitation and mode transition within the instability strip.

RR Lyrae stars have been observed for more than a century, mainly in photometry. They are subdivided into three *Bailey classes*: RRa, RRb and RRc stars. This classification is based upon the amplitude and the skewness of the light curve and on the oscillation period. RRab stars are now considered as one class, pulsating in the radial fundamental mode and having asymmetric light curves. RRc stars, on the other hand, oscillate in the first overtone and have sinusoidal variations. Two prototypical OGLE light curves, phased according to the dominant period, are shown in Figs 2.28 and 2.29.

In the mid 1980s, a fourth class of RR Lyrae stars was introduced: the RRd stars. The amplitudes of these group members change on relatively short time scales. Such stars have periods between 0.3 and 0.5 d and their light curves have more scatter than for the RRabc stars (see Figs 2.30 and 2.31 for a prototypical case observed within the MACHO project). It turns out that the RRd stars oscillate in both the fundamental and first overtone, *i.e.*, they are *double-mode* oscillators with a period ratio near 0.74 (Kovacs 2001). RRd stars are found in both the Galactic plane and in globular clusters. They have the advantage that the excitation of two oscillation modes allows us to characterize the stellar parameters, such as the mass, with much higher precision that for RRabc stars (*e.g.*, Popielski *et al.* 2000, Szabó *et al.* 2004).

Another old classification for RR Lyrae stars concerns their host clusters. Oosterhoff (1944) pointed out that some clusters have mainly RRab stars, while others have an equal contribution in RRab and RRc stars. The former are called *Oosterhoff I* type clusters and the latter *Oosterhoff II*. The average oscillation period of the RR Lyrae stars in Oosterhoff I clusters is 0.1 d shorter than for those in the Oosterhoff II clusters. This

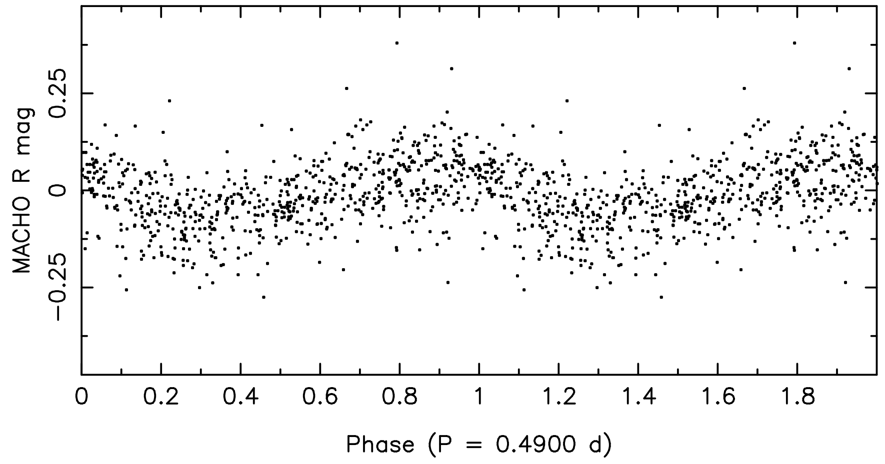

Figure 2.31: Residual MACHO light curve of the RRd star shown in Fig. 2.30 after prewhitening with the dominant oscillation period and folded according to the second period. Data taken from Kovacs (2000).

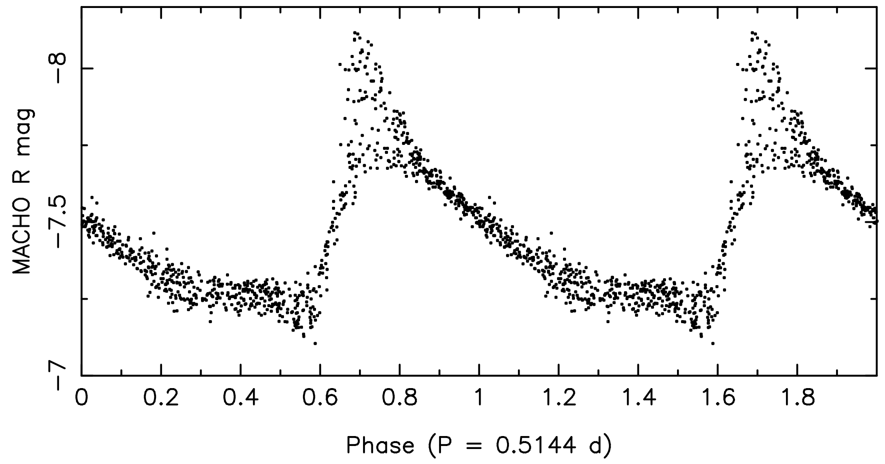

Figure 2.32: MACHO light curve of a Blazhko star observed by MACHO folded according to the dominant oscillation period. Data taken from the Kurtz *et al.* (2000).

phenomenon is called the *Oosterhoff-period-dichotomy* (*e.g.* Catelan 2007 for a discussion).

The absolute visual magnitudes of RR Lyrae stars have values roughly between 0 and 1. Although less bright than Cepheids (see further on) their large amplitude and their brightness makes them easy to recognize and hence suitable to be identified in globular clusters. Just as with Cepheids, they are used as distance indicators to these clusters. While more accurate and larger distances can be derived from the more luminous Cepheids, globular clusters do not have a population of the latter stars and so they cannot be considered for globular cluster distance determination. The RR Lyrae stars are therefore an important and good alternative.

Finally, we turn to the phenomenon called the *Blazhko effect*. For 25% of the RR Lyrae stars one observes amplitude modulation in the light curve (see Fig. 2.32 for a prototypical example from the MACHO database) on a timescale that is typically 100 times longer than the oscillation period. This modulation is observed in all three classes RRabc. It was observed for the first time by Blazhko (1907) for the star EW Dra and is named after its discoverer. RR Lyrae itself is a Blazhko star (*e.g.,* Kolenberg *et al.* 2006), with a modulation period, also termed Blazhko period, of 40.8 d. Over the Blazhko cycle the maximum brightness changes considerably, while there is hardly any change in minimum brightness (Fig. 2.32). The Blazhko effect has also been detected in line-profile variations of RR Lyrae itself (Chadid *et al.* 1999). Smolec (2005) pointed out that the Blazhko effect does not correlate with metallicity.

Jurcsik *et al.* (2005) proposed a correlation between the oscillation period and the modulation period, which made them conclude that the modulation period must be equal to the rotation period. However, for some of the Blazhko stars a third, much longer modulation period is also well established, *e.g.,* seven years for RW Dra and four years for RR Lyrae. The start of a new long modulation cycle is accompanied with a phase jump of several days in the light curve. It is difficult to understand this in terms of rotation of the star.

For many years now there have been two competing theoretical explanations for the Blazhko effect:

1. It is caused by the excitation of a nonradial oscillation mode of low degree, besides the main radial mode, through non-linear resonant mode coupling. In this model the Blazhko period is interpreted as the beat period between the radial fundamental and a nonradial mode (*e.g.,* Van Hoolst *et al.* 1995; Dziembowski & Cassisi 1999).
2. It is caused by a magnetic field which influences the oscillations (similar to the oblique pulsator model for the roAp stars). In this case the Blazhko period must be interpreted as the rotation period of the star (*e.g.,* Shibahashi & Takata 1995).

There is no consensus about the correct interpretation of the Blazhko effect, particularly not in view of the variety of Blazhko light curve characteristics discovered from the MACHO database (Kurtz 2000). The extensive efforts to search for a magnetic field in the best studied and brightest Blazhko star, RR Lyrae itself, and the failure to detect one with modern instruments to confirm previous claims (Chadid *et al.* 2004), have not resolved the issue. Moskalik & Poretti (2003) rejected the oblique magnetic pulsator model on the basis of the properties of Blazhko stars discovered from the OGLE project.

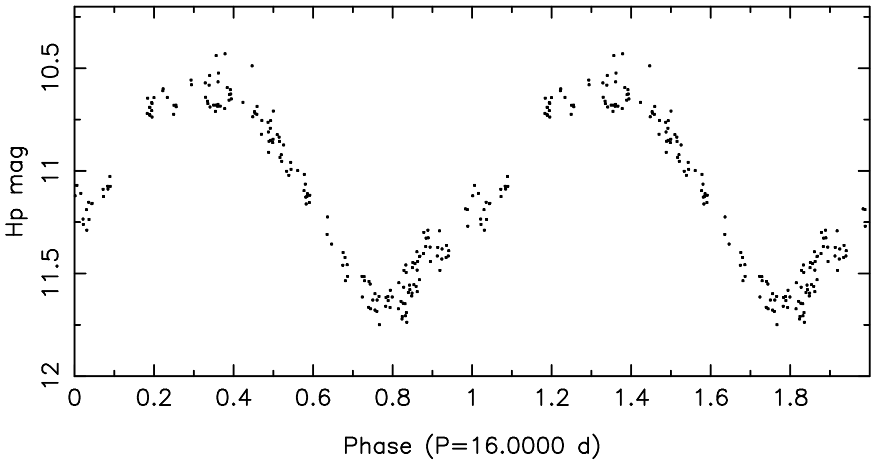

Figure 2.33: Hipparcos light curve of the Population II Cepheid CO Pup folded according to the oscillation period. Data taken from ESA (1997).

2.5.2 Population II Cepheids

After central helium burning, stars of Population II with masses higher than 0.5 $M_\odot$ evolve from the horizontal branch towards the AGB. During their evolution away from the horizontal branch, or during the numerous thermal pulses on the AGB, the stars may cross the instability strip and start oscillating. Such stars are called *type II Cepheids* or *Population II Cepheids*. Their periods range from 1 d for stars with luminosities similar to those of the RR Lyrae stars to about one month at higher luminosities. An example of a light curve is shown in Fig. 2.33.

The oscillations are caused by the heat mechanism active in both the partial ionization zone of He II – He III and of H I – H II. Theory predicts the excitation of either the radial fundamental mode or the first overtone (see, *e.g.*, Bono *et al.* 1995, 1997). Despite numerous efforts, the derivation of the precise location of the instability strip of Population II Cepheids remains uncertain. As for all monoperiodic radial oscillators, the stars are not well suited for seismic studies.

The longer-period Population II Cepheids were originally discovered by Henrietta Leavitt (Harvard University) early in the $20^{\rm th}$ century; they have been called the *W Virginis stars* for a long time. Today, the Type II Cepheids are divided in groups by period, such that the stars with periods between 1 and 5 d (BL Her class), 10 to 20 d (W Virginis class), and longer than 20 d (RV Tauri class, see below) have differing evolutionary histories (Wallerstein 2002). A period gap thus occurs for Population II Cepheids as there are no stars with periods between 5 and 10 d. It is believed that stars with periods shorter than 5 d are on their way to the AGB while stars with periods longer than 10 d move bluewards in the HR diagram due to thermal pulses or because they are on their way to the white-dwarf phase (Wallerstein 2002). For a review on Type II Cepheids we refer to Pollard & Evans (1999).

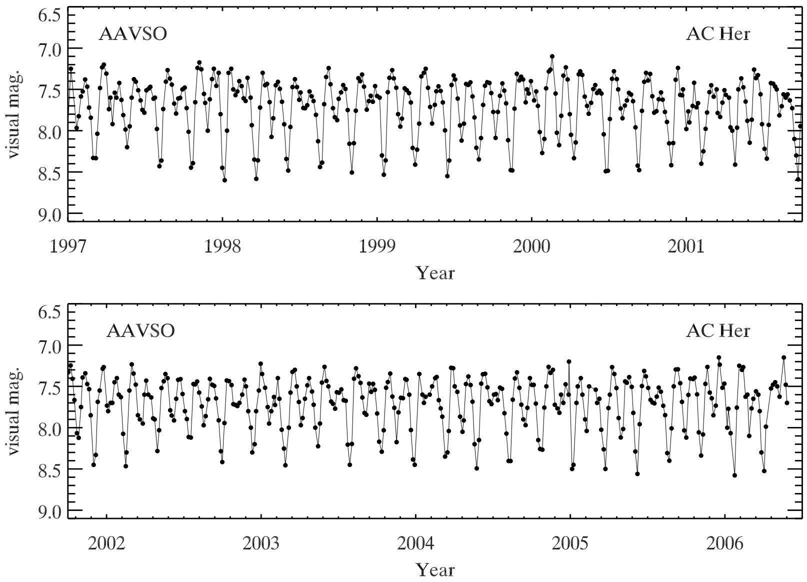

Figure 2.34: The visual light curve of the RV Tauri star AC Her as observed by amateur astronomers of the American Association of Variable Star Observers (AAVSO). Figure courtesy of Matthew Templeton.

2.5.3 RV Tauri stars

The longest-period W Virginis seem to merge continuously into yet another group of oscillators in that part of the HR diagram, namely the *RV Tauri stars* (see Pollard *et al.* 2000 for a review). These F to K supergiant stars could also have been called the longest-period W Virginis stars, but are usually considered as a separate class. For an enlightening discussion on the relation between Population II Cepheids and RV Tauri stars, and their evolutionary history, we refer to the review by Wallerstein (2002).

The oscillations of the RV Tauri stars are driven by the heat mechanism which is active in both the partial ionization zone of He I – He II and of H I – H II. A remarkable feature of RV Tauri stars is that their light curves have alternating deep and less deep minima, in a very regular way. In fact, this property is used to classify an object as an RV Tauri star. An example collected by amateur astronomers is provided in Fig. 2.34 for the star AC Her. It is evident from this figure that the light variability follows a double-wave pattern. The alternations of the minima and maxima do not always repeat strictly for all RV Tauri stars as some of them have cycle-to-cycle changes. RV Tauri stars are further divided in RVa and RVb subclasses, the RVa stars being those without long-term photometric trends and the RVb stars with such trends.

The radial-velocity curves of RV Tauri stars have large amplitudes, as can be seen from Fig. 2.35. The shapes of the radial-velocity curves of AC Her and R Sct were interpreted in terms of shock waves in their atmosphere by Gillet (1990). The spectroscopic study of 11 RV Tauri stars by Pollard *et al.* (1997) indeed confirmed that the data are compatible with two shock waves propagating in the atmosphere per pulsation period, because the metallic lines show a double-peaked profile which is characteristic of an atmospheric

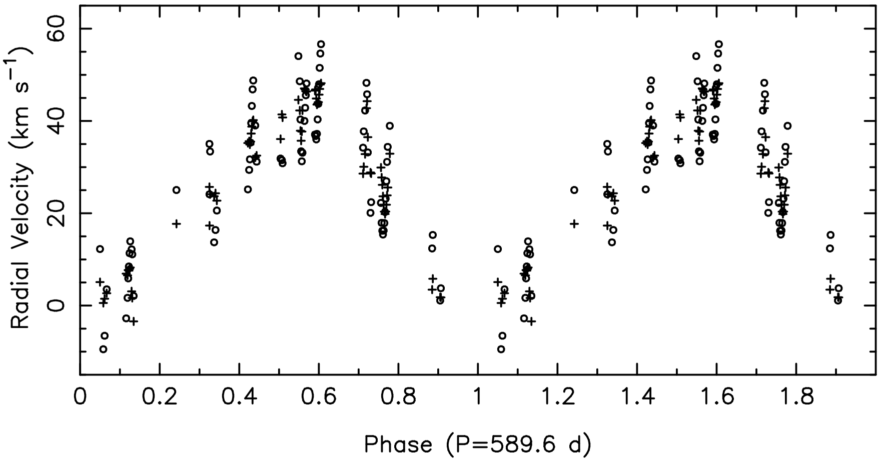

Figure 2.35: The measured radial-velocity variations (open circles) and those prewhitened for the dominant oscillation mode (crosses) of RVb star SX Cen, obtained from long-term monitoring, folded according to the orbit. The variability due to the oscillations with a period of 16.4 d has an amplitude which is a large fraction of the orbital amplitude. Figure courtesy of Hans Van Winckel.

shock as already outlined by Schwarzschild (1952).

Infra-red observations of RV Tauri stars clearly reveal the existence of circumstellar matter (Lloyd Evans 1985; Oudmaijer *et al.* 1992). This implies that the RV Tauri stars are low-mass stars in the early post-AGB phase (Jura 1986). As this phase has a very short duration compared with the lifetime of the star, it is difficult to catch the objects in this stage.

A definitive interpretation for the alternating minima is not yet available. It may be that a resonant oscillation pattern is active (Fokin 1994). The oscillation periods range from 30 to 150 d which creates an observational challenge to obtain a good inventory of the oscillatory behaviour of such stars. A further complication is that variable circumstellar absorption occurs, and is, in fact, sometimes sufficient to explain the photometric variability (Pollard *et al.* 1996). This led Van Winckel *et al.* (1999) to propose that the photometric subclasses RVa and RVb are simply due to a geometric projection effect, and not to a physical difference.

Finally, it is found that a very high fraction of the RV Tauri stars turn out to be long-period binaries (Van Winckel 2003, see Fig. 2.35). It may be that the long-term variability possessed by the RVb stars is due to the binarity (*e.g.*, Maas *et al.* 2002).

2.5.4 Cepheids

After the start of central helium burning in their non-degenerate cores, stars with initial masses above $\simeq 2.3\,M_\odot$ decrease in luminosity while they descend the giant branch. Stars below $3\,M_\odot$ settle on the horizontal branch while their more massive counterparts exhibit loops in the HR diagram. For the stars with

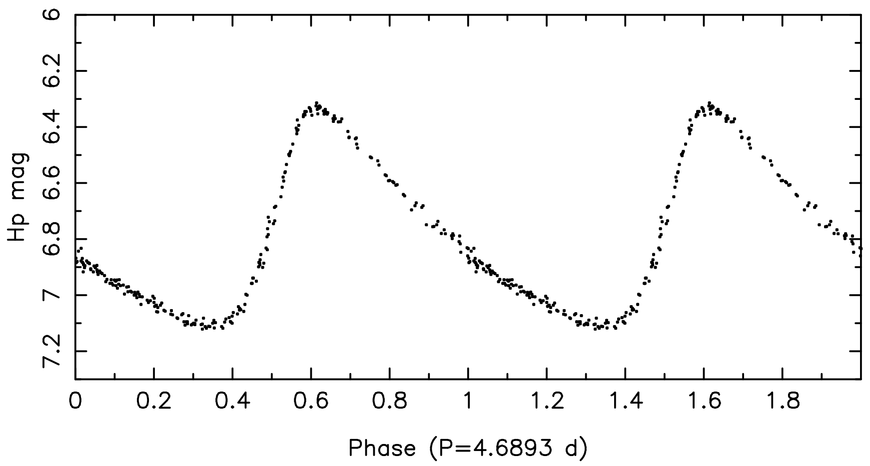

Figure 2.36: Hipparcos light curve of the classical Cepheid HD 112044 folded according to the oscillation period. Data taken from ESA (1997).

masses below 5 $M_\odot$ these loops are too limited to bring them into the instability strip. For more massive stars, however, the loops do extend far enough so that they become pulsationally unstable and are observed as Cepheids.

The *classical Cepheids*, named after the prototype δ Cephei, are probably the best-known and most homogeneous group of pulsating stars. The variability of δ Cephei was discovered in 1784 by John Goodricke, while Henrietta Leavitt made extensive investigations of Cepheids early in the 20^{th} century. A Hipparcos light curve of a classical Cepheid is shown in Fig. 2.36. In general, the periods of the Cepheids range from 1 to 50 d and their spectral types are between F5 and G5. They are all giants or supergiants. In our Galaxy, the Cepheids are situated in the Galactic plane and they take part in the rotation of the Galaxy. Thus they are Population I objects and are therefore also called type I Cepheids. Below, we provide only a brief summary of the properties of Cepheids, referring to the recent monograph by Szabados (2007) for more details.

The light curves of the Cepheids are skew and extremely periodic (see Fig. 2.36). The amplitudes are on average about one magnitude at visual wavelengths. Such brightness variations are accompanied by changes in the spectral type, colour, temperature and luminosity. For the prototype δ Cep itself, for example, the spectral type is F5 at maximum brightness and G2 at minimum brightness, while the corresponding change in temperature amounts to some 1 500 K. In general for Cepheids, the luminosity classes change roughly from III at minimal brightness to Ib at maximum brightness for periods below 25 d and to Ia for longer periods.

Bersier *et al.* (1991) produced an extensive radial-velocity catalogue of bright Cepheids. In Fig. 2.37 we notice a so-called *stillstand* in the radial-velocity curve they obtained for the star X Cyg. Such a phenomenon occurs whenever a strong shock wave propagates in the atmosphere of the star in such a way that the downfall of matter after maximum radius is stopped by rising gas due to the next shock. This shock is also markedly present at the same phase in the cycle in the Hipparcos light curve, which was taken about ten years later (Fig. 2.37).

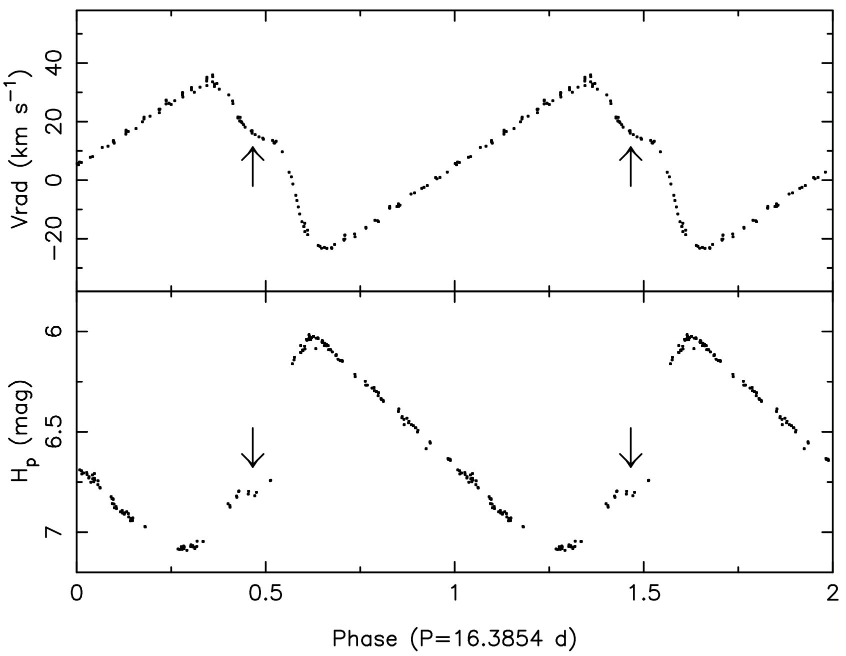

Figure 2.37: The radial-velocity and Hipparcos light curve of X Cyg folded according to the radial fundamental mode period of 16.38538 d. The stillstand is indicated by an arrow. Data taken from Bersier *et al.* (1991) and from ESA (1997).

In general, maximum brightness occurs near minimal velocity. However, detailed comparison of the phased light and radial-velocity curves suggests the occurrence of a small *phase lag* between the photometric and spectroscopic signatures of the oscillation. This lag typically amounts to a tenth of the period and can be spotted for X Cyg in Fig. 2.37. There also occurs a clear relation between the colour, or $B - V$, of the Cepheids and their oscillation period. This is called the *period-colour relation*. At a given luminosity, the stars shift to later spectral types for longer periods.

For several Cepheids a bump occurs in the light curve. Such a phenomenon occurs for Cepheids with periods between 4 and 20 d. It is due to a coincident occurrence of a 2:1 ratio between the period of the fundamental and the second overtone. The bump shifts as a function of oscillation period. This is called the *Hertzsprung progression*.

As is the case for the RR Lyrae stars, there are Cepheids in which both the fundamental mode and first overtone, or the first and second overtone, are excited. These are called *beat Cepheids* or also *double-mode Cepheids*. Poretti & Pardo (1997) have made a thorough study of galactic double-mode Cepheids. The MACHO and OGLE projects revolutionized our knowledge of the statistical properties of Cepheids in general. In particular, numerous double-mode Cepheids were found in the LMC (Alcock *et al.* 1998), and later even more in the SMC (Udalski *et al.* 1999a). These include both first-overtone/second-overtone and fundamental/first-overtone Cepheids. Only two first-overtone/second-overtone Cepheids are known in the Galaxy (Beltrame & Poretti 2002).

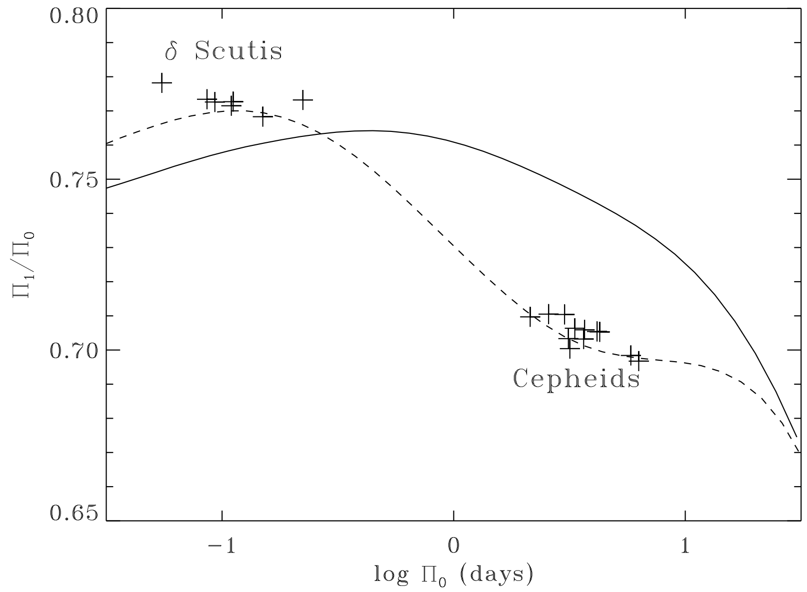

Figure 2.38: Petersen diagram, plotting the ratio between the first overtone and fundamental radial period against the logarithm of the latter. The observed values are shown by crosses. The curves show the variation along the instability strip; the solid curve was based on models computed with the Cox & Tabor (1976) opacities, whereas the dashed curve used OPAL tables from Rogers & Iglesias (1992). (From Christensen-Dalsgaard 1993).

The double-mode Cepheids may be said to constitute the first application of asteroseismology to determine stellar properties. Petersen (1973) showed that the two periods could be used to infer the mass and radius of the star. The results were in striking disagreement with the masses obtained from the position of the stars in the HR diagram, on the basis of evolutionary calculations (for reviews of this and other 'Cepheid mass problems', see for example Cox 1980; Simon 1987), suggesting potential problems with the understanding of stellar evolution and pulsations and leading to extensive efforts to remove the discrepancy. It is common to illustrate the problem in a *Petersen* diagram, where the ratio Π_1/Π_0 between the periods Π_1 and Π_0 of the first radial overtone and the fundamental is plotted against $\log \Pi_0$. The observed location of a star in such a diagram is given with great precision. An example is illustrated in Fig. 2.38; the solid curve shows theoretical results for models along the instability strip, based on the theoretical relation between mass and luminosity and using pre-1980 opacities, compared with observations of double mode HADS and Cepheids. The discrepancy is obvious. It was suggested by Simon (1982), and demonstrated in greater detail by Andreasen & Petersen (1988), that the discrepancy could be eliminated through a substantial increase of the opacity in the range $5.2 < \log T < 5.9$. Remarkably, such an increase was found in the OPAL calculations (*e.g.,* Rogers & Iglesias 1992) through increased contributions from bound-bound transitions in iron-group elements; it was the same effect that led to excitation of modes in, *e.g.,* SPB and β Cep stars (*cf.* Sect. 2.3.6). The effect on the period ratios is shown by the dashed curve in Fig. 2.38; obviously, with the revised opacities there is excellent agreement between the computed and observed period ratios (see also Moskalik *et al.* 1992; Kanbur & Simon 1994; Christensen-Dalsgaard & Petersen 1995).

Three stars in the galaxy, AC And, V823 Cas and V829 Aql, are known to be triple-mode pulsators, pulsating in the fundamental, and first and second overtone modes (Jurcsik *et al.* 2006). The longest-known of these is AC And which Fitch & Szeidl (1976) and Kovács & Buchler (1994) thought to be possibly similar to the δ Sct stars. Fernie (1994) argued that this star lies intermediate between the δ Sct stars and Cepheids. Thanks to the OGLE survey, two more triple-mode Cepheids have been found. Moskalik & Dziembowski (2005) interpreted their oscillation periods as the first three radial overtones. This interpretation imposed stringent constraints on their metallicity Z, which must be in the range 0.004 to 0.007, and on their evolutionary status, indicating that the stars must be crossing the instability strip for the first time. The models also imposed an upper limit of 0.33 times the pressure scale height to the extent of overshooting from the convective core during the main-sequence phase. Meanwhile the galactic triple-mode Cepheid V823 Cas, originally discovered by Antipin (1997), was subjected to a thorough photometric study. The lack of agreement between the observed periods and period ratios and those of evolutionary models led Jurcsik *et al.* (2006) to propose that this star is in a transient state during which its oscillations are probably affected by resonances.

Finally, we mention the existence of short-period Cepheids with periods shorter than 7 d and sinusoidal, low-amplitude light curves. They are called *s-Cepheids* or *overtone* Cepheids. They indeed oscillate in the first overtone, just as the RRc stars do. Their light curves and radial-velocity curves often show a discontinuity due to a resonance between twice the first overtone and the fourth overtone radial mode frequencies. We refer to Kienzle *et al.* (1999) for a homogeneous observational study of a sample of 24 overtone Cepheids.

The importance of Cepheids is not their asteroseismic potential, except perhaps for the double- and triple-mode pulsators mentioned above, but their fundamental power for distance determinations through

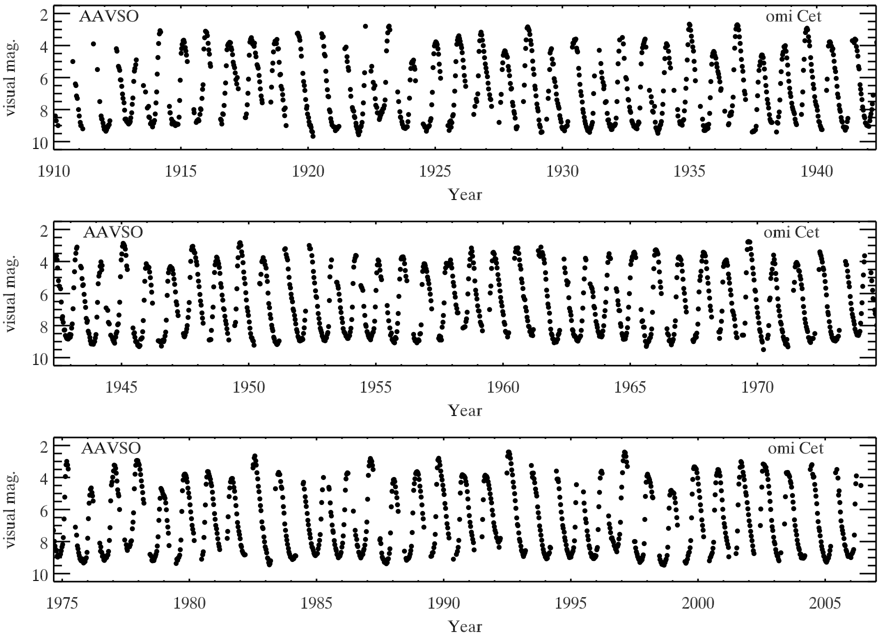

Figure 2.39: The visual light curve of the Mira itself, o Ceti, as observed by amateur astronomers of the AAVSO. Figure courtesy of Matthew Templeton.

the well-known *period-luminosity relation*, again found by Henrietta Leavitt (Leavitt & Pickering 1912)[16] and first calibrated by Ejnar Hertzsprung (1914). By measuring the oscillation period of a Cepheid and by using the period-luminosity relation, one can derive the absolute magnitude, hence the distance to the star. For this reason, Cepheids are also called *distance indicators*. In principle, the relation could be calibrated by means of an accurate independent distance determination to one Cepheid. In practice, however, one tries to determine accurately the zero-point of the relation by inclusion of as many stars as possible for which accurate distance determinations are available. Given the importance of cosmological distance scales, the derivation of the zero points, including appropriate statistical error estimates, remains a matter of intense debate in the literature (see, *e.g.*, these conference proceedings: Kurtz & Pollard 2004; Kurtz 2005; Walker & Bono 2006 for recent compilations). For more information on Cepheids, we refer to Szabados (2007).

2.5.5 Mira stars and semi-regular variables

Population I variable stars with long periods ($P > 80$ d) which are situated at luminosities between about 10^3 $L_\odot$ and $7{\times}10^3$ $L_\odot$, and at low effective temperatures between 2500 and 3500 K, are called Mira variables (Miras) when their amplitudes are larger than 2.5 in V (see Fig. 2.39). Semi-regular (SR) variables with similar periods but smaller amplitudes are termed SRa (see Fig. 2.40). This term is highly misleading,

---

[16] Although the paper is signed by Edward Pickering, its first line reads, "The following statement regarding the periods of the 25 variable stars in the Small Magellanic Cloud has been prepared by Miss Leavitt." History and Web-site referencing services are fair and attribute the circular to Leavitt & Pickering (Rubin 2005).

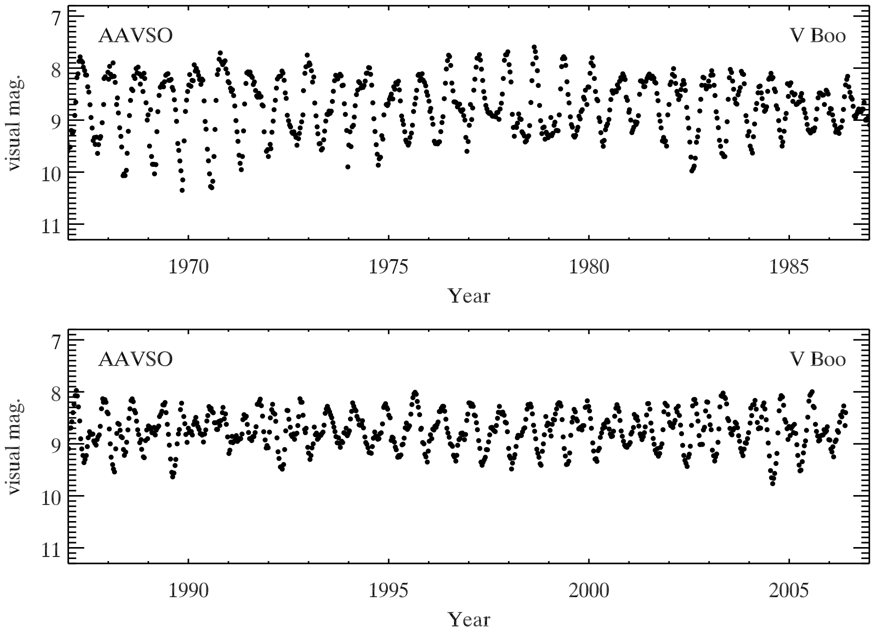

Figure 2.40: The visual light curve of the SRa star V Boo as observed by amateur astronomers of the AAVSO. Figure courtesy of Matthew Templeton.

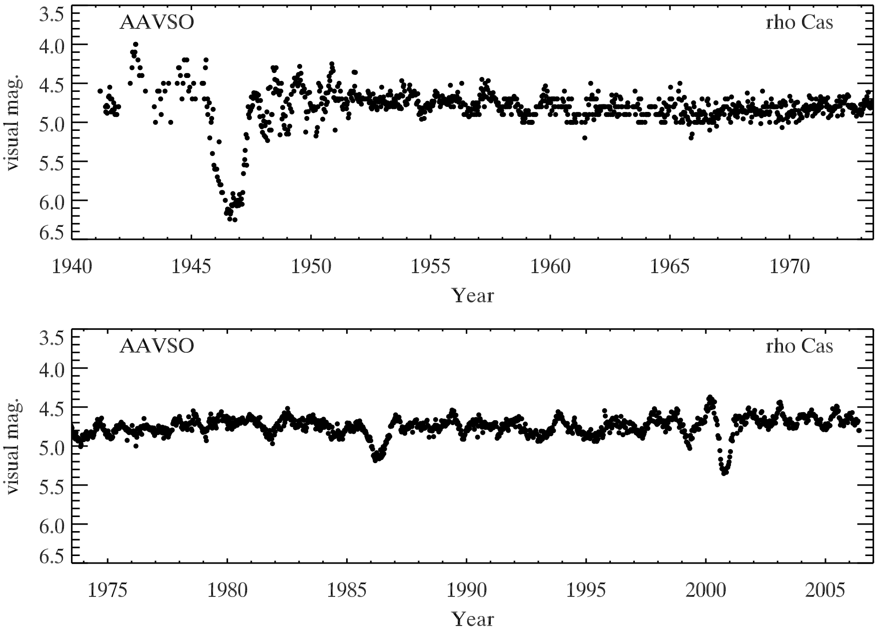

Figure 2.41: The visual light curve of the SRd star ρ Cas as observed by amateur astronomers of the AAVSO. Figure courtesy of Matthew Templeton.

because most of these stars have light curves as regular as Miras (compare Figs 2.39 and 2.40, see also Lebzelter *et al.* 2002 for a discussion), but an amplitude below 2.5 in V, which implies a totally arbitrary division between the Miras and SRa stars. SRb stars, on the other hand, have lower amplitudes than the SRa stars and semi-regularity in their light curves, *i.e.*, their periodicity is poorly defined. They often show alternating intervals of periodic and slow irregular changes. The SRc stars are periodic supergiants with an amplitude below 1.0 in V. A class called the SRd stars has also been introduced. This term is again misleading, because, unlike the RRd stars which are double-mode RR Lyrae stars, the SRd variables are not double-mode pulsators. Rather, they are weak-lined variable giants and supergiants of spectral types FGK. They are considered to be metal-poor shorter-period analogues of the Miras (Lloyd Evans 1975). One of the best monitored SRd variables is ρ Cas, whose visual light curve is provided in Fig. 2.41. The Miras and SRa stars are AGB stars with large mass loss and are about to start their way to the planetary nebula phase. Some of the SRb stars are still on the RGB.

The Miras and SRs are situated to the red of the classical instability strip, at lower temperatures. They have radial oscillations which, according to modelling by Ostlie & Cox (1986), are heat-driven in the partial ionization zones of H I – H II and He I – He II. Although Ostlie & Cox obtained reasonable results for the location of the instability region, they recognized that their use of the 'frozen-convection' approximation for the pulsations was a serious limitation. In fact, convection totally dominates the energy transport in the regions responsible for the driving. Effects of convection were considered by, *e.g.*, Xiong *et al.* (1998), Munteanu *et al.* (2005) and Olivier & Wood (2005) with somewhat conflicting results. It is evident that a full understanding of the driving of these oscillations will require a more secure treatment of the interaction between convection and pulsations.

The huge amplitudes seen in visible light in some Mira variables (*e.g.*, Fig. 2.39) do not reflect similar variations in the total luminosity. As discussed by Reid & Goldston (2002) the reduction of the visible magnitude at minimum is dominated by the cooling of the atmosphere and the conversion of the emitted radiation to the infrared by the effect of the resulting formation of metal oxides.

The MACHO and OGLE databases generated a real breakthrough in the study of long period variables. The MACHO data led to the discovery of five distinct period-luminosity (PL) sequences for the low-mass giant branch, as first suggested by Cook *et al.* (1996) and worked out in detail by Wood (2000). This gave unambiguous confirmation that the Miras are radial fundamental pulsators while SR variables can pulsate in the 1st, 2nd, 3rd radial overtone, as well as in the fundamental mode. Similar results were obtained from OGLE data in a series of papers (Ita *et al.* 2004; Kiss & Bedding 2004; Soszyński *et al.* 2004; Groenewegen 2004). Fraser *et al.* (2005) made a careful analysis of the full 8-yr MACHO database, and disentangled six rather than five PL sequences, which they termed 1, 2, 3, 4, D and E (see Fig. 2.42). The first four sequences are interpreted in terms of radial pulsations at rising radial order. Cioni *et al.* (2001) already showed that the large-amplitude SRa stars fall on sequence 1 together with the Miras, while the low-amplitude SRa stars fall on sequences 2, 3, 4. The sequences 3 and 4 contain RGB stars as well as oxygen-rich AGB stars which did not yet undergo the 3rd dredge-up, *i.e.*, less evolved stars than those in sequences 1 and 2. The interpretation of the sequences D and E is less clear. It was suggested by Wood *et al.* (1999) that the sequence E is comprised of ellipsoidal or eclipsing red-giant binaries with an invisible companion and sequence D of stars with a short primary period and a long secondary period. Later on, however, Wood *et al.* (2004) considered different physical causes for the long secondary periods of stars in sequence D and came to the conclusion that a low-degree g-mode oscillation combined with large-scale spots of a single red star

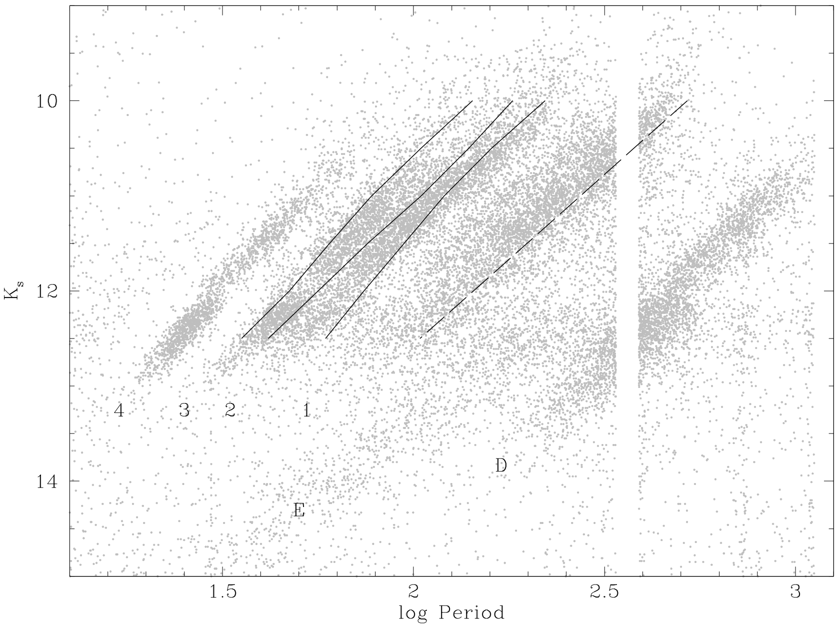

Figure 2.42: Period-Luminosity diagram for MACHO data of long-period variables (grey dots). The observed LMC Mira relation for the fundamental mode by Feast *et al.* (1989) is indicated as dashed line. The 3rd, 2nd and 1st overtone models of Wood & Sebo (1996) are indicated as solid lines (from left to right). Note that stars with periods near 1 yr were removed from the analysis, due to aliasing problems. (From Fraser *et al.* 2005.)

offers the most likely interpretation. Soszyński *et al.* (2004), on the other hand, concluded that sequence D contains a mixture of AGB, RGB, Mira, SRa, SRb and small-amplitude pulsators. In a follow-up study, Soszyński (2007) noted that sequence D forms a continuation of the ellipsoidal and eclipsing red giants of sequence E and therefore argued in favour of the binary hypothesis for both sequences D and E.

Given these disagreements, we must conclude that it is still unclear which physical mechanism causes red pulsators to become a Mira or an SRa/b/c/d. The latter are only rather arbitrarily defined categories introduced by observers to differentiate among the red variables from the morphology of their light curves. One suggestion for the discrimination in the physics of these different types of star is a small difference in chemical composition, and hence in molecular grain types, resulting in a different mass loss. Another idea is that the very tenuous envelopes of these stars imply shock waves of different strength in their outer atmospheres and that these cause quasi-periodic cycles. Recently, Christensen-Dalsgaard *et al.* (2001) suggested stochastically-excited modes as an explanation for the semi-regularity. Indeed, all these stars have huge outer convection zones, so one would expect them to undergo solar-like oscillations. These of course have much longer periods in supergiant stars than in main-sequence stars. It may therefore very well be that the differences between Miras and SRa or SRb stars simply reflect the fact that radial modes are active in the former, while there is beating with solar-like oscillations in the latter. This idea, tested on amateur-astronomer data from the American Association of Variable Star Observers (AAVSO), seems to be confirmed by OGLE data (Kiss & Bedding 2003). If accurate frequencies of solar-like oscillations in AGB stars can be measured, then these objects will suddenly become very interesting stars from a seismic point of view. This will indeed allow us to probe in detail the very complex stellar structure of stars that are about to end all the phases of nuclear burning they went through during their complete evolution. It is a major observational challenge to measure these frequencies for future seismic studies, given the long periods of these stars, hence the long-term observational commitment needed. However, the stars have such large amplitudes that this is an area of asteroseismology where amateur astronomers can play a significant role.

2.5.6 Solar-like oscillations in red giants

As already mentioned in Sect. 2.3.1, one expects solar-like oscillations to be excited in all stars with an outer convection zone. Such oscillations are very hard to establish in red supergiants with large-amplitude heat-driven modes, such as the Miras or large-amplitude semi-regulars. However, they have become obvious in red-giant stars.

The first announcements of short-period variability with periods of the order of hours in a giant star were made by Smith *et al.* (1987) and Innis *et al.* (1988) for the star α Boo (Arcturus, K1III), on the basis of radial-velocity observations. Hatzes & Cochran (1994) found radial-velocity variations, with an amplitude near 50 $\mathrm{m\,s^{-1}}$, for the K2III star β Oph; no firm periodicity could be derived, although the candidate periods ranged from 0.25 up to 0.8 d. Also, using the Hubble Space Telescope Edmonds & Gilliland (1996) found photometric variations in K giants in the globular cluster 47 Tuc which appeared to be consistent with solar-like oscillations. Merline (1999) subsequently reported solar-like oscillations from further long-term radial velocity monitoring of Arcturus, with periods ranging from 1.7 to 8.3 d. This result was later confirmed by space photometry taken with the WIRE satellite, from which Retter *et al.* (2003) deduced an oscillation period of 2.3 d. The WIRE mission had been used before to claim solar-like oscillations in the K0III giant α UMa (Buzasi *et al.* 2000). The longest among the ten detected periods was 6.4 d and the amplitudes ranged from 100 to 400 μmag. Although Guenther *et al.* (2000) interpreted these frequencies as due to low-order p modes of a 4 $\mathrm{M}_\odot$ giant, Dziembowski *et al.* (2001) pointed out that the model predictions for appropriate stellar masses of α UMa and with appropriate input physics disagree with the claimed modes, as far as the predicted amplitudes, frequencies and excitation are concerned.

The first firm establishment of solar-like oscillations in a giant was made for the G7III star ξ Hydrae (Frandsen *et al.* 2002). Nine frequencies were found in the radial-velocity data of the star, spanning one full month. The strongest mode has an amplitude of about 2 $\mathrm{m\,s^{-1}}$. An average large spacing of 6.8 μHz was found, in agreement with radial mode frequencies of adjacent radial order. Modelling of the pulsations by Houdek & Gough (2002), using Gough's (1977) treatment of the interaction between convection and pulsations, yielded amplitudes in good agreement with the observed values. Stello *et al.* (2006) used the data to estimate the mode lifetime of ξ Hydrae and found it to be of the order of 2 d. Such a short lifetime, if confirmed for other giants, would limit the power of asteroseismology in this part of the HR diagram. Also, interestingly, the lifetimes were far shorter than indicated by the calculations by Houdek & Gough.

A subsequent clear detection of solar-like oscillations in a giant from space-based photometry was achieved for the Hubble Space Telescope guide star GSC 09137-03505. Kallinger *et al.* (2005) found three

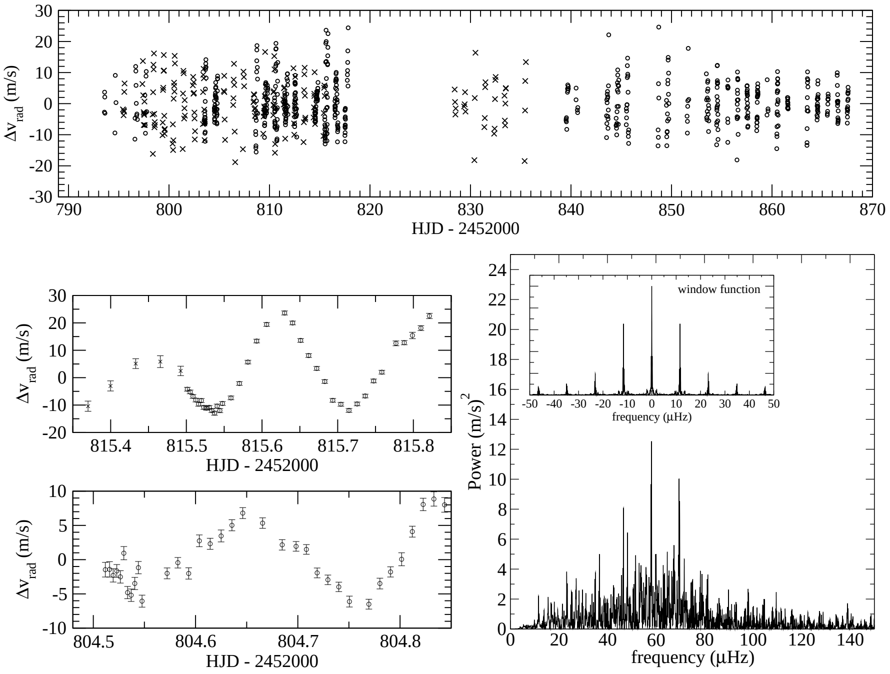

Figure 2.43: Top: radial-velocity data of ϵ Oph from a two-site campaign (dots: CORALIE data taken with the 1.2-m Swiss Euler telescope at La Silla, crosses: ELODIE data taken with the 1.9-m telescope at Haute Provence observatory). Bottom left: two enlarged parts of the dataset. Bottom right: power spectrum. (From De Ridder *et al.* 2006.)

frequencies ranging from 21 to 71 μHz in the 19 million data points spanning 8 d.

The most recent detections of solar-like oscillations in a giant were achieved from a two-site radial-velocity campaign spanning 2 full months. De Ridder *et al.* (2006) discovered an excess power near 60 μHz for the G9.5III star ϵ Oph (see Fig. 2.43). They derived two possible values for the large spacing (4.8 or 6.7 μHz). The star was subsequently monitored from space by the MOST mission during 37 d. The MOST light curve is in full agreement with the velocity data and, having no aliasing problems, pointed out that 4.8 μHz is the correct value for the spacing (Barban *et al.* 2007). Finally, oscillations were also firmly established for the K0III star η Ser from the same two-site campaign (Carrier *et al.* 2007, see also Fig. 2.4).

Red giants could potentially show a complicated mixed mode frequency structure containing a lot of information on the interior physics of evolved stars, although the short mode lifetimes obtained by Stello *et al.* (2006) may render the predictive power of their observed frequency spectra. Moreover, theoretical computations by Dziembowski (1977), Dziembowski *et al.* (2001), and Gough & Houdek (2002) predict the nonradial modes to be damped far more strongly than the radial modes, due to the high density contrast between the core and the extended envelope. This may imply that only radial modes reach observable amplitudes. This is consistent with the observed frequency spacings detected so far in ground-based radial-velocity data. On the other hand, Hekker *et al.* (2006) investigated the variability in the cross-correlation profiles of four pulsating red giants and came to the conclusion that this variability can only be understood in terms of the presence of nonradial modes. Clearly, more observational and theoretical work is needed to obtain a better understanding of the oscillations in red giants. Undoubtedly, observations with CoRoT will be of much value in this respect.

2.6 Pulsations in evolved stars with $M \geq 9\,\mathbf{M}_\odot$

In the current section we describe the variable nature of stars with initial masses above $9\,\mathrm{M}_\odot$ which are evolved off the main sequence. These stars never encounter degeneracy in their core and experience different burning cycles until they have an iron core, after which they explode as supernova.

Their luminosity-to-mass ratios increase significantly as they evolve off the main sequence. Indeed, during their evolution past the TAMS towards the red supergiant phase, and then back in the direction of the ZAMS, they lose a lot of mass while keeping almost the same luminosity. Because of this, L/M increases and the stars come close to their *Eddington limit*, the upper value of L/M determined by the requirement that the inward gravitational acceleration is larger than the outward acceleration due to the strong radiation pressure. Any star close to its Eddington limit cannot be very stable. This is particularly relevant for the lifetimes of stars born with $M > 40\,\mathrm{M}_\odot$. For recent compilations of studies of the most massive stars we refer to, *e.g.*, Massey (2003), Heydari-Malayeri *et al.* (2004), Humphreys & Stanek (2005), Ignace & Gayley (2005). Here, we concentrate on those variability aspects of such stars which may be related to oscillations.

The overall variability of this group of stars in the upper HR diagram occurs at different timescales and may have very different physical causes. Sometimes, the lowest-amplitude variability is periodic. We term such stars *Periodically Variable Supergiants*, irrespective of the cause of the periodic variability. These stars are indicated as such in the grey upper zone in Fig. 2.2. It is unfortunate that seismic modelling is not yet reached at these high masses, because stellar structure and evolution models are most uncertain for such stars, due to badly understood phenomena such as rotational mixing and meridional circulation, semi-convection, strong core convective overshooting and mass loss. We provide an overview of the variable nature of such massive objects in this chapter but we will not return to them further on in the book.

2.6.1 Periodically variable B and A supergiants

The A-type supergiants

Supergiant stars of spectral type A showing variations in photometry with amplitudes of tenths to hundredths of a magnitude were termed α Cyg variables, after the A1I prototypical star α Cygni. They have been monitored for decades by different teams, *e.g.*, Sterken (1977, 1983), Burki *et al.* (1978), van Genderen *et al.* (1989), Lamers *et al.* (1998), van Genderen (2001), and references therein. Burki (1978) and van Leeuwen (1998) focused on a sample of 32 and 24 late-B to G supergiants, describing the variability of these α Cyg variables from ground-based Geneva and Hipparcos data, respectively. The periodicities found by these authors range from 10 to 100 d and are too long to be due to the radial fundamental mode of such objects (Lovi *et al.* 1984). It should be pointed out, however, that significant uncertainties in the theoretical oscillation calculations occur for stars of such high luminosity, as they undergo all sorts of mixing processes in their interior as well as instabilities in their atmosphere due to the large radiation pressure. These effects are usually ignored when predicting p- and g-mode frequencies.

Line-profile variations in supergiant stars were discovered by Baade *et al.* (1990), who studied the O9I companion of the WR binary γ^2 Velorum. An extensive line-profile study based on years of monitoring of 6 BA-type supergiants was made by Kaufer *et al.* (1997). These authors concluded that the variability patterns in the line profiles are extremely complicated and seem to point towards cyclic variations in the deduced radial velocities. Besides these cyclic changes, they concluded nonradial oscillations to be present from travelling sub-features across the line profiles whose periodicities are not compatible with the rotation of the stars.

No detailed modelling of the observed periodic variability was achieved so far. Non-linear radial instabilities in so-called *strange modes*, with periods between 10 and 100 d roughly, have been put forward as an explanation for the variations in stars with masses above $40\,\mathrm{M}_\odot$ (Kiriakidis *et al.* 1993; Glatzel *et al.* 1999; Dziembowski & Slawinska 2005 and references therein). Such strange modes are caused by a strong enhancement in the opacity in the second partial ionization layer of helium and of the heavy elements. They are excited due to strong non-adiabatic conditions in stars with a high L/M ratio, *i.e.*, stars not too far from their Eddington limit. These strange modes are predicted to have amplitudes that are much larger than those found for the classical radial oscillators. From this, one speculates that they could perhaps be responsible for triggering the outbursts accompanying the moderate to low-amplitude periodic variability of the A-type supergiants and the *Luminous Blue Variables* (see below). The occurrence of strange modes has not yet been firmly established observationally in the most massive stars.

The B-type supergiants

Oscillations as in β Cep stars have not yet been firmly established in luminous stars with $\log L/\mathrm{L}_\odot > 5$ and $M > 20\,\mathrm{M}_\odot$, although they are predicted in that part of the HR diagram as well (Pamyatnykh 1999 and Fig. 2.20). The reason is probably that the instability strip no longer coincides with the entire main sequence, but is shifted towards more evolved stars. Pamyatnykh (1999) predicted SPB-type g modes to be unstable at such high luminosities in pre-TAMS stars (*i.e.*, stars near the end of their central hydrogen-burning stage, see Fig. 2.45). The post-TAMS evolution during the hydrogen-shell burning phase of such objects is so fast that it is hard to find stars in that evolutionary state in the first place. On the other hand, the stars do not spend long in the red part of the HR diagram, and return quickly to the position of their pre-TAMS stage (*e.g.*, Maeder & Chiosi 2000 for a thorough review). It is very difficult to unravel the evolutionary state of stars in that part of the HR diagram from classical observations. Seismic information could help a great deal here. However, at that stage in their evolution, significant mass loss in the form of a line-driven stellar wind (*e.g.*, Kudritzki & Puls 2000 for a review) complicates the unambiguous detection of possible oscillatory motion at the stellar surface.

Waelkens *et al.* (1998) discovered a sample of B supergiants to be periodically variable with SPB-type periods from the Hipparcos mission. These stars, and additional similar ones, were subjected to detailed

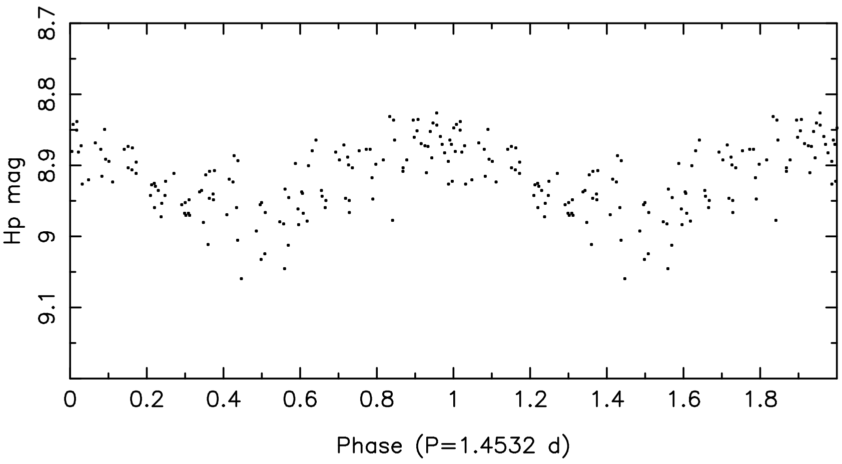

Figure 2.44: Hipparcos light curve of the B2/B3Ib/II HD 98410 folded according to the dominant period. Data taken from ESA (1997).

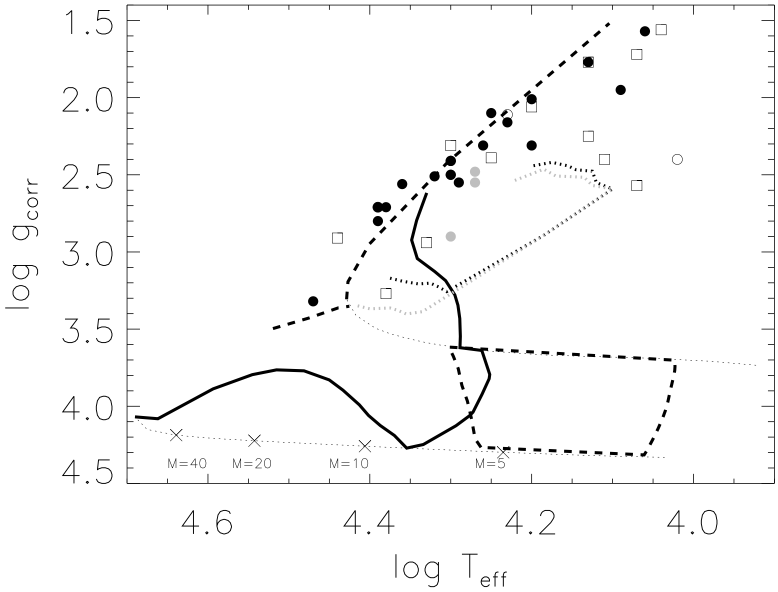

Figure 2.45: The position of the sample of B supergiants discovered to be periodically variable from the Hipparcos mission is compared with Pamyatnykh's (1999) pre-TAMS instability computations for p modes (full lines) and g modes (dashed lines). The instability strips of post-TAMS g modes computed by Saio *et al.* (2006) are indicated as dotted lines (grey: $l = 1$ modes, black: $l = 2$ modes). (From Lefever *et al.* 2007.)

spectroscopic and frequency analyses by Lefever *et al.* (2007), who found their masses to be below 40 $M_\odot$ and photometric periods between 1 and 25 d, *i.e.*, shorter than the periods of the periodic variations found in the more massive A-type supergiant variables. An example light curve is shown in Fig. 2.44. The stars in the sample perfectly fulfil the wind-momentum-luminosity relation derived for galactic A- and B-supergiants by Kudritzki *et al.* (1990). Their line-driven wind thus behaves normally. Lefever *et al.* (2007) found the sample periodic supergiants to be placed near the high-gravity limit of Pamyatnykh's (1999) heat-driven g-mode instability strip for evolved stars (see Fig. 2.45). This implies that the interpretation of their variability in terms of nonradial oscillations excited by the heat mechanism, as first suggested by Waelkens *et al.* (1998), is plausible. The authors found marginal evidence for a connection between the wind density and the photometric amplitude.

A new step ahead in the understanding of such stars was achieved by Saio *et al.* (2006), who detected both p and g modes in the B2Ib/II star HD 163899 from MOST space-based photometry. The authors deduced 48 frequencies below 2.8 d^{-1} with amplitudes below 4 mmag and constructed post-TAMS stellar models that led to g-mode frequencies which are compatible with the observed frequency spectrum.

Further research is needed to evaluate if seismic modelling in terms of internal physics parameter evaluation of individual periodically variable B-type supergiants is feasible. In order to achieve this, the current mode identification methods (see Chapter 5) must be adapted to the case of a dynamical atmosphere dominated by radiative forces.

Luminous Blue Variables

Some of the most luminous stars undergo sporadic violent outbursts, the cause of which is not yet well understood, but may be due to strange-mode instabilities. These objects are called Luminous Blue Variables or LBVs. Their irregular behaviour is comparable to that of a geyser on earth:

quiet period → moderate activity → heavy dredge-up → violent eruption → quiet period → . . .

Half a century ago the existence of some very peculiar, strongly variable massive stars in our Galaxy, such as P Cygni and η Carinae, was already known. Moreover, a few such stars were also known in the Magellanic Clouds, *e.g.*, S Doradus. However, it was not clear yet at that time that all of these very massive objects were undergoing the same type of instabilities. The newly discovered members were called P Cygni or S Doradus star, depending on their presence in our Galaxy or in the Magellanic Clouds. Moreover, similar objects began to be found in nearby galaxies, such as the so-called Hubble-Sandage variables in M 31 and M 33.

It took until the 1970s before a lot of progress was made in the interpretation of these objects. Space observations in the ultraviolet (UV) made it clear that all of them are losing significant amounts of mass. Moreover, they all showed excess fluxes at infrared wavelengths. This class of stars was termed “Luminous Blue Variables” (Conti 1984).

The outbursts of LBVs can take several decades and are of irregular nature, with long periods of quiescence in between. The stars are optically faint when they are quiet as their outer layers have temperatures

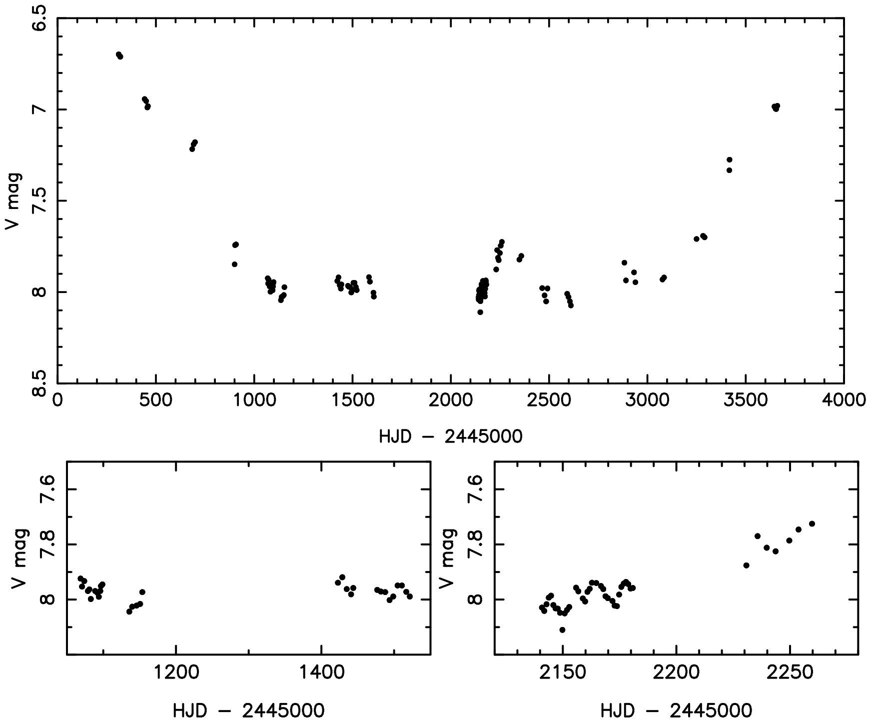

Figure 2.46: Top: Light curve of the LBV AG Car obtained in the framework of the Long-Term Photometric Variables programme of ESO. The bottom panels show two enlarged sections. Data taken from Sterken *et al.* (1995).

of typically 12 000 K – 30 000 K and so they mainly emit energy in the UV. During the outbursts, however, the LBVs can increase their brightness by two or three orders of magnitude because the outer layers cool significantly, typically to some 8 000 K, so they emit much more of their energy in the visual. The stars eject about a whole solar mass of their material during such a heavy eruption. More regular and less violent eruptions also occur. In that case they only take about one year and they occur almost periodically.

At present there are several tens of confirmed LBVs and some tens of candidates known in our galaxy and in nearby galaxies. Their luminosities are all more than six orders of magnitude above the solar value and remain almost constant, even during the violent eruptions.

Very different timescales and amplitudes are present in the light curves of LBVs. As an example we show in Fig. 2.46 the light curve of AG Carinae observed over almost a decade. These variations are mainly caused by a change in the temperature of the visible surface layers of the star, not in its luminosity. We can subdivide the variations of LBVs in four different kinds:

1. Giant outbursts with brightness changes larger than 2 mag, which are the consequence of eruptions of large amounts of stellar matter. Examples are the eruptions of P Cygni in 1600 and of η Carinae in 1841 (*e.g.*, de Groot & Sterken 2001 for a compilation). During its giant eruption, η Carinae clearly went past its Eddington limit. The time scale of these giant eruptions is not well known for the simple

reason that we have witnessed very few of them so far. For this reason one assumes that a reasonable estimate is one eruption every few hundred to thousand years.

2. Eruptions accompanied with brightness differences of one to two magnitudes. These smaller eruptions occur on time scales of 10 to 40 yr. The visual magnitude usually increases by some 2 mag during a few months and then a very slow brightness decrease occurs, which takes several years. The stars S Doradus and R 127 in the Magellanic Clouds, and AG Carinae in our Galaxy experience these types of eruptions.
3. Smaller variations of about half a magnitude in brightness occur on a time scale of several months to a few years. These variations are superposed on the moderate eruptions described in 2.
4. Low-amplitude (below 0.1 mag) variations occur on a time scale of several days to weeks. These variations are probably the same as those observed in the B- and A-type supergiants discussed above and may thus be due to stellar oscillations.

Since the heat mechanism is so successful in explaining the variability of many types of stars, particularly B stars on the main sequence, g modes have been proposed to be the cause of the low-amplitude variations of LBVs from observations (Lamers *et al.* 1998). However, any theoretical computations needed to check the excitation of modes are very dependent on the physical parameters, which are very badly constrained for LBVs and supergiants in general. Also, one needs to combine the effect of being very close to the Eddington limit with instability calculations, which evidently leads to quite uncertain predictions.

As already mentioned above, it may very well be that strange-mode instabilities with periods near 100 d are responsible for the observed variations, and perhaps even the outbursts, in stars with masses above 40 $\mathrm{M}_\odot$. The periodic variations of supergiants with masses below 40 $\mathrm{M}_\odot$ having stable periods less than 20 d are due to the classical heat mechanism, as suggested by Pamyatnykh (1999), Saio *et al.* (2006) and Lefever *et al.* (2007).

2.6.2 Wolf-Rayet stars

A star is called a *Wolf-Rayet (WR) star* when a hot helium core is left after the evolution of a massive star that has lost its entire hydrogen envelope due to a radiation-driven wind. The spectra of WR stars show strong emission lines caused by the rapidly expanding thick atmosphere. WR stars are situated in the HR diagram at luminosities of $4.5 \leq \log L/\mathrm{L}_\odot \leq 6$ and temperatures $\log T_{\mathrm{eff}} \geq 4.6$. They are the remnants of stars with initial masses above 40 $\mathrm{M}_\odot$ which have lost so much mass that only a helium core of some 4 $\mathrm{M}_\odot$ is left.

The WR stars are subdivided into two groups: the carbon-rich WC stars and the nitrogen-rich WN stars. These classes are subsequently subdivided into WC5 – WC9 and WN3 – WN8 according to the presence of particular lines in the spectrum. The WN and WC stars represent different evolutionary phases. The WN stars evolve towards WC stars as more and more stellar material gets lost through the stellar wind. For a catalogue of WR stars, we refer to van der Hucht (2001).

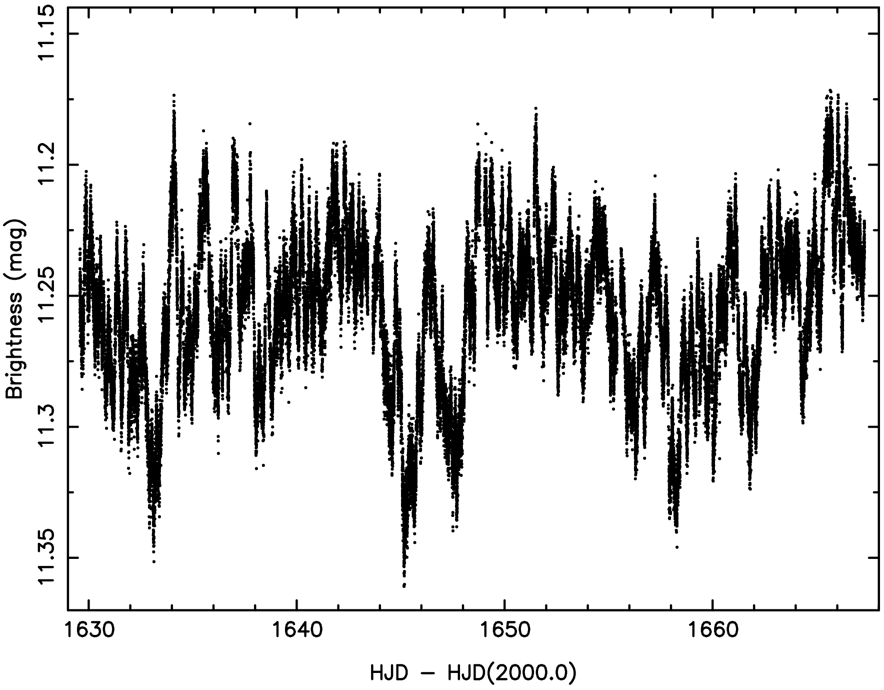

Figure 2.47: The light variations of WR 123 as observed by the MOST satellite. Data taken from Lefèvre *et al.* (2005).

The fundamental parameters of WR stars are extremely hard to determine, because of their high level of activity in terms of a strong stellar wind and due to the complex surface phenomena (*e.g.*, Crowther & Smith 1997 and references therein). The determination of their general properties constitutes a very active area of research which we will not review here. Mainly, we will focus on their variable character and even more specifically on the periodic variability.

The WR stars have quasi-periodic variability with periods ranging from a few hours to a few days. One of the earliest systematic studies of their variability was done by van Genderen *et al.* (1987), who interpreted the data in terms of temperature-induced changes in the continuum emission. Numerous studies done by the same team followed this initial investigation. Marchenko *et al.* (1998a) presented an extensive study of WR stars from the Hipparcos data and found a very large diversity in these stars' variability. The three case studies of the stars WR 6, WR 134, and WR 123, based on long strings of homogeneous photometry, did not allow a conclusion about whether their variability is due to a gradual restructuring of the stellar wind or nonradial oscillations (Marchenko & Moffat 1998). Moreover, the result of coordinated multisite photometric and spectroscopic observations of WN8 stars in 1989 and 1994-1995 by Marchenko *et al.* (1998b) still did not allow an unravelling of the cause of the high level of variability, although the authors state that it "may be supported/induced by pulsational instability". A good example of the difficulty in interpreting the variability is in Veen *et al.* (2002), who did not even manage to discriminate between orbital and pulsational variability for WR 46 after years of monitoring.

An important achievement was made by Lefèvre *et al.* (2005), who used MOST photometry to analyse the light variability of WR 123 with unprecedented precision from a 38 d uninterrupted time series (see Fig. 2.47). They found periodic signals with periods below 1 d, but none of them turned out to be stable for more than several days, except for a stable 9.8 h periodic signal superposed on stochastic variability throughout the whole run. In an attempt to interpret this observation, Townsend & MacDonald (2006) investigated the stability of WR stars and suggested unstable g modes of intermediate radial orders excited by a heat mechanism operating on an opacity bump at an envelope temperature near 1.8 million K. The periods they find range from 11 to 21 h for a WR model containing some surface hydrogen ($X_{\rm surface} = 0.12$), and from 3 to 12 h in a hydrogen-depleted WR model. This suggests that self-excited g modes may be the source of the 9.8 h periodic variation of the star disentangled in the MOST data. Dorfi *et al.* (2006), on the other hand, explained the observed variability in terms of a strange mode oscillation due to the iron-opacity bump in a hydrogen-rich ($X = 0.35$) stellar model.

We must conclude that strict periodicity has not yet been found so far in WR stars except for the recent case of WR 123's 9.8 h period derived from uninterrupted space photometry. The physical origin of the complete observed variability remains unclear, but as far as oscillations are concerned, the promising computations pointing towards the excitation of heat-driven g modes or strange modes will hopefully be continued in the near future and be confronted with more high-quality data.

Some of the LBVs have exactly the same characteristics as WN9 stars during their visual minimum. For this reason, the LBVs are considered to be the immediate progenitors of WR stars and it makes sense to try to understand the LBV microvariability in terms of g modes similar to those found by Townsend & MacDonald (2006). This has so far not been done.

Once a star has reached the WR phase there is no way back: it will soon explode as a supernova, leaving a compact remnant (neutron star or black hole).

2.6.3 The role of core g modes in supernova explosions

There are several observational facts that demand asymmetric supernova explosions. Many pulsars, *e.g.*, have high proper motions and a large fraction of neutron stars have such high velocities that they must have experienced a large kick at birth. Neutrino-driven convection was put forward as a viable non-spherical supernova mechanism (Burrows *et al.* 1995), although it cannot explain the highest observed velocities of neutron stars.

In order to solve this problem, Goldreich *et al.* (1997) proposed the ϵ mechanism to be the cause of the necessary asymmetry before the onset of core collapse. Murphy *et al.* (2004) have further explored the viability of g-mode oscillations excited by nuclear reactions to be at the origin of pre-collapse asymmetries by performing an eigenmode analysis. They indeed found unstable outer core g modes in all progenitor models with initial masses between 11 and 40 $M_\odot$, with oscillation periods between 1 and 10 s. These modes are trapped by discontinuities between the fossil Fe core and either the O shell (lower masses) or the Si burning shell (higher masses). However promising this mechanism was, the growth time scale of the core modes ranged between 10 and 10 000 s, which is far too long for the ϵ mechanism to become effective in the supernova progenitors. Indeed, the asymmetries must typically be achieved within one second after the onset of the collapse.

An entirely new view on core-collapse supernova explosions was proposed by Burrows *et al.* (2005). They found the agent of the explosion to be the acoustic power generated by the excitation and sonic damping of core g-mode oscillations. Their 2D hydrodynamical computations for a $13\,\mathrm{M}_\odot$ star show that a proto-neutron star is a self-excited oscillator in which an $l = 1$ mode with a period of $\sim 3\,$ms (besides lower-amplitude modes) grows and becomes prominent 500 ms after bounce. The source of the acoustic power is the gravitational energy of infall and the core oscillation acts like a transducer to convert this accretion energy into sound, resulting in an asymmetric ejection of the mantle. While neutrinos do not drive the explosion in this model, they do contribute to the deposition of energy in the shock. This mechanism is currently the most promising one to explain the observed morphologies and r-process properties of supernovae. Obviously, it is very hard to test this model observationally, except for the behaviour of the ejecta and the predicted neutrino fluxes.

2.7 Compact oscillators

Stars at the end of the AGB phase leave the red part of the HR diagram to become white dwarfs. This happens whenever their dust-driven and pulsation-induced wind comes to an end. During their post-AGB phase, which lasts typically only 10 000 years, they travel through the HR diagram with constant luminosity towards higher effective temperature because their outer envelope expands quickly and the hot CO core becomes better visible. For some stars, the last thermal pulse causes a very efficient mixing with large convective overshooting, implying a drastic change in surface composition and a return towards the AGB. During this very short born-again phase, the star may cross the instability strip while moving red- and blueward in the HR diagram. Examples of such fast-evolving stars are V605 Aql and Sakurai's object (*e.g.,* Clayton *et al.* 2006). On their blueward path back from the AGB, they join the Wolf-Rayet central stars of planetary nebulae in the sense that they end up as hydrogen-deficient stars whose surface layers are rich in helium, carbon and oxygen. We will soon turn to the description of the oscillations in such hot (pre-)white dwarfs.

Some low-mass stars, however, end up in the extreme horizontal branch and do not become AGB stars as their hydrogen envelope contains too little hydrogen to keep the hydrogen-shell burning going. These objects are situated to the left of the RR Lyrae stars and have masses below $0.5\,\mathrm{M}_\odot$. They turn immediately towards the white-dwarf phase once their central helium is exhausted. Some of these subdwarf B (hereafter sdB) stars turn out to have oscillations and so we describe them here as well because they are also compact stars whose oscillations have many similar characteristics to those of white dwarfs.

Some white dwarfs accrete matter in a binary and explode as supernovae of Type Ia. This extreme form of white-dwarf variability plays a crucial role as standard light sources in cosmology (*e.g.,* Perlmutter *et al.* 1999).

Finally, the core-collapse supernovae, originating from exploding massive single stars, leave behind very compact stellar remnants, such as neutron stars or black holes. We discuss the current status and

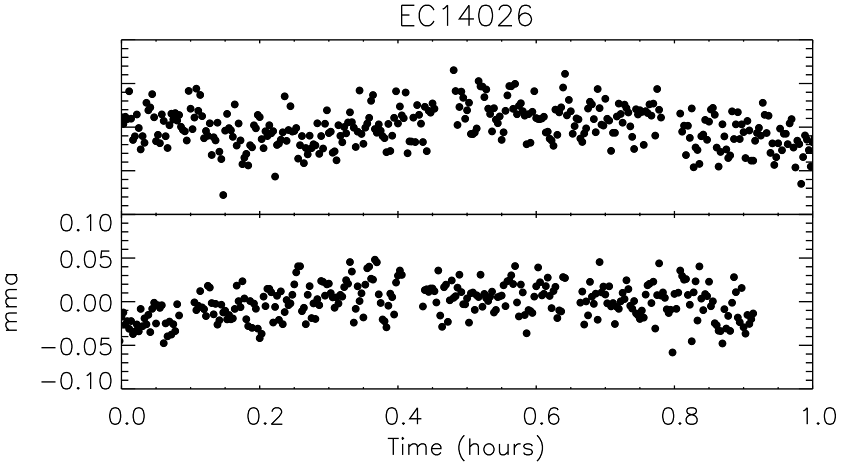

Figure 2.48: The light variations in the prototype of the short-period sdBV stars. The employed unit is mma, which stands for milli-modulation amplitude. This differs by a factor $2.5 \log e = 1.08574$ from mmag. Data taken from Kilkenny *et al.* (1997).

prospects of asteroseismology of these most compact objects as well.

We start off with the least evolved of the compact oscillators, but not before pointing out that pulsating hydrogen-poor carbon stars and extreme helium stars will additionally be discussed in the last section of this chapter, since binarity plays a crucial role in our understanding of this diverse group of stars.

2.7.1 Variable subdwarf B stars

In 1997, a team of South-African astronomers discovered a new class of pulsating stars among the sdB stars. Periodic variations with 144 s were discovered in the sdB star EC 14026 (Kilkenny *et al.* 1997, see Figs 2.48 and 2.49). The "EC" notation stands for the catalogue of the "Edinburgh-Cape Blue Object Survey", which was the southern extension of the PG (Palomar-Green) survey.

The sdB stars are helium-deficient sub-luminous B stars at relatively high galactic latitude whose spectra show broad Balmer lines and very weak He I lines. They have effective temperatures between 23 000 and 32 000 K, values of $\log g$ between 5 and 6, and masses below 0.5 $M_{\odot}$. They have lost almost their entire hydrogen envelope at the tip of the red-giant branch such that their thin hydrogen layer does not contain enough mass to burn hydrogen. The sdB stars therefore evolve immediately from the giant branch towards the extreme horizontal branch (EHB) and have only central-helium burning. They all show a deficiency in helium and chemical anomalies of carbon and silicon, which supports the idea that they are low-mass old Population I stars. They are the immediate progenitors of low-mass white dwarfs.

Currently some 30 short-period sdB pulsators are known among the 300 in which variability has been sought. These 30 all have multiple periods ranging from 80 to 600 s and amplitudes between 0.001 and

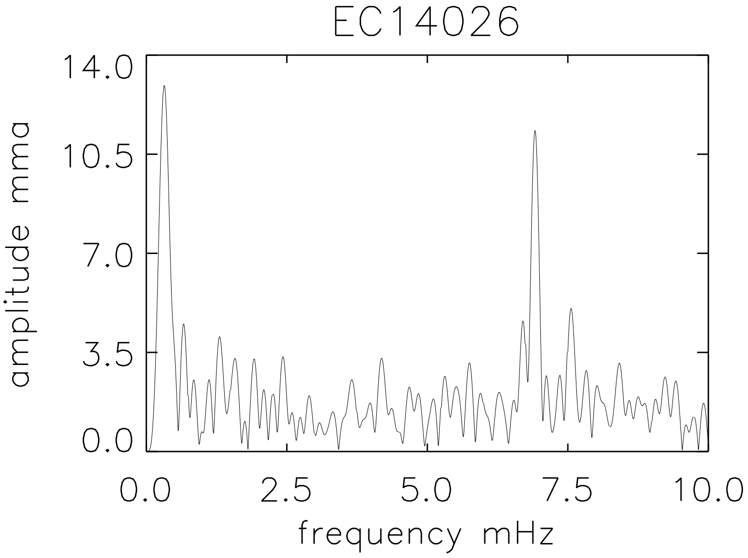

Figure 2.49: The amplitude spectrum of the light curve of EC 14026 shown in Fig. 2.48. Data taken from Kilkenny *et al.* (1997).

0.3 mag. They are nowadays also termed V361 Hya stars, which is the official variable star name for the prototype. We will term these objects sdBV stars for simplicity.

The existence of pulsating sdB stars was predicted independently of, and simultaneously with, their observational discovery by a Canadian team (Charpinet *et al.* 1996). An opacity bump associated with iron ionization turns out to be an efficient driving mechanism. The diffusion processes that are at work in sdB stars, particularly radiative levitation, imply that iron becomes overabundant in the driving zone. Whenever this overabundance leads to a local Z-value above 0.04 in the partial ionization zone of iron, low-order p-mode oscillations are excited (Charpinet *et al.* 1997).

During the course of an ongoing monitoring program to investigate light variations in additional sdB stars in the northern hemisphere, a group of some 20 sdB stars turned out to have multiperiodic light variations with individual periods around one hour and very low amplitude (Green *et al.* 2003). These stars are termed PG 1716+426 stars after the prototype, but they have also been called “Betsy” stars as of the scientific meeting at which the discoverer announced their existence. We term them g-mode sdBV stars. Their periods are an order of magnitude longer than those in the p-mode sdBV stars (see Fig. 2.50), while they are located in a similar position in the HR diagram, at slightly cooler temperatures. This situation is very similar to the one of the β Cep stars and the SPB stars near the main sequence. It is therefore logical to interpret these longer periods in terms of high-order g modes.

It was indeed found that the same instability mechanism as for the p-mode oscillators predicts such modes to be unstable whenever the iron abundance in the driving region is sufficiently high (Fontaine *et al.* 2003). Nevertheless, only modes with degree $l = 3$ or 4 are found to be excited, in contrast to the

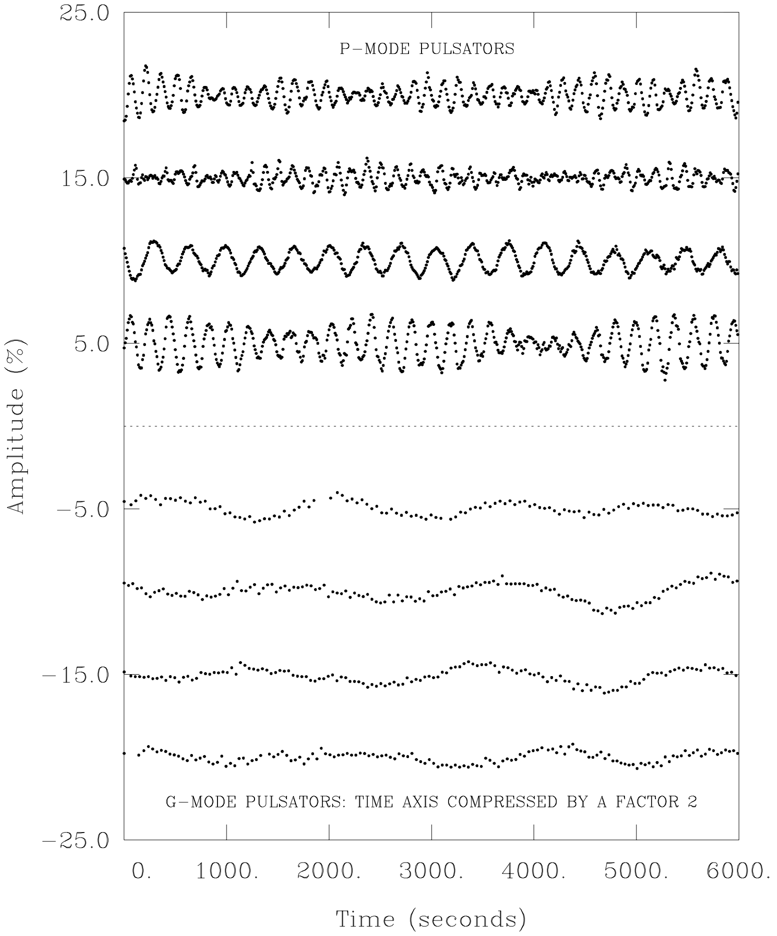

Figure 2.50: Comparison between the light variations of four sdB p-mode oscillators (upper panel) and four sdB g-mode oscillators (lower panel). The time axis refers to the top half of the figure; the light curves in the bottom half have been compressed by a factor two for visual purposes. (From Fontaine *et al.* 2003.)

results found for the p modes. This is rather unsatisfactory, since it does not seem evident from a physical viewpoint to excite only higher-degree modes. In this respect, the work by Jeffery & Saio (2006) is very promising. These authors studied mode excitation using models with envelopes having an artificial but homogeneous iron enhancement and found $l = 1, 2$ g modes to be excited for appropriate temperature ranges of the observed g-mode sdBV stars. Both different approaches, *i.e.*, using a stratified composition with iron enhanced in the critical layers for excitation (Fontaine *et al.* 2003) versus a global iron enhancement in the envelope (Jeffery & Saio 2006), are precisely the same as those used by Pamyatnykh *et al.* (2004, local iron enhancement) versus Ausseloos *et al.* (2004, global iron enhancement) to explain all the excited observed modes for the β Cep star ν Eri, discussed earlier in this chapter.

A summary of sdB star research is provided in the volume edited by Østensen (2006). There are at present insufficient frequencies found in any of the g-mode sdBV stars to perform in-depth seismic studies, but the observational efforts to obtain more data are ongoing. The best light curve, as far as the sampling is concerned, was obtained from space with MOST (Randall *et al.* 2005). It revealed three frequencies corresponding to periods of 5227 s, 2650 s, and 7235 s, with amplitudes of 0.054%, 0.041%, and 0.038%, respectively, in fractional brightness.

2.7.2 White dwarfs

White dwarfs are the end-products of stars born with initial masses below some 9 $M_\odot$. Observationally, as with main-sequence, giant and supergiant stars, they are classified as DO, DB, DA, DF and DG with further refinements that were introduced as better data became available (Sion *et al.* 1983). As with other stars, these spectral types characterize the apparent chemical composition of the atmospheres of the stars and are connected to the effective temperature. In white dwarfs, however, the temperature scale is significantly different from that of main-sequence stars in the sense that the white dwarfs are generally hotter than their main-sequence counterparts with the same nominal spectral type, and the temperature spread for the DA and DB stars, in particular, is wide and not continuous.

By far most white dwarfs, some 75%, belong to the DA class. DA white dwarfs have pure hydrogen atmospheres, resulting in very strong and broad Balmer lines in their spectrum. About 25% of the white dwarfs show only neutral helium lines in their spectrum. These are called the DB white dwarfs. Finally, a tiny fraction (less than 1%) shows only ionized helium lines. These are called the DO white dwarfs. In order to keep life simple, white dwarfs with helium-rich atmospheres are often also termed non-DA white dwarfs. Moreover, there are also a few DAB and DAO white dwarfs, which have both hydrogen and helium lines in their spectrum. They seem to originate from a variety of circumstances, including convective mixing in single stars, accretion of hydrogen from the interstellar medium onto a helium atmosphere, as well as interacting compact binaries with white-dwarf or subdwarf components (Vennes *et al.* 2004 and references therein).

The hottest hydrogen-rich DA white dwarfs typically have surface temperatures near 80 000 K and the ratio of DA to non-DA white dwarfs increases with decreasing temperature. On the other hand, all DO white dwarfs have temperatures above 45 000 K while DB white dwarfs have temperatures between 30 000 K and 12 000 K (and perhaps even lower since helium lines become invisible below this temperature). The occurrence of only one dominant chemical species in the atmosphere is rather well explained by diffusion processes, as was shown by Fontaine & Michaud (1979).

A remarkable and intriguing fact is that no DB white dwarfs, *i.e.*, objects with a helium-rich atmosphere, occur in the effective temperature range between 30 000 K and 45 000 K. This exclusion is known as the DB gap. Fontaine & Wesemael (1997) explained this gap as a natural consequence of the evolution of all white dwarfs from planetary nebula nuclei, because the absence of turbulent mixing, due to an insufficient amount of hydrogen, results in only DA white dwarfs in the temperature range of the DB gap. Shibahashi (2005), on the other hand, gave a slightly different explanation in terms of chemical separation due to gravitational settling in a convectively stable atmosphere, which occurs exactly in the temperature range between the He II/He III and He I/He II ionization zones. Either explanation implies that DB white dwarfs become DA for the temperatures in the DB gap, and then return to become DBs.

Among each of the three main types of white dwarfs, periodic variables occur. These used to be termed DAV, DBV and DOV white dwarfs. Their multiperiodic variations are due to low-degree, high-order g modes, excited by the heat mechanism active in different ionization layers for the two classes DO and DB and by convective driving for the DA class (see below). Because of the tight mass-radius relation of white dwarfs, their oscillation periods necessarily are similar and are typically of order a few minutes. Very specific to white-dwarf oscillations is the occurrence of strong mode trapping caused by the stratified envelopes, which affects the eigenfrequencies (Winget *et al.* 1981; Brassard *et al.* 1992). A recent compilation of studies of (pulsating) white dwarfs is available in Koester & Moehler (2005).

A particularly interesting aspect of the pulsating white dwarfs is the possibility to investigate the cooling mechanisms of white dwarfs, through observations of period changes. For the hotter classes (DO and DB) neutrino emission through plasmon and other processes plays an important and potentially detectable role (O'Brien & Kawaler 2000; Kim *et al.* 2005). For cooler white dwarfs effects of crystallization, which play an important and uncertain role for white-dwarf cooling, may be detectable (*e.g.*, Montgomery & Winget 1999; Córsico *et al.* 2005).

We discuss below the oscillations of the three classes of white dwarfs separately. First, however, we discuss the variable central stars of planetary nebulae. These were historically treated as a separate class, termed PNNV, but it has recently become clear that several of these actually behave as the DOV pulsators. This had led to the definition of one global class of GW Vir pulsators, which is the terminology we adopt here.

Variable central stars of Planetary Nebulae: oscillations or stellar winds?

Central stars of planetary nebulae, often abbreviated as CSPN, constitute a group of stars of which some exhibit photometric and spectroscopic variability with periods from several hours to days (*e.g.*, Handler 1995). This variability has been ascribed to either a variable stellar wind (Hutton & Méndez 1993; Patriarchi & Perinotto 1997) or stellar oscillations (Zalewski 1993; Gautschy 1995). The periods of order hours are much longer than those of the g modes detected in the GW Vir stars and cooler pulsating white dwarfs, as discussed below, and thus require a different interpretation.

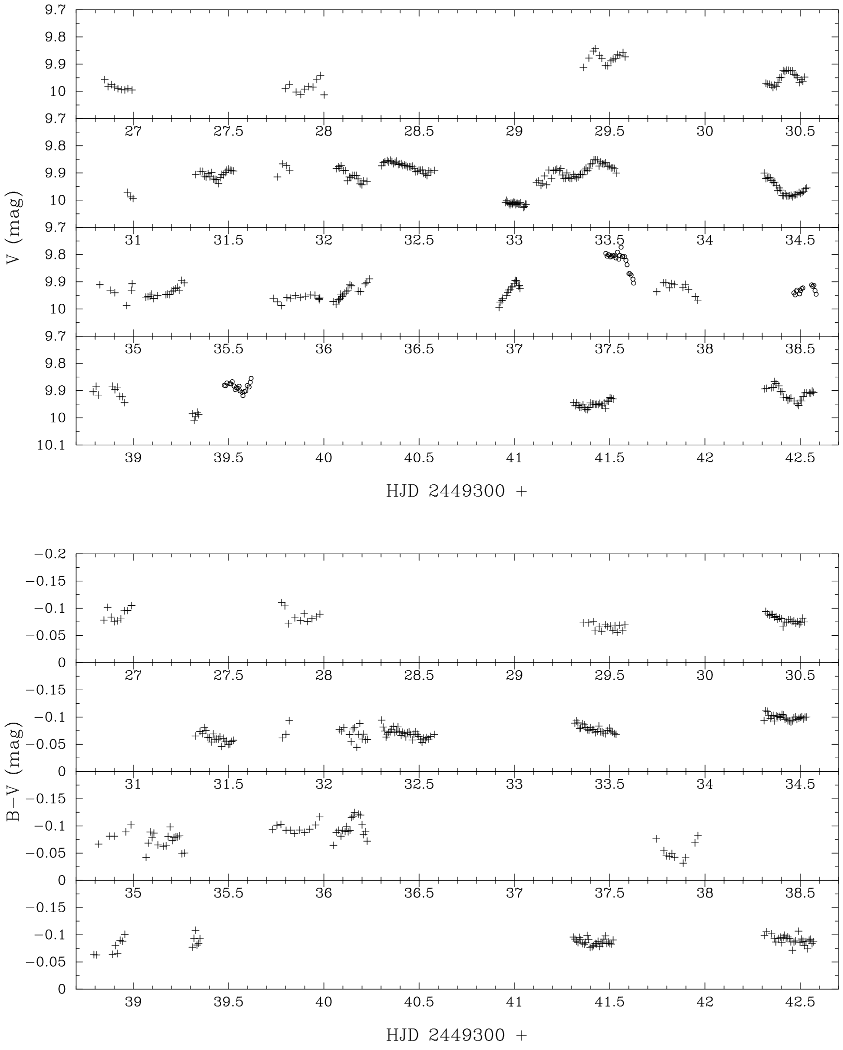

Figure 2.51: Top panel: V light curve of CSPN HD 35914 from a multisite campaign. The plus signs denote photoelectric measurements and the open circles CCD data. Bottom panel: $B-V$ variations. (From Handler *et al.* 1997.)

While Méndez *et al.* (1983) reported the variability of HD 35914 (the CSPN of planetary nebula IC 418, also known as the “Spirograph Nebula” for which there is a beautiful Hubble Space Telescope picture[17]) and interpreted it as modulation in the outflow, Liebert *et al.* (1988) found the star VV 47 (CSPN of NGC 2474-5) to exhibit variability similar to the pulsating white dwarfs. The optical spectrum of VV 47 is also similar to those of the pulsating GW Vir stars, although somewhat broader absorption lines occurred for VV 47. The similarity to the behaviour of GW Vir made Liebert *et al.* (1988) suggest that some CSPN have oscillations similar to the white dwarfs. Hence he termed these objects *Planetary Nebulae Nuclei Variables* or PNNV in analogy to the naming for the variable white dwarfs at that time.

Extensive multisite observations of the best studied variable among the CSPN, HD 35914, led Handler *et al.* (1997) to detect irregular light modulation with a time scale of days, as well as cyclic semi-regular variations with a time scale of 6.5 h (see Fig. 2.51). The periodicity of hours was found to be stable over more than a decade. Unfortunately, it was impossible, even from such an extensive data set, to discriminate between oscillations and wind variability for the interpretation of the data, but rotational modulation and binarity could be excluded as the dominant cause of the variability. A similar conclusion was reached for the central star of M 2-54 (Handler 1999).

Besides “normal” CSPNs, which show absorption lines in their spectra, also Wolf-Rayet stars occur among the central stars of planetary nebulae. Their spectra are characterized by emission lines, pointing towards a strong stellar wind. They are usually denoted as [WCE] stars. Their characteristics were summarized by Górny *et al.* (1995) and Tylenda (1996), and further refined by Górny *et al.* (2004). These works point towards the presence of helium, carbon and oxygen and a deficiency of hydrogen at their surface. Their masses and luminosities are somewhat higher than those of normal CSPNs, explaining the stronger wind and the disappearance of hydrogen. Their evolutionary status is still unclear, but may involve binary evolution for some stars (De Marco *et al.* 2003). On the other hand, their characteristics are generally not different from those of normal CSPN stars (Girard *et al.* 2007). Their infrared properties even point to the presence of dust produced during a carbon-rich AGB phase before the atmospheres of these stars became hydrogen poor (Hony *et al.* 2001). Werner & Herwig (2006) found a strong evolutionary connection between the [WCE] and DO white dwarfs. The variability of the [WCE] stars was interpreted in terms of oscillations by Gautschy (1995).

To make the picture even more complicated, we point out that Handler (2003) performed a systematic study of what he termed variable Central Stars of young Planetary Nebulae, and baptized them *ZZ Leporis stars* after the prototype in his sample. This consisted of 14 members and he found these stars to exhibit roughly sinusoidal (semi-)regular photometric and/or radial velocity variations with time scales of several hours. The sample stars’ temperatures are below 50 000 K and they all show hydrogen-rich spectra. Although Handler (2003) concluded that stellar pulsation is the most likely cause of the variability, he could not exclude variable mass loss. This group of stars has not been studied further, as far as we are aware.

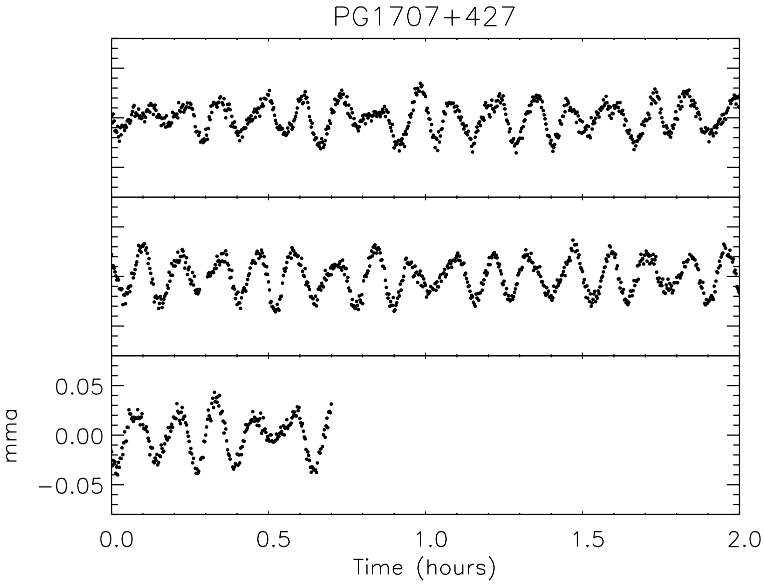

Figure 2.52: Part of the light curve of the DOV white dwarf PG 1707+427 obtained during a WET campaign. Data taken from Kawaler *et al.* (2004).

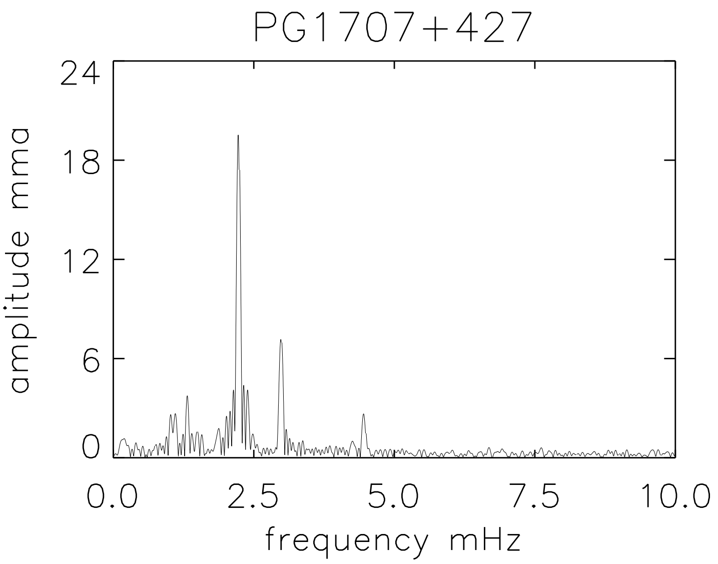

Figure 2.53: The amplitude spectrum of the light curve of PG 1707+427 shown in Fig. 2.52.

GW Vir stars

Among the DO white dwarfs, the *PG 1159 stars* or, more recently termed the *GW Vir stars*, constitute a well established class. The DO white dwarfs are situated at the position in the HR diagram where the post-AGB track stops and turns down towards the white-dwarf cooling sequence. They have extremely high effective temperatures in the range 70 000 K to 170 000 K. Their spectra show a large deficiency in hydrogen and high helium, carbon and oxygen abundances due to their stellar wind and helium burning, respectively. The determination of the hydrogen abundance is rather difficult due to the high temperature. As outlined above, some GW Vir stars are termed PNNVs because a planetary nebula still occurs around them. DO white dwarfs are indeed the direct descendents of planetary nebulae nuclei.

The DOV pulsators are often named after their prototype, PG 1159-035 or GW Vir. This star, GW Vir itself, was discovered to be an extremely hot pulsating degenerate star by McGraw *et al.* (1979). GW Vir's light variations observed by the Whole Earth Telescope[18] (WET, Nather *et al.* 1990) and their interpretation implied a very important step for asteroseismology. Part of the WET light curve of the DOV star PG 1707+427, and its resulting frequency spectrum, are shown in Figs 2.52 and 2.53 (Kawaler *et al.* 2004). These two plots are prototypical for most of the GW Vir pulsators.

Kawaler *et al.* (1985) presented linear, nonradial adiabatic oscillation computations for evolutionary pre-white-dwarf models, leading to predictions for the DOV star frequencies and eigenfunctions. The oscillation periods range from about 7 to 30 min. The modes are driven by the heat mechanism active in the partial ionization zones of carbon and/or oxygen, as already suggested earlier by Starrfield *et al.* (1984). The exact shape of the instability domain near the kink of the evolutionary track was found to depend on the distribution of helium in the CO-rich envelope.

It is clear that the oscillation periods of several PNNVs are at least a factor of three longer than those of the DOV stars. The latter are white dwarfs that are about to start cooling, while the PNNVs are still increasing their effective temperature while keeping their luminosity essentially unchanged, *i.e.*, their radius is still decreasing quite drastically. This different evolutionary status is thus reflected in the oscillation period difference between the DOV stars and the PNNVs and is in agreement with the scenario of Werner & Herwig (2006).

The theoretical instability strip of both the PNNV and DOV stars was revisited by Quirion *et al.* (2004), Gautschy *et al.* (2005), Córsico *et al.* (2006) and Quirion *et al.* (2007). From these studies which include mass loss and diffusion, it became clear that one and the same instability mechanism, *i.e.*, the heat mechanism associated with the opacity bump due to partial ionization of the K-shell electrons of partial ionization zones of carbon and oxygen, leads to an instability domain containing both the observed GW Vir stars and the [WCE] stars (see Fig. 6 of Córsico *et al.* 2006). The instability requires the presence of carbon and oxygen in the atmosphere. This can only be achieved when the stars undergo a strong radiation pressure, causing the carbon and oxygen to remain in the envelope thanks to radiative levitation while the hydrogen is blown away in a stellar wind. As the luminosity of the star decreases, the wind becomes less strong and gravitational settling causes carbon and oxygen to sink, while helium will start floating to the surface.

---

[17] `http://heritage.stsci.edu/2000/28/big.html`

[18] `http://www.iastate.edu/wet`

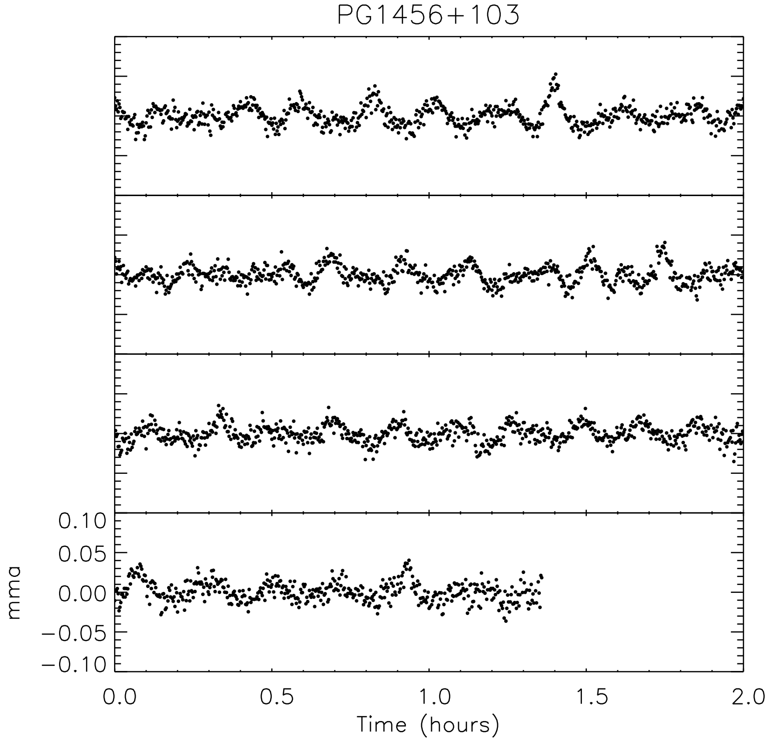

Figure 2.54: Part of the light curve of the DBV white dwarf PG 1456+103 obtained with the Nordic Optical Telescope by Jan-Erik Solheim during a WET campaign (unpublished); from data provided by the WET consortium.

This diminishes the excitation of the GW Vir oscillations. This is in complete agreement with the strong evolutionary connection between the [WCE] and GW Vir stars derived by Werner & Herwig (2006). This scenario also leads to a natural explanation of the DBV pulsators whose oscillations are excited by the same heat mechanism, but this time acting on helium once it is sufficiently dominant and in the appropriate partial ionization stage in the envelope.

The seismic analysis of GW Vir presented in the seminal work by Winget *et al.* (1991) implied not only a first test case for the technique of asteroseismology, but at the same time a real breakthrough in the derivation of white-dwarf structure models. This study paved the road for many more seismic studies of compact stars since 1990. White dwarfs thus became the main targets of the WET consortium, although numerous other types of pulsators have been added since.

Variable DB white dwarfs

Excitation of g-mode oscillations in DB white dwarfs due to the heat mechanism acting in the second partial ionization zone of helium was predicted by Winget (1982) (see also Winget *et al.* 1983). This led to the discovery of the first such *variable DB white dwarf*, also termed DBV star, namely GD 358 (Winget *et al.*

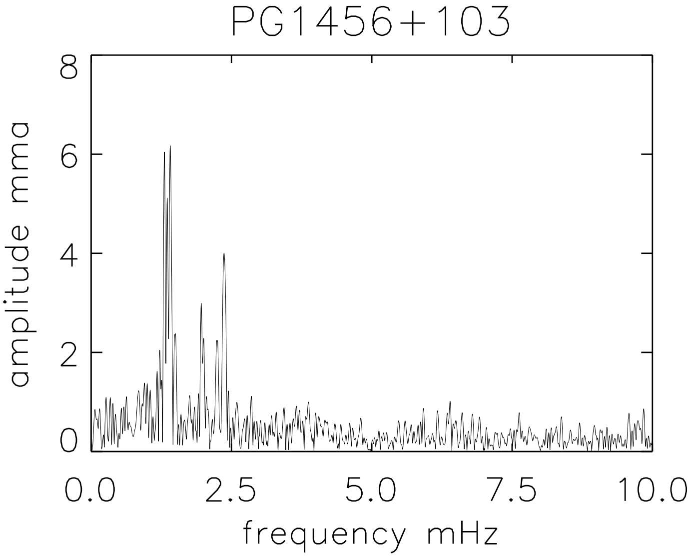

Figure 2.55: The amplitude spectrum of the light curve of PG 1456+103 shown in Fig. 2.54.

1982). Only 13 DBVs are known to date (Kepler 2007 and references therein), probably due to their faintness (V near 16, except for the prototype GD 358 with a $V = 13.6$). Their oscillation periods range from 4 to 12 min and their amplitudes are relatively large, from a few mmag to 0.2 mag. Bradley (1995) reviewed the properties of these stars. They are situated in a broad range of effective temperature, from 11 000 to 30 000 K and the mass of their helium-rich envelope is estimated to be between 10^{-6} and 10^{-2} times their total mass. As already mentioned above, this is in full agreement with the excitation computations for hot compact stars by Quirion *et al.* (2007). It should be noted that convective driving, introduced by Brickhill (1991) for variable DA white dwarfs, may also play an important role for the DB variables.

The light variations measured by the WET consortium of the simplest among the DBV pulsators, PG 1351+489, showed the star to have only two modes, with periods of 489 s and 333 s (Winget *et al.* 1987). The prototypical DBV star GD 358, on the other hand, has a very complex frequency spectrum (Nather *et al.* 1990) with several tens of peaks. These two stars can be considered to capture the range of complexity across the DBV class. An intermediate case and its frequency spectrum are shown in Figs 2.54 and 2.55. This is for the star PG 1456+103 with data obtained during the WET run XCOV22 (extended coverage campaign 22, unpublished; see the WET website for more information).

Although the beating effect in GD 358 is prominent, the position of the frequency peaks in the spectrum turn out to be quite stable over long timescales while the amplitudes clearly vary (Kepler *et al.* 2003). Since GD 358 is by far the best studied DBV star, it was thought until recently that the frequency spectra of all the class members were stable. Handler *et al.* (2003), however, performed extensive monitoring of two DBV stars with the WET and found evidence for amplitude and frequency variability. They suggested non-linear resonant mode coupling to be the cause of the complex variability in these two stars (see, *e.g.*, Buchler *et al.* 1997).

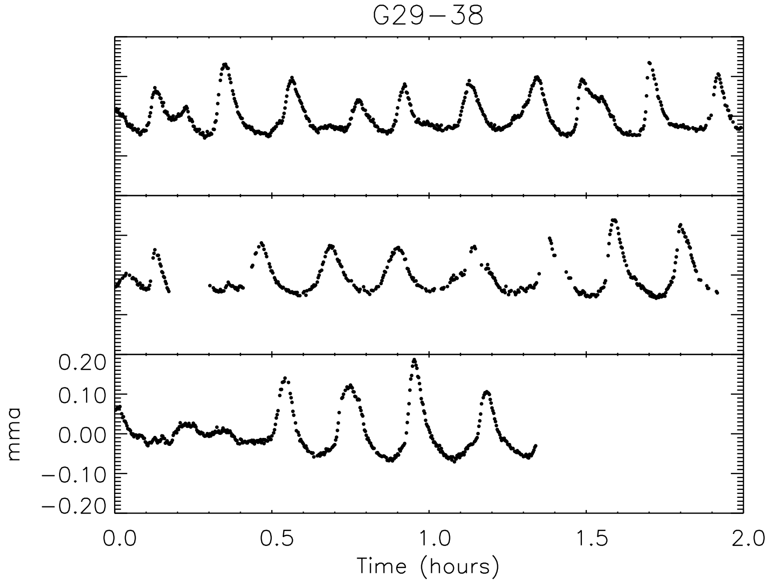

Figure 2.56: Part of the light curve of the DAV white dwarf G29-38 obtained with the 0.75-m at SAAO by Retha Pretorius in the framework of a WET campaign (unpublished); data courtesy of the WET consortium.

The potential of asteroseismology of DBV stars was highlighted by Bradley *et al.* (1993). Moreover, extensive seismic models and their oscillation properties for DBV and DAV stars had already been presented by Tassoul *et al.* (1990) and Bradley & Winget (1991), pointing out the maturity of this branch of asteroseismology more than a decade ahead of any other type of star, except the Sun.

Variable DA white dwarfs

Further along the white-dwarf cooling track one finds the hydrogen-rich *variable DA white dwarfs*, also called DAV or ZZ Ceti stars. The DAV mode excitation results from convective driving, a mechanism first proposed by Brickhill (1991) and further developed by Goldreich & Wu (1999) and Wu & Goldreich (1999). The shape of the strip was found to be mainly determined by the effective temperature and the mass of the white dwarf, the most uncertain factor in theoretical mode prediction being the poorly known efficiency of convection. This is in very good agreement with empirical determinations of the instability strip leading to a very narrow range of less than 1 000 K in effective temperature, from 10 850 to 11 800 K (Bergeron *et al.* 2004, Mukadam *et al.* 2004b).

The DAV stars vary multiperiodically with low amplitudes and fulfil a period-amplitude relation (Clemens 1994). The periods range from less than 100 s to more than 1 000 s. Their frequency spectra also show multiplets and are, in general, simpler than those of the DBV and GW Vir stars. This may be an observational bias because the DAV pulsators have been less intensively monitored than the GW Vir and DBV pulsators. Indeed, the spectrum of the well-studied DAV star G29-38 appears to be very different, with numerous harmonics and beat and sum frequencies, from season to season (Vuille *et al.* 2000 and Figs 2.56 and 2.57).

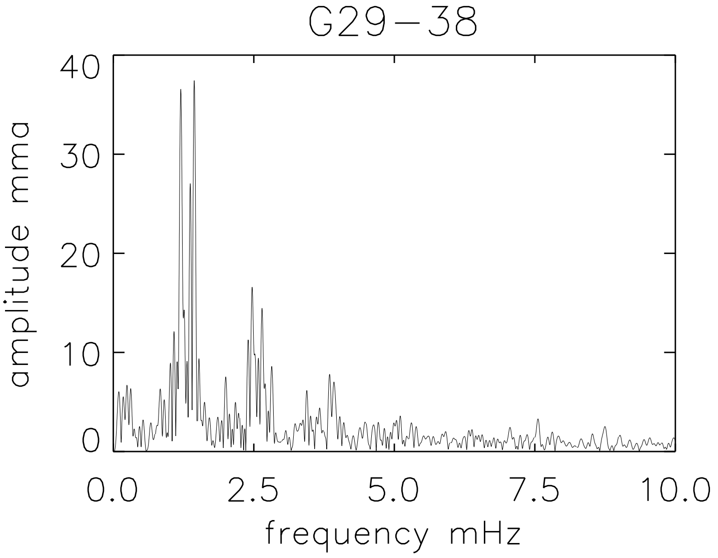

Figure 2.57: The amplitude spectrum of the light curve of G29-38 shown in Fig. 2.56.

While empirical mode identification in selected DAV stars is mostly achieved from multiplet structures in the frequency spectrum, or from amplitude ratios based on multicolour photometry, time-resolved spectroscopy of G29-38 with the Keck telescope has allowed the identification of the modes from line-profile variations as well (Clemens *et al.* 2000). All these mode identification techniques confirm the low-degree nature of the oscillations. The thickness of the hydrogen envelope governs the mode selection. Typically, the mass of the hydrogen-rich envelope is estimated to be about 10^{-4} times the mass of the white dwarf.

Up to 2004, 39 DAV pulsators were known (*e.g.*, Bergeron *et al.* 2004 and references therein), most of them discovered from photometry but 7 among them from spectroscopy. A remarkable step ahead in the understanding of the class was achieved by Mukadam *et al.* (2004a), who almost doubled the number of class members with their discovery of 35 new pulsating DAV stars selected from the Sloan Digital Sky Survey and the Hamburg Quasar Survey. Mullally *et al.* (2005) subsequently found 11 new DAV stars, Kepler *et al.* (2005) another 14, and Castanheira *et al.* (2006) yet another 11, almost all again first selected from the Sloan Digital Sky Survey. This brings the number of class members to 107. This led Mukadam *et al.* (2006) to examine changes in the pulsation properties of DAV pulsators across the instability strip. They found a well-established trend of increasing pulsation period with decreasing effective temperature. Also, they showed that the pulsation amplitude decreases just before pulsations shut down at the empirical red edge of the instability strip.

2.7.3 Neutron stars

Neutron stars are the compact remnants that become gravitationally decoupled from the expanding ejecta of a supernova explosion, resulting from a core collapse of a single star with initial mass above $9\,\mathrm{M}_\odot$. The collapse results either in a compact neutron star with a mass between 1.5 and $3\,\mathrm{M}_\odot$ and a diameter of about 12 km, or in a black hole (when the remnant mass is above about $3\,\mathrm{M}_\odot$). The precise upper mass limit of a neutron star is not yet known, since the correct equation of state for a fully degenerate relativistic neutron gas is still much debated. Hence there is as yet no firm value for the analogue of the Chandrasekhar limit for the upper mass limit of a neutron star.

At birth, the infall causes a dramatic spin-up of the neutron star and a strengthening of its magnetic field by factors of millions, leading to a rotation period of only a few milliseconds to seconds, and likely causing the star to send out radiation along the magnetic field lines. As a result, the neutron star is observed as a *pulsar*, with regular pulses at radio, visible, X-ray or gamma-ray wavelengths, whenever the magnetic axis is inclined with respect to the rotation axis and when the geometry of the beam is such that the radiation passes in our line-of-sight during each rotation period. The radio waves originate from material above the magnetic poles, while the X- and gamma-rays are caused by the accretion of matter on the very hot magnetic poles of the neutron star.

Straight after the discovery of pulsars by Jocelyn Bell in the framework of her PhD Thesis (Hewish *et al.* 1968), nonradial oscillations were proposed as the explanation of the pulses (Ruderman 1968). Nevertheless, the pulsating model was quickly abandoned in favour of an oblique rotation model to explain the observed features of pulsars (Gold 1969). Only many years later, Strohmayer (1992) and Strohmayer *et al.* (1992) re-introduced nonradial oscillations to account for the numerous complex observed properties of pulsars, including drifting pulses and stationary sub-pulses, because the rotating models failed to explain all these details in the observed variability. The observational and theoretical progress in the understanding of pulsar beams was summarized by Graham-Smith (2003).

Clemens & Rosen (2004) recently presented an oblique pulsator model based on high-overtone nonradial surface g-mode oscillations of very high degree (l near a few hundred and n near a few tens), aligned to, and symmetric about, the magnetic axis of the pulsar, as an explanation of the complex observed phase behaviour of the pulses and sub-pulses and of the morphology of pulsar beams. Such modes have periods near 10 s and were shown to have low energy and large surface amplitude (McDermott *et al.* 1988), in contrast to core g modes. The quasi-periodic changes in the data are explained as switching between modes of different l and n, while negative beating is held responsible for null detections occurring in the observed time series of the flux once in a while. These features of this model were claimed to be similar to mode changes observed for white dwarfs on the one hand, and to the oblique pulsator model explaining the roAp stars on the other hand.

A relatively new aspect of neutron star physics, in which nonradial oscillations play an important role, are the gravitational waves radiated during the formation process of the neutron star. After the gravitational collapse, the proto-neutron star radiates its binding energy through neutrino emission on a timescale of tens of seconds before the final neutron star is formed. This formation process is obviously very hard to study, unless we could detect the gravitational radiation associated with the birth of the hot compact remnant.

Indeed, the oscillation spectrum of a forming neutron star changes quite drastically during the formation. This is easily understood from the argument that the frequencies are mainly dependent on the mass and radius of the object. Typically, the neutrino emission during the formation results in a mass decrease of 0.1 $M_\odot$ and a radius decrease from 35 km to 12 km. Such changes will have a significant effect on the mode frequency values.

Ferrari *et al.* (2003) have computed the changing frequency spectra and damping times of the oscillations of forming neutron stars. They found the oscillation spectra of p, g, and f modes of forming neutron stars to be remarkably different from those of cold old neutron stars. The frequencies of the modes cluster typically between 900 and 1500 Hz at the start of the formation process, but evolve to very distinct values for these three different types of modes about 5 s after the formation. Also, the different modes keep very different levels of the mechanical energy reservoir to send out in the form of gravitational waves after the completion of the formation. The authors ignored the effect of rotation, even though a significant amount of angular momentum is generated during the birth of the neutron star, and they ignored the bounce and the first 200 ms after collapse which needs to be studied hydrodynamically; even so, this pioneering study gives hopeful prospects for the near future. Ferrari *et al.* (2003) also showed that the first-generation gravitational-wave detectors (VIRGO[19], LIGO[20], EURO[21]) should be able to detect the gravitational signals connected to the nonradial oscillations sent out during these different stages in the life of the neutron star, within much of the Milky Way Galaxy. This would open up the field of gravitational-wave asteroseismology. Similarly, the processes leading to the formation of stellar black holes may involve oscillations that can be detected through observations of gravitational waves.

2.8 Pulsations in binaries

For all the classes considered above, numerous examples occur where the pulsating star resides in a binary or, more generally, in a multiple system. When this is a wide visual binary, *i.e.*, for cases where the components do not affect each other's behaviour and evolution, the binarity is of not much importance for the oscillation study, other than being an asset because it allows a more accurate determination of the fundamental parameters (such as mass, radius and age) of the pulsating component compared with a single pulsator. A notable example is the visual binary α Cen A (G2V) and α Cen B (K1V), whose components both show p-mode oscillations. At the upper end of the mass range, the visual binary WR 86 is worth mentioning. It is a variable WC7 Wolf-Rayet star with an initial mass of some 40 $M_\odot$ having a 20-$M_\odot$ β Cep companion (Paardekooper *et al.* 2002). This companion pulsates in p modes with frequencies of 6.914 d^{-1} and 7.236 d^{-1}. Contrary to the α Cen binary, the oscillations of this very massive binary have not yet been exploited seismically, because of lack of mode identification.

Binarity offers the same advantage of providing accurate fundamental parameters in close unevolved detached binaries for which the tidal interaction is negligible. In general, this is the case for orbital periods above some 20 d for ZAMS components and above some 100 d for TAMS components (Willems 2003).

---

[19] `http://wwwcascina.virgo.infn.it/`

[20] `http://www.ligo.caltech.edu/`

[21] `http://www.astro.cardiff.ac.uk/geo/euro/`

In such cases, a complication may, however, occur when both components have the same spectral type, implying a merging of their oscillatory signature in the data and hence in the Fourier spectrum. As long as the contributions of the different components can be unravelled, seismic modelling can be achieved to at least the same level as for single stars.

Another type of complication occurs when one of the components of a currently detached close binary system has already gone through one or more phases of mass loss during its evolution, usually implying that mass transfer between the components has taken place. In such a situation, the gainer star is polluted by material of the donor star. This may have led to different surface compositions and internal structures of both the gainer and the donor, depending on whether the outer envelope is radiative or convective. Hence, if one of them is oscillating, the mass transfer will have affected the oscillatory behaviour. In fact, asteroseismology may in this case be a good tool to reconstruct the mass transfer and angular momentum history within the binary. Unfortunately, we do not know of any example where such reconstruction of the evolutionary history from oscillations has been achieved.

Extreme cases of interaction occur when a binary system enters a *common-envelope phase* where a compact component of the system effectively orbits within the envelope of a more tenuous component. This leads to rapid loss of mass and angular momentum, and hence to a drastic shrinking of the orbit.

Eclipsing binaries are of special value, because they deliver the most stringent constraints on the physical parameters of the components. For many of the classes of pulsating stars discussed above, we know of components residing in an eclipsing binary. The number of such cases is low, however, ranging from none for solar-like oscillators, roAp, γ Dor, RR Lyrae stars and Cepheids, to a few for B-type pulsators and compact oscillators, to a few tens for δ Sct stars, Miras and semi-regulars (Pigulski 2006). In principle, the oscillation modes can be identified from eclipse mapping in such cases.

Excellent recent overviews of pulsating stars in multiple systems (including clusters) were provided by Pigulski (2006) and Lampens (2006). In the following, we describe in detail some situations where the binarity is more than just a happy circumstance that delivers better fundamental parameters. In doing so, we do not consider disk oscillations as in, *e.g.*, X-ray or Be binaries; we focus entirely on cases where the oscillations can, in principle, be used to probe the stellar interiors rather than focusing on stellar disk properties.

2.8.1 Tidal perturbations of free oscillations

An extensive recent compilation of studies on the tidal evolution and oscillations in binary stars is available in Claret *et al.* (2005). Free oscillation modes excited by mechanisms intrinsic to the star (see the following chapter for a detailed explanation of such excitation mechanisms) may be altered by tidal effects, in the sense that their frequencies may undergo shifts. Rigorous and detailed mathematical descriptions of tidal effects on free oscillation modes can be found in Smeyers & Denis (1971), Saio (1981), Reyniers & Smeyers (2003a,b), Willems & Claret (2005), and references in these works.

Detections of tidal effects were first suggested by Fitch (1967, 1969) in some δ Sct and β Cep stars, but it became evident later on that these were premature. The first firm observational establishment of tidally affected oscillation frequencies was achieved by Fitch & Wisniewski (1979) for the δ Sct star 14 Aur Aa. The authors showed that the departure from equidistance in the observed frequency triplet can be explained by tidal splitting of the mode, as was confirmed by Reyniers & Smeyers (2003b). Goossens *et al.* (1984) suggested the variations of the oscillation frequency of the 33 d circular binary β Cep star σ Sco to be due to modulation by tidal action. Smith (1985a,b) subsequently made a thorough study of the line-profile variability of the binary β Cep star Spica (α Vir), with period 4.015 d and eccentricity $e = 0.146$, and interpreted the retrograde, toroidal-like oscillation mode he detected to be due to tidal shear exerted by the B2 companion.

There are also a number of pulsating stars in ellipsoidal variables, in which the tidally deformed components cause variability with twice the orbital frequency (*e.g.*, Aerts 2007 for a review). A noteworthy example is the star XX Pyx (Handler *et al.* 1998) which was long considered as a prototypical young δ Sct star suitable for seismic modelling (Pamyatnykh *et al.* 1998) until Arentoft *et al.* (2001) and Aerts *et al.* (2002) found it to be 1.15 d circular binary with ellipsoidal variations in which tidal effects dominate over rotational effects. Henry *et al.* (2004) found HD 207651 to be a triple system with δ Sct and ellipsoidal variations but no g modes triggered by tides. Lampens *et al.* (2005) also found the presence of ellipsoidal variations in the spectroscopic triple system DG Leo, which is composed of three stars of late-A spectral type. The wide component is a δ Sct star while the inner binary consists of two Am components of which at least one is not yet rotating synchronously although the orbit is circular. De Cat *et al.* (2006, 2007), finally, list several ellipsoidal variables among their samples of candidate γ Dor and pulsating B stars.

Numerous other pulsating stars reside in close binaries, but their detected frequencies, or differences among them, are not an exact multiple of the orbital frequency. Aerts & Harmanec (2004) compiled a list of close binaries with confirmed light and/or line-profile variability, several of which are confirmed pulsators, so these are all good candidates to continue the search for tidally affected and/or induced oscillations. This list originated from two independent approaches, *i.e.*, the search for close binarity among confirmed oscillators and the search for oscillations in confirmed close binaries. The authors found no obvious relations between the orbital eccentricity, the orbital frequency, the rotational frequency and the intrinsic frequencies of oscillations.

2.8.2 Tidally induced oscillations

It was realized long ago that resonant excitation of free oscillation modes by the tidal action of a companion can in principle be an effective way to trigger oscillations in binary components (Cowling 1941). Tidally induced oscillations and their effect on evolution and energy dissipation within a binary have been studied theoretically, for very different types of situations, by numerous authors, *e.g.*, Kato (1974), Zahn (1975), Savonije & Papaloizou (1984), Kosovichev & Novikov (1992), Diener *et al.* (1995), Kumar *et al.* (1996), Witte & Savonije (1999, 2001), Savonije & Witte (2002), Willems *et al.* (2003), Rathore *et al.* (2005) and references in these works. These authors show that the occurrence of suitable resonances depends not only on the properties of the oscillation modes of the stars, but mainly also on the period and the eccentricity of the orbit, as well as on the component masses and radii. The theoretical computations show that the tide-generating potential within an eccentric binary implies an infinite number of partial dynamic tides with forcing angular frequencies. Whenever one of those forcing frequencies comes close to an eigenfrequency of a free oscillation mode of one of the components, it is possible that the tidal action exerted by the companion is sufficiently enhanced to excite this mode resonantly. The occurrence of such resonances between partial dynamic tides and free oscillation modes is particularly relevant for the excitation of g modes, because their frequencies are similar to those of the orbital frequencies in close binaries. Moreover, the tide-generating potential is dominated by spherical harmonics of degree $l = 2$. Most computations for resonant excitation are therefore restricted to these modes. As discussed by, for example, Kosovichev & Novikov (1992) the excitation of modes through tidal interaction and the subsequent dissipation of the pulsation energy may play an important role in the capture of stars by massive black holes, through the loss of orbital energy by the star.

From an observational viewpoint, the detection of a tidally induced oscillation may seem simple at first sight. Indeed, whenever variations with an exact multiple of the orbital frequency are found, one may interpret these as due to a resonantly excited mode. In practice, it turns out to be extremely difficult to establish proof of tidally induced oscillations, despite numerous long-term efforts to search for a relationship between the orbital frequency and variability in close binaries (*e.g.*, Aerts & Harmanec 2004; Claret *et al.* 2005, and references therein).

The detection of frequencies which are an exact multiple of the orbital frequency has, as far as we know, been established for only two stars so far: the hybrid δ Sct/γ Dor star HD 209295 (Handler *et al.* 2002) and the SPB star HD 177863 (De Cat *et al.* 2000; Willems & Aerts 2002). These two stars reside in short-period eccentric binaries such that the circumstances are indeed favourable for tidal resonant excitation. Seismic modelling has not yet been possible for either of these stars. For HD 209295 the modes could not be identified, while only one pulsation frequency was firmly established for HD 177863.

2.8.3 Are the SX Phe stars all blue stragglers?

Blue straggler stars get their name from the fact that they appear close to the main sequence in stellar clusters, but substantially hotter and bluer, and hence presumably more massive, than the turn-off in the colour-magnitude diagram as defined by the bulk of the stars in the cluster. They are believed to be formed from the evolution and mass exchange of primordial binaries or from direct stellar collisions between main-sequence stars in dense globular clusters (*e.g.*, Bailyn 1995; Hurley *et al.* 2001; Sandquist 2005; Sils *et al.* 2005, and references therein). The blue stragglers have significantly smaller projected rotational velocities, but the same chemical peculiarities, as ordinary cluster and galactic field stars of the same spectral type (Andrievsky *et al.* 2000). Recently, Ferraro *et al.* (2006) detected 300 candidate blue stragglers in the galactic globular cluster ω Cen. They used the absence of central concentration in the blue straggler distribution across ω Cen as an argument to rule out a collisional origin for all of the blue stragglers and suggest a non-collisional origin for some of these stars. Hurley *et al.* (2005) used M67 as a test-bed for cluster evolution models and found different formation paths for the 28 observed blue stragglers in that cluster. In particular, a substantial population of short-period primordial binaries is needed to explain the observed blue straggler population of M67.

It is a lucky circumstance that many of the SX Phe stars were found to be blue stragglers. They seem to have a relatively high mass (Rodríguez & López-González 2000). These pulsating blue stragglers are thus interpreted in terms of binary mergers leading to a globally mixed helium-enriched star and their oscillations may provide clues to the formation scenario. Gilliland *et al.* (1998) made an extensive study of six SX Phe variables in the globular cluster 47 Tuc with the Hubble Space Telescope. Two of them oscillate in the fundamental and first overtone, two others oscillate simultaneously in the fourth and fifth radial overtones and two have multiple nonradial oscillations. This allowed the authors to combine evolution and pulsation constraints, resulting in mass estimates for the four double-mode SX Phe stars ranging from $1.3 \pm 0.1\,\mathrm{M}_\odot$ to $1.6 \pm 0.2\,\mathrm{M}_\odot$, and additional stellar parameters which are in excellent agreement with the cluster properties. Zhang *et al.* (2005) analysed two SX Phe stars in M 67. They found these stars to have, respectively, four and five radial modes. One of them has fundamental parameters in line with an unevolved late A star. The other one is the primary of a 4.2-d eccentric spectroscopic binary and has subsynchronous rotation. This SX Phe star was probably formed through stable Roche lobe overflow.

The global enrichment of helium in blue stragglers strongly affects the temperature and luminosity of a given star, but the location of the instability strip blue edge and the slope of the period-luminosity (PL) relation are unchanged. This suggests that the PL relation is not affected by blue straggler formation provided that blue stragglers are fully mixed stellar mergers (Templeton *et al.* 2002). Nevertheless, Bono *et al.* (2002) found that the modal stability and the pulsation amplitudes are somehow affected by the He content. The detailed properties of SX Phe stars could thus supply hints on the He content and on the formation history of these stars, but we believe it is fair to state that this stage has not yet been reached.

2.8.4 Are all dusty RV Tauri stars binaries?

Binaries make up a significant fraction of the post-AGB stars known to date (Van Winckel 2003). It was suggested by Lloyd Evans (1999) that IRAS infrared colours imply that RV Tauri stars are stars within the Cepheid instability strip with dusty circumstellar disks. By comparing the observational characteristics of RV Tauri stars and the class of extremely iron-deficient post-AGB objects, Van Winckel *et al.* (1999) concluded that binarity is indeed a widespread phenomenon among RV Tauri stars.

More recently, Yudin *et al.* (2003) monitored eight RV Tauri and five R CrB stars (see below) polarimetrically, and established the presence of permanent clumpy non-spherical dust shells around them. Moreover, De Ruyter *et al.* (2006) provided compelling evidence from spectral energy distributions extending to 850 μm that all six well-studied dusty RV Tauri stars are binaries with a circumbinary disk originating from the AGB evolutionary stage.

The question naturally arises whether all RV Tauri stars are binaries. In any case, the large-amplitude oscillations play a key role in the rapid mass-loss phase on the AGB where the stars undergo a dust-driven stellar wind. Mass transfer between evolving stellar components in a binary then leads to a natural explanation of a dusty circumbinary configuration and the observed infrared properties of the RV Tauri stars. This, together with the fact that their binary nature is very hard to establish on a case-by-case basis, makes it quite likely that all dusty RV Tauri stars result from the evolution of a pulsating AGB binary that managed to avoid a common-envelope phase. It requires very long-term spectroscopic monitoring to establish firm observational proof of this, because the pulsations cause radial velocity variations which are of similar magnitude

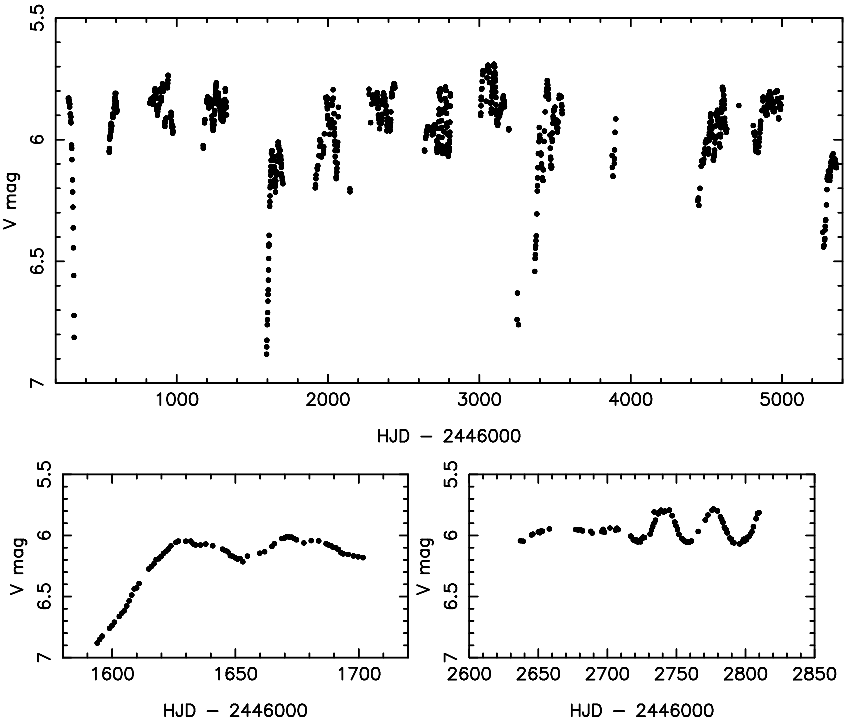

Figure 2.58: Top: Light curve of the HdC pulsator R CrB. The bottom panels show two enlarged sections. Data taken from Yudin *et al.* (2002).

to the orbital variations (see Fig. 2.35).

2.8.5 Hydrogen-deficient carbon stars and extreme helium stars

R Coronae Borealis (R CrB) stars are a particular subset of evolved pulsating hydrogen-deficient carbon (HdC) stars with large amplitudes. They have periods between 40 and 100 d, amplitudes of a few tenths of a magnitude in brightness (see Fig. 2.58) and a few km s^{-1} in velocity, and they have multiperiodic light curves (*e.g.*, Lawson & Kilkenny 1996). In general, the HdC stars are variables with an order of magnitude lower amplitudes than the R CrB stars. Both the R CrB stars and the HdC stars seem to be fundamental mode pulsators (Weiss 1987) with semi-regular light and radial-velocity curves. In addition to pulsational variations, from extensive long-term infrared photometry, Feast *et al.* (1997) concluded that the R CrB and HdC stars in general show variations due to their circumstellar dust on timescales of a few hundred to a few thousand days.

Extreme helium (eHe) stars, on the other hand, are highly evolved luminous stars (*e.g.*, Jeffery 1996). Their surfaces are characterized by a mixture consisting of the remnant of a H envelope, CNO-processed helium, and carbon products resulting from He burning. The eHe stars have high L/M ratios. They are expected to pulsate, either due to the heat mechanism based on the Z-bump (Saio 1993, 1995; Jeffery &

Saio 1999) or due to strange-mode instabilities (Saio & Jeffery 1988). The variable eHe stars are sometimes subdivided into categories according to their type of oscillation: V652 Her variables are radial and nonradial Z-bump pulsators with periods near 0.1 d, PV Tel variables have radial strange modes with characteristic periods near 20 d (Kilkenny *et al.* 1999) while V2076 Oph variables seem to have nonradial strange modes with timescales between 0.5 and 8 d (Jeffery & Heber 1992, Glatzel & Gautschy 1992). The variations turn out to be very complex, with quasi-multiperiodicity only, and imply an observational challenge in view of the long periods. In fact, Wright *et al.* (2006) made a very extensive long-term observational study of the hottest pulsating eHe star, V2076 Oph, and found no coherence at all in its variability. In particular, they did not manage to recover the periods reported earlier in their photometry and spectroscopy of the star. For an enlightening review on eHe stars we refer to Jeffery (2007).

From an evolutionary point of view, all of the R CrB, HdC and eHe stars lie on post-AGB evolutionary tracks. Iben *et al.* (1996) originally considered three scenarios to form HdC and R CrB stars, but only two of them are commonly accepted now. A first one explains the HdC and R CrB stars as hydrogen deficient due to a late thermal pulse at the end of the post-AGB phase. The result of this born-again scenario is an HdC star with chemical surface composition in agreement with progenitors of WR stars or of hot planetary nebulae nuclei. De Marco *et al.* (2002) tested the born-again scenario on four stars but concluded that they cannot have the same evolutionary history since only two of the targets are compatible with the proposed scenario. The second scenario involves the merging of two low-mass white dwarfs, one CO white dwarf and one lower-mass He white dwarf, resulting in a luminous He star (Saio & Jeffery 2002). This is much more plausible as an explanation for the eHe stars, and as these show many similarities to the HdC and R CrB stars, it is probably also an important route to explain these latter objects.

2.8.6 Pulsating sdB primaries

The prototypical pulsating sdB star EC 14026-2647 is a binary system, as is the case for about two thirds of the group members (Maxted *et al.* 2001; Morales-Rueda *et al.* 2003; Moralez-Rueda 2005). It is very likely that the binarity is of fundamental importance for the formation of all the sdB stars.

The sdB stars are believed to evolve directly to the white-dwarf stage and so they are the immediate progenitors of low-mass white dwarfs. Two of the members are indeed found in a post-EHB stage (Morales-Rueda *et al.* 2003). The details of the evolutionary state of the sdB stars is still largely unknown. In order to end up on the EHB they must lose nearly all of their hydrogen at almost exactly the same phase, *i.e.*, when the helium core has attained the minimum mass required for the helium flash to occur. Moreover, many of them have short orbital periods between a few hours and a few days and several known companions are white dwarfs. These observational facts have led to the proposal of three evolutionary channels for the formation of sdB stars (see Han *et al.* 2002, 2003 and references therein):

1. common-envelope ejection, leading to short-period binaries with periods between 0.1 and 10 d and an sdB star with a very thin hydrogen envelope; these sdB stars have a mass distribution that peaks sharply at 0.46 $M_\odot$;
2. stable Roche lobe overflow, resulting in similar masses as in case 1, but with a rather thick hydrogen-

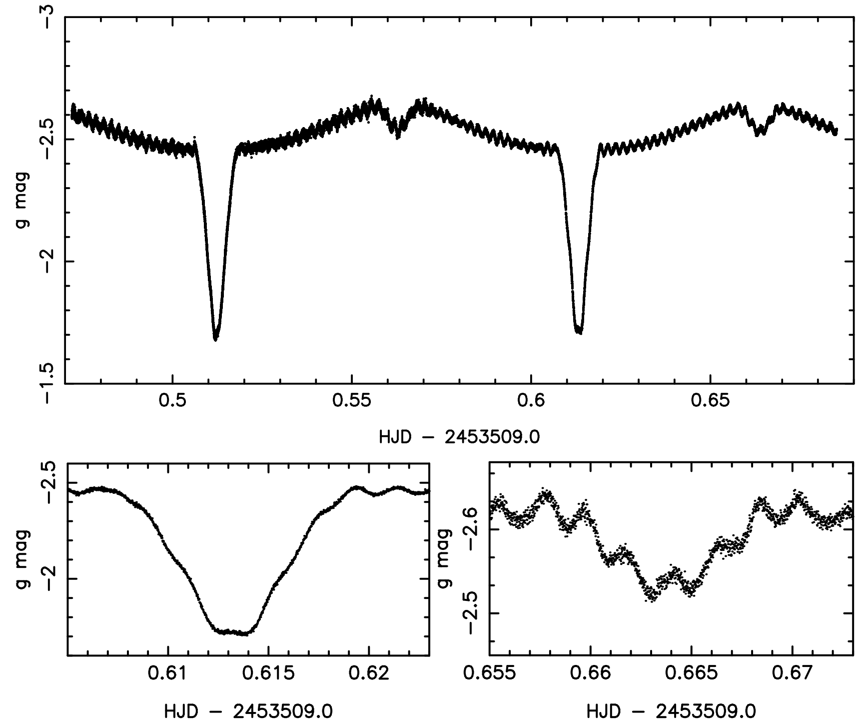

Figure 2.59: Top: ULTRACAM/VLT g’ light curve of the eclipsing sdBV star PG 1336-018. The bottom panels show two enlarged sections of the primary and secondary eclipse. Data taken from Vučković *et al.* (2007).

rich envelope and longer orbital periods between 10 and 100 d;

3. double helium white-dwarf mergers giving rise to single sdB stars with a wide distribution of masses.

An example of case 1 is the eclipsing binary pulsating sdBV PG1336-018 whose stunning light curve was discovered Kilkenny *et al.* (1997). This star has been intensively studied ever since, including during two WET runs (Kilkenny *et al.* 2003). We show its g' light curve obtained with ULTRACAM[22] on the VLT in Fig. 2.59. The circular binary orbit has a period of 2.4 h and the companion is an M dwarf, leading to a large reflection effect. As can be seen in Fig. 2.59, the oscillations of the primary remain visible during the primary eclipse.

An important question is the possible role of the binarity in triggering the oscillations of sdB stars. This has been tackled by Fontaine *et al.* (2003), who found that, indeed, the work done by the tidal force through the resonant excitation of a g mode becomes significant as the order of the mode increases. Thus, it seems plausible that some of the g modes observed in sdB binary pulsators may be tidally excited. It is unlikely that the p modes are tidally excited, because their frequencies are too high for that. They may, however, turn out to be affected by the binarity (see, *e.g.,* Reed *et al.* 2005).

2.8.7 Pulsating Cataclysmic Variables

Cataclysmic Variables (CVs) are short-period interacting close binaries with a white-dwarf component. The white dwarfs within such systems undergo mass accretion from their companion. The white-dwarf component itself is quite often invisible, because the accretion process dominates the flux we receive from CVs. The accretion rates vary a lot from one CV to the other. For those systems with a low mass transfer rate, the gas of the donor settles in a disc. This stored gas settles onto the white dwarf at semi-regular intervals, leading to a dwarf nova eruption. The white-dwarf components of such systems are detectable in visible light when the systems are in a low quiet state. Such CVs are, however, intrinsically faint. Several of them have been discovered from the Sloan Digital Sky Survey (Szkody *et al.* 2004).

Several CVs turn out to have a pulsating DAV primary. The first such discovered system was GW Lib (Warner & van Zyl 1998), a dwarf nova with an orbital period of 76.8 min for which three oscillation modes with periods of 646 s, 377 s, and 236 s were established in the discovery paper. Several additional discoveries, involving systems with similar orbital periods, followed soon (Warner & Woudt 2005 and references therein). All of them turn out to have similar oscillation periods ranging from 100 s to 1 400 s. The present number of pulsating CV primaries amounts to 11 (Marsh, private communication).

Townsley *et al.* (2004) managed to derive estimates of the white-dwarf mass, the accreted mass and the mass-transfer rate for GW Lib from seismic modelling. The rotation rate could not be derived, because the multiplet structure in its Fourier spectrum has not been resolved, despite extensive observational effort (van Zyl *et al.* 2004). It turns out that the accretion rate of the pulsating CV primaries is sufficiently low to keep the white-dwarf component in the DA instability strip, even though a white dwarf of its age should be much

---

[22] `http://www.shef.ac.uk/physics/people/vdhillon/ultracam/`

too cool to be a DAV star. A natural question of course emerges: are the accretion rates within CVs with DO or DB primaries suitable to keep these white dwarfs in the corresponding instability strip as well?

AM CVn is the prototype of a class of ultra-short period helium-accreting cataclysmic binaries. It turns out that the AM CVn stars probably have a mass transfer rate that is too high for them to remain in the DO or DB instability strips, so it is unlikely that there will be many discoveries of pulsating primary AM CVn stars. Nevertheless, Solheim *et al.* (1998) monitored AM CVn in photometry over a 12-d time span during a WET run. While several periodic light modulations with harmonics of the basic frequency near 950 μHz can be explained as a two-armed spiral structure (Savonije *et al.* 1994), the authors also found evidence for a g-mode pulsation, which indicates that the central white dwarf may in fact be a DO variable. Arras *et al.* (2006) indeed concluded from theoretical instability computations for a wide range of WD masses that g-mode oscillations are predicted in a diversity of CVs.

2.8.8 X-ray burst oscillations

Many of the currently known neutron stars reside in close binaries, as this is a very convenient location to allow their observational detection. Besides the importance of surface oscillations in explaining the observed complex features of neutron stars discussed above, Piro & Bildsten (2006) provided evidence that nonradial surface g modes are also a good explanation for X-ray burst oscillations. Such burst oscillations are thought to be a modulation of the neutron star rotation frequency. Piro & Bildsten's model builds further on the original ideas by Lee (2004) and Heyl (2004) that a retrograde surface mode with an observed frequency just below the rotation frequency is the cause of the burst oscillations.

Chapter 3

Theory of non-radial oscillations in a nutshell

In this chapter we describe the basic theory of non-radial oscillations and of mode excitation in stars. We provide only a very concise overview, skipping many of the mathematical details. The reason is that the students at Leuven University have the option to follow a 6 ECTS course entitled "Theory of stellar oscillations", which is taught in the same year as the current course on Asteroseismology. It is therefore evident that a detailed outline of the theoretical aspects of stellar pulsation is beyond the scope of the current course, in which the applications of asteroseismology are the main topic. The interested student can find details on the theory of stellar oscillations in:

- *the lecture notes entitled "Theorie van Stertrillingen" by T. Van Hoolst (only in Dutch) taught at Leuven University;*
- *the lecture notes entitled "Stellar Oscillations" by J. Christensen-Dalsgaard (2003, Aarhus University, English version) available from* `http://astro.phys.au.dk/~jcd/oscilnotes/`*;*
- *the lecture notes entitled "Stellar Stability" by. R. Scuflaire and A. Thoul (2002, Liège University, English version) available from* `http://www.asteroseismology.be/activities.html`*;*
- *the book entitled "Nonradial Oscillations of Stars" by Unno et al. (1989).*

Our theoretical description is based upon the stellar structure equations (outlined in very much detail in the 3-rd year course entitled "Stellar Structure and Evolution"). If you do not have any pre-knowledge thereof, and/or if mathematics is not your favourite subject, you can easily skip large parts of this chapter and limit yourself to the brief descriptive text on the introduction into the theory of oscillations given in Chapter 1 and to the sections 3.7 and 3.8 below. The rest of the course can be followed keeping in mind the expression for the displacement field due to a non-radial oscillation, given in (1.4).

Much in this chapter is based upon the course notes "Stellar Structure and Evolution" (C. Aerts, University of Leuven, 2002) and on the PhD thesis of M.-A. Dupret (University of Liège, 2002). We refer to these works for more information.

3.1 General equations of hydrodynamics

We consider in the following a star that can be approximated as a spherically symmetric gaseous sphere in the absense of visceous effects, magnetic fields and strong rotation (i.e. we neglect the Coriolis and centrifugal forces).

Two types of description are common to study the hydrodynamics of stars: the *Lagrangian* and the *Eulerian* description. In the Lagrangian description, a label $\vec{a}$ is assigned to each infinitesimal mass element in the star. The local physical quantities, such as the position, density, temperature, etc. are a function of $\vec{a}$ and of time t. For any quantity X the time derivative of X following the movement of a mass element will be denoted by dX/dt. The Eulerian description, on the other hand, makes use of the position vector $\vec{r}$ and the time t to describe the local physical quantities. The time derivative in the Eulerian desciption, which is valid for a given fixed position in space, will be denoted as $\partial X/\partial t$.

The equations of hydrodynamics that apply to stars under the approximations mentioned above are the following:

1. The equation of mass conservation:

$$\frac{d\rho}{dt} + \rho\nabla.\vec{v} = \frac{\partial\rho}{\partial t} + \nabla.(\rho\vec{v}) = 0, \tag{3.1}$$

   where $\vec{v}$ and ρ are respectively the local velocity and density.

2. The equation of momentum conservation:

$$\frac{d\vec{v}}{dt} = \frac{\partial\vec{v}}{\partial t} + \vec{v}.\nabla\vec{v} = -\nabla\psi - \frac{\nabla P}{\rho}, \tag{3.2}$$

   where P is the total pressure (gas, radiation and turbulent pressure) and ψ is the gravitational potential. The latter fulfills the equation of Poisson:

$$\triangle\psi = 4\pi G\rho. \tag{3.3}$$

3. The equation of energy conservation:

$$T\frac{dS}{dt} = \varepsilon - \frac{\nabla.\vec{F}}{\rho}, \tag{3.4}$$

   where T is the local temperature, S the entropy, ε the rate of energy generation and $\vec{F}$ the energy flux.

The energy transport in a star is either achieved through radiation or through convection so we note the total flux as $\vec{F} = \vec{F}_R + \vec{F}_C$ with $\vec{F}_R$ the radiative flux and $\vec{F}_C$ the convective flux. In the bulk of the star the *diffusion approximation* is valid because the mean free path of the photons (typically some cm in the solar interior) is much smaller than the distance to overcome to reach the surface. The radiative flux is therefore, to a good approximation, given by the diffusion equation:

$$\vec{F}_R = -\frac{4acT^3}{3\kappa\rho}\nabla T, \tag{3.5}$$

with κ the Rosseland mean opacity. This equation results in the following value for the radiative temperature gradient:

$$\frac{d\ln T}{d\ln P} = \nabla_{\rm rad} = \frac{3}{16\pi acG}\frac{\kappa lP}{mT^4}, \tag{3.6}$$

with l and m the local luminosity and mass respectively, i.e. the luminosity and mass contained within the sphere of radius r. Whenever this radiative temperature gradient exceeds the *adiabatic* gradient

$$\frac{d\ln T}{d\ln P} = \nabla_{\rm ad} = \left(\frac{\partial\ln T}{\partial\ln P}\right)_S, \tag{3.7}$$

the energy transport will no longer be achieved by radiation but instead by convection. A generally applicable description for the convective flux is difficult to derive and is in fact not available. Usually, one relies on the *mixing-length theory* of convection. This is a local time-independent theory in which one assumes that the mean free path of a convective element, l, can be well described as

$$l = \alpha H_p = -\alpha\left(\frac{d\ln P}{dr}\right)^{-1}, \tag{3.8}$$

where H_P is the pressure scale height and α is the mixing-length parameter, which is of order unity ($\alpha \approx 1.8$ for the Sun). The precise location of the transformation from a radiative to a convective region is very difficult to determine. The reason is that it depends on a poorly known phenomenon called *convective overshooting*, which is a term to express that the convective cells do not stop abruptly once entering a radiative zone. Convective overshooting is usually parametrised by the so-called *overshooting parameter* $\alpha_{\rm ov}$ defined as the fractional length, expressed in units of H_P, over which the convective cells still move while entering the radiative zone. Typical values for $\alpha_{\rm ov}$ considered in stellar modelling range from 0.0 to 0.3. A very important subject of research in stellar structure is to find accurate observational constraints on this poorly known parameter.

In order to solve the equations of hydrodynamics we need to take into account the relations between the different variables. One speaks of the *equations of state*: $P = P(\rho, T, \chi_i)$, $S = S(\rho, T, \chi_i)$, $\kappa = \kappa(\rho, T, \chi_i)$ where χ_i denotes the chemical composition in terms of i different elements. Moreover, we need to determine $\varepsilon(\rho, T, \chi_i)$ from nuclear physics. Finally, we need to specify a certain number of well-chosen boundary conditions. We will not go into details in these matters.

3.2 Perturbation approach

At each given time a pulsating star is not in equilibrium but the position, density, pressure and temperature of a mass element vary periodically around their equilibrium value. The equations presented in the previous section are therefore not fulfilled during the oscillation cycle. For any physical quantity X we denote by X_0 its equilibrium value. Let $\vec{a}$ be a label assigned to a mass element and $\vec{r}$ a particular position in space. The Lagrangian perturbation of X is defined as

$$\delta X(\vec{a},t) \equiv X(\vec{a},t) - X_0(\vec{a}\,). \tag{3.9}$$

It represents the variation of X while following the mass element labeled $\vec{a}$. Its Eulerian perturbation is

$$X'(\vec{r},t) \equiv X(\vec{r},t) - X_0(\vec{r}\,) \tag{3.10}$$

and represents the variation of X at a given fixed position $\vec{r}$ in space.

We assume that the amplitude of the variation of each physical quantity remains small. In that case it is justified to use the *linear approximation,* in which all second and higher order terms in the perturbations are neglected. In what follows we present the perturbed equations to solve, while omitting the subscript "0" for the equilibrium values of the quantities X for simplicity. In this approximation, the Lagrangian and Eulerian perturbations relate as follows:

$$\delta X = X' + \nabla X_0 . \vec{\delta r}. \tag{3.11}$$

The perturbed version of the equations given in the previous section, which are obtained by taking either the Lagrangian or the Eulerian perturbation on both sides of the equations, are as follows:

1. mass conservation:
$$\rho' + \nabla . \left(\rho \vec{\delta r}\right) = \delta\rho + \rho\nabla.\vec{\delta r} = 0. \tag{3.12}$$
2. momentum conservation:
$$\frac{\partial^2 \vec{\delta r}}{\partial t^2} = -\nabla\psi' + \frac{\rho'}{\rho^2}\nabla P - \frac{\nabla P'}{\rho}. \tag{3.13}$$
3. energy conservation:
$$T\frac{d\delta S}{dt} = T\left(\frac{\partial S'}{\partial t} + \vec{v}.\nabla S\right) = \varepsilon' + \frac{\rho'}{\rho^2}\nabla.\vec{F} - \frac{\nabla.\vec{F}'}{\rho}. \tag{3.14}$$

The perturbed diffusion equation reads:

$$\vec{F}'_R = \left(3\frac{T'}{T} - \frac{\kappa'}{\kappa} - \frac{\rho'}{\rho}\right)\vec{F}_R - \frac{4acT^3}{3\kappa\rho}\nabla T'. \tag{3.15}$$

The perturbed equations of state are not outlined here in detail. We do point out that one usually assumes *local thermodynamic equilibrium* in their derivation. This is a very good approximation in the stellar interiors of all stars but not necessarily in the outer envelope where the density is low. Also one usually neglects the perturbation of the chemical composition. This approximation is valid whenever the time scales of diffusive and rotational mixing are much longer than the oscillation periods in parts where no nuclear reactions takes place. In the core, however, the time scale of some nuclear reactions is short and we need to take into account $\delta\varepsilon$ there.

The system of equations has to be closed by adding the perturbed versions of the chosen boundary conditions, which we do not outline here for brevity.

3.3 Linear non-radial oscillations

The differential equations obtained in the previous section are linear and have coefficients which are not dependent on time. We can therefore find a solution to these equations by expressing each of the unknowns as an infinite linear combination, each term having a time-dependence of the form $\exp(\mathrm{i}\,\omega t)$. Moreover, the spherical harmonics $Y_l^m(\theta,\varphi)$, $l = 0 \rightarrow +\infty; m = -l, \ldots, l$ are a family of orthogonal functions defined on the sphere which form a complete basis. It is therefore appropriate to write a general solution of the system of differential equations (3.12), (3.13), (3.14) as

$$\vec{X}(r,\theta,\varphi,t) = \mathrm{Re}\left(\sum_{l=0}^{+\infty}\sum_{m=-l}^{+l}\sum_{n=0}^{+\infty} A_{l,m,n}\vec{X}_{l,m,n}(r)Y_l^m(\theta,\varphi)\exp(\mathrm{i}\sigma_{l,m,n}t)\right), \tag{3.16}$$

where "Re" denotes the real part and $\sigma_{l,m,n} = \omega_{l,m,n}/2\pi$ are the complex oscillation frequencies of the different spheroidal modes of oscillation. The real part of $\sigma_{l,m,n}$ is usually called the cyclic frequency and is also denoted as $f = (1/\text{period})$ while the real part of $\omega_{l,m,n}$ is called the angular frequency; the opposite of the imaginary part of $\sigma_{l,m,n}$ is called the *growth rate* of the mode. Whenever the imaginary part is positive the mode is said to be *vibrationally stable*, which means that the oscillation is damped and the oscillation amplitude decreases exponentially. If the imaginary part is negative, however, the mode is *vibrationally unstable* and the oscillation is excited.

After some elaborate mathematical manipulations, which we omit here, one finds the following form for the differential equations:

1. Conservation of mass:

$$\frac{\delta\rho}{\rho} + \frac{1}{r^2}\frac{d}{dr}\left(r^2\xi_r\right) - \frac{l(l+1)}{\sigma^2 r^2}\left(\delta\psi + \frac{\delta P}{\rho}\right). \tag{3.17}$$

2. The three components of the equation of momentum conservation:

$$\sigma^2\xi_r = \frac{\partial\psi'}{\partial r} + \frac{\rho'}{\rho}\frac{Gm}{r^2} + \frac{1}{\rho}\frac{\partial P'}{\partial r}, \tag{3.18}$$

$$\sigma^2\xi_\theta = \frac{1}{r}\frac{\partial}{\partial\theta}\left(\psi' + \frac{P'}{\rho}\right), \tag{3.19}$$

$$\sigma^2\xi_\varphi = \frac{1}{r\sin\theta}\frac{\partial}{\partial\varphi}\left(\psi' + \frac{P'}{\rho}\right). \tag{3.20}$$

3. Conservation of energy:

$$\begin{aligned}\mathrm{i}\,\sigma T\delta S \;&= -\frac{1}{4\pi r^2\rho}\frac{d\delta L}{dr} + \varepsilon\left(\frac{\delta\varepsilon}{\epsilon} + \frac{\delta\rho}{\rho} + \frac{1}{r^2}\frac{d(r^2\xi_r)}{dr}\right) \\ &+\frac{l(l+1)}{4\pi\rho r^3}\left[L_R\left(\frac{\delta T}{r(dT/dr)} - \frac{\xi_r}{r}\right) - L_C\frac{\xi_h}{r}\right].\end{aligned} \tag{3.21}$$

where m is the mass contained within the sphere of radius r, L_R and L_C the radiative and convective luminosity and where we have used the following expression for the Lagrangian displacement vector:

$$\vec{\delta r}(r,\theta,\varphi) = \mathrm{Re}\left\{\left[\xi_r(r)Y_l^m(\theta,\varphi)\vec{e}_r + \xi_h(r)\left(\frac{\partial Y_l^m}{\partial\theta}(\theta,\varphi)\vec{e}_\theta + \frac{1}{\sin\theta}\frac{\partial Y_l^m}{\partial\varphi}(\theta,\varphi)\vec{e}_\varphi\right)\right]\exp(\mathrm{i}\,\sigma t)\right\}, \tag{3.22}$$

with

$$\sigma^2\xi_h = \frac{1}{r}\left(\psi' + \frac{P'}{\rho}\right) = \frac{1}{r}\left(\delta\psi + \frac{\delta P}{\rho}\right). \tag{3.23}$$

Together with the boundary conditions (which we did not specify for brevity), the system of equations (3.17),…,(3.21) forms an eigenvalue problem whose perturbed quantities are the eigenvectors and σ are the eigenvalues (which are both complex).

3.4 The quasi-adiabatic approximation

Throughout most of the star, the thermal relaxation time is much longer than the observed oscillation periods, i.e. the heat capacity is so high that the layers are unable to exchange heat with their environment in a short time. In such a case the entropy cannot change during the oscillation cycle. One speaks of the *adiabatic approximation*, for which $\delta S = 0$. In this approximation the energy equation is decoupled from the equations of mass and momentum conservation and the solution to the problem is much easier to find. This leads to the following relations between the pressure, density and temperature:

$$\frac{\partial P}{P} = \Gamma_1\frac{\delta\rho}{\rho} \quad\text{and}\quad \frac{\delta T}{T} = (\Gamma_3 - 1)\frac{\delta\rho}{\rho}, \tag{3.24}$$

where

$$\Gamma_1 \equiv \left(\frac{\partial\ln P}{\partial\ln\rho}\right)_S \quad\text{and}\quad (\Gamma_3 - 1) \equiv \left(\frac{\partial\ln T}{\partial\ln\rho}\right)_S. \tag{3.25}$$

Moreover, the conservation of energy equation reduces to

$$T\delta S = \frac{\mathrm{i}}{\sigma}\left(\frac{d\delta L}{dm} - \delta\varepsilon\right) \tag{3.26}$$

for a radial mode (we omit the more complex equation for a non-radial mode for the time being). In this case, the eigenfunctions and eigenvalues of interest are all real (hermitian eigenvalue problem).

Unfortunately, it is impossible to determine whether or not a mode is unstable or not in the adiabatic approximation. In principle, one needs to solve the complex system of fully non-adiabatic equations (3.17),…,(3.21). However, one can also get a good impression about excitation in the so-called *quasi-adiabatic approximation*. In this approximation one proceeds as follows:

1. For any given mode characterised by (l, m, n), one determines the adiabatic eigenfunctions and eigenvalues.
2. The right-hand side of equation (3.26) is computed by using the adiabatic values for δL and $\delta\varepsilon$. A value different from zero is then obtained for $T\delta S$.
3. Subsequently, one derives the imaginary part of the eigenvalue. This is done by multiplying the radial component of the momentum equation (3.18) by $4\pi r^2\rho$ and by the complex conjugate of ξ_r and by subsequent integration over the radius r. The result is:

   $$\mathrm{Im}(\sigma) = \frac{1}{2\sigma_{\mathrm{ad}}^2}\frac{\int_0^M \frac{\delta T}{T}\left(\frac{d\delta L}{dm} - \delta\varepsilon\right) dm}{\int_0^M \xi_r^2 dm}, \tag{3.27}$$

   where σ_{ad} is the adiabatic value of the eigenfrequency. One then substitutes the value of $T\delta S$ obtained in item 2. in the integrand of this equation.

We stress that this procedure is inconsistent as it relies on the adiabatic approximation for the first two steps and no longer for the third step. The approximation is fine in the adiabatic regions of the star, i.e. from the center to the partial ionisation zones. One avoids problems by truncating the integral in (3.27) so that only the valid region is considered in the integration.

3.5 The Cowling approximation

In the approximation introduced by Cowling in 1941, the Eulerian perturbation of the gravitational potential is neglected: $\psi' = 0$. This approximation is generally good in the outermost stellar layers where the local density is small. The condition $\psi' = 0$ and the equations (3.18) and (3.24) lead to

$$\frac{dP'}{dr} + \frac{g}{c^2}P' = (\sigma^2 - N^2)\rho\,\xi_r, \tag{3.28}$$

with N and c respectively the Brunt-Väisälä frequency and the sound speed:

$$N^2 \equiv \frac{Gm}{r^2}\left(\frac{1}{\Gamma_1}\frac{d\ln P}{dr} - \frac{d\ln\rho}{dr}\right) \quad \text{and} \quad c^2 \equiv \frac{\Gamma_1 P}{\rho}. \tag{3.29}$$

On the other hand, $\psi' = 0$ and the equations (3.17) and (3.24) result in

$$\frac{P'}{\rho c^2}\left(1 - \frac{L_l^2}{\sigma^2}\right) - \frac{g}{c^2}\xi_r + \frac{1}{r^2}\frac{d}{dr}\left(r^2\xi_r\right) = 0, \tag{3.30}$$

where L_l is the Lamb frequency

$$L_l^2 \equiv \frac{l(l+1)c^2}{r^2}. \tag{3.31}$$

In this adiabatic and Cowling approximation one then subsequently introduces new variables to simplify the equations:

$$v = f_1 r^2 \xi_r \ \ ; \ \ w = f_2 \frac{P'}{\rho}, \tag{3.32}$$

with

$$f_1 \equiv \exp\left(\int_0^r \frac{1}{\Gamma_1}\frac{d\ln P}{dr}dr\right) > 0 \ \text{ and } \ f_2 \equiv \exp\left(-\int_0^r \frac{N^2}{g}dr\right) > 0. \tag{3.33}$$

With this change of variables, equations (3.28) and (3.30) take the following form:

$$\begin{aligned} \frac{dw}{dr} &= \left(\sigma^2 - N^2\right)\frac{f_2}{r^2 f_1}v, \\ \frac{dv}{dr} &= \left(\frac{L_l^2}{\sigma^2} - 1\right)\frac{r^2 f_1}{c^2 f_2}w. \end{aligned} \tag{3.34}$$

This system of differential equations is easily simplified into one second-order differential equation, either by eliminating w which gives

$$\frac{d}{dr}\left(\frac{1}{1 - L_l^2/\sigma^2}\frac{c^2 f_2}{r^2 f_1}\frac{dv}{dr}\right) + \left(\sigma^2 - N^2\right)\frac{f_2}{r^2 f_1} = 0, \tag{3.35}$$

or by eliminating v which gives

$$\frac{d}{dr}\left(\frac{1}{N^2 - \sigma^2}\frac{r^2 f_1}{f_2}\frac{dw}{dr}\right) + \left(\frac{L_l^2}{\sigma^2} - 1\right)\frac{r^2 f_1}{c^2 f_2}w = 0. \tag{3.36}$$

These two equations naturally give rise to two types of modes. For modes with very high frequencies σ, L_l^2/σ^2 can be neglected in equation (3.35). With this simplification and from $f_1, f_2 > 0$, equation (3.35) with appropriate boundary conditions transforms into a Sturm-Liouville type equation which has an infinitely countable number of increasing eigenvalues $\sigma^2 \to \infty$. These modes are named *pressure modes*. On the other hand, for very low frequencies $N^2 - \sigma^2 \approx N^2$ and equation (3.36) with appropriate boundary conditions now takes Sturm-Liouville form, this time with decreasing eigenvalues $\sigma^2 \to 0$. These modes are called *gravity modes*. We restrict to the gravity modes that are dynamically stable ($\sigma^2 > 0$). These are the g$^+$-modes. For $l \geq 1$ there is one additional mode with a frequency in between those of the p- and g$^+$-modes. This mode is called the f-mode. A schematic representation of the eigenvalues is given in Figure 3.1. Usually, the superscript "$+$" is dropped and one simply uses the term g-modes.

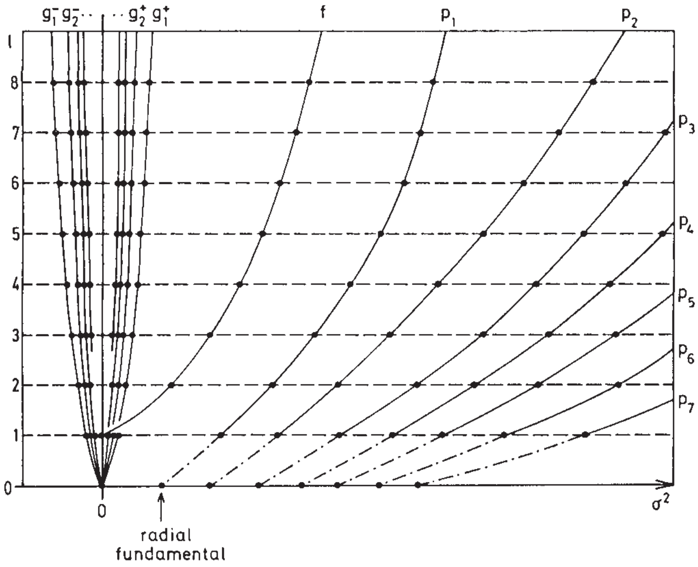

Figure 3.1: Schematic representation of the eigenvalues σ^2 of non-radial modes with different degree l. The eigenvalues of modes with the same radial order are connected by a full line. The dashed-dotted lines connect the radial modes. The f-mode of $l = 1$ has an eigenvalue equal to zero.

The p- and g-modes have an oscillatory behaviour only in the so-called *trapping regions* or *mode cavities*. Outside of these regions they decrease exponentially. The localisation of the cavities depends on the frequency of the mode and so is different for different modes. For p-modes, we see from equation (3.35) that an oscillatory motion occurs for $\sigma^2 > N^2$ and $\sigma^2 > L_l^2$. This denotes the p-mode cavity. The g^+-modes, on the other hand, are trapped whenever $0 < \sigma^2 < N^2$ and $\sigma^2 < L_l^2$ – see equation (3.36). These g-mode cavities are situated much deeper in the star than the p-mode cavities. We show the p- and g-mode cavities (indicated as respectively A and G) for a polytropic stellar model in Figure 3.2.

We finally mention that, during the course of the evolution of a star, its modes may become of *mixed nature*, i.e. an oscillatory behaviour in an inner g-mode cavity but in an outer p-mode cavity. In such a case the A and G mode cavities are situated much closer to each other than in Figure 3.2.

3.6 Driving mechanisms

We now discuss the mathematics behind the two common driving mechanisms known so far in asteroseismology. This part of the text is particularly concise for reasons already outlined in the first paragraph of this chapter.

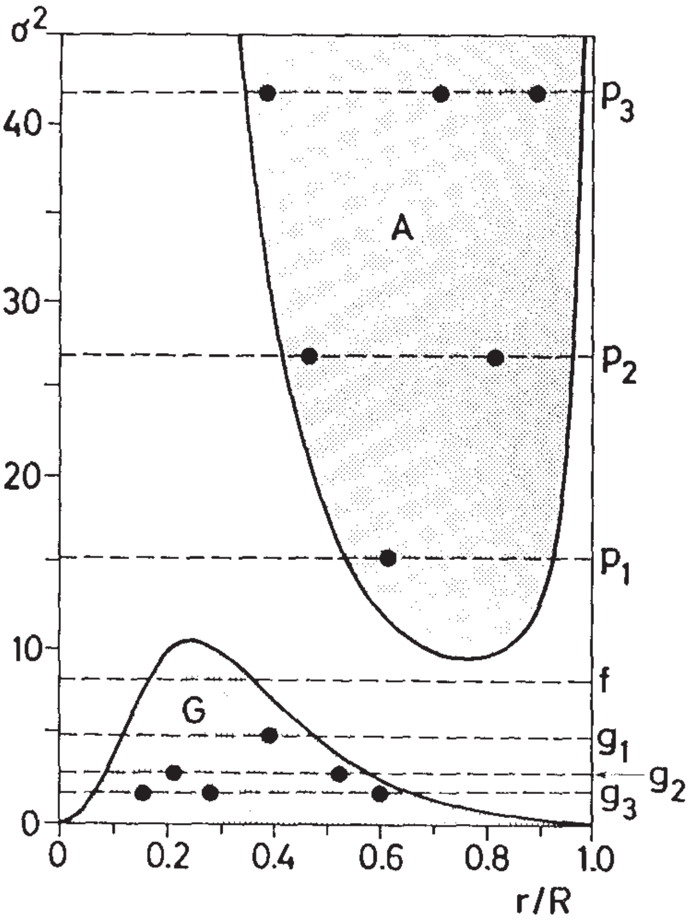

Figure 3.2: The p- and g-mode cavities in a stellar model of polytropic index 3. “A” stands for acoustic mode cavity and G for gravity mode cavity. The eigenfrequencies and node positions of the lowest-order modes are indicated as dashed lines and bullets.

3.6.1 Modes excited by the opacity mechanism

As already emphasised above, the growth or damping rate of a mode (i.e. its stability or instability) follows from the imaginary part of its frequency. We have already given an expression for Im(σ) in (3.27) for a radial mode in the quasi-adiabatic approximation. We will restrict to this case here; the same discussion can be held for the more generalised case of fully non-adiabatic non-radial oscillations.

We recall that the time-dependence of a mode is $\exp(\mathrm{i}\,\sigma t)$ with σ a complex number. Therefore, driving is obtained when Im$(\sigma) < 0$ and the growth rate of the mode is given by –Im(σ). Whenever Im$(\sigma) > 0$ damping of the mode occurs with damping rate Im(σ).

The two effects that determine the driving of a mode result from the Lagrangian perturbation of the nuclear reactions and of the luminosity. The first one is only significant in the central parts where the fusion takes place and where the adiabatic approximation is very good. It is therefore not important for the driving of the oscillations. The second effect is also called the transport effect and is at the origin of the driving. From (3.27) we see that the regions where δL is increasing outwards during the hot phase $\delta T > 0$ have a driving effect. This case is similar to a heat engine in thermodynamics: energy is taken from the system during the hot phase of a cycle and is released during the cold phase. Inversely, regions where δL is decreasing outwards during the hot phase have a damping effect. One can shown that, for frozen convection (i.e. with neglect of the Lagrangian perturbation of the convective flux) and a radial mode, the Lagrangian perturbation of the luminosity is given by

$$\frac{\delta L}{L} = \frac{L_R}{L}\left(4\frac{\xi_r}{r} + 3\frac{\delta T}{T} - \frac{\delta\kappa}{\kappa} + \frac{\partial\delta T/\partial r}{dT/dr}\right). \tag{3.37}$$

In general, the term with the opacity is dominant in this expression for the determination of the luminosity variation. In the quasi-adiabatic approximation we can write

$$\frac{\delta\kappa}{\kappa} = \frac{(\Gamma_3 - 1)\,\kappa_T + \kappa_\rho}{\Gamma_1}\frac{\delta P}{P}. \tag{3.38}$$

In most cases, i.e. in homogeneous stellar layers, δP is increasing outwards at the hot phase and so the contribution of $\delta\kappa$ to δL implies that the latter is increasing outwards during this phase so that damping occurs. However, in partial ionisation zones large opacity bumps occur (see e.g. Figure **??**). These bumps can have a significant driving effect because $\delta\kappa$ can increase very steeply outwards and can take positive values implying that δL decreases outwards during the hot phase. Because of the dominant role of the Lagrangian perturbation of the opacity κ in the driving, one speaks of the κ *mechanism*.

3.6.2 Stochastically excited modes

Stars possessing surface convection zones undergo mode instability by perturbations of their convective flux. The study of such mode instabilities therefore demands a theory for convection that includes the interaction of the turbulent velocity field with the pulsation, which is far from straightforward.

The power spectrum of acoustic modes caused by convection in its simplest description consists of an ensemble of intrinsically damped, stochastically driven, harmonic oscillators, provided that the background equilibrium state of the star is independent of time. If one further assumes that mode phase fluctuations do not contribute to the width of the frequency peaks, then the intrinsic damping rates of the modes can be determined from the linewidths of the frequency peaks. Indeed, consider a damped oscillator forced by a random function $f(t)$:

$$\frac{d^2A}{dt^2} + 2\eta\frac{dA}{dt} + \omega_0^2 A = f(t). \tag{3.39}$$

In the case of a free oscillation ($f = 0$) one finds as solution:

$$A(t) \propto \exp(-\eta t)\cos(\omega t + \delta), \tag{3.40}$$

where $\omega^2 = \omega_0^2 - \eta^2$. In the case of a forced oscillation one introduces the Fourier transforms

$$\tilde{A}(\omega) = \int A(t)\exp(\mathrm{i}\omega t)dt, \tilde{f}(\omega) = \int f(t)\exp(\mathrm{i}\omega t)dt, \tag{3.41}$$

which turns the equation (3.39) into

$$-\omega^2\tilde{A} - 2i\eta\omega\tilde{A} + \omega_0^2\tilde{A} = \tilde{f}\ . \tag{3.42}$$

The solution of this equation leads to the following expression for the power:

$$\begin{aligned} P(\omega) = |\tilde{A}(\omega)|^2 &= \frac{|\tilde{f}(\omega)|^2}{(\omega_0^2 - \omega^2)^2 + 4\eta^2\omega^2} \\ &\simeq \frac{1}{4\omega_0^2}\frac{|\tilde{f}(\omega)|^2}{(\omega_0 - \omega)^2 + \eta^2}, \end{aligned} \tag{3.43}$$

which implies an average power of

$$\langle P(\omega)\rangle \simeq \frac{1}{4\omega_0^2}\frac{\langle P_f(\omega)\rangle}{(\omega - \omega_0)^2 + \eta^2}, \tag{3.44}$$

where P_f is called the power of the stochastic forcing. The forcing function $f(t)$ may be evaluated from turbulent flow calculations based on the mixing-length theory or from simulations. It is beyond the scope of these lectures to describe such details. However, we do point out that the amplitudes of stochastic modes scale roughly as L/M.

From (3.44) it follows that the damping rates can be estimated from the line widths of Lorentzian fits to the observed peaks in the power spectrum, provided that the time series is sufficiently long. Subsequently one can compare the “observed” damping rates with those predicted by the theoretical simulations using different stochastic forcing models to better understand the latter. The observational derivation of damping rates of stochastically excited modes is still in its infancy given that relatively few firm detections have been made so far. The current status is discussed in Chapter 6.

3.7 Asymptotic behaviour

The asymptotics of oscillation theory allows one to study the behaviour of the equations of non-radial oscillations and their solutions for the extreme case of very high radial orders $n \to \infty$. The asymptotic theory of non-radial oscillations is appropriate for modes of high radial order n and of low degree l. It was mainly developed in the 1980s when it had become clear that it is very useful and accurate to explain the acoustic frequency spectrum of the Sun. Moreover, asymptotic approximations turned out to be very appropriate for the high-order g-modes in white dwarfs in the 1990s.

An asymptotic analysis of the stellar oscillation equations is beyond the scope of this course. We only report the results for the frequency behaviour for both p- and g-modes:

1. a characteristic period spacing occurs for high-order g-modes of the same low degree l and with subsequent values of the radial order n:
$$\Pi_{nl} \simeq \frac{\Delta\Pi}{\sqrt{l(l+1)}}\left(n + \frac{l}{2} + \epsilon\right) \tag{3.45}$$
with
$$\Delta\Pi = (2\pi)^2 \left(\int_0^R \frac{N(r)}{r} dr\right)^{-1}. \tag{3.46}$$
In this expression, ϵ is a constant that depends on the surface properties of the star.
2. a characteristic frequency spacing occurs for high-order p-modes with the same low degree l and with subsequent values of the radial order n:
$$\sigma_{nl} \simeq \Delta\sigma \left(n + \frac{l}{2} + \epsilon\right) \tag{3.47}$$
with
$$\Delta\sigma = \left(2\int_0^R \frac{dr}{c(r)}\right)^{-1}. \tag{3.48}$$

This gives rise to the *large frequency separation* $\Delta_{nl} \equiv \sigma_{nl} - \sigma_{n-1,l}$ (see Figure 1.3).

In the framework of helioseismology, one has refined the characteristic frequency spacing by taking into account an additional term:
$$\sigma_{nl} \simeq \Delta\sigma \left(n + \frac{l}{2} + \epsilon\right) + l(l+1)\frac{\Delta\sigma}{4\pi^2\sigma_{nl}} \int_0^R \frac{dc}{dr}\frac{dr}{r}, \tag{3.49}$$
which subsequently led to the definition of the *small frequency separation*:
$$\delta_{nl} \equiv \sigma_{nl} - \sigma_{n-1,l+2} \simeq -(4l+6)\frac{\Delta\sigma}{4\pi^2\sigma_{nl}} \int_0^R \frac{dc}{dr}\frac{dr}{r} \tag{3.50}$$
also indicated on Figure 1.3 for the Sun.

The asymptotic relations will be used in Chapters 6 and 7.

3.8 Rotational splitting

The theoretical approach leading to the asymptotic relations described above were derived under the assumption of a non-rotating star. However, rotation lifts the degeneracy with respect to the azimuthal number m, which gives rise to different frequency values for modes with the same degree l and the same radial order n:

$$\omega_{nlm} = \omega_{nl} - m\Omega(1 - C_{nl}) + \text{higher-order terms in } \Omega, \tag{3.51}$$

with C_{nl} a constant depending on n and l and on the stellar structure model. The constant C_{nl} is called the *Ledoux constant* after its inventor. Expression (3.51) points out that *rotational splitting* of the frequencies occurs. One obtains a *frequency triplet* in the case $l = 1$, a *quintuplet* for $l = 2$, a *septuplet* for $l = 3$ and so on.

One can shown that, for high-order g-modes, the approximation $C_{nl} \approx 1/[l(l+1)]$ is appropriate. For p-modes, $C_{nl} \approx 0$.

Frequency spacings and rotational splitting of course occur simultaneously. In principle, the frequency patterns of modes in the asymptotic regime should be easy to recognise in the periodogram of high-quality data of which the overall time base covers all beat patterns. However, rotation can lead to very complex frequency patterns which are hard to disentangle, even for a star in which only a limited number of modes is excited. This situation occurs whenever the star's modes are not really in the asymptotic regime and/or the star is a fast rotator.

Part II

Methodology

Chapter 4

Frequency Analysis

As already discussed in Chapter 3, the three components of the Lagrangian displacement vector of an undamped oscillator contain a time-dependent factor $\exp(-\mathrm{i}\,\omega t)$, with $\omega = 2\pi\nu$ the angular frequency of the oscillation mode and $\Pi = 2\pi/\omega = 1/\nu$ its period. It is therefore clear that stellar oscillations give rise to periodic variations of the physical quantities. These translate into periodic variations of observables, such as the brightness, the colours, the radial velocity and the spectral line profiles. In this chapter we describe methodology to derive the oscillation frequencies from time series of data of pulsating stars.

Time series analysis is a well-developed field in statistics (e.g. Bloomfield 1976; Kendall & Ord 1990). Unfortunately, the available classical theory is not appropriate to analyse data of pulsating stars because this theory almost always assumes uninterrupted measurements which are evenly spaced in time. Astronomical time series usually contain large gaps and *unevenly spaced data*. Moreover, the gaps themselves may have quasi-periodicities, e.g. daily interruptions of single-site measurements by the sun, monthly interruptions because of telescope scheduling based on the phases of the moon and annual interruptions because of the Earth's orbital motion for the large majority of stars that are not circumpolar. While techniques to treat several types of missing data (missing completely at random, missing at random, missing not at random) are also well developed in statistics (e.g. Little & Rubin 2002; Molenberghs & Verbeke 2005), it is not advised to apply them to astronomical time series because

- the oscillation frequencies need to follow a well-known deterministic distribution in order to make an appropriate reconstruction to fill the gaps, which is not always a safe assumption;
- the amount of missing data is often larger than the available data, i.e. one usually deals with low duty cycles implying uncertain reconstruction by interpolation as well.

The latter concern is particularly relevant for ground-based data, even those assembled from multi-site campaigns. It is less of a problem for data assembled from space with missions dedicated to oscillation studies, where duty cycles above 90% can be achieved. However, here we provide methodology which is appropriate to treat the hardest possible type of time series of pulsating stars, i.e. unevenly spaced data with a low duty cycle. The methods will also work for data sets with a high-duty cycle that are (quasi-)equidistant. In such cases, additional classical methods, such as those based on Fast Fourier Transforms (e.g. Press et al. 1992, Chapter 12; Bracewell 1999), will also be applicable and may imply faster computations.

In the present chapter, illustrations of the theory are based on simulated data. The reader is referred to Chapter 2 and later chapters in these notes for extensive applications of the methodology to real modern data.

4.1 Harmonic analysis by least squares

With a harmonic analysis we mean the search for a certain sum of harmonic functions that best describe the data in the least-squares sense. Least-squares fitting is a well-known statistical technique familiar to most readers, which is why we consider it here as a first easy case of a parametric method for frequency search in time series of stellar oscillations, before treating other methods. The particular case of harmonic fitting described here is equivalent to taking a Fourier transform of the time series, which will be considered in Section 4.3.

Consider measurements of a quantity x at different times t_i: $x(t_i) \equiv x_i$ with $i = 1, \ldots, N$. Considering the time dependence of the oscillation modes, we aim at using a model of the following form:

$$x(t_i) = \sum_{k=1}^{M} a_k \cos[2\pi\nu_k(t_i - \tau)] + b_k \sin[2\pi\nu_k(t_i - \tau)] + c + \epsilon_i, \tag{4.1}$$

describing the variations due to M oscillation modes with frequencies ν_k, $k = 1, \ldots, M$ which are excited with amplitudes above the detection threshold, with τ an arbitrary reference epoch, a_k, b_k and c the free fitting parameters and ϵ_i the measurement errors. The latter are usually assumed to be independent and normally distributed with average zero and constant variance σ_N^2. We come back to this assumption in Section 4.5. We have to find a way to derive each frequency ν_k, as well as the unknowns a_k, b_k and c, from the data.

4.1.1 Searching for a single frequency

Let us first assume that the time series is due to one single undamped oscillation mode whose frequency ν_1 we seek to find, i.e. $M = 1$ and $a_1 = a, b_1 = b$. For each test frequency ν we determine the unknowns a, b, c by means of a least-squares algorithm. The best estimates for a, b, c are those that minimise the quadratic deviations between the observed and calculated values. We define the likelihood function L as:

$$L \equiv \sum_{i=1}^{N} \left\{x_i - a\cos[2\pi\nu(t_i - \tau)] - b\sin[2\pi\nu(t_i - \tau)] - c\right\}^2, \tag{4.2}$$

with τ a fixed reference epoch. We then find a, b, c by solving the set of equations:

$$\frac{\partial L}{\partial a} = 0, \frac{\partial L}{\partial b} = 0, \frac{\partial L}{\partial c} = 0. \tag{4.3}$$

After some manipulation this results in the following values for the unknowns:

$$\begin{cases} a = \dfrac{c_x}{c_2} - \dfrac{c_1}{c_2} \dfrac{\dfrac{c_x c_1}{c_2} + \dfrac{s_x s_1}{s_2} - x_{\text{sum}}}{\dfrac{c_1^2}{c_2} + \dfrac{s_1^2}{s_2} - N}, \\ b = \dfrac{s_x}{s_2} - \dfrac{s_1}{s_2} \dfrac{\dfrac{c_x c_1}{c_2} + \dfrac{s_x s_1}{s_2} - x_{\text{sum}}}{\dfrac{c_1^2}{c_2} + \dfrac{s_1^2}{s_2} - N}, \\ c = \dfrac{\dfrac{c_x}{c_2} c_1 + \dfrac{s_x}{s_2} s_1 - x_{\text{sum}}}{\dfrac{c_1^2}{c_2} + \dfrac{s_1^2}{s_2} - N}, \end{cases} \tag{4.4}$$

in which we have used the following definitions:

$$\begin{aligned} & c_2 \equiv \sum_{i=1}^{N} \cos^2[2\pi\nu(t_i - \tau)],\ s_2 \equiv \sum_{i=1}^{N} \sin^2[2\pi\nu(t_i - \tau)], \\ & c_x \equiv \sum_{i=1}^{N} x_i \cos[2\pi\nu(t_i - \tau)],\ s_x \equiv \sum_{i=1}^{N} x_i \sin[2\pi\nu(t_i - \tau)], \\ & c_1 \equiv \sum_{i=1}^{N} \cos[2\pi\nu(t_i - \tau)],\ s_1 \equiv \sum_{i=1}^{N} \sin[2\pi\nu(t_i - \tau)], \\ & x_{\text{sum}} \equiv \sum_{i=1}^{N} x_i. \end{aligned} \tag{4.5}$$

The solutions for a, b, c allow us to compute the predicted value of $x_i^c(t_i)$ for the test frequency ν :

$$x_i^c(\nu) \equiv a \cos[2\pi\nu(t_i - \tau)] + b \sin[2\pi\nu(t_i - \tau)] + c. \tag{4.6}$$

The difference between the measured value $x_i(t_i)$ and the predicted value $x_i^c(t_i)$ is called the *residual* at time t_i:

$$R_i(\nu) \equiv x_i - x_i^c(\nu). \tag{4.7}$$

Searching for the most likely frequency comes down to searching for the frequency ν for which the sum of squares of the residuals is minimal, i.e. searching for a minimum of the function

$$R^2(\nu) = \sum_{i=1}^{N} R_i^2(\nu) = \sum_{i=1}^{N} \left[x_i - x_i^c(\nu)\right]^2. \tag{4.8}$$

We note that estimating the best value of a, b, c for the test frequency ν is equivalent to searching for the best value of A, δ, c such that

$$x_i^c = A \cos\left\{2\pi[\nu(t_i - \tau) + \delta]\right\} + c. \tag{4.9}$$

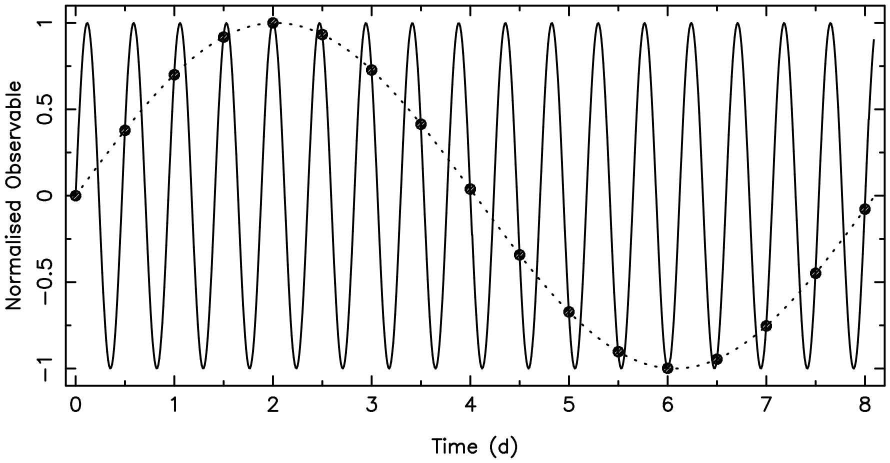

Figure 4.1: Simulated data (dots) representing a periodic signal with frequency $\nu = 0.123456789\,\mathrm{d}^{-1}$. The dotted line is a harmonic fit for this frequency. The full line represents a fit with the frequency $2.123456789\,\mathrm{d}^{-1}$.

This is perhaps a more often used harmonic model, as the *amplitude* A and the *phase* δ of the frequency ν are readily interpretable observables that result from the data, unlike a and b whose meaning is more complicated. It is indeed easy to show that $A^2 = a^2 + b^2$ and $2\pi\delta = \arctan(-b/a)$.

After having determined the value of A, δ, c such that the curve describes as well as possible the data with the least-squares method for each test frequency ν, we derive the variance of the data with respect to the best average curve. Whenever this variance is small we have found a frequency that explains a large percentage of the variability in the data. This percentage is called the *variance reduction* or *fraction of the variance* (f_v) and is defined as:

$$f_v = 1 - \frac{\sum\limits_{i=1}^{N} \left(x_i - \{A\cos\{2\pi\left[\nu(t_i - \tau) + \delta\right]\} + c\}\right)^2}{\sum\limits_{i=1}^{N} (x_i - \overline{x})^2} = 1 - \frac{L}{\sum\limits_{i=1}^{N} (x_i - \overline{x})^2}. \tag{4.10}$$

with $\overline{x} \equiv \sum_{i=1}^{N} x_i/N$. The search for a minimum of $R^2(\nu)$ is, in fact, a search for a maximal variance reduction in the data. We thus assign to ν_1 the test frequency ν with the largest variance reduction and our procedure at once gives us its amplitude A and phase δ.

As the very simple example shown in Fig. 4.1 demonstrates, one can easily have equivalent solutions whenever the observed time series is limited in number of points and in time coverage. It is important to keep in mind that almost equivalent solutions occur whenever the times of measurement cover a limited number of cycles and are taken with intervals equal to the beat periods of the occurring frequencies.

4.1.2 Searching for multiple frequencies

In principle, we could now repeat the previous derivation in order to find the most likely set of frequencies $\nu_k, k = 1, \ldots, M$ of the model fit in Eq. (4.1) from the data. Unfortunately, we are unable to predict the amplitude of excited oscillation modes in a star. Thus, we do not know the number M of oscillations that will be excited with detectable amplitude in the observed time series. This implies that this discrete unknown M has to be estimated along with the frequency search itself.

Estimation of discrete parameters is a very poorly developed field in statistics. This is a mathematical problem with very important implications for many fields, among which is asteroseismology. Besides causing a problem here for frequency determination, a similar situation will occur in Chapter 5 on mode identification, where the discrete wavenumbers of each of the detected oscillation modes (l, m, n) have to be estimated. A consequence of this is that frequency analysis for asteroseismology is unavoidably *data-driven*. This is a huge disadvantage from a statistical viewpoint compared with the situation where we would be able to estimate simultaneously the number of frequencies present in the data and their value from a model description.

We cannot but conclude that the search for multiple oscillation frequencies necessarily must be done by means of some kind of *prewhitening* procedure by which we mean that, at each stage of the frequency search, a fit with the selected frequency is computed and subtracted from the data values before a subsequent frequency search is started. The statistical interpretation of such a data-driven approach is much more challenging than one based on a model-driven treatment, unfortunately.

A prewhitening strategy thus has to be chosen to perform the frequency analysis. The simplest such strategy is to prewhiten the data according to Eqs (4.9) and (4.7) after the frequency ν_1 with the largest variance reduction was derived and to start a new frequency analysis to search for ν_2 in the residuals, and so on. One thus determines, at each stage of prewhitening, the values of ν_k, A_k, δ_k.

As pointed out by Vaníček (1971), one can improve this procedure by fitting the original data at each step with all the frequencies found up to then (he termed them “known constituents”), fixing only the frequency values and leaving their amplitudes and phases (the “unknown constituents”) free during the whole procedure. Vaníček showed that these unknown constituents determine “systematic noise” which is present in the data, besides the additional random noise, and there is in principle no need to fix them while searching for additional frequencies.

A rather evident next step is then to recompute a least-squares solution according to Eq. (4.1) at every prewhitening stage, starting each time from the original data and leaving also the frequency values ν_k free in making the fit, using the outcome of one or several different frequency search methods described here as a good starting value. This procedure is most commonly used nowadays in asteroseismology. It works fine as a prewhitening strategy and as a method to derive the most likely values for the frequencies, amplitudes and phases, provided that good starting values for the frequencies, already very close to their true values, are known and that a sufficient number of data points is available with respect to the degrees of freedom of the fit. As a rule of thumb we advise against making such a fit for data sets with fewer points than ten times the number of degrees of freedom. Additional requirements have to be fulfilled for such a fit to be meaningful.

We discuss these in Sects 4.3 and 4.4 and the reader is strongly advised to take these into account. Error estimation is treated in Sect. 4.5.

4.2 Non-parametric frequency analysis methods

Non-parametric methods imply that one does not *a priori* assume a chosen model function to describe the data. This is in contrast to the search for the maximal variance reduction described above, as well as to any method based on Fourier transforms discussed further on, where harmonic model functions are assumed from the start.

4.2.1 String length methods

The *string* or *rope length methods* are also based on the principle of least squares. Lafler & Kinman (1965) initially introduced such a method with the purpose to determine periods of RR Lyrae stars from small samples of visual data. Clarke (2002) presented a clear recent evaluation of these methods and proposed their generalisation to the application for multivariate data, the so-called Rope Length Method. This methodology is very suitable to analyse time series of multicolour photometric observations or of radial velocity variations from different spectral lines. The prime disadvantage of these methods, the long computation time needed, has largely been reduced with current speed of modern computers, except for very rich data sets. Nevertheless, the string and rope length methods are much less often applied compared with those discussed in the following sections. This has to do with the multitude of false peaks compared with Fourier methods, as we will show below. On the other hand, the non-parametric methods may be preferred to search for periodicity in strongly non-sinusoidal variations. These not only occur for large-amplitude pulsators, but also for eccentric and/or eclipsing binary lightcurves.

Consider again measurements of a quantity x at different times t_i, $x(t_i)$ with $i = 1, \ldots, N$. The *phase* $\phi(t_i)$ corresponding to the frequency ν, or to the period $\Pi = 1/\nu$, with respect to the reference epoch τ is defined as follows:

$$\phi(t_i) = [\nu(t_i - \tau)] = \left[\frac{t_i - \tau}{\Pi}\right], \tag{4.11}$$

where $[y]$ stands for the decimal part of y, increased by one if y is negative. From this definition it follows that $0 \leq \phi < 1$. A plot of the observations $x(t_i)$ as a function of $\phi(t_i)$ is called a *phase diagram*. An example for the simulated data shown in Fig. 4.1 is provided in Fig. 4.2.

For each trial frequency ν, taken from a grid of test frequencies, the original data $x(t_i)$ are first assigned phases $\phi(t_i)$, which are then ordered in ascending value $0 \leq \phi_1, \ldots, \phi_N < 1$. For each trial frequency, the original Lafler-Kinman statistic performs a "string length" summation of the squares of the differences between the consecutive phase-ordered values. Following Clarke (2002), we advise the use of the following

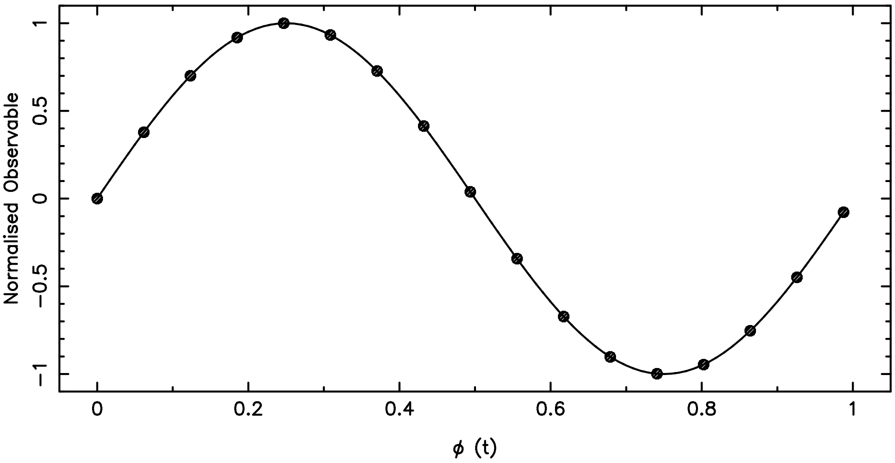

Figure 4.2: Simulated data from Fig. 4.1 drawn in a phase diagram where the arbitrary reference epoch τ was chosen such as to place the maximum of the observable at phase $\phi = 0.25$. The full line is the phased fit for the frequency 0.123456789 d^{-1} or for 2.123456789 d^{-1} shown as dotted and full line in Fig. 4.1.

modified string length statistic:

$$\Theta_{\mathrm{SL}}(\nu) \equiv \frac{\sum\limits_{i=1}^{N} [x(\phi_{i+1}) - x(\phi_i)]^2}{\sum\limits_{i=1}^{N} [x(\phi_i) - \overline{x}]^2} \times \frac{N-1}{2N}, \tag{4.12}$$

where $\overline{x}$ is the mean value of the measurements and $x(\phi_{N+1})$ is taken to be equal to $x(\phi_1)$. The sum in the denominator of Eq. (4.12) is nothing but the product of the number of measurements with the variance of the data set such that Θ_{SL} is independent of the noise in the data. Moreover, the factor 2 results in a normalised statistic with continuum level unity. If the time series contains periodicity with frequency ν, then Θ_{SL} will reach a minimum at ν while fluctuations in Θ_{SL} due to the noise will result in a level $\Theta_{\mathrm{SL}} \approx 1.0$.

A typical example of a simulated single-site time series of a star discovered as a new variable is shown in Fig. 4.3. These data represent the following situation. The discovery of the variability is made in one season. A few follow-up tests are being done some months later, confirming the variability, and a dedicated campaign is then undertaken to derive the periodicity in the next year. The simulated data have a standard deviation of 0.696 and a variance of 0.485. The white noise has a standard deviation of 0.01111 and a variance of 0.00012.

The string-length statistic of this prototypical time series is shown in Fig. 4.4. One notices clear minima with a daily repetition, the minimum of Θ_{SL} occurring at the input frequency 5.123456789 d^{-1}. A forest of peaks also occurs for frequencies below 2 d^{-1}. The occurrence of minima at subharmonics of the frequency and of their *aliases* (see Sect. 4.3 for a definition) is a general property of the frequency analysis methods based on phase diagrams (see, e.g., Cuypers 1987 for an extensive discussion) and is considered as one of its disadvantages.

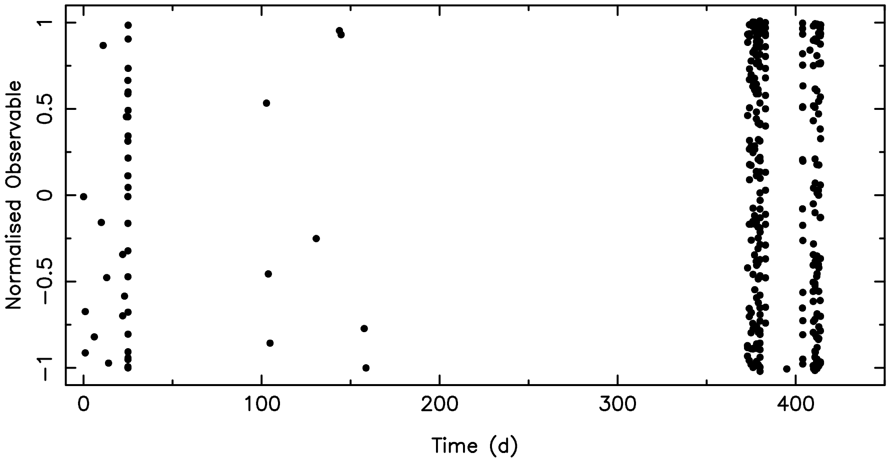

Figure 4.3: Simulated gapped data representing a typical time series for a single-site campaign of a pulsating star.

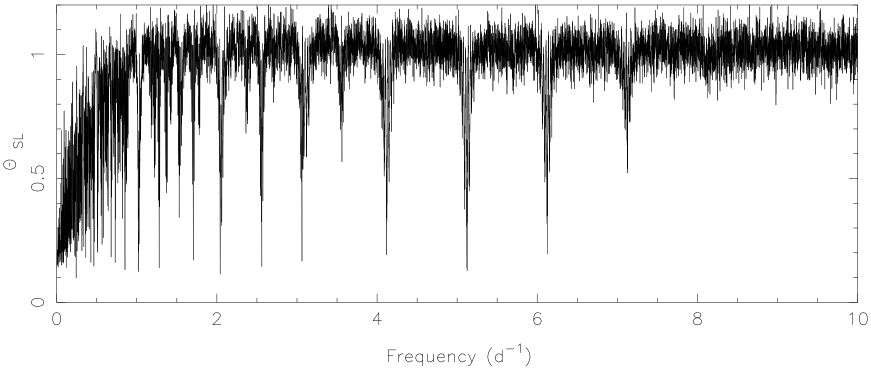

Figure 4.4: Statistic Θ_{SL} according to Eq. (4.12) of the data shown in Fig. 4.3.

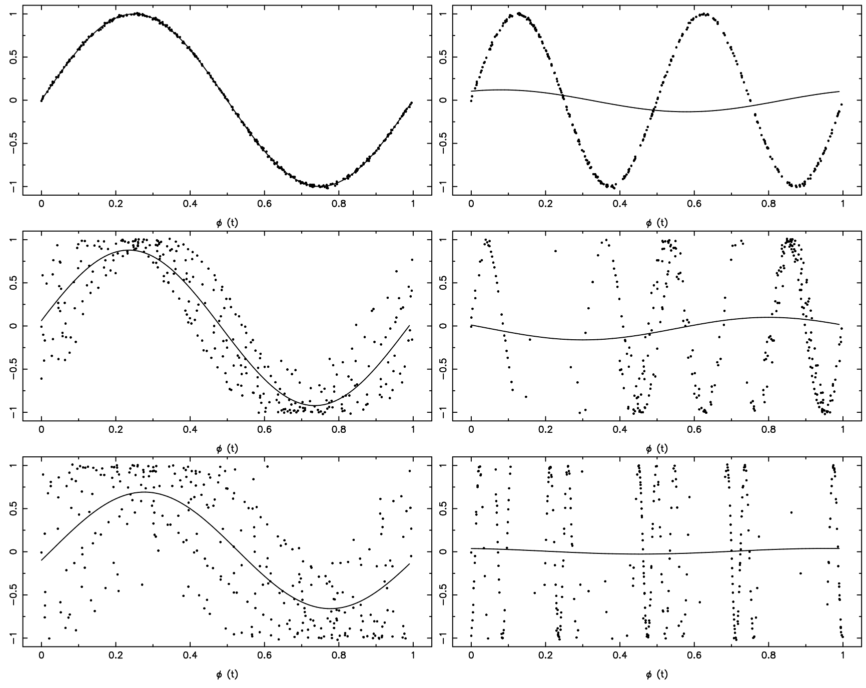

Figure 4.5: Phase diagrams for six minima in $\Theta_{\rm SL}$ found from Fig. 4.4. The phases for the data (dots) and harmonic fit (full lines) are computed for 5.123 $\rm d^{-1}$ (upper left), 4.121 $\rm d^{-1}$ (middle left), 7.129 $\rm d^{-1}$ (lower left), 2.562 $\rm d^{-1}$ (upper right), 1.021 $\rm d^{-1}$ (middle right), 0.244 $\rm d^{-1}$ (lower right).

After having computed $\Theta_{\rm SL}$ comes the task to try and disentangle which of the minima is the real oscillation frequency. In principle, this is the one corresponding to the deepest minimum. In practice, however, the interaction between the effects of the time sampling and (non-white) noise may imply a minimum in $\Theta_{\rm SL}$ deeper than the one for the true oscillation frequency. It can be helpful to draw phase diagrams of the few deepest peaks in $\Theta_{\rm SL}$ to discriminate the true frequency from false ones, besides comparing their variance reduction f_v from a least-squares fit using the peak values of the candidate frequencies as starting values for the fit. In Fig. 4.5 six such phase diagrams are shown. These make it evident, in this prototypical example, that $5.123\,{\rm d}^{-1}$ is the true frequency. Note, however, that also its alias frequencies near $4.121\,{\rm d}^{-1}$ (middle left) and $7.129\,{\rm d}^{-1}$ (lower left) give "good" phase diagrams in the sense that the periodic variability is clearly present in them. These phase diagrams also make it clear why the string-length statistic leads to a minimum for them. One should therefore not mistakenly belief that the frequency is real as soon as clear variation is seen in its phase diagram. All apparently significant deep minima in the statistic (or high peaks in Fourier analysis, see further) will produce phase diagrams in which one can see the variability, even if the selected frequency is a noise peak. The right panels are those for half of the true frequency, and for frequencies due to a mixture of effects due to harmonics, the noise and the sampling. From the upper right panel it is again apparent why subharmonics of the true frequency also deliver a low value of the string-length statistic. The examples for the other two spurious frequencies show that the phase diagram can be a very useful tool. The phase coverage of the data and the amplitude of the fit with respect to the peak-to-peak variation is bad for these diagrams. This would also have been clear from a least-squares fit as it would result in an insignificant amplitude and a low variance reduction f_v for these cases. If the data are not well-spread in phase for limited data sets, but cluster narrowly at particular phases and/or the variability occurs mainly at phases where there are no data points, then one is probably also dealing with a false frequency. These issues are important to check for and justify the use of phase diagrams besides computation of f_v.

The behaviour of $\Theta_{\rm SL}$ was studied extensively from simulations by Clarke (2002), to whom we refer for more information. He computed cumulative distribution functions for $\Theta_{\rm SL}$ in order to develop confidence levels for it as a function of data sampling and size. His work mainly focused on small time series, though. This is also the case for the evaluation of earlier versions of different string length statistics as those by Lafler & Kinman (1965), Burke, Rolland & Boy (1970), Renson (1978) and Dworetsky (1985).

With the goal to perform empirical mode identifications, asteroseismologists often gather multicolour observations of their target stars. The measurements in different filters of a photometric system are usually taken as close as possible in time, or ideally simultaneously, as explained in Chapter 5. Most often, however, the frequency analysis is performed for the different colours separately. One then either accepts the frequency value derived from the filter that delivered the highest *signal-to-noise ratio* (S/N ratio), or determines a weighted average frequency based on the values obtained for the different colours. The same is true for observables derived from different spectral lines, which are of course necessarily simultaneous. Although it is in principle possible to extend most frequency analysis techniques to multivariate data (see Sect. 4.6), such an endeavour is usually not undertaken. Nevertheless, using a weighted statistic has significant advantages in some cases, as we will discuss below for the parametric methods. It is a major advantage of the string length methods that they allow straightforward generalisation to a multivariate treatment.

The brightness variations in different photometric bands due to oscillations are strongly correlated. Depending on whether or not there are phase differences between the colour curves of the pulsating star, the measurements plotted in a brightness-brightness diagram for two different filters lie on a straight line or an ellipse-like structure. They can hence be connected by a “rope” consisting of various connecting strings, whose squared length can be added, again after assigning a phase to each measurement and ordering the data according to increasing phase. The same reasoning can be repeated for all the $k = 1, \ldots, Z$ filters in which a photometric time series has been obtained or for the Z spectral lines from which a radial velocity has been derived. Clarke (2002) proposes the following statistic for multivariate time series:

$$\Theta_{\mathrm{RL}}(\nu) \equiv \frac{1}{Z} \sum_{k=1}^{Z} \left(\frac{\sum\limits_{i=1}^{N[k]} \left[x_k(\phi_{i+1}) - x_k(\phi_i)\right]^2}{\sum\limits_{i=1}^{N[k]} \left[x_k(\phi_i) - \overline{x_k}\right]^2} \times \frac{N[k]-1}{2N[k]} \right), \tag{4.13}$$

where $x_k(\phi_i)$ is the magnitude in filter k or radial velocity from line profile k for each of the measurements taken at times $t_1, \ldots, t_N$ after re-arranging the data such that $\phi_1, \ldots, \phi_N$ increases from 0 to 1 for each of the test frequencies ν. It is rather cumbersome, however, to interprete the outcome of this statistic for extensive multicolour asteroseismic time series due to the numerous false frequency peaks.

4.2.2 Phase dispersion minimisation

The *Phase Dispersion Minimisation*, or briefly PDM method, is another non-parametric approach. It was introduced as an improved method compared with string length methods. One searches for the frequency by requiring that the spread of the data around an average curve in the phase diagram reaches a minimum. The average curve is determined from average values of the data in different phase intervals. We describe here the method as developed by Stellingwerf (1978).

For each test frequency ν one divides the phase interval $[0,1]$ into B equal sub-intervals, called *bins*. The bin index $J_i = \mathrm{INT}(B\phi_i) + 1$, with $\mathrm{INT}(x) \equiv x - [x]$, determines to which bin each observation $x(t_i)$ belongs. Suppose that the $j-$th bin contains N_j measurements. The average value of the data, the sum of the quadratic deviations and the variance for this bin are

$$\overline{x_j} = \sum_{i=1}^{N_j} \frac{x_{ij}}{N_j}, \tag{4.14}$$

$$V_j^2 = \sum_{i=1}^{N_j} (x_{ij} - \overline{x_j})^2 = \sum_{i=1}^{N_j} x_{ij}^2 - N_j \overline{x_j}^2, \tag{4.15}$$

$$s_j^2 = \frac{V_j^2}{N_j - 1}, \tag{4.16}$$

with x_{ij} the observation $x(t_i)$ with bin index $J_i = j$. The analogous quantities for all data, $\overline{x}, V^2$ and s^2, are defined as

$$\overline{x} = \sum_{i=1}^{N} \frac{x_i}{N}, \tag{4.17}$$

$$V^2 = \sum_{i=1}^{N} (x_i - \overline{x})^2 = \sum_{i=1}^{N} x_i^2 - N\overline{x}^2, \tag{4.18}$$

$$s^2 = \frac{V^2}{N-1}. \tag{4.19}$$

For the B bins we introduce the following quantities:

$$V_B^2 = \sum_{j=1}^{B} V_j^2, \tag{4.20}$$

$$V_G^2 = \sum_{j=1}^{B} N_j \left(\overline{x_j} - \overline{x}\right)^2. \tag{4.21}$$

We hence find that

$$V^2 = V_B^2 + V_G^2. \tag{4.22}$$

The differences between the bin averages $\overline{x_j}$ and the average of the entire data set are small whenever the test frequency is not present in the data. In that case V_G^2 is small compared with V^2. In the case where the true frequency is close to the test frequency, the bin averages are very different from the overall average and V_G^2 is comparable with V^2. The search for the most likely frequency in the data hence comes down to the search for a maximum of V_G^2, which is equivalent with a search for the minimum of V_B^2.

The partition of the phase diagram into B equal bins can have disadvantages. It may very well happen that some bins are almost empty if B is chosen to be large or if we have only few data points with a particular time spread. For this reason one makes use of a more complicated *bin/cover structure* (B, C). The phase diagram is divided into B bins, each of length $1/B$. This partition is then applied C times, such that each partition is shifted over $1/(B.C)$ with respect to the previous one. The incomplete bin near phase 1 is completed with the data of the corresponding phase interval near $\phi = 0$. In this way one covers the phase diagram C times, and each partition contains B bins. Such a bin structure allows one to make sure that each observation belongs to at least one bin. Further on we denote the total number of bins $B \times C$ by B_C.

We subsequently introduce the statistic Θ_{PDM}:

$$\Theta_{\mathrm{PDM}} \equiv \frac{\left(\sum_{j=1}^{B_C} (N_j - 1)\, s_j^2\right) / \left(\sum_{j=1}^{B_C} N_j - B_C\right)}{\left(\sum_{i=1}^{N} (x_i - \overline{x})^2\right) / (N-1)}, \tag{4.23}$$

where s_j^2 is defined as:

$$s_j^2 \equiv \frac{\sum_{i=1}^{N_j} (x_{ij} - \overline{x_j})^2}{N_j - 1}. \tag{4.24}$$

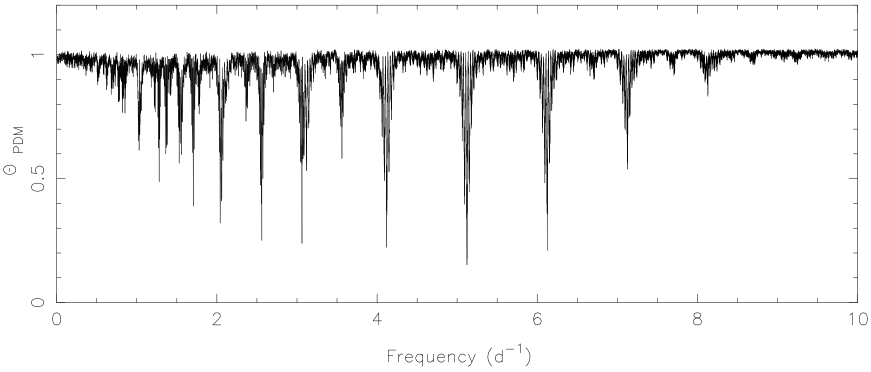

Figure 4.6: Statistic $\Theta_{\rm PDM}$ according to Eq. (4.23) of the data shown in Fig. 4.3 using 10 bins and 2 covers.

With the notation introduced we can also write $\Theta_{\rm PDM}$ as:

$$\Theta_{\rm PDM} = \frac{V_{B_C}^2 / \left(\sum_{j=1}^{B_C} N_j - B_C \right)}{V^2 / (N-1)} = \frac{V_{B_C}^2 / C\,(N-B)}{V^2/(N-1)}. \tag{4.25}$$

A minimum in the $\Theta_{\rm PDM}-$statistic corresponds to a minimum of V_{B_C} and so this statistic is suitable to search for frequencies in the data. For each test frequency that is not present in the data we will find $\Theta_{\rm PDM} \simeq 1$.

The $\Theta_{\rm PDM}-$statistic defined in (4.23) was introduced by Stellingwerf (1978) and is a generalisation of the Θ statistic used by Jurkevich (1971) which is only based on bins. Jurkevich's method is therefore equivalent to Stellingwerf's for $C = 1$.

The more covers one uses, the larger the probability of finding the true frequency, but the longer the computation time. In practice one usually takes B between 5 and 20, so that sufficient data points per bin occur in order to guarantee a well-determined bin average. Typical values for the number of covers is from 1 to 10.

In Fig. 4.6 we show $\Theta_{\rm PDM}$ for the time series shown in Fig. 4.3. Comparing this statistic with Θ_{SL} shown in Fig. 4.4 highlights a much "cleaner" statistic. The peak structure is similar, except for the low frequency region where we see much less false peaks for the PDM version of the statistic. This is due to the far better ability of $\Theta_{\rm PDM}$ to judge the spread of data within the bins with respect to the average bin value, compared with Θ_{SL}'s evaluation of the string lengths across the phase diagram as a whole. This comparison at once makes it clear why users prefer the PDM statistic among the non-parametric methods. Subharmonics still occur prominently, though.

Far more in use in asteroseismology these days are, however, the parametric methods to which we turn now.

4.3 Parametric frequency analysis methods

All the methods described in this category are based upon Fourier analysis, i.e. one fits a harmonic model function to the data. One must therefore keep in mind that these methods will do a very good job as long as the signal consists of a combination of sine (or cosine) functions. Of course, any function that has a more or less smooth behaviour can always be approximated by a Fourier series, such that the applicability of the parametric methods discussed here is very good, particularly for frequency search. The methods are less suited to analyse time series with strong discontinuous behaviour.

In frequency analysis based on Fourier transforms one also defines a function of test frequencies in such a way that it reaches an extremum for the test frequency that is close to the true frequency present in the data, just as for the non-parametric methods. The plot of this function is usually called the *periodogram*, rather than the terminology of a statistic used in the non-parametric methods.

We first recall some useful properties of Fourier analysis and subsequently introduce different types of periodograms in use today.

4.3.1 The continuous Fourier transform of an infinite time series

The *Fourier transform* of a function $x(t)$ that fulfils the necessary conditions of continuity and finiteness is given by

$$F(\nu) \equiv \int_{-\infty}^{+\infty} x(t) \exp(2\pi \mathrm{i}\, \nu\, t) dt. \tag{4.26}$$

Whenever we perform this transformation, we move from the time domain to the frequency domain. The Fourier transform of the constant function 1, e.g., is *Dirac's delta function*:

$$\delta(\nu) \equiv \int_{-\infty}^{+\infty} \exp(2\pi \mathrm{i}\, \nu\, t) dt, \tag{4.27}$$

which has the following properties:

$$\int_{-\infty}^{+\infty} \delta(\nu) d\nu = 1, \quad \int_{-\infty}^{+\infty} \delta(\nu - \xi) g(\nu) d\nu = g(\xi). \tag{4.28}$$

Frequency determination from Fourier analysis is based on the fact that the Fourier transform $F(\nu)$ of a function $x(t)$, which can be written in terms of a sum of harmonic functions with frequencies $\nu_1, \ldots, \nu_M$ and amplitudes $A_1, \ldots, A_M$:

$$x(t) = \sum_{k=1}^{M} A_k \exp(2\pi \mathrm{i}\, \nu_k t), \tag{4.29}$$

is given by

$$F(\nu) = \sum_{k=1}^{M} A_k \delta(\nu - \nu_k). \tag{4.30}$$

Whenever $x(t)$ is a sinusoidal function with frequency ν_1, the Fourier transform of x is only different from zero for $\nu = \nu_1$ and $\nu = -\nu_1$. The Fourier transform of a multiperiodic function $x(t)$, which is the sum of M harmonic functions with frequencies $\nu_1, \ldots, \nu_M$, is a sum of $\delta-$functions which are different from zero for the frequencies $\pm\nu_1, \ldots, \pm\nu_M$.

4.3.2 The continuous Fourier transform of a finite time series

In practice, we never have the luxury to work with infinite continuous time series. Let us go back to the definition of the Fourier transform of a signal $x(t)$ given in Eq. (4.26) and consider the case of a signal $x(t) = A\cos[2\pi(\nu_1 t + \delta_1)]$ for which we have observations from $t = 0$ until $t = T$. In that case, the continuous Fourier transform is

$$\begin{aligned}
F(\nu) &= \int_0^T x(t)\exp(2\pi\mathrm{i}\,\nu\,t)dt \\
&= \frac{A}{2}\int_0^T \exp(2\pi\mathrm{i}\,\nu\,t)\,\{\exp[2\pi\mathrm{i}\,(\nu_1\,t+\delta_1)] + \exp[-2\pi\mathrm{i}\,(\nu_1\,t+\delta_1)]\} \\
&= \frac{A}{2}\left\{\frac{\exp(2\pi\mathrm{i}\,\delta_1)}{2\pi\mathrm{i}\,(\nu+\nu_1)}\,[\exp[2\pi\mathrm{i}\,(\nu+\nu_1)T-1] + \right. \\
&\qquad \left. \frac{\exp(-2\pi\mathrm{i}\,\delta_1)}{2\pi\mathrm{i}\,(\nu-\nu_1)}\,[\exp[2\pi\mathrm{i}\,(\nu-\nu_1)T-1]\right\} \\
&= A\left\{\exp[\mathrm{i}\,T\pi(\nu+\nu_1)+2\pi\mathrm{i}\,\delta_1]\frac{\sin[\frac{T}{2}2\pi(\nu+\nu_1)]}{2\pi(\nu+\nu_1)} + \right. \\
&\qquad \left. \exp[\mathrm{i}\,T\pi(\nu-\nu_1)-2\pi\mathrm{i}\,\delta_1]\frac{\sin[\frac{T}{2}2\pi(\nu-\nu_1)]}{2\pi(\nu-\nu_1)}\right\}.
\end{aligned} \tag{4.31}$$

The periodograms are often displayed as power periodiagrams, i.e. $|F(\nu)|^2$ is plotted as a function of frequency ν. In this case, their shape is determined by the function

$$\mathrm{sinc}(x)^2 \;\equiv\; \left(\frac{\sin x}{x}\right)^2. \tag{4.32}$$

We strongly prefer to work with amplitude periodograms, however, in which case $|F(\nu)|$ is displayed. This will be done throughout the book, except for some figures taken from the literature that display power. For simplicity we omit the notation of absolute values and note $F(\nu)$ on the periodograms. The function $\mathrm{sinc}(x)$ and its square are graphically depicted in Fig. 4.7. Whenever $T \gg 1/\nu_1$, the two frequency peaks following from Eq. (4.31) centred at $-\nu_1$ and ν_1 are well separated such that it is justified to limit display of the transform to $\nu_1 > 0$ as we will do throughout the book. In this simple case, the maximum of the sinc or sinc^2 and its centre of gravity occur exactly at ν_1.

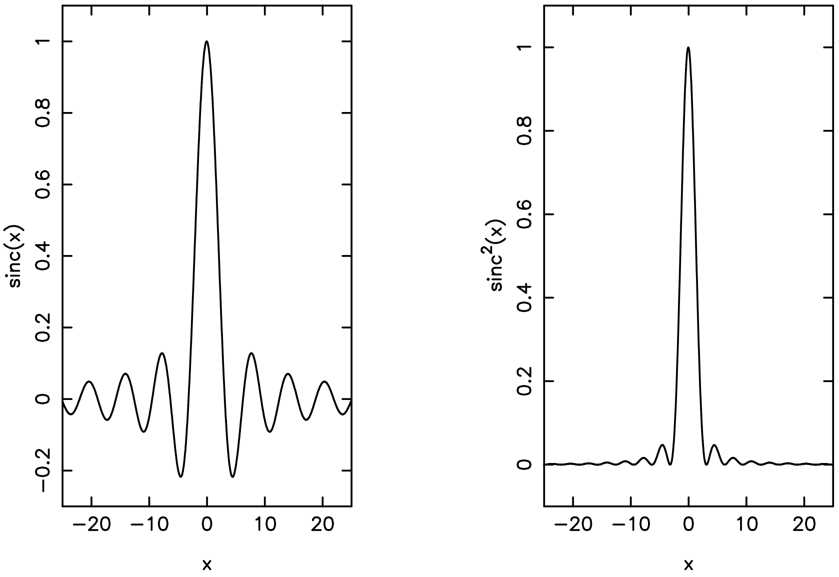

Figure 4.7: The sinc function (left) and its square (right).

As a *first rough* measure of the frequency accuracy, we could consider the width of the sinc peak, i.e. $\simeq 1/T$. This is sometimes termed the *Rayleigh criterion*. In practice, however, any observed peak will have a much more complex shape due to observational noise, to the finite number of measurements over the interval $[0, T]$, and to multiperiodic beating between oscillation modes resulting in frequency interference. As stressed by Schwarzenberg-Czerny (2003), the Rayleigh criterion only provides a *lower* limit to the accuracy reachable. The true accuracy is necessarily dependent on the S/N ratio. The realistic case thus requires a more sophisticated estimate of the frequency error, which will be treated in Sect. 4.5.

Whenever simultaneous oscillations occur, $x(t)$ will be of a form like Eq. (4.1). In such a situation, the frequencies $\nu_1, \ldots, \nu_k$ can only be well separated provided that $T \gg 1/|\nu_i - \nu_j|$ for all pairs $i \neq j$. When this condition is not fulfilled, interference occurs in the periodogram and the ability to identify the correct frequency values depends largely on the phase difference between the modes as well as on their amplitude ratios. Loumos & Deeming (1978) first studied the *resolving power* of a periodogram and derived that the frequencies ν_i and ν_j are separated when $1/T < |\nu_i - \nu_j| < 1.5/T$, but *the maxima do not occur necessarily at the real frequencies*. They also concluded that the difference between two peak frequencies in the periodogram and the real frequencies are negligible whenever $|\nu_i - \nu_j| > 2.5/T$, because the first sidelobe of one sinc function no longer interferes with the main peak of the other sinc function. This rule-of-thumb was further elaborated upon by Christensen-Dalsgaard & Gough (1982), who made a deeper investigation of the resolving power in a periodogram focussing on solar-like oscillations. They came up with a similar condition for accurate frequency separation of $|\nu_i - \nu_j| > 2/T$ covering all cases of relative phases of the modes.

Things get more complicated when the time series does not cover one time interval $[0, T]$, but is a concatenation of continuous data spread over several different time intervals $[0, T_1], [T_2, T_3], [T_4, T_5], \ldots$, i.e. in the case of *gapped* data. The degradation of the Fourier transform from dream to what is not even yet

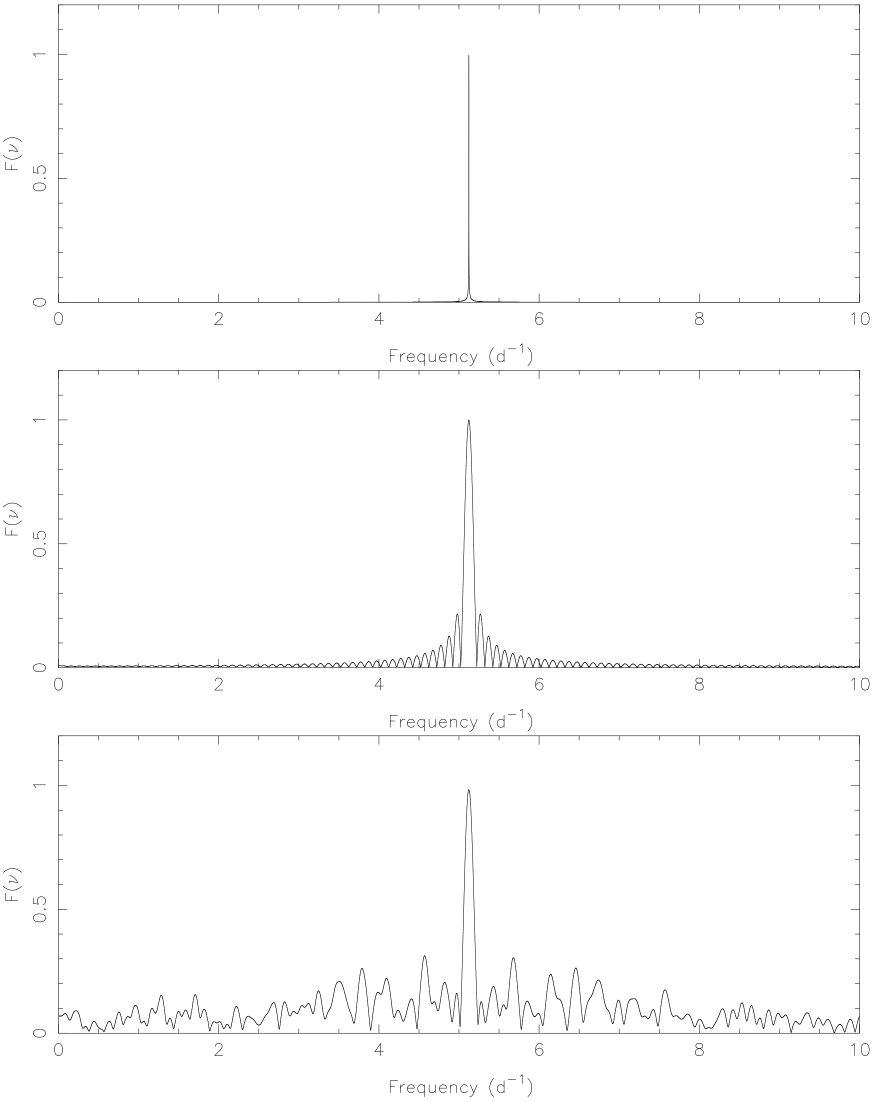

Figure 4.8: Fourier transforms of an almost infinite noiseless time series with one million points spread over thousand days for a harmonic signal with frequency $\nu = 5.123456789\,\mathrm{d}^{-1}$ (top), of a noiseles time series with ten thousand points and a finite time span of 10 days (middle) and of a gapped finite noiseless time series with 4472 points and a time span of 10 days (bottom).

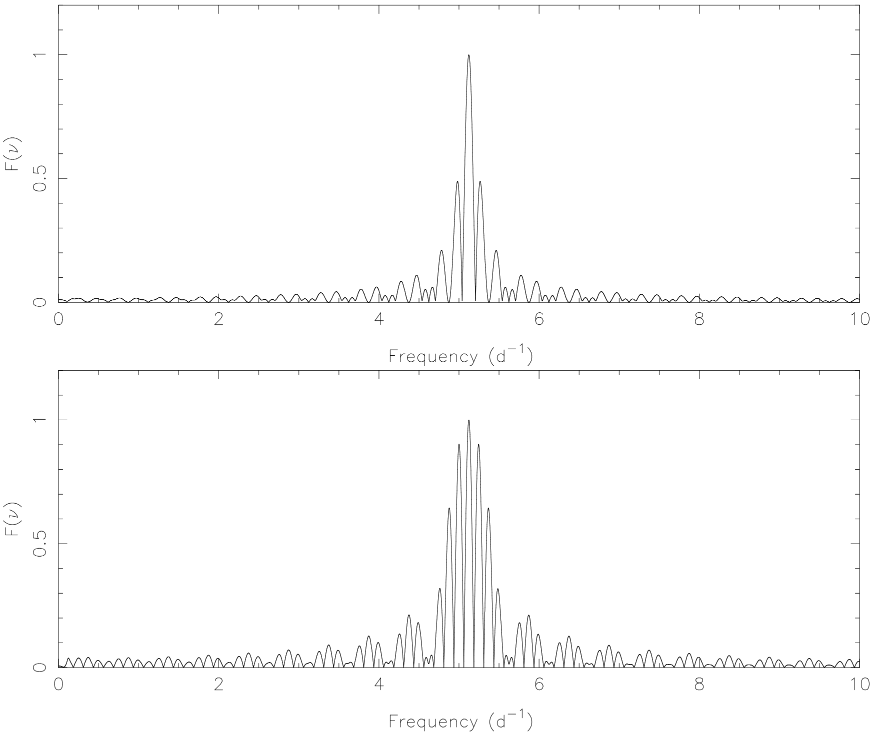

Figure 4.9: Fourier transforms of a noiseles time series of a sine function with frequency 5.123456789 d^{-1} generated for a finite time span of 10 days and containing one large gap from day 4 until day 6 (top) and from day 2 until day 8 (bottom).

reality in frequency analysis is illustrated in Fig. 4.8. In this figure, we compare the Fourier transforms for an almost infinite noiseless time series (1 000 000 data points spread over 1 000 days) with one of a finite noiseless series of 10 000 points spread over 10 days and a randomly gapped finite noiseless series of 4472 points with a total time span of 10 days, all for a simple noise-free sinusoidal signal in the approximation of continuous measurements (i.e. still far too optimistic). The graph speaks for itself and makes one realise why frequency analysis of astronomical time series is so inherently difficult even if the data are close to being noise-free.

In reality, the gaps in data sets are not randomly distributed. In the simple case with one interruption during a time ΔT, the sinc function determining the periodogram (see Fig. 4.7) will be modulated by a term $\cos[\Delta T\pi(\nu - \nu_1)]$. This modulation factor introduces fine structure in the periodogram peaks whose relevance depends mostly on the values of ΔT and T. Two examples are provided in Fig. 4.9 where the time series used in the middle panel of Fig. 4.8 was interrupted for respectively two days from day 4 until day 6 and for six days from day 2 until day 8. These interruptions imply a strong rise in the height of spurious frequencies that are due to the gap compared with the situation where there is no interruption in the data (middle panel of Fig. 4.8), particularly when the gap is large. These spurious frequencies are termed *alias frequencies* and will be defined in the following section. In real data, the value of the modulation factor will be affected by noise and may differ substantially from a simple cosine value, even if there is only one large gap.

4.3.3 Real life: the discrete Fourier transform

For a real data set, the function $x(t)$ is only known for a discrete number of time points $t_i, i = 1, \ldots, N$. We are thus unable to determine its $F(\nu)$. Following Deeming (1975), we introduce the *discrete Fourier transform* of the function $x(t)$:

$$F_N(\nu) \equiv \sum_{i=1}^{N} x(t_i) \exp(2\pi \mathrm{i}\, \nu t_i). \tag{4.33}$$

This transform can be calculated whenever the N measurements of the function $x(t)$ are available.

It is clear that F_N differs from F, but we can associate them with each other through the *window function* defined as

$$w_N(t) \equiv \frac{1}{N} \sum_{i=1}^{N} \delta(t - t_i). \tag{4.34}$$

The window function and the properties of the Dirac function allow us to transfer F_N to an integral form:

$$\frac{F_N}{N} = \int_{-\infty}^{+\infty} x(t) w_N(t) \exp(2\pi \mathrm{i}\, \nu t) dt. \tag{4.35}$$

The discrete Fourier transform of the window function is called the *spectral window* $W_N(\nu)$:

$$W_N(\nu) = \frac{1}{N} \sum_{i=1}^{N} \exp(2\pi \mathrm{i}\, \nu t_i). \tag{4.36}$$

The discrete Fourier transform can be written as the convolution of the spectral window and the Fourier transform:

$$F_N(\nu)/N = (F * W_N)(\nu). \tag{4.37}$$

If $F(\nu)$ is a δ-function at frequency ν_1, then $F_N(\nu)/N$ will have the same behaviour as the spectral window $W_N(\nu)$ at ν_1 because $F_N(\nu)/N = W_N(\nu) * \delta(\nu - \nu_1) = W_N(\nu - \nu_1)$. Comparison of the $W_N(\nu)$ with $F_N(\nu)/N$ near the frequency ν_1 thus helps one to conclude if the frequency ν_1 may be real or not. Whenever $F(\nu)$ is a sum of M $\delta-$functions we have:

$$\begin{aligned}
\frac{F_N(\nu)}{N} &= W_N(\nu) * \sum_{k=1}^{M} \delta(\nu - \nu_k) \\
&= \sum_{k=1}^{M} W_N(\nu) * \delta(\nu - \nu_k) \\
&= \sum_{k=1}^{M} W_N(\nu - \nu_k) \\
&= \frac{1}{N} \sum_{k=1}^{M} \sum_{i=1}^{N} \exp(2\pi \mathrm{i}\, (\nu - \nu_k) t_i).
\end{aligned} \tag{4.38}$$

Hence, $F_N(\nu)/N$ is the sum of M spectral windows that are all centred around the different frequencies ν_k. Due to the fact that $W_N(\nu)$ can differ from zero at frequencies ν that are not necessarily equal to

$\nu_k, k = 1, \ldots, M$, we expect the presence of interference. This will give rise to maxima in the periodogram that do not correspond to real frequencies. These maxima are due to noise and/or the times of observation, which introduce spurious frequencies in the periodogram. This phenomenon is called *aliasing* when it concerns peaks due to the times of measurement and the false frequencies are termed *alias frequencies*. The latter can be recognised as maxima in the window function at frequencies different from zero. This property of the alias frequencies occurring in the spectral window highlights one of the big advantages of Fourier analysis in frequency searches.

The question of course arises which alias frequencies are most common? Let us assume for simplicity that we are dealing with measurements that are evenly spaced: $t_j = \tau + j\Delta t$. In such a case of evenly spaced data, the spectral window is given by:

$$\begin{aligned} W_N(\nu) &= \frac{1}{N}\sum_{j=1}^{N} \exp(2\pi \mathrm{i}\,\nu\tau)\exp(2\pi\mathrm{i}\,\nu j\Delta t) \\ &= \frac{1}{N}\exp(2\pi\mathrm{i}\,\nu\tau)\sum_{j=1}^{N}\exp(2\pi\mathrm{i}\,\nu j\Delta t) \\ &= \exp(2\pi\mathrm{i}\,\nu\tau)\exp(\pi\mathrm{i}\,\nu\Delta t(N+1))\frac{\sin(\pi\nu N\Delta t)}{N\sin(\pi\nu\Delta t)}, \end{aligned} \tag{4.39}$$

in which we have made use of

$$\sum_{j=0}^{N-1} z^j = \frac{1-z^N}{1-z} \tag{4.40}$$

with $z = \exp(2\pi\mathrm{i}\,\nu\Delta t)$. For $\tau = -(N+1)\Delta t/2$ we obtain

$$W_N(\nu) = \frac{\sin(\pi N\nu\Delta t)}{N\sin(\pi\nu\Delta t)}. \tag{4.41}$$

The absolute value of this function is periodic with period $1/\Delta t$ because

$$\left|W_N\left(\nu + \frac{n}{\Delta t}\right)\right| = |W_N(\nu)|\,. \tag{4.42}$$

The function $F_N(\nu)$ hence reaches a maximum in an infinite number of frequencies $\nu_j = j/\Delta t$. Evenly spaced data therefore give rise to a strong aliasing effect.

The situation of unevenly spaced data does not allow one to derive the alias frequencies in such a straightforward analytical way. However, one can show by simulations that certain periodicities in the observation times, such as $\Delta t = 1$ sidereal day, 1 sidereal year, etc., will also give rise to alias frequencies. We call these the *one-day alias* occurring with intervals of ± 1, ± 2, ... when the frequency is expressed in d^{-1} or, equivalently, with intervals of multiples of $\pm 11.5741\,\mu$Hz. The *one-year alias* occurs with intervals of $0.00274\,\mathrm{d}^{-1} = 0.0317\,\mu$Hz, etc. Thus also aliases with intervals of $1.00274\,\mathrm{d}^{-1} = 11.6225\,\mu$Hz occur for data sets spanning more than one year. Such an alias structure was already very clearly seen in Figs 4.4 and 4.6.

The total time span of the data, as well as particular gaps in them, will give rise to additional alias frequencies which are due to uncertainties in the number of cycles in or between the gaps. Moreover,

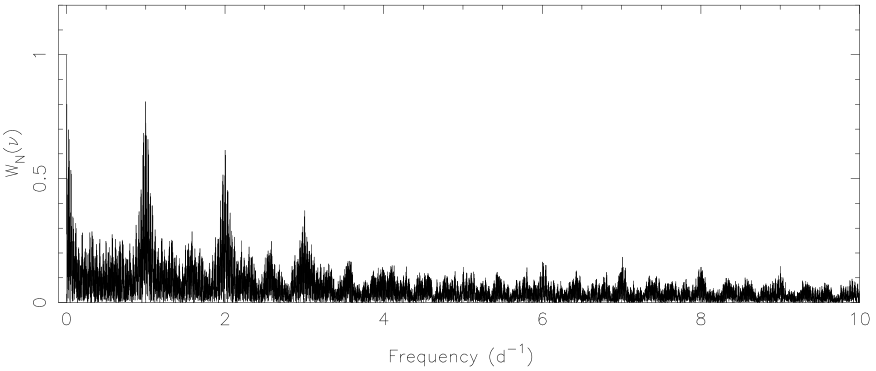

Figure 4.10: Spectral window of the data shown in Fig. 4.3 computed according to Eq. (4.36).

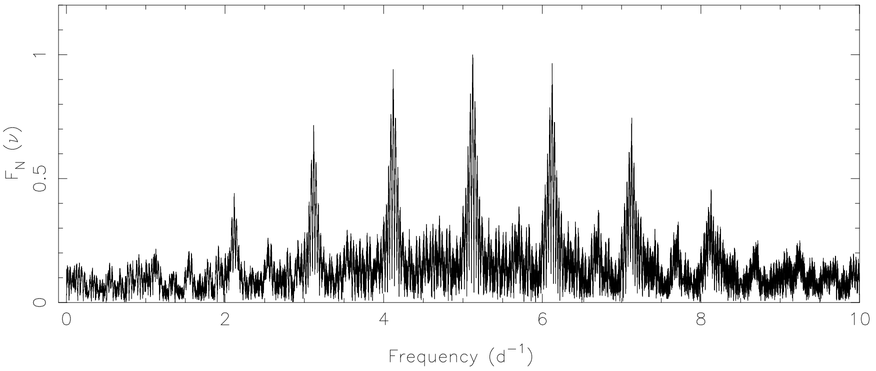

Figure 4.11: Discrete Fourier transform of an noise-free sinusoid with amplitude 1 at frequency 5.123456789 d^{-1} for the sampling shown in Fig. 4.3.

regularity in the sampling with intervals close to (a multiple of) the intrinsic periodicities of the star will inevitably hamper the discrimination between the true frequencies and their aliases. An example of the latter situation occurred in Figs 2.17 and 2.18, where peaks at ν and $1-\nu$ are almost indistinguishable in the single-site ground-based data of the slowly pulsating B stars HD 74195 and HD 123515 which exhibit periodicities near one day.

All these caveats due to aliasing should be checked carefully in any frequency analysis through a detailed study of the spectral window. We show in Fig. 4.10 the spectral window according to the definition in Eq. (4.36) of the time series shown in Fig. 4.3. Spectral windows computed according to Eq. (4.36) are symmetric with respect to zero frequency. The daily and yearly aliasing are apparent in this plot. Other examples were given in Figs 2.5 and 2.43 in Chapter 2. Nevertheless, we advise to take a different approach in practice. Indeed, for real data it is more informative to plot the discrete Fourier transform of an artificial, noise-free sinusoid at a determined frequency (or frequencies). The reason is that the negative part of the discrete Fourier transform may have an effect on the positive part of the periodogram. The latter approach therefore gives the best guidance to discriminate real from false frequencies. This approach is represented in Fig. 4.11 for the data shown in Fig. 4.3, in which the discrete Fourier transform of an artificial sinusoid computed at the sampling of the time series is shown. It gives us at once the complete picture of how

$F_N(\nu)$ would look like if only this one frequency is present in the data. In the current artificial example with only one periodic signal, the discrete Fourier transform of this artificial noise-free sinusoid will be almost indistinguishable from the one of the observed time series, since the latter had white noise with a low standard deviation of only 0.0111. For another example in the case of a multiperiodic pulsator we refer to Fig. 2.22 in Chapter 2.

All these examples, and numerous others in the literature as well as simulations, lead one to the following conclusions. The heights of the alias peaks and of the noise peaks in the spectral window express the lack of knowledge from the data set. One must realise that both the noise and the true signal have an amplitude and a phase and that both are convolved in complex Fourier space. The noise signal may thus add to or subtract from a real frequency peak. Noise may also add to or subtract from an alias peak. Finally noise may do nothing to real peaks. We therefore advise to study the spectral window in detail in any frequency analysis before making firm conclusions on frequencies.

So far, we have not discussed the practicalities of the interval of test frequencies one should consider. This can and should be derived from the data set. It is customary to take zero frequency as a lower limit, since the limiting case of an infinite oscillation period is then covered. The highest useful frequency to search for is the so-called *Nyquist frequency* $\nu_{\rm Ny}$. One can show that $\nu_{\rm Ny} = 1/2\Delta t$, with Δt the sampling step in the case of evenly spaced data. Some authors therefore use the same formula, taking as Δt the average of all the sampling intervals in the case of unevenly spaced data. In practice, however, the Nyquist frequency can be quite different from this value if numerous large gaps and/or serious undersampling or oversampling occur in the data set. In that case, it was shown by Eyer & Bartholdi (1999) that a better approach to obtain the Nyquist frequency is to take $\nu_{\rm Ny} = 1/2p$ with p the greatest common divisor of all differences between consecutive observation times. This is rather cumbersome to be used as daily approach in practice. A good and fast way to make a realistic estimate $\nu_{\rm Ny}$ in the case of unevenly sampled data, appropriate whenever the deviation from equidistance is not too severe, is to take the inverse of twice the median value of all the time differences between two consecutive measurements of the entire data set.

One should not blindly believe that peaks occurring above the Nyquist frequency in the periodogram cannot correspond to true frequencies. It may very well be that a particular frequency occurring as highest peak in the computed periodogram is, in fact, an alias of the true frequency which occurs above $\nu_{\rm Ny}$. This would still allow the detection of the true frequency, by implication, eventhough it occurs above $\nu_{\rm Ny}$. In any case, such a situation would call for further observations at higher sampling rate to rule out the original low-frequency aliases. If the type of star is known, one can also accept the frequency outside of the interval up to $\nu_{\rm Ny}$ on astrophysical arguments.

As we have shown, the irregular sampling of data usually implies a complicated response in the Fourier transform. It can alter the peak frequencies and the amplitudes of the signal, besides introducing the occurrence of very large false peaks. Several different definitions of periodograms have been devised to try and overcome impracticalities in the Fourier transform. We discuss some of them below.

4.3.4 The classical periodogram

Assume we have a time series of N measurements $(t_i, x(t_i))$. The *classical periodogram* was defined originally in meteorology (Schuster 1898) and is written as follows:

$$\begin{aligned} P_N(\nu) &= \frac{1}{N}\,|F_N(\nu)|^2 = \frac{1}{N}\left|\sum_{i=1}^{N} x(t_i)\exp(2\pi \mathrm{i}\,\nu t_i)\right|^2 \\ &= \frac{1}{N}\left\{\left(\sum_{i=1}^{N} x(t_i)\sin(2\pi\nu t_i)\right)^2 + \left(\sum_{i=1}^{N} x(t_i)\cos(2\pi\nu t_i)\right)^2\right\}. \end{aligned} \tag{4.43}$$

If the signal we are searching is a pure harmonic one of the form $x(t_i) = A\cos(2\pi\nu_1 t_i)$, the periodogram will have the value

$$P_N(\nu_1) = \frac{1}{N}\left\{\sum_{i=1}^{N} A\cos(2\pi\nu_1 t_i)\sin(2\pi\nu_1 t_i)\right\}^2 + \frac{1}{N}\left\{\sum_{i=1}^{N} A\cos^2(2\pi\nu_1 t_i)\right\}^2 \tag{4.44}$$

at frequency ν_1. For large N we have

$$\sum_{i=1}^{N}\cos(2\pi\nu_1 t_i)\sin(2\pi\nu_1 t_i) \approx 0, \quad \sum_{i=1}^{N}\cos^2(2\pi\nu_1 t_i) \approx N/2, \tag{4.45}$$

and so $P_N(\nu_1) \approx A^2 N/4$ for $N \to \infty$. For $\nu \neq \nu_1$, positive as well as negative terms occur and these will largely compensate each other. The overall sum will thus be small for such a test frequency.

The frequency ν for which $P_N(\nu)$ is maximal is the most likely one present in the data. For sufficiently extensive data sets, e.g. those with a couple of hundred data points (as in Fig. 4.3, e.g.), the approximation $P_N(\nu_1) \approx A^2 N/4$ is reasonably good. This is why we advise to consider the *amplitude spectrum* rather than the power spectrum, i.e. to plot and analyse

$$A(\nu) = \sqrt{\frac{4P_N(\nu)}{N}} \tag{4.46}$$

as a function of test frequency ν. After all, the amplitude of a mode is what we hope to interpret in terms of the physics of the star.

4.3.5 The Lomb-Scargle periodogram

The periodogram introduced by Lomb (1976) and further improved by Ferraz-Mello (1981) and Scargle (1982), is defined in a different way than the classical periodogram. We present here the formulation by Scargle (1982) and speak of the *Lomb-Scargle periodogram* as it is often done in the literature:

$$P_{\mathrm{LS}}(\nu) = \frac{1}{2}\frac{\left\{\sum_{i=1}^{N} x(t_i)\cos[2\pi\nu(t_i-\tau)]\right\}^2}{\sum_{i=1}^{N}\cos^2[2\pi\nu(t_i-\tau)]} + \frac{\left\{\sum_{i=1}^{N} x(t_i)\sin[2\pi\nu(t_i-\tau)]\right\}^2}{\sum_{i=1}^{N}\sin^2[2\pi\nu(t_i-\tau)]}. \tag{4.47}$$

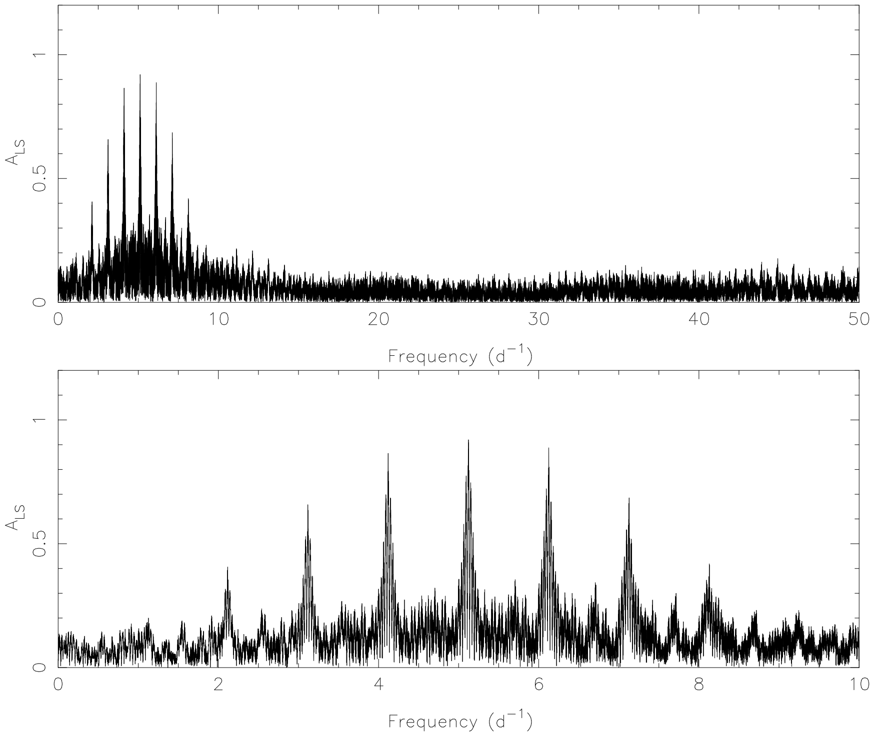

Figure 4.12: Lomb-Scargle periodograms according to Eq. (4.47) for the data shown in Fig. 4.3.

In this expression, the reference epoch τ is chosen in such a way that

$$\sum_{i=1}^{N} \cos[2\pi\nu(t_i-\tau)] \sin[2\pi\nu(t_i-\tau)] = 0, \tag{4.48}$$

or, equivalently

$$\tan(4\pi\nu\tau) = \frac{\sum_{i=1}^{N} \sin(4\pi\nu t_i)}{\sum_{i=1}^{N} \cos(4\pi\nu t_i)}. \tag{4.49}$$

Using the simplifications in notation introduced in Eqs (4.5), the Lomb-Scargle periodogram is written as:

$$P_{\rm LS}(\nu) = \frac{1}{2}\left\{\frac{c_x^2}{c_2} + \frac{s_x^2}{s_2}\right\}. \tag{4.50}$$

It takes the value $A^2N/4$ for a harmonic signal with frequency ν_1 and for sufficiently large N. The amplitude spectrum based on the Lomb-Scargle periodogram is therefore defined by Eq. (4.47):

$$A_{\rm LS}(\nu) = \sqrt{\frac{4P_{\rm LS}(\nu)}{N}}. \tag{4.51}$$

We show in Fig. 4.12 $A_{\rm LS}(\nu)$ for the simulated data shown in Fig. 4.3. The median value of the subsequent time differences for this data set amounts to 0.012 d, such that the Nyquist frequency is estimated to be near $42\,{\rm d}^{-1}$. The whole Lomb-Scargle periodogram up to that value is shown in the top panel, while the lower panel is an enlarged section focusing on the region $[0, 10]\ {\rm d}^{-1}$ where significant amplitude occurs. It can be seen that this lower panel is indeed almost indistinguishable from Fig. 4.11 as predicted for this monoperiodic signal with white noise of low standard deviation. Compare this with the idealised situation of having a continuous Fourier transform of an infinite noiseless signal at one frequency with which we started this section (upper panel of Fig. 4.8)!

One of the reasons to have introduced the Lomb-Scargle periodogram is that its value does not change when all time values t_i are replaced by $t_i + T$ because of the definition of τ. Another reason has to do with hypothesis testing (see Sect. 4.4).

Horne & Baliunas (1986) and Schwarzenberg-Czerny (1997) have proved the Lomb-Scargle periodogram to be equivalent to the variance reduction f_v obtained from fitting a sinusoid at test frequencies by least squares, as explained in Sect. 4.1. It is thus good practice to fit harmonic series of sinusoids at test frequencies to data to search for non-sinusoidal signals as well. This proof implied that the original motivation for the use of non-parametric methods as more efficient tools to detect non-sinusoidal signals than parametric ones weakened considerably, particularly so since they require a lot more computational time and introduce a complex spectrum with subharmonics and their aliases.

4.4 Significance criteria

During a frequency analysis, one of course needs to adopt a stop criterion to decide whether or not a candidate frequency is still *significant* or not. For obvious reasons, this aspect of frequency analysis has received a lot of attention. To derive the significance of a frequency one needs to know the distribution function of the employed frequency statistic. As a consequence of the data-driven approach of the frequency analysis methods outlined above, one is unable to construct appropriate distribution functions based on theoretical principles.

Stellingwerf (1978) and Cuypers (1987) derived that the significance of $\Theta_{\rm PDM}$ can be related to an $F-$test. However, Schwarzenberg-Czerny (1997) pointed out that the sensitivity of the significance test proposed by these authors is poor and he demonstrated that $\Theta_{\rm PDM}$ rather follows a β distribution. It was shown by Scargle (1982) that the distribution function for the Lomb-Scargle periodogram belongs to the exponential family, but it has to be kept in mind that this is only true for $N \rightarrow \infty$. Moreover, the author could not come up with a simple treatment of the statistical properties of $A_{\rm LS}$. Schwarzenberg-Czerny (1997) came to the important conclusion that all methods outlined in this chapter are mathematically equivalent for a given sampling, binning and weighting pattern.

Schwarzenberg-Czerny (1998) demonstrated that an empirically derived β distribution is the only valid approach to derive good significance levels and that theoretical distributions as used in e.g. Scargle (1982) or Horne & Baliunas (1986, the so-called False-Alarm Probability or FAP) have to be abandoned. It is

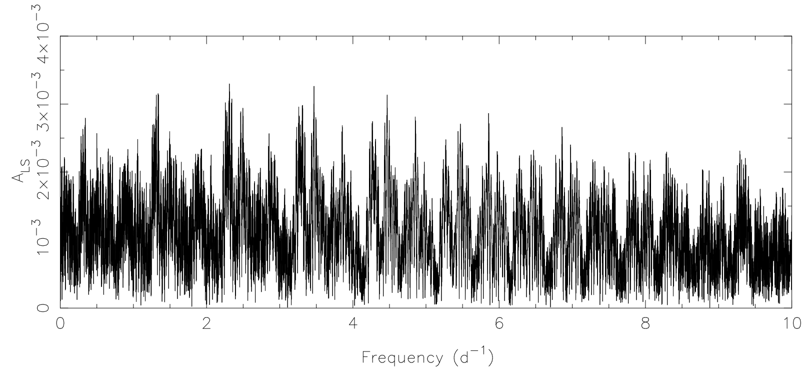

Figure 4.13: Lomb-Scargle periodogram of the residuals after subtracting the fit shown as full line from the data in the upper left panel of Fig. 4.5. Note that this periodogram's y-axis is enlarged with a factor 300 compared with the one for the original data before prewhitening shown in Fig. 4.12.

therefore common practice these days to take a frequency peak as significant whenever its amplitude in the periodogram is above a particular empirically determined critical value, i.e. to let the data speak for itself rather than relying on assumptions about the (uncertain) statistical model distributions.

Depending on the data set and authors, different so-called *S/N level significance criteria* are considered appropriate and adopted. The S/N level is computed as the average amplitude in a well sampled periodogram of the final residuals and for an appropriate interval in the frequency region where the candidate frequency is situated. We denote this level by $\sigma_{\rm res}$. The S/N level of a particular frequency is then computed as the ratio between its amplitude and $\sigma_{\rm res}$. Breger et al. (1993) derived empirically, from experience with numerous data sets resulting from δ Sct network campaigns, that a frequency can be very safely considered to be significant whenever its amplitude, computed either in the time domain or in the frequency domain, fulfils $A > 4\sigma_{\rm res}$. This result was supported from simulations based on data assembled with the Hubble Space Telescope Fine Guide Sensors and assuming photon-dominated white noise by Kuschnig et al. (1998). They concluded that the criterion $A > 4\sigma_{\rm res}$ corresponds to a 99.9% confidence level of having found an intrinsic peak rather than one due to noise. The confidence levels corresponding to $A > 3.6\sigma_{\rm res}$ and $A > 3\sigma_{\rm res}$ are respectively 95% and 80% for photon-dominated noise. Since noise peaks can reach a $3\sigma_{\rm res}$ level with 20% probability, we do not consider this to be a sufficiently safe significance criterion. In reality, the noise is not photon-dominated for most data sets, particularly those assembled from the ground. Moreover, the noise is usually correlated, i.e. non-white. Unfortunately, the true noise profile may be very hard to compute (see also Sect. 4.5). This is why this step is often omitted and the abovementioned criterion of $A > 4\sigma_{\rm res}$ is adopted as a very safe one, at least when only one data set is at hand.

For the example of the simulated data shown in Fig. 4.3, we derive the frequency from Fig. 4.12, compute the residuals from subtracting the least-squares fit shown in the upper left panel of Fig. 4.5 from the data, recompute the Lomb-Scargle periodogram for these residuals and derive the noise level of the residuals in the frequency domain. The periodogram of the residuals is shown in Fig. 4.13 and was computed with the same sampling as the original periodogram according to the frequency accuracy discussed in the following section. One should not undersample the periodogram for the S/N level computation (nor for the frequency derivation!). The average amplitude in Fig. 4.13 amounts to 0.0011 and is a good estimate of $\sigma_{\rm res}$ in the considered frequency interval of $[0, 10]\,\mathrm{d}^{-1}$. This implies that the frequency $\nu = 5.123456789\,\mathrm{d}^{-1}$ reaches a level of 909 σ_{res} for this example. One can easily derive from Fig. 4.13 that the highest noise peaks in $[0, 10]\,\mathrm{d}^{-1}$ reach a level of 3 σ_{res}. The highest noise peaks in the interval $[0, \nu_{\mathrm{Ny}}]\,\mathrm{d}^{-1}$ reach 3.6 σ_{res}.

Examples of significance level computations for real data were already shown graphically in Figs 2.22 and 2.27 for the multisite campaigns of the β Cep star 12 Lac (Handler et al. 2006) and of the pre-main-sequence star IP Per (Ripepi et al. 2006). We refer to the original papers for the details of the adopted criteria and their means of computation of the S/N level.

One can take a less conservative attitude than $A > 4\sigma_{\mathrm{res}}$ whenever more than one independent data set is available for analysis (see, e.g. Figs 2.17 and 2.18 and De Cat & Cuypers (2003) for additional examples). One is usually also less conservative when it concerns the acceptance of combination frequencies, such as multiples or linear combinations of frequencies, which have already passed the requirement of $A > 4\sigma_{\mathrm{res}}$. In both these cases, i.e. for frequencies present in independent data sets or for combination frequencies searched in one data set, we advise to use $A > 3.6\sigma_{\mathrm{res}}$ as a safe condition of acceptance.

4.5 Error estimation of the derived frequencies

Once the user has reached the stage to have concluded that M frequencies with determined values are present in the data, the question of final error estimation of all the unknowns needs to be settled. We limit ourselves here to the case of linear oscillations, with time dependence $\sim \cos[2\pi(\nu t + \delta)]$. In order to compute the errors in an appropriate way, one can consider the model described in Eq. (4.1), where M is assumed to be error-free due to our inability to treat discrete parameter estimation in the data-driven frequency analysis. The error estimation is done in the time domain here, by means of least-squares fitting, because the periodograms only give a good amplitude estimate in the limit of large N.

In general, error estimation is usually based on derivatives of a kind of likelihood function, e.g. the one defined in Eq. (4.2). The goal should be to make appropriate assumptions on the character of the data, on the properties of the noise and on the inter-dependence of the model parameters which are in our case the frequencies, their amplitudes and phases, and the mean value of the observable x_i, when deriving the errors. Appropriate error propagation is a poorly developed field in astronomy in general, and its application in asteroseismology is, unfortunately, no exception to this rule. We emphasise below the shortcomings we have to live with in current analyses. The reader is advised to keep these in mind in all the seismic interpretations based on observed frequencies.

4.5.1 Data without alias problems

As a first approach to the problem of error estimation, we consider data not suffering from aliasing. This implies that we assume there to be no ambiguity in selecting the true frequency values from the methods outlined above. We discuss the complication introduced by aliasing separately further on.

A first approximation usually adopted is to assume the times of measurement t_i, as well as the reference epoch τ, to be error-free. It is clear that the observers always should care about the accuracy of the clocks they are using during the data gathering, particularly when observing short-period oscillators. Even for data assembled with a carefully calibrated clock, the assumption of having instantaneous measurements with error-free timings is in general not valid. Indeed, the data gathering is done by adopting a certain integration time during which photons are detected by the instrument, and t_i is usually taken to be the error-free time of mid-exposure. The integration of course implies a smearing out of the oscillatory signal over a fraction of the oscillation cycle for each of the modes. Moreover, the integration time is sometimes not constant during an observing run, e.g. it is continuously adapted to the atmospheric conditions for ground-based spectroscopic data.

All this implies that the timings t_i cannot be error-free. Moreover, they are not independent of each other. The assumption of instantaneous measurements with error-free timings may be a good approximation as long as the *temporal resolution* of the data, i.e. the ratio of the integration times to the oscillations periods, is very small, let's say below 1%. This will in general not be the case for high-resolution spectroscopic time series or for ground-based photometric time series of compact oscillators. A remedy to this problem is achievable, but it requires a good model description of the oscillatory behaviour and it is time consuming. The user can check *a posteriori* how much the data set suffered from smearing over the oscillation cycles for each of the modes *after* the frequency derivation is finished. This allows a measure of the effect of this assumption on the frequency values and their amplitudes.

A second approximation in deriving error estimates is much more problematic than the first one: the assumption of having white uncorrelated noise with average zero and constant variance σ_N^2 in time. The overall noise profile of the data contains, in general, contributions from the instrument performance and from the environmental conditions, such as the behaviour of the atmosphere for ground-based data and the effect of stray light, satellite jitter, proton impact etc. for space data. It is clear that the noise profile must be time dependent and that the different noise factors are by no means uncorrelated. Unfortunately, it is in general impossible to propagate all the different noise factors appropriately, due to lack of good model descriptions for each of them. The conclusion must therefore be that any error estimate ignoring the correlations among the noise factors and their time dependence cannot be but lower limits of the true errors.

A third approximation is to assume that there is no interference between the different true frequencies and the noise peaks. This is an additional condition compared with the resolution issue described in Sect. 4.3.2, where interference among intrinsic frequencies was considered. For similar reasons as outlined there, this approximation is valid whenever the noise peaks are well separated from those of the intrinsic frequencies, a situation seldom encountered.

The three approximations described here are followed out of necessity to avoid an ill-conditioned statistical description for the error derivation. Indeed, in the derivation of the error of one particular parameter, a significant simplification is met when assuming that all other parameters are perfectly known. This situation occurs when adopting the discussed four approximations. In this case, one ends up with the following standard error estimate for the derived amplitudes, phases and frequencies:

$$\sigma_\nu = \frac{\sqrt{6}\,\sigma_N}{\pi\sqrt{N}\,A\,T}, \quad \sigma_A = \sqrt{\frac{2}{N}}\,\sigma_{\rm N}, \quad \sigma_\delta = \frac{\sigma_N}{\pi\,\sqrt{2N}\,A} \tag{4.52}$$

with T the total time span of the data and N the number of data points (Bloomfield 1976; Cuypers 1987; Montgomery & O'Donoghue 1999). In these formulae, $\sigma_{\rm N}$ stands for the average error on each of the data points. Quite often, error estimates are not available for individual measurements, even in the simplified assumption of uncorrelated time-independent noise. It is then good practice to take the standard deviation of the residuals after removal of all accepted significant frequencies as a realistic and conservative estimate of σ_N.

We note that the error estimates provided in Eq. (4.52) are 1σ errors, i.e. the true values of the frequency, amplitude and phase belong with 68.3% certainty to the intervals $[\nu - \sigma_\nu, \nu + \sigma_\nu]$, $[A - \sigma_A, A + \sigma_A]$, $[\delta - \sigma_\delta, \delta + \sigma_\delta]$ respectively. Much more common practice in statistics is to use the so-called 2σ error estimates, which imply that the true values are with 95.4% certainty in the intervals $[\nu - 2\sigma_\nu, \nu + 2\sigma_\nu]$, $[A - 2\sigma_A, A + 2\sigma_A]$, $[\delta - 2\sigma_\delta, \delta + 2\sigma_\delta]$.

Schwarzenberg-Czerny (1991) has shown that the error estimate of the frequency can also be done in the frequency domain, leading to the same accuracy as the one discussed above in the time domain. Since he proved both methods to be statistically equivalent, error estimation in the frequency domain suffers from the same limitation of underestimating the variance due to the four assumptions outlined above.

For the choice of the interval of test frequencies it does not make sense to search for frequencies with a step much smaller than the value of σ_ν given in Eq. (4.52). A good guideline to start the first frequency search, before an estimate of σ_ν can be made, is to take a step of $0.1/T$. Once the first frequency is found, one can improve the frequency step by calculating σ_ν and adapting the step to this value for all subsequent frequency searches.

Another issue in the derivation of the errors is to assume that the oscillation frequencies are independent. As described in Chapter 3, the oscillation spectrum of a star is determined by its stellar structure and follows a clear pattern dependent on the internal physical properties. So, even in the linear approximation, the oscillation frequencies cannot be independent because they are determined by the same stellar structure. Deviations from linearity even imply complex coupling between oscillation modes and their frequencies which are also dependent on the stellar model. This is usually ignored in the error estimation of frequency analysis.

4.5.2 Data suffering from aliasing

Most data sets have gaps, quite often leading to ambiguity in the selection of the true frequency peak from its aliases when the duty cycle is limited. The situation is usually far more complex than having one simple modulation factor as in Fig. 4.9, because numerous data gaps, all with different ΔT's, occur. An accurate study of the spectral window, or the consideration of independent data sets of the same star if available, may help to discriminate between the true frequency peaks and their aliases. Sometimes, however, this is impossible and in such a situation one has to take the uncertainty due to alias confusion into account in the error estimate of the frequency. As a rule-of-thumb, one can take a peak to be uncertain when the difference between its amplitude and the one of its aliases is less than the height of the highest noise peaks. Indeed, noise peaks and real peaks convolve with each other in complex space, such that they may add in amplitude, subtract in amplitude, or anything in between.

The best way to proceed when alias confusion cannot be overcome is to determine the full-width-at-half-maximum of the envelope of all alias peaks that bring confusion, and to add this value to the frequency error given in Eq. (4.52). While the full-width-at-half-maximum of the central peak depends on the total time span of the data, as shown by Eqs (4.52), the one of the envelope depends mainly on the duty cycle, as is clear from Fig. 4.9.

Finally, if the addition of a new frequency implies a modification of the derived amplitudes and phases for previously determined frequencies (say by more than 3σ) during the process of fitting multiple frequencies by least squares, then there is *interaction* between the spectral window patterns of the frequencies. In that case, the formal errors on amplitude and phase given in Eqs (4.52) underestimate the true uncertainties.

4.6 The use of weights in merging different data sets for frequency analysis

Very often, more than one time series is available for the analysis of a pulsator and the question arises if one should merge them or simply analyse each of them separately before making final conclusions. The goal of merging them would be to reach a lower noise level in the Fourier transform, or a higher frequency precision or a cleaner spectral window. In any case, appropriate weights cannot be but data-driven, i.e. based on the noise properties and the sampling of each of the separate data sets. This is why one cannot provide one simple theoretical statistical treatment, nor perform all-encompassing simultations encapsulating each of the different circumstances. We therefore limit ourselves here to a brief discussion of some prototypical situations.

As a first example, we consider the situation of a white-light photometric multisite campaign with different instruments attached to telescopes of different apertures and data gathered in different atmospheric conditions. In this case, the data from the smaller telescopes have higher noise level, but, on the other hand, they usually imply a better duty cycle. In such a situation one wants to investigate what data to include in the final analysis, and whether weights should be used or not in the computation of the Fourier transforms. It was shown in the highly recommended seminal paper by Handler (2003), who studied in detail the merging of such type of data from the different telescopes of the WET consortium and for different targets, that the use of appropriate weights is indeed advantageous compared with the use of unweighted merged sets. He considered three different weighting schemes and concluded that weights proportional to the inverse local scatter in the light curves produce the best result in Fourier space. The advised procedure is as follows. After having completed the frequency analysis for the unweighted merged data set, one computes the residuals and their standard deviation σ. Each individual point is then weighted as follows:

$$\begin{cases} w_i = 1 & \text{if } R_i \leq K\sigma, \\ w_i = (K\sigma/R_i)^{\alpha} & \text{if } R_i > K\sigma, \end{cases} \tag{4.53}$$

where R_i is the residual of data point i with respect to the unweighted least-squares solution and K and α are free parameters to be adapted to the merged data set. A Fourier transform of the weighted data is then computed to try and improve the result in terms of finding the frequencies with amplitudes of better S/N level and/or to find more significant frequency peaks. The best values of K and α must be derived by using a few trial values and evaluating the noise level in the Fourier transform. Typical values turn out to be $K, \alpha \in [0, 2]$. Since this method depends on the frequency solution found from the unweighted merged data set, a scheme with a few iterations is the best approach. A similar strategy may be advantages to follow when new data are merged with archival ones of the same kind. Recent applications of the methodology evaluated by Handler (2003) are available in Rodriguez et al. (2003) for a δ Sct star and in Vučković et al. (2006) for an sdB star.

As a second example, we consider the case of multicolour photometric data obtained with the same instrument and having (almost) the same sampling. This is also an often encountered situation, because the identification of the degree l of the oscillation may be within reach in this circumstance. In this case, the duty cycle is not improved by merging the different sets. As we will show in the following chapter, the amplitude of a mode is different in different wavelengths and it depends also on the geometry of the mode (i.e. the number and position of the surface nodal lines l and m) and on the direction to the line of sight (inclination angle). For a specific star, the amplitude ratios will be shown to be dependent on l only (Chapter 5). This implies that the best wavelength to detect a mode is dependent on its degree. In addition, it involves limb-darkening effects, as well as flux, gravity and temperature variations and these may be quite different for different types of oscillations in different types of stars. Pulsating B stars, e.g., have their largest amplitude in the U filter, while the amplitude of pulsating A or F stars peaks at wavelengths of the B filter, irrespective of the mode geometry. For one and the same star, the l-dependence of the amplitudes implies that a particular mode may have an amplitude just above the detection treshold of $A > 4$ S/N in one or a few of the used filters, but not in all of them. It is therefore surely necessary to analyse the time series of the different filters explicitly to decide upon the reality of all the significant oscillation frequencies, and not just look at the filter where the best S/N is reached. Indeed, the difference in detected mode amplitude for the various filters may be larger than the difference in the noise level among the filters. Recent examples of this situation can be found for B pulsators in De Cat et al. (2007) and for A and F pulsators in Cuypers et al. (2007). The modes that have significant amplitude in all filters will pop up better after (weighted) merging of the data sets because the noise level is proportional to the number of data points as $\sqrt{N}$, but those that are only significant in a subset of the filters may increase or decrease in significance.

A similar situation to the previous one occurs for radial-velocity measurements of different line profiles from échelle spectra. The amplitudes of the modes may turn out to be quite different for different spectral lines because of various reasons, such as a different intrinsic profile (Gaussian broadening due to temperature versus Stark broadening due to pressure, e.g.), a different line depth, a different skewness due to blending, different formation depth in the atmosphere, a different limb darkening effect, etc. It may therefore be worthwhile to consider merged data sets for the different spectral lines with the same sampling, in the same way as outlined for the multicolour photometry.

Finally, we consider the case of having data sets of very different nature, i.e. different quantities obtained for different sampling, for one and the same star. Examples are shown in Figs. 2.17 and 2.18 where Hipparcos, Geneva and radial-velocity data of two SPBs are displayed. In this case, it is not obvious to think of an appropriate weighting scheme similar to the one in (4.53) because of the different physical units. Usually, the data are analysed separately first. In a second step, one could simply lower the treshold of accepting a peak in terms of amplitude, e.g. take $A > 3.6$ S/N as a necessary condition whenever it is met for all the available independent time series. Sometimes, however, oscillation frequencies are easier to detect in spectroscopy than in photometry, depending on their l-value and one would want to give different weights to the various data sets and lower the detection treshold further. This holds the danger of taking noise peaks for real. A simple test in such a case may be to standardise each of the separate Fourier transforms, i.e. to rescale them to $[0, 1]$ by dividing through the amplitude of the highest peak, and then multiply them with the idea that, if additional frequencies at S/N below 4 would be present in each of the periodograms, they would have an improved S/N in the multiplied periodogram while they would reduce in amplitude if the frequency was a spurious peak present in only one of the independent data sets. This method was employed by Aerts et al. (2006) to unravel low-amplitude frequencies from MOST, Hipparcos and radial-velocity data of the β Cep star δ Ceti.

4.7 Damped oscillations

The descriptions in the preceding parts were valid under the assumption that the oscillation amplitude A and phase δ are constant in time, i.e. that the modes under consideration have an infinite lifetime or a lifetime several orders of magnitudes longer than the time series and that phase coherence is preserved over the entire observing run. This assumption is not valid whenever growth and/or decay of modes occur during the obtained time series. The best known example of such a situation is, of course, the one of stochastically excited solar-like oscillations. Also modern high-precision radial-velocity measurements of roAp stars contain evidence of growing and damping of mode amplitudes.

We recall that, whenever an oscillation with frequency ν_1 is damped, one has, instead of Eq. (4.9):

$$x(t_i) = A \cos\left[2\pi(\nu_1 t_i + \delta)\right] \exp(-\eta t) + c, \tag{4.54}$$

with η the damping rate which is also the inverse of the mode lifetime. Suppose such a signal would be observed continuously over an infinite amount of time. In that case, it is easy to show that the power at a test frequency ν equals

$$P(\nu) = \frac{A^2}{4(\nu - \nu_1)^2 + \eta^2}. \tag{4.55}$$

The power spectrum thus takes a Lorentzian profile around the frequency ν_1 with a half-width-at-half-maximum equal to η. If the signal is continuously observed during a finite time T, then the resulting peak in the power spectrum is intermediate between the sinc^2 function and the Lorentzian, tending to the former for $\eta T \ll 1$, and towards the latter for $\eta T \gg 1$.

Even Eq. (4.54) is an idealisation in that it implicitly assumes a sudden excitation of the mode, followed by an exponential decay. The modes are stochastically excited by random fluctuations due to the turbulent motions in the convection zone. In this case, one has

$$P(\nu) = \frac{P_f(\nu)}{4\nu_1^2\left[(\nu - \nu_1)^2 + \eta^2\right]}, \tag{4.56}$$

with $P_f(\nu)$ the average power spectrum of the forcing function. Given that the forcing function is a slowly varying function of frequency, the result is a Lorentzian spectrum with a width determined by the linear damping rate of the mode.

Whenever the observed time series is a single realisation of the spectrum, the result is only a random function with a Lorentzian envelope. In that case, the observed profiles are asymmetric in this case and representing them by a Lorentzian cannot be but an approximation. Neglecting such asymmetries in the fitting of the frequency peak causes systematic errors in the inferred frequencies. The best way to proceed in the case of damped oscillations is, therefore, to perform simulations and fit the Fourier transforms of the observed time series with Lorentzian profiles to determine acceptable ranges for the frequency, amplitude, and the mode lifetime. Such simulations have been performed extensively for the solar oscillation spectrum. It was found that the stochastic nature of the excitation gives rise to a number of sharp frequency peaks, with a distribution around the Lorentzian envelope. It thus cannot be assumed that the maximum observed amplitude corresponds to the true frequency of the mode. Substantial care is required in analysing data of this nature and the simulations have to be designed on a case-by-case basis.

4.8 Eliminating aliases

Several methods designed to “remove” false peaks from a periodogram have been devised. The widest used one among them is the so-called CLEAN method. The original CLEAN algorithm was written by Hogbom (1974) in the context of aperture synthesis. It was developed to help radio astronomers in their interpretation of interferometric data by cleaning up the *spatial* window pattern. This algorithm was later adapted by Roberts et al. (1987) to clean up the spectral window pattern for frequency analysis.

CLEANing implies that one first constructs the *dirty* spectrum, which is the Fourier transform of the data. Subsequently, one deconvolves this observed spectrum with the window function shifted to the highest peak of the dirty spectrum (cf. Figs 4.10 and 4.11). This deconvolution is done by first applying a particular scaling to the window function according to the gain factor g, with $0 < g < 2$. Thus, one subtracts the scaled spectral window from the dirty spectrum to produce a residual spectrum. This deconvolution process is repeated until the strongest residual peak is below a specified cutoff level or for a chosen number of iterations. At that point, the CLEAN algorithm restores the removed frequency to the spectrum by convolving it with the CLEANed residual spectrum. This process can be repeated at each prewhitening stage.

The first application of the adapted CLEAN version by Roberts et al. (1987) in pulsating star research was made by Gies & Kullvanijaya (1988), who used it to treat their data of line-profile variations of the B2III star ε Per, an archetypical line-profile variable without clear periodic photometric variations due to high-l modes. Numerous applications have followed since.

Foster (1996) developed the CLEANest frequency spectrum. The naming is quite unfortunate, because CLEANest has not much to do with CLEAN. The CLEANest spectrum is the sum of a discrete amplitude spectrum and the residual spectrum. The discrete spectrum is derived from a model fit of the best M frequencies to the data according to Eq. (4.1). This is done for one frequency at a time, i.e. one starts with one frequency, tests the significance of its amplitude, next one makes a fit to find the best pair of frequencies, tests their amplitudes, continues with a fit for the best triple of frequencies, etc. At a certain point, the fit for the best $(M + 1)$ frequency set does no longer lead to a significant peak for the $(M +$

$1)$th frequency. At that stage, one constructs a composite graphical representation of the optimal discrete amplitude representation of the M accepted frequencies and the amplitude spectrum of the residuals after prewhitening the best fit for M frequencies. This CLEANest spectrum thus is not a true frequency spectrum, but merely a convenient graphic that captures the different stages of a least-squares fitting procedure and its resulting residual spectrum.

Following Kurtz (2002), we issue some warnings in the use of these two methods that were designed to eliminate aliases. It is in fact a crucial mistake in frequency analysis to think that methods capable of eliminating aliases exist. Alias confusion in a data set can only be overcome by additional data. All the two methods described above do, is to *hide* the aliases for the user, seemingly easying the interpretation in terms of intrinsic frequency detection. One must keep in mind that the final result obtained by CLEANing depends crucially on the choices of highest peaks made during the deconvolution, while the CLEANest spectrum assumes that frequencies are not confused with their aliases in the least-squares fitting. So both the CLEAN and CLEANest methods are ambiguous.

The main danger of CLEANing occurs in situations where the noise in the data set under analysis has added amplitude to an alias or subtracted amplitude from the true peak. If this is the case in such a way that the alias peak has become the highest one in the periodogram, then this false peak will be selected as the true frequency by the algorithm. The subsequent iteration schemes of CLEAN will take away an amount of amplitude of the true frequency according to the gain and number of iterations.

CLEANest will consider the least-squares fit at the alias frequency if the noise has boosted its amplitude above the one of the true peak. It will then start or continue an iterative least-squares fitting scheme based on one or more alias frequencies rather than on true frequencies.

The user is thus easily fooled by these algorithms if they are used as a black boxes without making a careful analysis of the spectral window at each step of the prewhitening. We disadvice their use for this reason, particularly for unexperienced frequency analysts.

4.9 Conclusions

We provided the most commonly used methods to treat frequency analysis of unevenly spaced data with large gaps of observables of variable stars. All methods discussed here in detail are suitable to determine the oscillation frequencies of stars whose modes have infinite lifetime. The string length methods and the phase dispersion minimisation methods are of broader application than stellar oscillations because they can handle non-sinusoidal signals or signals with variable amplitude without loss of accuracy. On the other hand, the approximation of having sinusoidal signals, the basic assumption of the methods based on Fourier transforms, is usually very good in the study of stellar oscillations.

The reader has hopefully learned that frequency analysis of unevenly spaced gapped data with noise is an inherently difficult mathematical problem to solve. Methods based on Fourier analysis are best suited to apply significance criteria and to obtain frequency error estimation. One should never forget to make a detailed inspection of the spectral window before coming to final conclusions on the detected significant frequencies.

Frequency analysis of data resulting from stars with damped modes is much more cumbersome and requires a specific treatment, whose basic ingredients have been pointed out here but whose detailed application will be omitted here.

Chapter 5

Mode identification

The basic data for asteroseismology are the pulsation frequencies, and we have just shown in Chapter 4 how those are derived from the observations. But before the frequencies can be used for detailed modelling, it is imperative to know what pulsation mode gives rise to each frequency. Determining this is called *mode identification*. The reason it is so important can easily be understood for p modes (the situation is similar for g modes). The frequency of pulsation is a measure of the sound travel time along the ray path for p modes, and that is determined by the variable sound speed and the length of the ray path itself. It is thus critical to know the ray path, and that is specified by the pulsation mode geometry. Mode-identification techniques assign values to the discrete spherical harmonic quantum numbers (l, m) of each of the detected oscillation modes. The amount of astrophysical information that can be derived from the observed pulsations depends directly on the number of successfully identified modes. Therefore, great effort is put into mode identification in any seismic analysis.

For oscillations in the asymptotic frequency regime, the derivation of frequency or period spacings often suffices to identify the modes. This can be achieved for the Sun, for solar-like oscillators and for white dwarfs. However, when only a limited number of modes is excited to observable amplitudes, or when the modes do not follow particular frequency patterns, or whenever a very dense frequency spectrum is predicted, the frequency values alone are insufficient to derive the (l, m, n). In this case, one cannot proceed with seismic modelling considering *all* values for (l, m, n) for any of the detected frequencies. In order to limit the computation time of such forward modelling, the values of the degree l are usually limited from arguments of partial cancellation. As we will show later on in this chapter (see Fig. 5.5), the observed photometric amplitude of modes with $l \geq 3$ are a factor five to ten less than those of modes with $l < 3$ having the same intrinsic amplitude (Dziembowski 1977). It is then customary to consider modes with $l \leq 2$ and to assume $m = 0$ when no obvious evidence for rotational splitting is found in the Fourier transform of the time series.

This procedure is not very satisfactory, though, because rotation can easily result in non-equidistant splitting and imply merging of frequency multiplets in such a way that they cannot be unravelled. Moreover, quite a number of classical pulsators show evidence for modes with degree $l \geq 3$ from spectroscopy, where the partial cancellation has a different effect than in photometry (see Figs 5.5 and 5.15). In these cases, the assumption of $l \leq 2$ or $m = 0$ is unjustified. Within asteroseismology the quest for *empirical mode identification* has therefore become an extended topic by itself. By this term we mean the assignment of values of the spherical harmonic quantum numbers (l, m) to each of the frequencies derived from the data, without relying on the (unknown) details of the model properties of the star. To obtain a correct mode identification for each detected oscillation frequency is usually impossible. However, even only one correct (l, m) identification, *e.g.*, the one for the dominant mode, can imply a significant reduction of the free parameter space in the modelling, and is therefore worthwhile to attempt.

Empirical mode identification is a sophisticated and time-consuming task. It requires a detailed confrontation between oscillation theory applied to the outer stellar atmosphere and observational characteristics different from the frequencies, such as observed amplitudes and phases. All the methods we present in this chapter were developed for the identification of heat-driven nonradial modes whose lifetimes can be assumed infinite for their application. The reason is that it is relatively easy to establish a value for the large frequency separation of damped stochastically-excited oscillations and this usually suffices to start the process of forward modelling efficiently. Numerous examples of mode identification from pattern recognition of solar-like oscillation frequencies will be treated in Chapters 7, 8, and 9. The current chapter is thus restricted to mode identification of heat-driven modes. In what follows, we will speak of the *atmosphere* of the star as the regions with negative $\log \tau$, τ being the optical depth, while the parts where $\log \tau$ is positive will be termed the *stellar envelope*.

Essentially two types of diagnostics are in use to identify the modes. One of them is based on time series of multicolour photometry, and the other relies on time series of line-profile variations detectable from high-resolution spectroscopy. The introduction of high-resolution spectrographs with sensitive detectors in the 1980s, as outlined in Chapter 4, had a large impact on the field of empirical mode identification. Spectroscopic data indeed offer a very detailed picture of the pulsation velocity field, as will be outlined below. On the other hand, it requires moderate to large telescopes equipped with sophisticated instrumentation to be available for extended observing time spans. It remains a challenge to obtain spectra covering the overall beat period of the multiperiodic oscillation, with a high resolving power and with a high signal-to-noise ratio for a good temporal resolution, *i.e.*, for a ratio of the integration time to the oscillation periods below a few percent. The latter condition is necessary in order to avoid smearing out the oscillations during the cycle. Also, the methodology to derive the full details of the pulsational velocity field (at least six unknowns – see Sect. 5.2) is complicated. For this reason, multicolour photometric observations, which can only lead to an estimate l, but which can be obtained from small telescopes, are still of utmost importance for mode identification. These kinds of data are especially more suitable to study long-period pulsations because small telescopes are available on longer time scales. The most reliable results are obtained from the exploitation of simultaneous multicolour photometry and line-profile data.

One remark we wish to repeat here was already made in Chapter 4: seeking mode identification from observables implies the estimation of the discrete numbers (l, m). However, while doing so, one also must estimate real-valued unknowns, such as amplitudes and phases of observable quantities. This mixture of real and discrete unknowns cannot be treated simultaneously with standard statistical techniques to estimate (l, m). Therefore, any of the discriminating functions that will be defined below will be computed for each set of (l, m) separately, and its minimal value for the best choice of the continuous parameters will subsequently be compared among the (l, m) couples to decide about the most likely one.

In the following, we describe the methods for empirical mode identification. We divided the chapter according to the observational data available to apply them. This also corresponds to the historical progression in this field of research.

5.1 Mode identification from multicolour photometry

A pulsating star changes in temperature and in geometrical cross-section over its pulsation cycle, both of these contributing to variations in its bolometric luminosity. As we discussed in Chapter 4, photometric observations measure the intensity of the starlight reaching us – usually through various filters, and never bolometrically; no photometer can measure the entire electromagnetic spectrum! So in all observational cases we are measuring the starlight and its variations over some wavelength range. The wavelength dependence of the effect of the temperature variation on the light variability in a pulsating star can be easily seen in Fig. 5.1 which shows some schematic black-body curves for stars of different temperatures. Notice how much greater the intensity change is in the blue than it is in the red – just because of the shape of the black-body curves. That effect alone means that most pulsating stars will have larger photometric variations in the blue than in the red.

In addition to this basic effect, the light variations at different wavelengths depend on the geometry of the temperature variations – hence on the spherical harmonic of the pulsation mode – and on the change in geometrical cross-section, also dependent on the pulsation mode. Both the pulsation amplitude and phase as a function of wavelength are affected by the geometry of the temperature changes and the cross-section changes; thus observations of the pulsation amplitudes and phases in different photometric passbands can constrain mode identification. In the best cases the spherical degree l can be uniquely determined – an important step for asteroseismology.

The mode-identification method that uses photometric amplitudes and phases is based on the time variations of the stellar magnitude measured with different filters of a photometric system. One considers only the oscillation frequencies that are found in all the different filters for the mode identification; when the amplitude is too small in one or more filters of the system being used, then there is too little information for that mode. For reasons given above the amplitudes of a mode can be markedly different in the different filters. This is illustrated for two main-sequence stars in Fig. 5.2. As will be explained below, this amplitude difference depends on the kind of oscillation mode – more particularly on the degree l of the mode as illustrated in Fig. 5.3. Similarly, the difference in phase behaviour of the light curves in the different photometric bands is connected to the degree of the mode. This implies that, for a certain oscillation mode whose frequency is detected with sufficient signal-to-noise in all the filters of the photometric system, the comparison of the amplitude and phase values for the different filters allows one to derive the mode degree. This can be seen for the case of the amplitude ratios by comparing Figs 5.2 and 5.3.

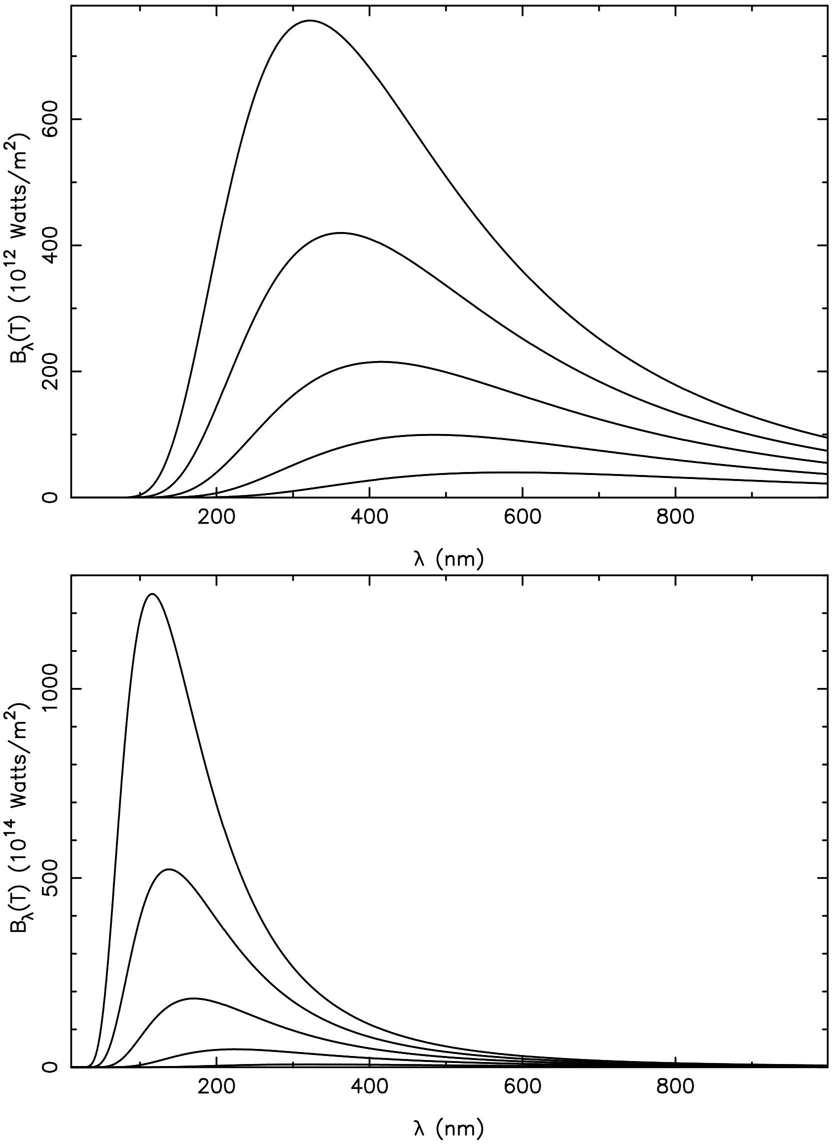

Figure 5.1: Black-body curves for stars of various temperatures. Top: temperatures range from 5000 K (lower line) to 9000 K (upper line) in steps of 1000 K; bottom: temperatures range from 9000 K (lower line) to 25000 K (upper line) in steps of 4000 K.

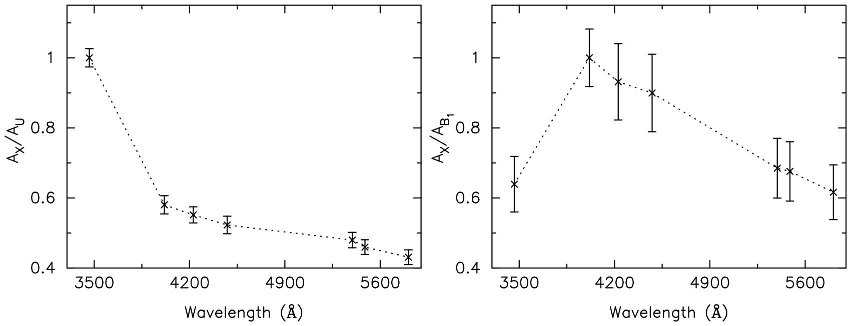

Figure 5.2: Observed amplitude ratios from long-term monitoring of the $l = 0$ mode of the B2 β Cep star HD 71913 (left, Aerts 2000) and for the $l = 1$ mode of the F2 γ Dor star HD12901 (right, Aerts *et al.* 2004) in the Geneva 7-band photometric system with filters X=UB_1B$B_2$$V_1$VG.

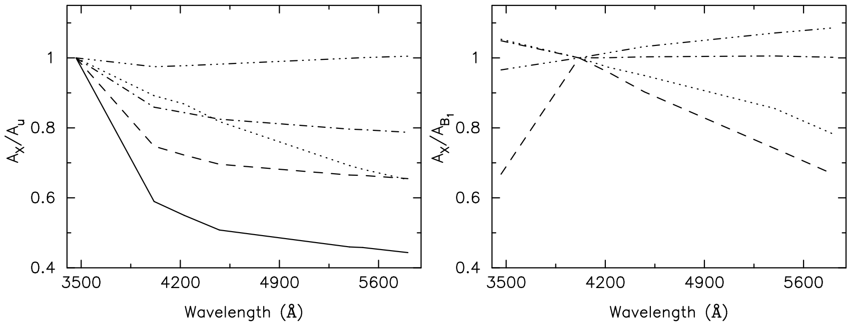

Figure 5.3: Theoretically predicted amplitude ratios for various degrees l of a typical B2 star for the dominant p-mode frequency of HD 71913 (left) and of a typical F2 star for the dominant g-mode frequency of HD 12901 (right). The computations were done in the adiabatic approximation and assumed $Z = 0.02$. The line style coding is as follows: full for $l = 0$ (not applicable in the right panel), dashed for $l = 1$, dashed-dot for $l = 2$, dotted for $l = 3$ and dashed-dot-dot-dot for $l = 4$. Comparison of these predictions with the observations shown in Fig. 5.2 allows the identification of the mode degree l. In the current examples we find $l = 0$ for HD 71913 and $l = 1$ for HD 12901.

5.1.1 General considerations

Different versions of the photometric mode-identification method are present in the literature. It was originally proposed by Watson (1981), relying on the work by Dziembowski (1977), Balona & Stobie (1979) and Buta & Smith (1979). A specific treatment for the case where temperature variations dominate the light variations was provided in Robinson *et al.* (1982), with an application to white dwarfs. Watson (1988) improved the Balona & Stobie (1979) method by bringing it into applicable form, while Garrido *et al.* (1990) and Heynderickx *et al.* (1994) included the perturbation of the limb darkening and, subsequently, of the surface normal, respectively, in a proper way. All these versions are based on adiabatic oscillation theory, and treat the non-adiabaticity of the oscillatory behaviour in the outer atmosphere by means of an ad-hoc parameter. For an extensive review of the methods in this approximation, we refer to Garrido (2000).

The theoretical expressions of the amplitude and phase of the light curve in the different filters (*i.e.*, as a function of wavelength) depend on, among other things, the geometrical configuration of the nodal lines with respect to the observer, *i.e.*, on the values of (l, m, i), where i is the inclination angle between the symmetry axis of the oscillation and the line-of-sight, as defined in Eq. (5.1) further on. The symmetry axis of the oscillation is usually taken to be the rotation axis, except for stars with a strong magnetic field, such as the rapidly oscillating Ap stars, where the magnetic axis is probably a more natural and better choice, and possibly for some close binaries where the pulsation axis could be the tidal axis. It was already realised by Watson (1988) that the functional dependence of the amplitude and phase on the mode geometry allows one to group the terms depending on m and i into one single factor which is independent of wavelength. One can thus make this factor disappear, and with it the very disturbing and unknown inclination angle, by considering amplitude ratios and phase differences among the different filters. This is the procedure that is usually adopted. The disadvantage is that one loses the information on the m-value and one can thus only identify the degree l of the mode.

A big step forward was achieved by the new versions of the method developed by Cugier *et al.* (1994) and Cugier & Daszyńska (2001) for β Cep stars, by Brassard *et al.* (1995) for ZZ Ceti stars, by Balona & Evers (1999) for δ Sct stars, by Townsend (2002) for slowly pulsating B stars, and by Dupret *et al.* (2003) for all main-sequence oscillators. In these works, a non-adiabatic treatment of the oscillations was included, with different levels of sophistication, through which the unknown ad-hoc factor was eliminated. Dupret *et al.* (2003) included for the first time a detailed non-adiabatic treatment of the oscillations in the optically-thin atmosphere of main-sequence stars. They illustrated the applicability of their method to β Cep stars, slowly pulsating B stars, δ Sct stars, and γ Dor stars. A non-adiabatic treatment similar to the one by Dupret *et al.* (2003) was presented by Randall *et al.* (2005) in the context of pulsating subdwarf B stars. It does not contain an equally detailed treatment of the oscillations in the outer atmosphere, however.

In order to achieve identification of l, the theoretical expressions for amplitude ratios and phase differences must be computed, and this requires the computation of the perturbed version of the adopted limb darkening and of the perturbed stellar flux as a function of the effective temperature and the gravity, which are also affected by the oscillations. This brings us to the need for good atmosphere models and an appropriate limb-darkening description. In particular, it turns out that this identification method is rather sensitive to the adopted treatment of convection when constructing the atmosphere models for stars with outer convection zones, such as δ Sct and γ Dor stars (Garrido 2000; Dupret *et al.* 2005). This treatment of convection is not a problem in the application of the method to stars with a radiative envelope, but here, the results of the identification turn out to depend on the adopted metallicity (Dupret *et al.* 2003). These two dependencies must always be kept in mind when making conclusions about the l-value.

The theoretical amplitude ratios and phase differences are dependent on the stellar flux, which is determined by the metallicity, the effective temperature, and the mass and radius, or, equivalently the gravity, of the star. These parameters are often not known with high precision. Their uncertainties must be propagated into the final selection of the best value for l from the observed amplitude ratios. This was often ignored in the past, but is accounted for in modern applications of this method, following Balona & Evers (1999). Examples of such applications were provided by Handler *et al.* (2003, 2005, 2006), De Ridder *et al.* (2004) and Shobbrook *et al.* (2006) for β Cep stars, by De Cat *et al.* (2005, 2007) for slowly pulsating B stars, by Dupret *et al.* (2005a,b) for δ Sct and γ Dor stars, and, finally, by Jeffery *et al.* (2004, 2005) and Tremblay *et al.* (2006) for subdwarf B stars. We refer the reader to these papers for more detailed information.

5.1.2 Detailed description

In the following, we provide a detailed mathematical description of the photometric mode-identification method. In doing so, we use two reference frames: a first one with Cartesian coordinates (x, y, z) and spherical coordinates (r, θ, ϕ) such that the unit vector $\vec{a_z}$ coincides with the symmetry (*i.e.*, polar) axis of the star and the origin at the stellar centre; and a second one with Cartesian coordinates (x', y', z') and spherical coordinates (r', θ', ϕ'), also with origin at the centre of the star but with $\vec{a_{z'}}$ pointing towards the observer. As origin for the angular coordinates ϕ and ϕ', we take the meridian passing through the $\vec{a_z}$ and $\vec{a_{z'}}$ axes. We define the *inclination angle* of the star as the angle between $\vec{a_z}$ and $\vec{a_{z'}}$ such that

$$\vec{a_{z'}} = -\sin i\ \vec{a_x} + \cos i\ \vec{a_z} \tag{5.1}$$

and we adopt the usual definitions of μ and μ':

$$\begin{aligned} \mu &= \cos\theta = \vec{a_r} \cdot \vec{a_z}, & (5.2) \\ \mu' &= \cos\theta = \vec{a_{r'}} \cdot \vec{a_{z'}}. & (5.3) \end{aligned}$$

Treatment of the atmosphere

The equations valid in the interior of the star, as described in Chapter 3, are no longer valid in the outer stellar atmosphere. First of all, the diffusion approximation, which connects the radiative flux to the temperature gradient, does not hold when the density is very low, *i.e.,* when the mean free path of the photons becomes a considerable fraction of the remaining distance to the surface. Secondly, the approximation that the radiation field is isotropic is no longer appropriate, implying that the momentum equation must be modified. The approximations made in Chapter 3 are fine for the computation of the oscillation frequencies, which are determined by the interior structure of the star, as well as for the instability computations, but they are not sufficient for the description of the photometric amplitudes and line-profile variations. In the following, we adopt the approach outlined in detail in Dupret (2002) and summarised in Dupret *et al.* (2003).

It is assumed that the local atmosphere characterised by the coordinates θ and ϕ remains in radiative equilibrium during the oscillation. This approximation is valid because the heat capacity in the atmosphere is very low, such that its thermal relaxation time is far shorter than any of the relevant oscillation periods. In that case, a plane-parallel atmosphere in hydrostatic equilibrium is fully described by its effective temperature $T_{\rm eff}$, its gravity g and its chemical composition. For a given chemical composition, we write the temperature of the local atmosphere as

$$T = T(\tau, T_{\rm eff}, g), \tag{5.4}$$

with τ the Rosseland mean optical depth, and we assume that this temperature law does not change during the oscillation cycle. Hence, the temperature of the local atmosphere at position (τ, θ, ϕ) varies according to

$$\begin{aligned} T(\tau, \theta, \phi) &= T_0 + \delta T(\theta, \phi) \\ &= T(\tau_0 + \delta\tau(\theta, \phi), T_{\rm eff,0} + \delta T_{\rm eff}(\theta, \phi), g_0 + \delta g_{\rm e}(\theta, \phi)), \end{aligned} \tag{5.5}$$

where $\delta g_{\rm e}$ is the Lagrangian perturbation of the gravity corrected for the pulsational acceleration. In the linear approximation, Eq. (5.5) can be written as

$$\frac{\delta T}{T_0} = \frac{\partial \ln T}{\partial \ln T_{\rm eff}} \frac{\delta T_{\rm eff}}{T_{\rm eff,0}} + \frac{\partial \ln T}{\partial \ln g_{\rm e}} \frac{\delta g_{\rm e}}{g_0} + \frac{\partial \ln T}{\partial \ln \tau} \frac{\delta \tau}{\tau_0}. \tag{5.6}$$

From the definition of the Rosseland mean optical depth we find

$$\frac{\partial \delta\tau}{\partial \tau_0} = \frac{\delta\kappa}{\kappa_0} + \frac{\delta\rho}{\rho_0} + \frac{\partial \xi_r}{\partial r}. \tag{5.7}$$

As in Eqs (**??**), (**??**), *etc.* the Lagrangian perturbations again contain a common factor $\sqrt{4\pi} Y_l^m(\theta, \phi) \exp{(-{\rm i}\omega t)}$. Elimination of $\delta\tau$ between Eqs (5.6) and (5.7), and division by this common factor leads to

$$\begin{aligned} \frac{\partial(\delta\tilde{T}/T_0)}{\partial \ln \tau_0} &= \frac{\partial \ln T}{\partial \ln \tau} \left(\frac{\delta\tilde{\kappa}}{\kappa_0} + \frac{\delta\tilde{\rho}}{\rho_0} + \frac{\partial \tilde{\xi}_r}{\partial r} \right) \\ &- \left(1 - \frac{\partial^2 \ln T / \partial \ln \tau^2}{\partial \ln T / \partial \ln \tau} \right) \left(\frac{\delta\tilde{T}}{T_0} - \frac{\partial \ln T}{\partial \ln T_{\rm eff}} \frac{\delta\tilde{T}_{\rm eff}}{T_{\rm eff,0}} - \frac{\partial \ln T}{\partial \ln g_{\rm e}} \frac{\partial \tilde{g}_{\rm e}}{g_0} \right) \\ &+ \frac{\partial^2 \ln T}{\partial \ln \tau \, \partial \ln T_{\rm eff}} \frac{\delta\tilde{T}_{\rm eff}}{T_{\rm eff,0}} + \frac{\partial^2 \ln T}{\partial \ln \tau \, \partial \ln g_{\rm e}} \frac{\delta\tilde{g}_{\rm e}}{\tilde{g}_0}. \end{aligned} \tag{5.8}$$

This equation, rather than Eq. (**??**) is used as energy equation in the atmosphere. The derivatives in Eq. (5.9) must be estimated numerically from a set of atmosphere models with effective temperatures and gravities surrounding those of the star.

While the temperature variation in the atmosphere can be computed locally, as just explained, the variation of the density, pressure and Lagrangian displacement must come from the solution of the mass and momentum equation considering the entire outer atmosphere. In general, the momentum equation contains a pressure gradient with a contribution from the gas pressure and one from the radiation pressure. The latter implies a radiative acceleration vector, which is, in the case of continuum radiation, given by $\vec{g}_{\rm rad} = \kappa_{\rm F}\vec{F}/c$ with $\kappa_{\rm F}$ the flux weighted mean opacity (*e.g.*, Lamers & Cassinelli 2001). It is in general safe to ignore the line radiation, except for the hottest main-sequence stars ($T_{\rm eff} > 25\,000\,{\rm K}$) and for supergiants ($\log g < 3.0$), which suffer from a line-driven stellar wind (*e.g.*, Kudritzki & Puls 2000). In that case, one is dealing with a dynamical atmosphere and the treatment we present here is not strictly valid (but a better approximation is not available).

While solving the continuity and momentum equations one assumes that $\delta|\vec{F}|$ remains constant from the base of the atmosphere to the outermost layer, that $\vec{F}$ remains parallel to the temperature gradient during the oscillation cycle and that the relative variation of $\kappa_{\rm F}$ equals the relative variation of the Rosseland opacity: $\delta\kappa_{\rm F}/\kappa_{\rm F} \simeq \delta\kappa/\kappa$. The first two assumptions are again related to the short thermal relaxation time in the very thin outer layer, which allows the plane-parallel approximation. The validity of the third assumption was checked numerically by Dupret (2002). The first assumption implies, through Stefan's law, that

$$\frac{\delta|\vec{F}|}{\vec{F}_0} = \frac{\delta F_r}{F_{r,0}} = 4\frac{\delta T_{\rm eff}}{T_{\rm eff,0}} \tag{5.9}$$

and leads to the radial component of $\delta\vec{g}_{\rm rad}$:

$$(\delta\vec{g}_{\rm rad})_r = g_{\rm rad}\left(\frac{\delta\kappa}{\kappa_0} + 4\frac{\delta T_{\rm eff}}{T_{\rm eff,0}}\right), \tag{5.10}$$

where $g_{\rm rad}$ is the equilibrium value of the radial component of $\vec{g}_{\rm rad}$. This leads to the following expression for the radial component of the equation of motion:

$$\begin{aligned} \omega^2\tilde{\xi}_r &= \frac{\partial(\delta\tilde{p}_{\rm g}/\tilde{p}_{\rm g})}{\partial r}\frac{p_{\rm g,0}}{\rho_0} \\ &+ \frac{\partial\tilde{\Phi}'}{\partial r} + \frac{\partial(g_0\tilde{\xi}_r)}{\partial r} + \left(\frac{\delta\tilde{\rho}}{\rho_0} - \frac{\delta\tilde{p}_{\rm g}}{p_{\rm g,0}}\right)(g_0 - g_{\rm rad}) \\ &- g_{\rm rad}\left(\frac{\delta\tilde{\kappa}}{\kappa_0} + 4\frac{\delta\tilde{T}_{\rm eff}}{T_{\rm eff,0}} + \frac{\partial\tilde{\xi}_r}{\partial r}\right). \end{aligned} \tag{5.11}$$

This equation is used in the atmosphere, instead of Eq. (**??**). The horizontal component of the momentum equation becomes, through the assumption that $\vec{F}$ remains parallel to the temperature gradient:

$$\omega^2\tilde{\xi}_{\rm h} = \frac{1}{r}\left(\frac{\delta\tilde{p}_{\rm g}}{\rho_0} + \tilde{\Phi}' + g_0\tilde{\xi}_r - g_{\rm rad}\frac{\delta\tilde{T}}{\partial T/\partial r}\right). \tag{5.12}$$

This equation replaces Eq. (**??**). And, finally, the continuity equation Eq. (**??**) is replaced by its version valid in the outer atmosphere:

$$\omega^2\left[\frac{\delta\tilde{\rho}}{\rho_0} + \frac{1}{r^2}\frac{\partial}{\partial r}\left(r^2\tilde{\xi}_r\right)\right] = \frac{l(l+1)}{r^2}\left(\frac{\delta\tilde{p}_{\rm g}}{\rho_0} + \tilde{\Phi}' + g_0\tilde{\xi}_r - \frac{g_{\rm rad}\delta\tilde{T}}{\partial T/\partial r}\right). \tag{5.13}$$

Following Dupret *et al.* (2002), appropriate boundary conditions are imposed at the outermost layer of the star. This requires a little more attention than the discussion in Chapter 3. Contrary to several other versions of the method, it is preferable to choose a mechanical boundary condition that is valid for application to all stars, *i.e.*, for the case where both the gas and radiation-pressure accelerations may be significant. Therefore, Dupret *et al.* (2002) considered as boundary condition the version of Eq. (5.11) in which the contribution of the gas pressure at the surface is ignored, but not the radiation pressure, thus deleting the first term of the right-hand side of Eq. (5.11). As boundary condition for the gravitational potential, we impose, as usual, continuity of $\tilde{\Phi}'$ and its first derivative between the inner solution given by the Poisson equation and the outer solution given by the Laplace equation:

$$\frac{\partial\tilde{\Phi}'}{\partial r}+\frac{l+1}{r}\tilde{\Phi}'=-4\pi G\rho_0\tilde{\xi}_r. \tag{5.14}$$

As boundary condition for the energy equation, Eq. (5.9), Eq. (5.6) is evaluated in the outermost layer by computing $\lim_{\tau\rightarrow 0}\delta\tau/\tau$ from Eq. (5.7), resulting in

$$\frac{\delta\tilde{T}}{T_0}=\frac{\partial\ln T}{\partial\ln T_{\rm eff}}\frac{\delta\tilde{T}_{\rm eff}}{T_{\rm eff,0}}+\frac{\partial\ln T}{\partial\ln g_{\rm e}}\frac{\delta\tilde{g}_{\rm e}}{g_0}+\frac{\partial\ln T}{\partial\ln\tau}\left(\frac{\delta\tilde{\kappa}}{\kappa_0}+\frac{\delta\tilde{\rho}}{\rho_0}+\frac{\partial\tilde{\xi}_r}{\partial r}\right) \tag{5.15}$$

(Dupret 2002).

In order to solve for the unknown quantities $\tilde{\xi}_r, \tilde{\xi}_{\rm h}, \tilde{T}, \ldots$, we must require continuity of these variables at a so-called connecting layer, bridging the stellar interior and the outer atmosphere. As explained in Dupret (2002) and for the reasons outlined below, this connecting layer must be chosen carefully, *i.e.*, at a position where the flux is predominantly radiative. In this case, Dupret (2002) derived the following matching conditions for the connecting layer:

$$3\frac{\delta\tilde{T}}{T_0}-\frac{\delta\tilde{\kappa}}{\kappa_0}-\frac{\delta\tilde{\rho}}{\rho_0}+\frac{{\rm d}\delta T/{\rm d}r}{{\rm d}T/{\rm d}r}-\frac{{\rm d}\tilde{\xi}_r}{{\rm d}r}=4\frac{\delta\tilde{T}_{\rm eff}}{T_{\rm eff,0}} \tag{5.16}$$

and

$$\frac{\delta\tilde{g}_{\rm e}}{g_0}=\frac{\partial\tilde{\Phi}'/\partial r}{g_0}+\frac{4\pi\rho_0 r^3}{m}\frac{\tilde{\xi}_r}{r}-\left(2+\frac{\omega^2 r}{g_0}\right)\frac{\tilde{\xi}_r}{r} \tag{5.17}$$

which reduces to the simpler condition

$$\frac{\delta\tilde{g}_{\rm e}}{g_0}=-\left(2+\frac{\omega^2 r}{g_0}\right)\frac{\tilde{\xi}_r}{r} \tag{5.18}$$

in the Cowling approximation, if one ignores the surface density divided by the mean density of the star. By means of Eqs (5.16) and (5.17), Dupret (2002) showed that the continuity of the derivatives of $\tilde{\xi}_r/R$ and $\delta\tilde{p}_{\rm g}/p_{\rm g,0}$ is guaranteed. Following Dupret *et al.* (2002), the continuity of $\delta\tilde{T}/T_0$ should be checked *a posteriori*. These authors achieved this condition by placing the connecting layer at $\log\tau=1$ for main-sequence B stars and at $\log\tau=0$ for δ Sct stars, confirming the validity of their treatment.

The theory presented here is more sophisticated than what is often used in the literature, where the Eddington approximation with temperature distribution

$$T^4(r)=\frac{3}{4}T_{\rm eff}^4\left(\tau+\frac{2}{3}\right) \tag{5.19}$$

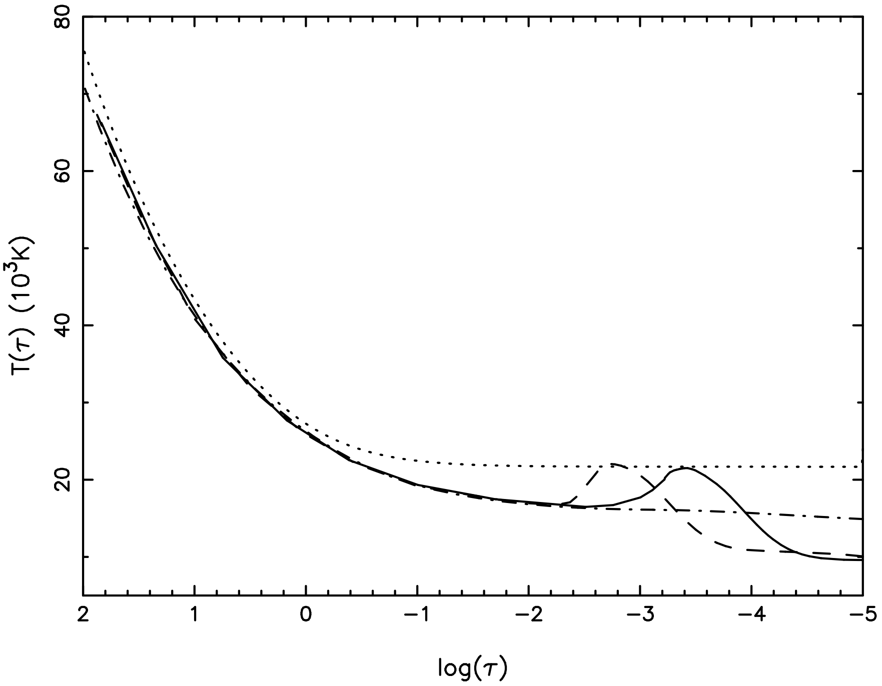

Figure 5.4: Temperature distributions in the envelope and outer atmosphere of a hot star with $T_{\rm eff} = 24\,000\,{\rm K}$ and $\log g = 4.5$ for different approximations. Dotted line: grey atmosphere as in Eq. (5.19), dot-dashed line: NLTE plane-parallel line-blanketed static atmosphere model without wind (Lanz & Hubeny 2006), full/dashed line: NLTE spherical unified atmosphere model with weak/strong wind (Lefever *et al.* 2006).

is regularly adopted for the stellar atmosphere rather than the general form given by Eq. (5.4) for a non-grey atmosphere. The advantage of the treatment presented above is mainly important for hot stars as it includes the radiative acceleration due to continuum radiation. The current treatment also allows one to use any type of equilibrium atmosphere model, as long as it is static, *i.e.*, whenever the acceleration due to line-driving can be ignored. When the atmosphere is perturbed due to the oscillations, it is, in fact, no longer strictly static. Dupret *et al.* (2002) checked for the difference between the perturbed atmosphere due to an oscillation and the static one in the LTE approximation with corresponding temperature and gravity, and found relative differences less than 20% in the quantities, depending on the order of the oscillation mode. This slight inconsistency is negligible compared with the gain of using much better equilibrium atmosphere models.

We compare in Fig. 5.4 the temperature structure of an Eddington atmosphere with state-of-the-art NLTE line-blanketed atmosphere models with and without a line-driven wind, for a star with $T_{\rm eff} = 24\,000\,{\rm K}$ and $\log g = 4.5$. It can be seen that significant deviations from the Eddington model are encountered for the atmosphere region where $\log\tau < 0$, even for the static plane-parallel non-grey atmosphere without mass loss (dashed-dot line). This discrepancy in $T(\tau)$ for $\log\tau < 0$ is a general property for all effective temperatures of relevance for mode identification. The Eddington approximation is thus only appropriate for the connecting layer, provided that it can be positioned in the regime of $\log\tau > 0$. We therefore advise that any user of the methodology checks for the validity of the Eddington approximation for the connecting layer and for the outer atmosphere. In any case, when computing the amplitude ratios and phase differences it can easily be replaced by the treatment provided here, based on a non-grey static plane-parallel atmosphere model.

Coming back to Fig. 5.4, the discrepancy between the grey atmosphere and more realistic models is particularly significant for hot stars and supergiants. One can see from Fig. 5.4 that even a state-of-the-art NLTE plane-parallel model (Lanz & Hubeny 2006) does not give a good description of the temperature distribution in the atmosphere where a temperature bump occurs near $\log\tau < -2$ in the case of a unified spherical NLTE line-blanketed atmosphere with a line-driven wind. This bump is generally understood in terms of line-heating (*e.g.,* Mihalas 1978) but its exact position and height depend on the presence of particular ions in the wind (see, *e.g.,* Pauldrach *et al.* 2001; Puls *et al.* 2005 for discussions of this effect). As can be derived from Fig. 5.4, the current treatment of the outer atmosphere in mode identification should be improved by also considering the line acceleration in the dynamical atmospheres of OB-type stars and supergiants, but this has not yet been done to our knowledge.

Finally, we come back to the prerequisite that the connecting layer must be situated in a part of the atmosphere where the flux is predominantly radiative. The reason is that the assumptions made about the link between the temperature structure and the flux are no longer valid when the convective flux dominates. It is therefore important to position the connecting layer in the very outer part of the envelope for stars with envelope convection zones, such as δ Sct and γ Dor stars along the main sequences and any type of evolved pulsator.

Non-adiabatic observables

In what follows, we adopt the single-layer approximation as has always been done so far in photometric mode identification. This means we assume there to be a single stellar photosphere, whose distance to the stellar centre is characterised by the stellar radius R and whose temperature equals the effective temperature of the star. Moreover, it is assumed that the outward flux does not depend on the optical depth in the atmosphere. The deformation of the photosphere is thus derived from the evaluation of the displacement vector $\vec{\xi}$ at $r = R$ in the linear approximation.

We seek to determine the monochromatic amount of energy radiated by the star as measured by a distant observer: $E(\lambda, t)$. In doing so, we again recall the short thermal relaxation time of the atmosphere which has led us to assume that, at each moment in the oscillation cycle, the atmosphere remains in radiative equilibrium and the temperature distribution in the atmosphere $T(\tau)$ remains the same as in the equilibrium model. We also use the same argument now to keep a fixed prescription for the monochromatic outgoing flux of the local atmosphere $\vec{F}_\lambda^+$ and limb-darkening law $h_\lambda(\theta)$ during the oscillation cycle. Moreover, we assume that the local atmosphere's chemical composition stays constant and that $\vec{F}_\lambda^+$ remains perpendicular to the local photosphere. Under these assumptions, the monochromatic flux variation in the local atmosphere is given by

$$F_{\lambda,0}^+ + \delta F_\lambda^+(\theta,\phi,t) = F_\lambda^+\left[T_{\rm eff,0} + \delta T_{\rm eff}(\theta,\phi,t), g_0 + \delta g_{\rm e}(\theta,\phi,t)\right], \tag{5.20}$$

where we have introduced the notation $F_\lambda^+ = |\vec{F_\lambda^+}|$. In the linear approximation, this can be written as

$$\begin{aligned}
\frac{\delta\tilde{F}_\lambda^+}{F_{\lambda,0}^+} &= \left(\frac{\partial\ln F_\lambda^+}{\partial\ln T_{\rm eff}}\right)\frac{\delta\tilde{T}_{\rm eff}}{T_{\rm eff,0}} + \left(\frac{\partial\ln F_\lambda^+}{\partial\ln g_{\rm e}}\right)\frac{\delta\tilde{g}_{\rm e}}{g_0} && (5.21)\\
&\equiv \alpha_{T,\lambda}\frac{\delta\tilde{T}_{\rm eff}}{T_{\rm eff,0}} + \alpha_{g,\lambda}\frac{\delta\tilde{g}_{\rm e}}{g_0}. && (5.22)
\end{aligned}$$

Similarly, the variation of the limb-darkening law $h_\lambda(\theta)$ in the linear approximation is written as

$$\frac{\delta_r\tilde{h}_\lambda}{h_{\lambda,0}} = \left(\frac{\partial\ln h_\lambda}{\partial\ln T_{\rm eff}}\right)\frac{\delta\tilde{T}_{\rm eff}}{T_{\rm eff,0}} + \left(\frac{\partial\ln h_\lambda}{\partial\ln g_{\rm e}}\right)\frac{\delta\tilde{g}_{\rm e}}{g_0} + \left(\frac{\partial\ln h_\lambda}{\partial\mu'}\right)\delta_r\left(\vec{n}\cdot\vec{a_{z'}}\right), \tag{5.23}$$

where $\vec{n}$ is the normal to the stellar photosphere and δ_r stands for the *radial Lagrangian perturbation* defined by

$$\delta_r X = \delta X \tag{5.24}$$

for a scalar quantity X, and

$$\delta_r\vec{Y} = \vec{Y}' + \frac{{\rm d}Y_r}{{\rm d}r}\xi_r\vec{a_r} \tag{5.25}$$

for a vector quantity $\vec{Y}$. With Eq. (5.23) we thus assume $\delta_r\theta = \delta_r\phi = 0$. It is noteworthy that Heynderickx *et al.* (1994) and De Ridder *et al.* (2002) did not make this approximation and considered the more general classical Lagrangian perturbation in their description. It was, however, shown explicitly by Dupret (2002) and by Townsend (2003) that these treatments are mathematically equivalent in the linear approximation for the perturbations. Hence, we limit ourselves to the simpler treatment here, which comes down to the approximation that the geometrical distortion is not affected by the horizontal components of the displacement field.

As we have shown in Eq. (5.18), $\delta g_{\rm e}/g_0$ is to a very good approximation in antiphase with the radial displacement. The phase of $\delta T_{\rm eff}/T_{\rm eff,0}$ can in principle take any value, depending on the kind of oscillation mode and on the stellar model. Therefore, it is customary to introduce the coefficients f_T, ψ_T and f_g defined as

$$\frac{\delta\tilde{T}_{\rm eff}}{T_{\rm eff,0}}(R,\theta,\phi) = f_T\frac{\tilde{\xi}_r(R)}{R}\exp\left(-{\rm i}\psi_T\right) \tag{5.26}$$

and

$$\frac{\delta\tilde{g}_{\rm e}}{g_0}(R,\theta,\phi) = -f_g\frac{\tilde{\xi}_r(R)}{R}. \tag{5.27}$$

We recall that these amplitude functions are the true amplitudes divided by the common factor

$$\sqrt{4\pi}Y_l^m(\theta,\phi)\exp\left(-{\rm i}\omega t\right).$$

The coefficients f_T, ψ_T and f_g are termed *non-adiabatic observables*; in particular, the coefficient ψ_T is called the *phase lag*. They follow directly from the integration of the basic equations in the stellar interior and in the atmosphere through the connecting layer, with the treatment of the atmosphere as discussed above. In models with an outer convection zone, their values depend on the treatment of convection, including the choice of mixing-length parameter and the possible inclusion of modelling of the coupling between

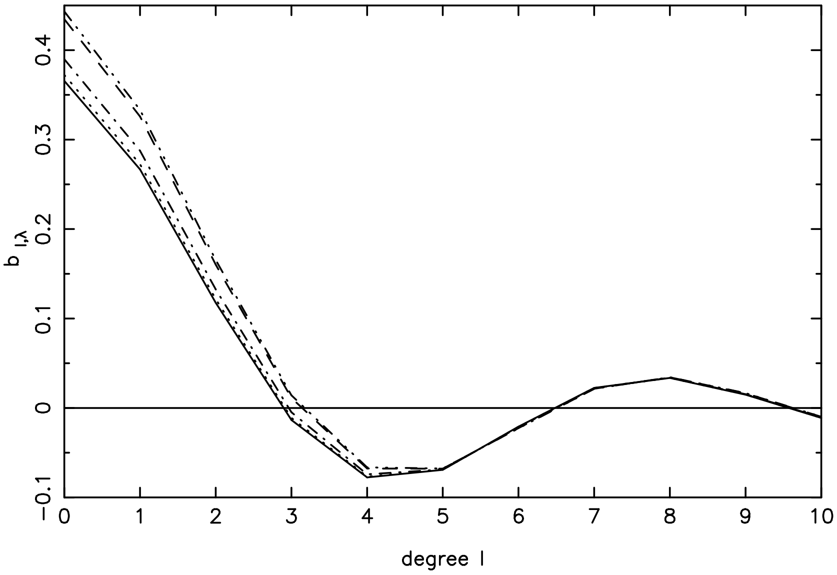

Figure 5.5: The integral $b_{l,\lambda}$ defined in Eq. (5.30) is shown for different mode degrees l for a linear limb-darkening law taken from Claret (2000). The lower three curves are for a star of $T_{\rm eff} = 6000$ K and $\log g = 4.0$ at the wavelengts of the U (full line), B (dotted line) and V (dashed-dot line) filters. The two upper curves are for a star of $T_{\rm eff} = 25000$ K and $\log g = 4.0$ at U and B (indistinguishable, shown as dashed line) and V (dashed-dot-dot-dot line) wavelengths.

convection and pulsations; thus, inferring them observationally provides a possibly diagnostic of the physics of convection in the outer layers (*cf.* Sect. 5.1.3).

For the equilibrium model, we have

$$E(\lambda) = \frac{R^2}{2\pi d^2} \int_0^1 \int_0^{2\pi} F_\lambda^+ h_\lambda(\mu')\mu' {\rm d}\mu' {\rm d}\phi', \tag{5.28}$$

with d the distance to the observer, so we must determine $\delta E(\lambda, t)$. We omit this long derivation here, as it is readily available in several papers in the literature, such as Cugier & Daszyńska (2001), Dupret (2002), Townsend (2002), Dupret *et al.* (2003), Daszyńska-Daszkiewicz *et al.* (2003), and Randall *et al.* (2005). The outcome, written in terms of the observed variation of the monochromatic visual magnitude at wavelength λ, can be written as

$$\begin{aligned} \delta m_\lambda &= -\frac{2.5}{\ln 10}\sqrt{4\pi}\,\frac{\xi_r(R)}{R}\,P_l^m(\cos i) b_{l,\lambda}\left[-(l-1)(l-2)\cos(\omega t)\right. \\ &+ \left. f_T \cos(\psi_T + \omega t)(\alpha_{T,\lambda} + \beta_{T,\lambda}) - f_g \cos(\omega t)(\alpha_{g,\lambda} + \beta_{g,\lambda})\right], \end{aligned} \tag{5.29}$$

with

$$b_{l,\lambda} = \int_0^1 \mu'\, h_\lambda(\mu')\, P_l {\rm d}\mu',\ \beta_{T,\lambda} = \frac{\partial \ln b_{l,\lambda}}{\partial \ln T_{\rm eff}},\ \beta_{g,\lambda} = \frac{\partial \ln b_{l,\lambda}}{\partial \ln g}. \tag{5.30}$$

The terms proportional to $(l-1)(l-2)$, f_T and f_g correspond to the variation of the surface, of the local effective temperature and of the gravity, respectively. We show the value of the integral $b_{l,\lambda}$ for different

l in Fig. 5.5, for two different types of stars and for the wavelengths of the U, B, V filters. It can be seen that there is a steep decrease in value as l increases from 0 to 3, and fluctuating values converging to zero as l raises above 9. While Eq. (5.29) makes it clear that the computation of the decrease in the observed amplitude of the brightness variations as a function of l is far more complex than simply considering $b_{l,\lambda}$, this dependence of $b_{l,\lambda}$ on l forms the basis of the so-called *partial cancellation effect*. We can see from Fig. 5.5 that $b_{l,\lambda}$ is a factor ~ 4 smaller for $l = 2$ than for $l = 0$. The factor is even larger for $l = 5, 6$, while $b_{3,\lambda} \approx 0$. This is the reason why one often assumes $l \leq 2$ in the modelling of the photometrically detected oscillation frequencies.

Another point of attention in Eq. (5.29) is the factor $P_l^m(\cos i)$. For each (l, m), there exists at least one inclination angle for which $P_l^m(\cos i) = 0$. Such angles are termed *Inclination Angles of Complete Cancellation*, abbreviated as IACC. You can easily compute them!

Observations usually do not provide us with the monochromatic magnitude, but rather magnitudes for particular filters j with transmission curves $w_j(\lambda)$ and a wavelength range from $\lambda_{j,\mathrm{blue}}$ to $\lambda_{j,\mathrm{red}}$. One thus computes

$$\delta m_j = \frac{\displaystyle\int_{\lambda_{j,\mathrm{blue}}}^{\lambda_{j,\mathrm{red}}} \delta m_\lambda \, w_j(\lambda) \, \mathrm{d}\lambda}{\displaystyle\int_{\lambda_{j,\mathrm{blue}}}^{\lambda_{j,\mathrm{red}}} w_j(\lambda) \mathrm{d}\lambda} \tag{5.31}$$

for comparisons with observations. It is readily seen from Eq. (5.29) that one eliminates the common factor $-(2.5/\ln 10)\sqrt{4\pi}(\xi_r(R)/R)P_l^m(\cos i)$, which is independent of wavelength, by considering amplitude ratios for different photometric bands. With it, the dependence on the inclination angle and on the position of the nodal lines on the stellar surface (by means of m) disappears. This is an asset of the method, because the inclination angle is often not, or only very poorly, known, but it is also a disadvantage as it cannot deliver an estimate of m.

Finally, we wish to emphasize that, in the early development phase of this method, some less accurate approximations have been proposed for the computation of f_T, f_g and δp_{g}. These were mainly based on adiabatic approximations or an ad-hoc generalization thereof, and/or the assumption that the Lagrangian perturbation of the local temperature equals that of the effective temperature. These assumptions are not appropriate for the outer stellar atmosphere. We advise against usage of the treatments published before 2000. Cugier & Daszyńska (2001) first came up with an improved computation of f_g in terms of the dimensionless frequency of a mode:

$$f_g \simeq 2 + \sigma^2 = 2 + \frac{\omega^2 R^3}{GM}. \tag{5.32}$$

This result is equivalent to the one we encountered in Eq. (5.18), which was a special case of the more general Eq. (5.17) in the Cowling approximation and ignoring the surface density divided by the mean density of the star in the outer atmosphere.

We point out that the inverse of σ^2, *i.e.*, the ratio between the horizontal and radial components of the displacement evaluated at the stellar surface, is termed *the K-value* of the mode by observers. They introduced this concept of K while interpreting data of stellar oscillations. One thus encounters both terms in the literature these days, depending on the background of the authors.

5.1.3 Mode identification schemes

Even though the oscillations always behave highly non-adiabatically in the outer atmosphere, some stars have ψ_T-values close to the adiabatic values. This is, for example, the case for main-sequence B stars and is understood in terms of their excitation by the heat mechanism acting on an opacity feature resulting from iron-like elements, near a temperature of $\log T \simeq 5.3$. This is rather deep in the star where the quasi-adiabatic approximation is still quite good. Therefore, the phase difference between the variation of the luminosity and the radial displacement amounts to almost the adiabatic value, *i.e.*, $180°$ for the p modes in β Cep stars and $0°$ for the high-order g modes in SPB stars. In such cases, it is customary to exploit only the amplitudes in the different photometric bands, and not the phase differences, when identifying the degree of the modes. The same holds true for the pulsating sdB stars. Other pulsators, such as δ Sct stars and all other pulsators in the classical instability strip, are predominantly driven by the partial ionization zone of once ionized helium. This layer is positioned near $\log T \simeq 4.6$, *i.e.*, much further out where the non-adiabatic effects are stronger. Non-adiabatic theoretical computations indeed predict large phase differences in the magnitude variations for different filters for such stars. This is confirmed by the observations. In that case, it is advantageous to exploit also these phase differences in identifying l, besides the amplitude ratios. We treat these two situations below.

Mode identification schemes using only amplitudes

When using only the amplitudes, the following scheme is advised, after Dupret *et al.* (2003):

1. Compute stellar models with appropriate effective temperatures and gravities. One must make sure to cover the observational error box in $(T_{\rm eff}, \log g)$ with models for a safe propagation of the uncertainty of these fundamental parameters on the mode identification. As $T_{\rm eff}$ and $\log g$ follow readily from an interpretation of the stellar spectrum, it is best to use these as constraints to construct the models. Observational values for the luminosity (or the absolute magnitude) require additional information, such as the distance which is often poorly known, or rely on calibrations which can suffer from unknown systematic uncertainties.

2. Perform non-adiabatic computations to derive f_T, ψ_T, f_g for modes with frequencies close to the observed ones, for different degree l, for all the models that pass through the observational error box computed in 1. Usually, one restricts the search to $l = 0, \ldots, 4$ by arguments of observational cancellation for higher degree modes.

3. For each filter j and for each degree l, compute the theoretical amplitude while omitting the common factor $-(2.5/\ln 10)\sqrt{4\pi}(\xi_r(R)/R)P_l^m(\cos i)$, *i.e.*, compute the amplitude factor:

$$A_{j,\rm th} = \frac{\displaystyle\int_{\lambda_{\rm blue}}^{\lambda_{\rm red}} |b_{l,\lambda}|\, |T_1 + T_2 + T_3|\, w_j(\lambda) {\rm d}\lambda}{\displaystyle\int_{\lambda_{\rm blue}}^{\lambda_{\rm red}} w_j(\lambda) {\rm d}\lambda}, \tag{5.33}$$

with

$$
\begin{aligned}
T_1 &\equiv (1-l)(l+2). && (5.34)\\
T_2 &\equiv f_T\ \exp(-\mathrm{i}\psi_T)\ (\alpha_{T,\lambda}+\beta_{T,\lambda}), && (5.35)\\
T_3 &\equiv -f_g\ (\alpha_{g,\lambda}+\beta_{g,\lambda}). && (5.36)
\end{aligned}
$$

4. Choose a reference filter $A_{\mathrm{ref,th}}$ to compute the amplitude ratios. The best choice is to take the particular filter for which the relative uncertainty of the measured amplitude is smallest. Quite often, this is the filter in which the highest intrinsic amplitude is reached, but not always as this also depends on the instrumental noise.

5. Compare the theoretical amplitude ratios $A_{j,\mathrm{th}}/A_{\mathrm{ref,th}}$ with the observed ones $A_{j,\mathrm{obs}}/A_{\mathrm{ref,obs}}$, *for all the stellar models that pass through the error box* in $(T_{\mathrm{eff}}, \log g)$. This comparison can be made by visual inspection, as is often done, as it makes it possible to see the confusion regions due to the uncertainty in $(T_{\mathrm{eff}}, \log g)$. It can also be done by computing the χ^2 function defined as:

$$\chi^2(l) = \sum_{j=1}^{\#\mathrm{filters}} \left(\frac{A_{j,\mathrm{th}}/A_{\mathrm{ref,th}} - A_{j,\mathrm{obs}}/A_{\mathrm{ref,obs}}}{\sigma_{j,\mathrm{obs}}} \right)^2 , \qquad (5.37)$$

   where $\sigma_{j,\mathrm{obs}}$ is the properly propagated standard error of the observed amplitude ratio for filter j and the reference filter, *i.e.*,

$$\sigma_{j,\mathrm{obs}} = \frac{A_{j,\mathrm{obs}}}{A_{\mathrm{ref,obs}}} \sqrt{\left(\frac{s_{A_{j,\mathrm{obs}}}}{A_{j,\mathrm{obs}}}\right)^2 + \left(\frac{s_{A_{\mathrm{ref,obs}}}}{A_{\mathrm{ref,obs}}}\right)^2} , \qquad (5.38)$$

   with $s_{A_{j,\mathrm{obs}}}$ the standard error of the observed amplitude in filter j. Also in this case, one must consider different stellar models across the entire observational error box.

While performing step 3, one needs to derive the coefficients $\alpha_{T,\lambda}$ and $\beta_{T,\lambda}$, which are derivatives of the monochromatic flux at wavelength λ, from appropriate stellar atmosphere models. Several grids of state-of-the-art models are available in the literature, well suited to particular kinds of pulsating stars, *e.g.*, the LTE plane-parallel models by Kurucz (1993) or Smalley & Kupka (1997) for main-sequence stars cooler than spectral type B and the NLTE plane-parallel line-blanketed models for B stars (Lanz & Hubeny 2006) and O stars (Lanz & Hubeny 2002) without wind. As already discussed in the context of the connecting layer and Fig. 5.4, one should in principle adapt the theory presented here to NLTE unified spherical line-blanketed models including winds, such as those computed by Lefever *et al.* (2006), for O and B stars. For the time being, such generalization is not available, but Dufton *et al.* (2005) made a comparison between the NLTE static plane-parallel models without wind and the dynamical spherical models with wind and concluded that most of the atmospheric parameters and chemical compositions are quite similar. One may thus hope that the current description and the use of static NLTE models are sufficient to compute appropriate values for $\alpha_{T,\lambda}$ and $\beta_{T,\lambda}$. Nevertheless, it would be very useful if the current treatment of the atmosphere were generalised to a dynamical spherical unified atmosphere with a line-driven wind for the identification of the oscillations of O and the hottest B stars.

One also needs good values for the limb darkening $h_\lambda(\mu')$ to perform step 3. In a series of papers, Claret (2000, 2003, 2004) has computed several limb-darkening laws for a very broad range of effective temperatures, gravities and metallicities, and for several photometric systems. These are ideally suited to be used for mode identification. In the approaches by Ramachandran *et al.* (2004) and Randall *et al.* (2005), on the other hand, the use of a perturbed atmosphere model is constructed in such a way that it automatically incorporates the wavelength-dependence of the limb darkening, so that approximate parameterised limb-darkening coefficients are not needed for the computation of $\beta_{T,\lambda}$ and $\beta_{g,\lambda}$.

In all of the applications of the method so far, steps 1 and 2 are done for non-rotating stellar models. For each evolutionary stage of each track through the error box, one selects, for each l, the mode with frequency closest to the observed one and considers its amplitude for comparison with the observed ones. *This implicitly assumes that the observed frequency corresponds to the central peak of a multiplet.* Given that the Ledoux constant is usually substantially smaller than 1, the assumption thus becomes that $m = 0$ or $\Omega \simeq 0$. This is invalid for many pulsators. For stars with rapid rotation, the first-order approximation of the rotational splitting breaks down, and even the central peaks of the multiplets are shifted (Goupil *et al.* 2000). Rotational mode coupling also occurs between modes whose degree l differs by 2 when they have the same azimuthal order m (Daszyńska-Daszkiewicz *et al.* 2002). All these effects are ignored in the mode identification. It is very important for readers to realise the limitation of assuming the measured frequency to be equal to the central peak of the excited modes. *This is, in fact, quite a weak point of the photometric mode-identification method, except when the star is a very slow rotator in the sense that its rotation period is far shorter than the pulsation periods in the corotating frame*. Indeed, in many cases, we have clear spectroscopic evidence that the observed mode has $m \neq 0$ (see Sect. 5.2), even for moderate rotators. This is particularly the case for the high-order g modes in SPB stars and γ Dor stars with their long pulsation periods, but also for some of the p modes in β Cep stars and δ Sct stars. One should, therefore, not expect perfect agreement between the theoretical and observed amplitude ratios. It should also be kept in mind that deviations from linearity may occur, and that non-linear effects can also be the cause of a departure from the theoretical predictions based on the linear approximation.

While performing step 2, one can take two attitudes. Either one gives full confidence to excitation computations, and one considers only the modes that are predicted to be excited when computing the theoretical amplitude ratios. Or, a more conservative approach is taken, and one does not restrict the search by using predicted theoretical amplitudes, but rather considers all modes with frequencies close the observed ones, irrespective of their excitation predictions. As we will show in Chapter 10, we have a good, but not perfect, view of mode excitation in main sequence stars. Thus we advise the conservative approach.

The most likely mode degree l is, obviously, the one with the best agreement between theory and observations. Discrimination among the l-values is achieved by comparing the results for the amplitude ratios, either by visual inspection or from comparison of the $\chi^2(l)$-values. These two approaches are illustrated in Figs 5.6 and 5.7 for nine of the ten independent oscillation frequencies detected for the β Cep star ν Eri, the values of which are available from De Ridder *et al.* (2004) and are repeated here in Table 5.1. As can be seen in Table 5.1, the frequency ν_7 is only detected in the spectroscopy and could thus not be identified from the photometry. In Fig. 5.6, all the modes of numerous models within the error box with frequencies close to the observed ones are considered for the theoretical predictions of the amplitude ratios (indicated as the grey zones). *With this way of working, one assumes that the theory is error-free, and that the uncertainty in the theoretical prediction of the amplitude ratios comes from the errors of the fundamental stellar parameters.* It can be seen that the first four dominant modes $\nu_1, \ldots, \nu_4$ are safely identified as a radial mode on the one hand and an $l = 1$ triplet on the other hand, given the similar frequency values of ν_2, ν_3, ν_4. The modes with

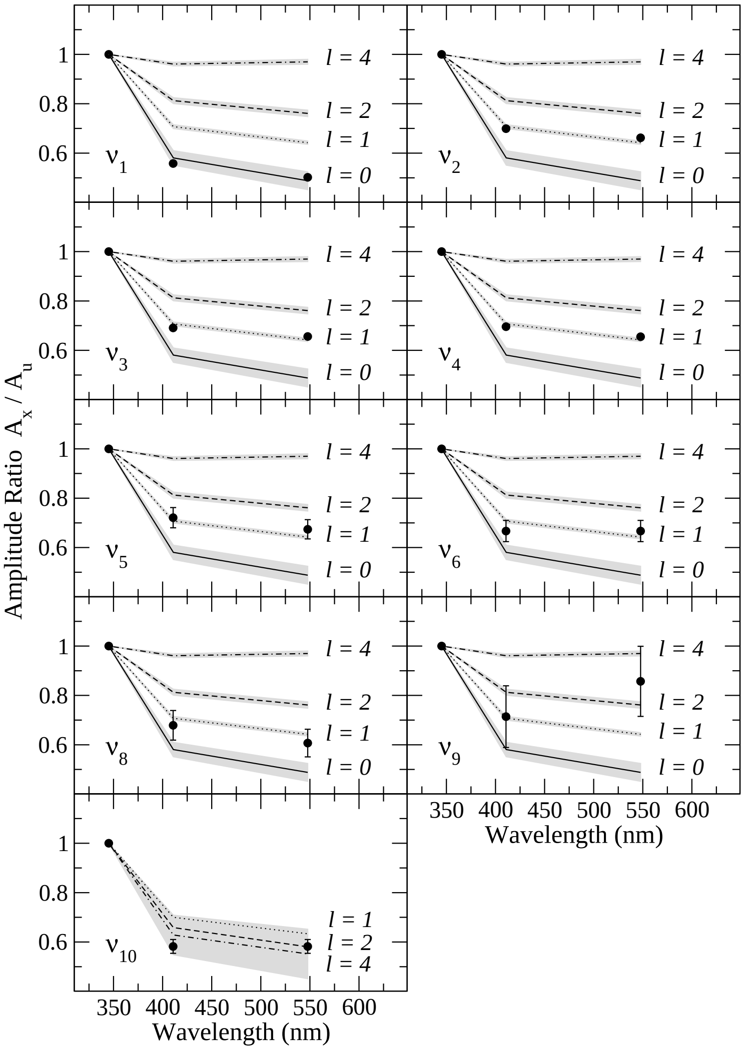

Figure 5.6: Amplitude ratios with respect to the Strömgren u filter for the β Cep star ν Eri, resulting from a 5-month multisite campaign. The dots are the observed values with their errors, and the full lines are the predicted values as a function of l, for a model in the centre of the observational $(T_{\rm eff}, \log g)$ box. The grey zones indicate the uncertainty of the theoretical prediction due to the observational error of $(T_{\rm eff}, \log g)$. All modes close in frequency to the observed ones were considered for the theoretical prediction, irrespective of their excitation. For a description of the data and the derived frequencies, we refer to Chapter 10. Figure taken from De Ridder *et al.* (2004).

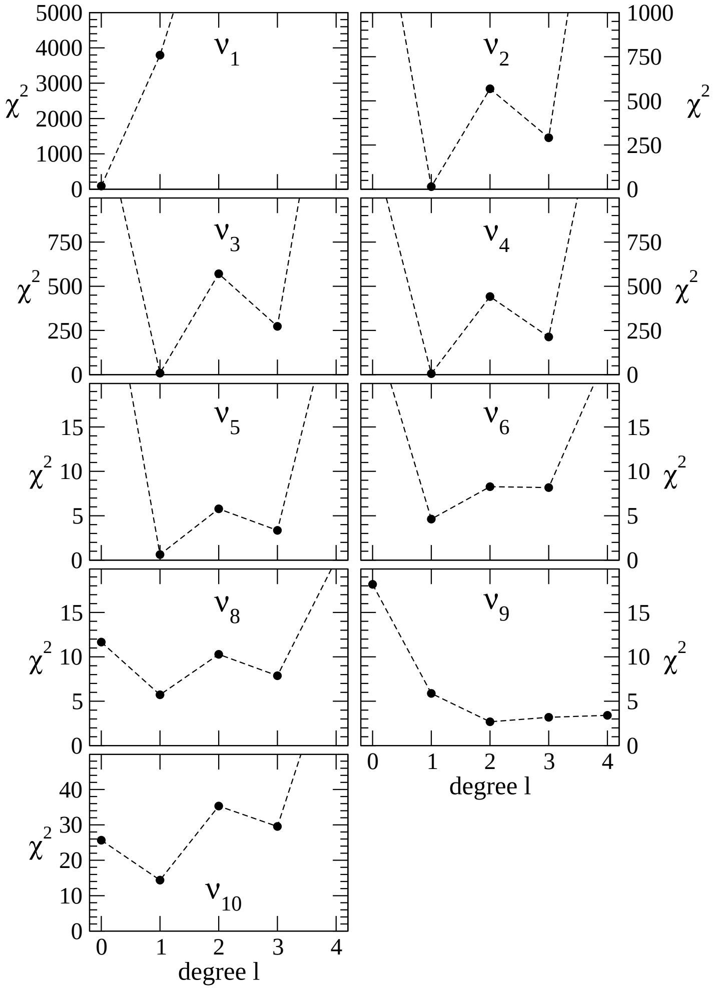

Figure 5.7: $\chi^2(l)$ as defined in Eq. (5.37) for the excited modes closest to the observed frequencies of one model in the observational error box $(T_{\rm eff}, \log g)$ of the β Cep star ν Eri. Compare this figure with Fig. 5.6.

Table 5.1: The ten independent frequencies for the β Cep star ν Eri, and their amplitude in the radial velocity derived from the Si III 455.3nm line as well as in the Strömgren u filter (from De Ridder *et al.* (2004).

ID	Frequency (d^{-1})	Amplitude ($km\,s^{-1}$)	Amplitude (mmag)	Degree l
ν_1	5.7633	22.4	73.5	0
ν_2	5.6539	8.9	37.9	1
ν_3	5.6201	8.1	34.6	1
ν_4	5.6372	7.9	32.2	1
ν_5	7.898	1.0	4.3	1
ν_6	6.244	1.0	3.9	1
ν_7	6.223	0.3	–	–
ν_8	6.262	0.8	2.8	1
ν_9	7.200	–	1.4	–
ν_{10}	0.432	–	5.5	–

frequencies ν_5, ν_6 and ν_8 are also still safely identified as $l = 1$ modes. The identification of ν_9 and ν_{10} is impossible. For ν_9 this due to the uncertainties on the observed amplitude. For ν_{10}, which corresponds to a high-order g mode, numerous such modes with different l- and n-values have almost similar frequency values which makes a discrimination among the possibilities impossible, as is reflected by the large grey area in the bottom panel of Fig. 5.6. The reader will have noticed that the theoretical predictions of the $l = 3$ modes do not occur in Fig. 5.6. This is due to the authors' choice to omit them in order to keep the graphs clear, because odd modes with $l > 1$ have a very specific wavelength dependence crossing the one of the even modes for B stars (see Fig. 5.2) which was not compatible with the observed ones. From Fig. 5.7 one would get the impression that all modes but the one with frequency ν_9 can be safely identified. We use this example to illustrate the importance of propagating the errors on $(T_{\rm eff}, \log g)$ into the theoretical predictions, as is done in Fig. 5.6, before making firm conclusions on the mode degree.

In principle, one could take one step further and use standard quality-of-fit measures of the χ^2 approach (*e.g.*, Press *et al.* 1986) to decide if a model is acceptable or not in an absolute sense, *i.e.*, as a deterministic tool to decide when to accept a mode identification as well as to decide which of the solutions $\chi^2(l)$ are statistically equivalent/different. However, we refrain from using such a cut-off value for χ^2 as a decision criterion to decide if we can accept the mode identification or not, because it assumes that the complicated non-adiabatic oscillation theory, the construction of the model atmospheres, the treatment of the oscillations in the atmosphere, and the input physics of the models (including the metal mixture, the description of convection and the ignorance of rotation) are error-free, besides the assumption that the determination of the fundamental parameters of the star does not suffer from systematic uncertainties. While all of this may be true, it is rather optimistic, to say the least. In fact, a discrepancy between the theoretical and observed amplitude ratios, translating into a high value for $\chi^2(l)$, was exploited by Dupret *et al.* (2003), by Daszyńska-Daszkiewicz *et al.* (2003) and by Daszyńska-Daszkiewicz *et al.* (2005) to improve the metallicity of main-sequence B stars, the treatment of convection of δ Sct stars, and the values for the opacities of β Cep stars, respectively, after securely identifying the degree(s) of the mode(s). Dupret *et al.* (2003) termed this *non-adiabatic asteroseismology*. Such fine-tuning can only be applied when there is no overlap among the amplitude ratios of different l-values, after consideration of the propagated uncertainties on the ratios due to the observational error box and after making sure that the total neglect of rotation and non-linear effects in the models and oscillations is justified.

A final remark on the amplitude-ratio method concerns the slightly different treatment of the deviation parameter by Randall *et al.* (2005). Instead of Eq. (5.37), they preferred to minimize

$$\chi^2(l) = \sum_{j=1}^{\#\text{filters}} \left(\frac{\frac{f_l^\star A_{\text{ref,obs}}}{A_{\text{ref,th}}} A_{j,\text{th}} - A_{j,\text{obs}}}{\sigma_{j,\text{obs}}} \right)^2 = \sum_{j=1}^{\#\text{filters}} \left(\frac{f_l A_{j,\text{th}} - A_{j,\text{obs}}}{\sigma_{j,\text{obs}}} \right)^2 , \qquad (5.39)$$

where $f_l^\star$ and f_l are free parameters that are solved for by minimizing the χ^2. The main difference with Eq. (5.37) is thus the introduction of the factor f_l. In this way, one still uses amplitude ratios, but one does not give preference any longer to the amplitude of one specific reference filter to compute the ratios. This is more objective in the sense that all filters are treated equally, but, on the other hand, introduces an additional free parameter that is adapted for each l separately. This is done in such a way that the shape of the amplitude-ratio distribution across the wavelength range is matched with the observed shape. This is a valid treatment within the χ^2 approach, where the number of degrees of freedom is simply increased by one. An example of this χ^2, as an application to identify the dominant mode of the sdBV star KPD 2109+4401, is shown in Fig. 5.8. The data have a very high S/N level and were taken with ULTRACAM by Jeffery *et al.* (2004). These authors also tentatively identified this mode in the adiabatic approximation and found it to be radial, albeit that confusion among the $l = 0, 1, 2$ solutions occurred. The results in the figure contain a non-adiabatic treatment and leave no doubt that the dominant mode is radial (Randall *et al.* 2005), thanks to the small error bars on the observed amplitudes.

Mode identification schemes also using phase differences

For the case of δ Sct oscillations, information is also encapsulated in the observed phase differences. Typical ψ_T-values for such oscillators range from 60° to 200°, depending on the mixing-length parameter, the mass and the degree of the mode. This strong dependence of ψ_T on the mode degree has led to a slightly different mode-identification method for such stars. Pioneering work in this respect was done by Garrido *et al.* (1990), who defined so-called *regions of interest* for the Strömgren system. These are areas in diagrams of, *e.g.*, v/y versus $\delta(v) - \delta(y)$ (where $\delta(x)$ is the phase of time series x) as a function of the degree l. The level of non-adiabaticity and ψ_T were rather arbitrarily treated as free parameters in the ranges $[0.25, 1]$ (where adiabatic equals 1) and $[90°, 135°]$, respectively, for the computation of these areas. Several examples of such regions are shown in Fig. 5.9, where a confrontation with the modes detected in several δ Sct stars is also shown. It can be seen that the identification of the degree is easiest to achieve by considering the u filter in combination with one of the three other filters. For an overview of applications of this method we refer to Garrido (2000). In particular, this method was applied by Breger *et al.* (1999) to identify several modes of the prototypical multiperiodic δ Sct star FG Vir.

A higher level of sophistication in δ Sct oscillation mode identification was reached by Dupret *et al.* (2003), following the scheme outlined above, and subsequently by Daszyńska-Daszkiewicz *et al.* (2003). These authors developed a method based on non-adiabatic computations similar to those described here, but

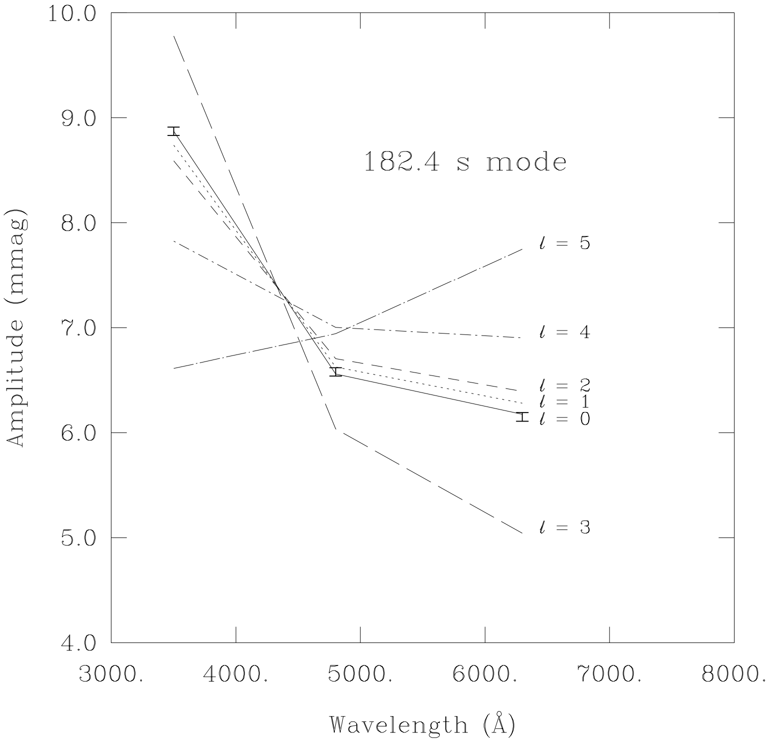

Figure 5.8: Identification of the dominant mode of the sdBV star KPD 2109+4401 from ULTRACAM photometry according to Eq. (5.39). The data are taken from Jeffery *et al.* (2004) while the identification was done by Randall *et al.* (2005).

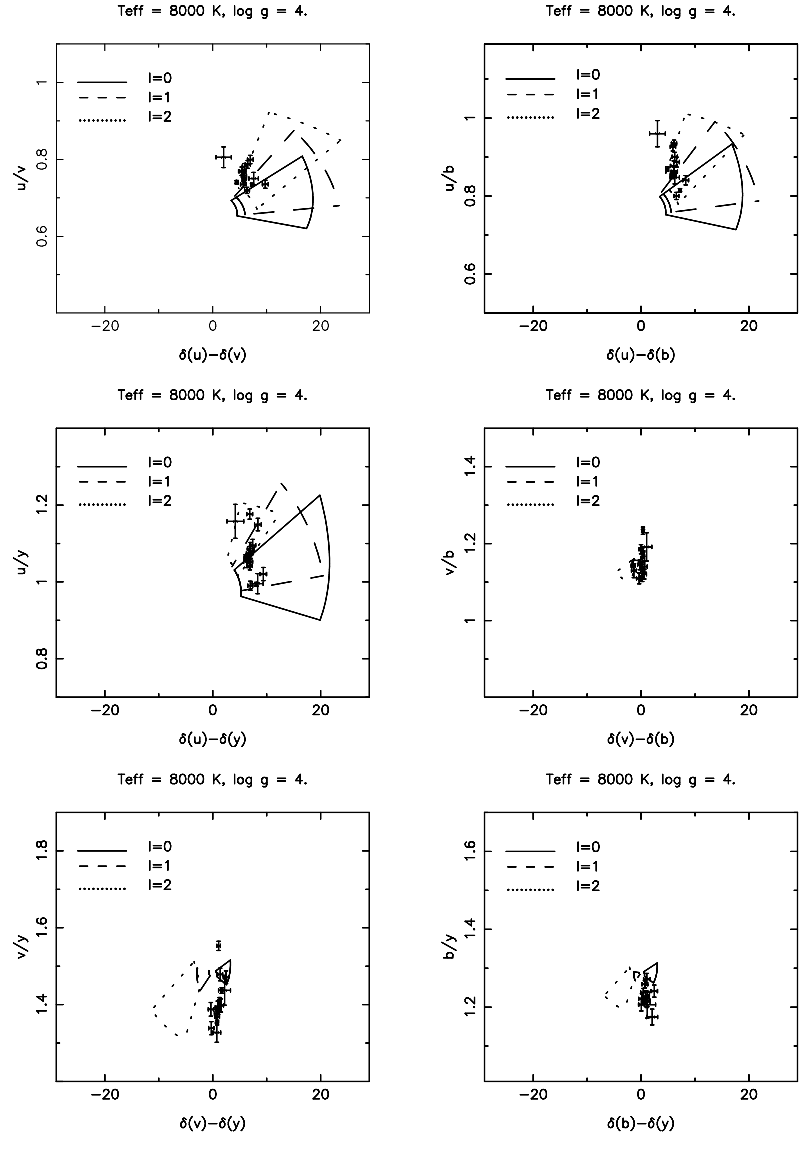

Figure 5.9: Regions of interest based on amplitude ratios and phase differences for the Strömgren system in the case of modes with degree $l = 0, 1, 2$. The dots with error bars denote the observed values for modes detected in several δ Sct stars. Figure kindly reproduced from Garrido *et al.* (1990) by Rafa Garrido.

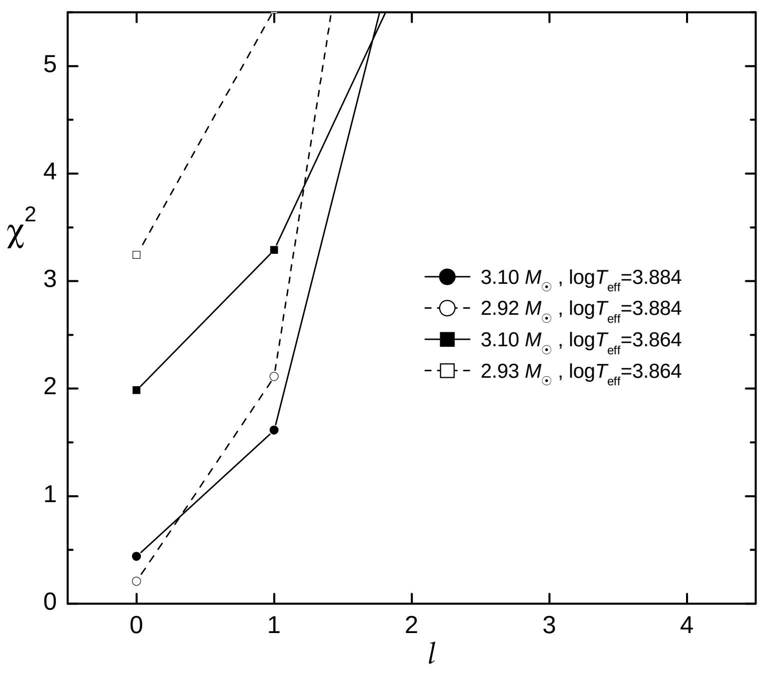

Figure 5.10: χ^2 for the observed photometric data of the δ Sct star 20 CVn for four models in the observational error box in the HR diagram (Daszyńska-Daszkiewicz *et al.* 2003).

considering the amplitudes and phases themselves in the different passbands by re-arranging the equations. While doing so, they defined a different type of χ^2, which they minimized as a function of the coefficients $[\xi_r(R)/R]\ P_l^m(\cos i)$ and $f_T\ [\xi_r(R)/R]\ P_l^m(\cos i)$. In this way, one does not need to know a value for the unknown factor $P_l^m(\cos i)$ because this factor is considered together with the unknown amplitude $\xi_r(R)/R$ of the mode. In fact, seeking the best solution for the two chosen unknowns by means of a minimum in their χ^2 for models with different parameters allowed them to constrain these parameters. The identification of l then comes as a by-product, excluding the l-values whenever their $\chi^2(l)$ turned out to be too high and discriminating among l whenever possible. We show in Fig. 5.10 the application of their method to the low-amplitude δ Sct star 20 CVn, which was already known to have a radial mode (see also Sect. 5.2 below). There is no ambiguity in the mode identification for this star, as all modes with $l > 0$ have much higher χ^2-values than the radial mode. The main goal of the authors was to constrain the properties of the convection treatment by comparing the value of f_T resulting from the fit with theoretically computed values. Using a simplified treatment of the convection-pulsation interaction by assuming 'frozen convection' they noted a preference for very small values of the mixing-length parameter α, although in all cases the agreement between the observationally inferred and computed values of f_T was rather poor; this clearly indicates inadequacies in the convection modelling.

Daszyńska-Daszkiewicz *et al.* (2005) applied a similar method, in which the radial velocity amplitude and phase is included and which will be discussed further in Sect. 5.3, to the data of FG Vir; this led to the same result for the eight dominant modes as the one obtained already by Viskum *et al.* (1998) and Breger *et al.* (1999). We display these results in Fig. 5.11 and compare them with the spectroscopic mode

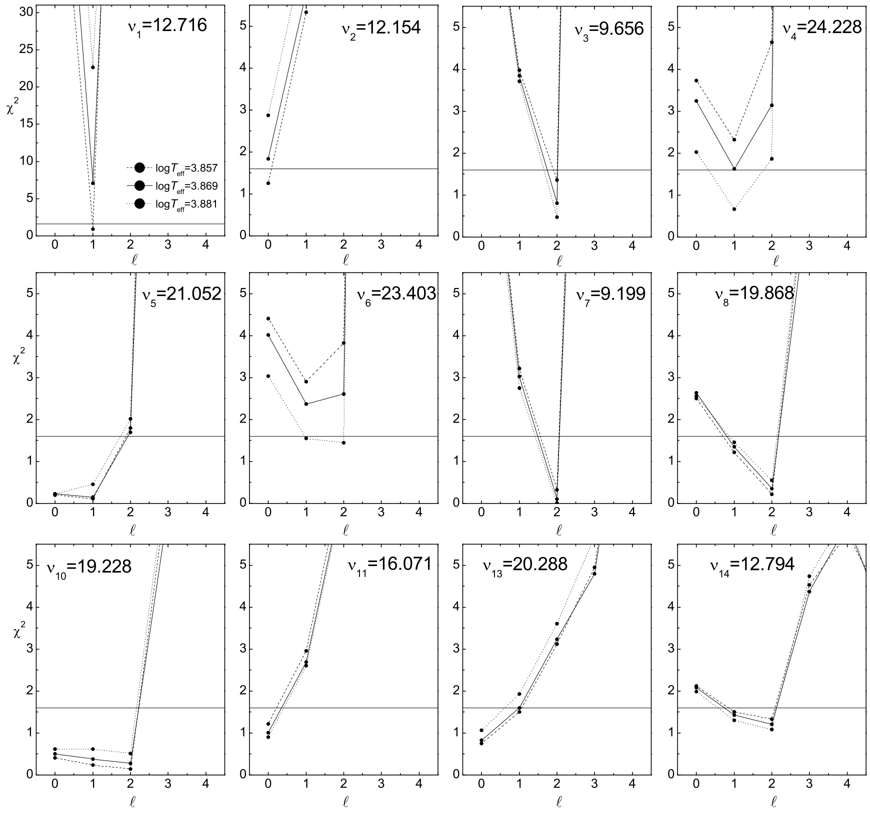

Figure 5.11: χ^2 for the twelve dominant modes in the photometry of the δ Sct star FG Vir, for three different stellar models characterised by the given effective temperature. The full horizontal line indicates a confidence level of 80% (Daszyńska-Daszkiewicz *et al.* 2005).

identification in Sect. 5.2 by means of Table 5.4. Here again a major goal was to investigate the treatment of convection. Using a time-dependent formulation of mixing-length theory originally proposed by Gough (1977) resulted in a somewhat better agreement between inferred and computed f_T than for the frozen-convection approximation, without requiring a possibly unrealistically low value of α.

Even though the method by Daszyńska-Daszkiewicz *et al.* (2003) is a significant improvement to the one by Garrido *et al.* (1990), it suffers from the same limitation as Dupret *et al.*'s (2003) amplitude-ratio scheme outlined above, *i.e.*, it uses model and oscillation computations for non-rotating stars and assumes the theory to be well enough developed so that the discriminating values of the χ^2 are mainly due to different l-values and not to limitations of the theoretical models.

The application of the above theory to the case of the high-overtone p modes of the roAp stars was used with a different goal. As explained in Chapter 2, some of these stars are known to have a dominant dipole $(l = 1)$ mode from frequency splitting in terms of the oblique pulsator model. This information can thus be used to derive observational information on the badly known limb darkening, and from it of the temperature structure $T(\tau)$ of the atmosphere, from a confrontation between observed amplitudes in different filters and Eq. (5.29). This idea was put forward by Matthews *et al.* (1990, 1996) who derived such an empirical $T(\tau)$ relation for the star HR 3831 in the approximation of a grey atmosphere as in Eq. (5.19) and assuming the steep amplitude decrease with increasing wavelength to be dominated by the limb-darkening variations. Kurtz & Medupe (1996), on the other hand, showed from an analytical derivation that the limb-darkening could not account for the observed steep decline of the amplitudes towards red wavelengths. They suggested instead that this is a consequence of a depth effect in the atmosphere, and settled the ambiguity between these two different interpretations by showing that the factor two difference between the theoretical predictions according to Eq. (5.29) and the observations cannot be due to limb-darkening variations alone. They re-affirmed the failure of the theory outlined above due to the basic assumption adopted at the start of Sect. 5.1.2, *i.e.*, the single-layer approximation. This is inappropriate for roAp stars, given that depth effects are clearly visible in the line-profile variations of such stars (*e.g.*, Mkrtichian *et al.* 2003; Elkin *et al.* 2005; Kurtz *et al.* 2007; Ryabchikova *et al.* 2007). The generalization of the method of photometric amplitudes to a multi-layer approach is still awaited.

To conclude this section, we stress that the photometric mode-identification methodology, in whichever of the modern formulations, has to be treated with care. It relies rather heavily on the theoretical models and assumes the input physics to be free of errors. In this sense, it is not really *empirical*. Nevertheless, it works well for the large-amplitude p-mode oscillations in β Cep and δ Sct stars, provided that they are not fast rotators. The performance of the method has not yet been tested properly for the very dense frequency spectra of high-order g modes in SPB stars and γ Dor stars, and it needs to be modified to include better atmosphere models and depth effects for the application to roAp stars. Despite these limitations, we stress once more that even the secure identification of the l-value of only one or two of the dominant modes is a huge step forward in the seismic modelling.

5.2 Mode identification from high-resolution spectroscopy

As already explained in Chapter 4, the velocity field caused by the non-radial oscillation(s) leads, through Doppler displacement, to periodic variations in the profiles of spectral lines. The introduction of high-resolution spectrographs with sensitive detectors in the 1980s thus had a large impact on the field of empirical mode identification. Spectroscopic data offer a very detailed picture of the pulsational velocity field. As we will show below, its interpretation in terms of (l, m) is far less dependent on the details of the oscillation theory in the outer atmosphere than multicolour photometry. Indeed, it basically relies on the interpretation of the data in terms of the oscillation velocity vector, derived from $\vec{\xi}$, and not so much on the Lagrangian variation of the temperature and of the flux.

From an observational point of view, it remains a challenge to obtain spectra covering the overall beat period of the multiperiodic oscillations, with a high resolving power (typically above 40 000) and with a high signal-to-noise ratio (typically above 200 and preferably much higher than that), for a good temporal resolution (typically below a few percent) in the sense of the ratio of the integration time to the oscillation period. The latter condition is necessary in order to avoid smearing out of the oscillations during the cycle.

The methodology to derive the full details of the pulsational velocity field at the stellar surface contains at least six unknowns, as will be shown below, and therefore tends to be complicated. For this reason, multicolour photometric observations, which can only lead to an estimate of the l, but which can be obtained from small telescopes, are still of utmost importance for mode identification. These kinds of data are in particular more suitable to study long-period pulsations because small telescopes are available on longer time scales. Ideally, one combines both types of data, in ways outlined in Sect. 5.3. In the current section we first explain how theoretical line-profile variations can be calculated. Subsequently we describe two modern mode-identification methods based on line-profile variations.

5.2.1 Calculation of theoretical line-profile variations

Osaki (1971) published a pioneering paper including a scheme on how to compute theoretical line-profile variations for non-radial oscillations. This is remarkable since, at the time Osaki published his work, high-resolution spectroscopy was not yet available. His scheme could therefore not be tested on real data. We follow below the basic ingredients of a modern line-profile generation code based on Osaki's description.

In the case of one linear spheroidal mode with infinite lifetime, the surface pulsation velocity vector expressed in the coordinate system (r, θ, ϕ) is given by

$$\begin{aligned} \vec{v}_{\rm osc}(R,\theta,\phi,t) &= (v_r, v_\theta, v_\phi, t) \qquad (5.40) \\ &= \Re\left\{-{\rm i}\omega\xi_r(R)\left(1, K\frac{\partial}{\partial\theta}, \frac{K}{\sin\theta}\frac{\partial}{\partial\phi}\right)Y_l^m(\theta,\phi)\exp\left(-{\rm i}\omega t\right)\right\}, \end{aligned}$$

in the approximation where one can ignore the effects of the rotation in the computation of the oscillation eigenfunctions. To this, we add the rotational surface velocity vector in the approximation of uniform time-

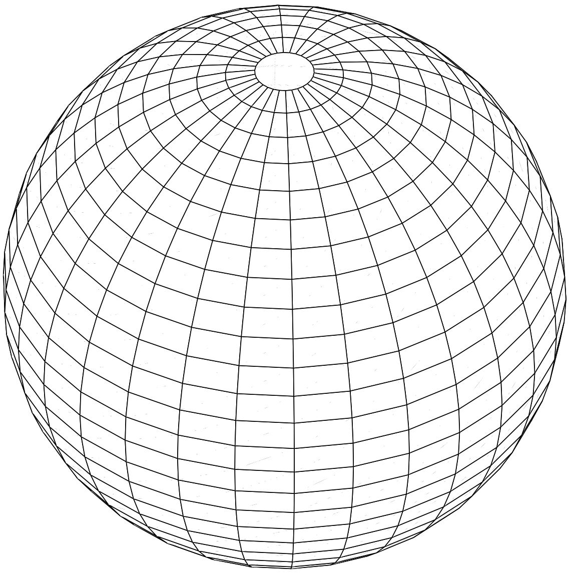

Figure 5.12: The stellar surface is subdivided into a finite number of surface elements determined by a step-size in θ and ϕ for the computation of theoretical line-profile variations.

independent rotation:

$$\vec{v}_{\rm rot}(R,\theta,\phi,t) = \Omega R \vec{a}_\phi \tag{5.41}$$

to obtain the total velocity vector $\vec{v}(R,\theta,\phi,t) = \vec{v}_{\rm osc}(R,\theta,\phi,t) + \vec{v}_{\rm rot}(R,\theta,\phi,t)$ at the stellar surface for the surface element with coordinates (R,θ,ϕ).

In order to compute the observed line-profile shape corresponding to this velocity vector field, denoted as $p(\lambda,t)$, we have to determine the velocity vector component, as well as the normalised flux of a particular stellar surface element with coordinates (R,θ',ϕ'), in the line-of-sight:

$$p(\lambda,t) \equiv \frac{\displaystyle\int_{\theta'=0}^{\pi/2}\int_{\phi'=0}^{2\pi} \left(d\vec{A}(R,\theta',\phi',t)\cdot\vec{a}_z'\right) I_\lambda(R,\theta',\phi',t,\vec{a}_z')}{\displaystyle\int_{\theta'=0}^{\pi/2}\int_{\phi'=0}^{2\pi} \left(d\vec{A}(R,\theta',\phi',t)\cdot\vec{a}_z'\right) I_\lambda^{\rm cont}(R,\theta',\phi',t,\vec{a}_z')}, \tag{5.42}$$

where $d\vec{A}$ is the local surface normal, $I_\lambda(R,\theta',\phi',t,\vec{a}_z')$ is the intensity of the point with coordinates (R,θ',ϕ') at time t in the line-of-sight and $I_\lambda^{\rm cont}$ is the continuous intensity, *i.e.*, the intensity that would be observed if the spectral line were absent. In practice, one subdivides the visible stellar surface into a large number of elements with central coordinates (θ_i',ϕ_j'), $i = 1,\ldots,N; j = 1,\ldots,M$ for the computation of the integrals in Eq. (5.42) (see Fig. 5.12). For present-day computational power, one usually takes a step of 1° in the angles θ' and ϕ', leading to $N = 180$ and $M = 360$. In order to get reliable results, N and M must be at least 45 and 90, respectively.

We now consider all the ingredients necessary for the computation of $p(\lambda,t)$ through Eq. (5.42). The velocity field due to the rotation and the pulsation leads to a Doppler shift at a point (R,θ',ϕ') on the visible equilibrium surface of the star. The local contribution of a point (R,θ',ϕ') to the line profile is proportional to the flux at that point. We assume that the intensity $I_\lambda(\theta',\phi')$ is the same for all points of the considered surface element. The flux through the surface element surrounding the point (R,θ',ϕ') thus is the product of the intensity $I_\lambda(\theta',\phi')$ and the projection on the line-of-sight of the surface element around the considered point:

$$I_\lambda(\theta',\phi')\; R^2\; \sin\theta'\; \cos\theta'\, {\rm d}\theta'\, {\rm d}\phi'. \tag{5.43}$$

An important effect that changes the flux over the visible surface is the limb darkening. The flux of a surface element centred around the point $P(R,\theta',\phi')$ of the equilibrium surface with size $R^2\sin\theta'\,{\rm d}\theta'\,{\rm d}\phi'$ is

$$F_\lambda(R,\theta',\phi') = I_0\; h_\lambda(\theta')\; R^2\; \sin\theta'\; \cos\theta'\, {\rm d}\theta'\, {\rm d}\phi', \tag{5.44}$$

where I_0 is the continuum intensity at $\theta' = 0$. For line-profile variation calculations, a linear approximation of the limb darkening largely suffices, because the profile variations are dominated by the Doppler shifts due to the surface velocity. One therefore often encounters the limb darkening in terms of one coefficient $u_\lambda(T_{\rm eff},\log g, Z)$ because this saves an order of magnitude in computation time for spectroscopic mode identification, where numerous parameter combinations must be considered.

Perturbations of the intensity and of the surface due to the oscillations change the line profile. Usually, however, these effects are far less important than the velocity effect for classical pulsators, and one often assumes $\delta F_\lambda(\theta',\phi') = 0$ during the oscillation cycle. However, one can easily generalise any line-profile generation code to include the non-adiabatic perturbation of the intensity, $\delta[I_0 h_\lambda(\theta')]$, as well as the perturbed surface due to the oscillation, according to the treatment in the outer atmosphere discussed above. This has been tested for the spectroscopic identification methods we discuss below and has been found to be an unnecessary complication.

A spectral line with central wavelength λ_0 is subject to different broadening mechanisms, which we also have to take into account in the computation of $p(\lambda, t)$:

1. *Atomic broadening* results in a Lorentz profile, which is caused by the finite lifetime of the energy levels of the ions responsible for the line.
2. Neighbouring particles disturb the energy levels of the ions, causing a small change in the wavelength of the spectral line. This *pressure broadening* results in a Lorentz profile. The higher the pressure the larger this broadening becomes.
3. All ions move on a microscopic scale due to thermal agitation. This *thermal broadening* leads to a Gaussian profile as the particles follow a Maxwellian velocity law with a temperature dependence $\sim \sqrt{T}$.
4. The stellar rotation causes *rotational broadening*. We assume the rotation to be uniform across the stellar disk, and time independent. The resulting line profile is then symmetrically broadened by the rotation.
5. Stellar oscillations give rise to periodic broadening of the line profile. The shape of the line profile is completely determined by the parameters occurring in the expression of the pulsation velocity given in Eq. (5.40). In particular, it is dependent on the (l, m) of all the oscillation modes.

In order to take into account such intrinsic broadening effects, the local line profile is convolved with an intrinsic profile, which, in the simplest approximation of thermal broadening, is taken to be Gaussian with variance v_{th}^2, where v_{th}^2 is an unknown parameter that depends on the spectral line considered. Generalisations to an intrinsic Voigt profile or a profile derived from a stellar atmosphere model are easily performed, but are not necessary for mode identification (see below) while implying much longer computation times. In principle, if the theory of model atmospheres and the time-independent broadening mechanisms were well enough understood, we would not need this free parameter v_{th}, but we could simply take the intrinsic shape of the considered spectral line. In practice, however, one is always faced with the need to introduce some unknown level of microturbulence, of up to several km s^{-1}, when fitting spectral line profiles. For this reason, we may as well omit the computation of the intrinsic line profile from atmosphere models and estimate a Gaussian with variance v_{th}^2 along with the pulsational and rotational parameters that affect the line profiles.

We have now considered all the ingredients for the computation of the observed line profile $p(\lambda, t)$. We represent by λ_{ij} the Doppler-corrected wavelength for a point on the star with coordinates $(R, \theta_i', \phi_j', t)$, *i.e.*,

$$\frac{\lambda_{ij} - \lambda_0}{\lambda_0} \equiv \frac{\lambda(R, \theta_i', \phi_j', t) - \lambda_0}{\lambda_0} = \frac{\Delta\lambda(R, \theta_i', \phi_j', t)}{\lambda_0} = \frac{v(R, \theta_i', \phi_j', t)}{\tilde{c}}. \tag{5.45}$$

An explicit expression for $v(R,\theta'_i,\phi'_j,t)$ can be found in, *e.g.*, Aerts *et al.* (1992):

$$\begin{aligned} v(R,\theta'_i,\phi'_j,t) &= - && v_\Omega \sin\theta' \sin\phi' \\ & + && v_\mathrm{p} \sum_{k=-l}^{l} a_{l,m,k}(i) \left(\cos\theta' P_l^k - K \sin\theta' \, \frac{dP_l^k}{d\theta'} \right) \\ & \times && \sin((\omega - m\Omega)t + k\phi')\,, \end{aligned} \tag{5.46}$$

where the velocity amplitude is defined as $v_\mathrm{p} \equiv \sqrt{4\pi} c_{lm} \tilde{\xi}_r(R)\omega$ with the normalization constant c_{lm} introduced in Chapter 3 and where we use $v_{_\Omega} \equiv \Omega R \sin i$, usually denoted as $v \sin i$, for the projected rotation velocity for convenience of shorter notation. Equation (5.46) is based on the transformation formula for spherical harmonics for two different coordinate systems whose polar axes are inclined with angle i:

$$Y_l^m(\theta,\phi) = \sum_{k=-l}^{l} a_{l,m,k}(i) Y_l^k(\theta',\phi'), \tag{5.47}$$

where

$$\begin{aligned} a_{l,m,k}(i) &\equiv (l+m)!(l-m)! \\ &\times \sum_r (-1)^{l+k+r} \frac{\sin(i/2)^{2l-2r-m-k} \cos(i/2)^{2r+m+k}}{r!(m+k+r)!(l-m-r)!(l-k-r)!}, \end{aligned} \tag{5.48}$$

with $r \geq 0$, $r \geq -k-m$, $r \leq l-m$, $r \leq l-k$ (Jeffreys 1965, Condon & Odabasi 1980).

The line profile is then approximated by

$$p(\lambda,t) = \frac{\displaystyle\sum_{i,j} \frac{I_0 h_\lambda(\theta'_i)}{\sqrt{2\pi}\sigma} \exp\left(-\frac{(\lambda_{ij}-\lambda)^2}{2v_\mathrm{th}^2} \right) R^2 \sin\theta'_i \cos\theta'_i \, \Delta\theta'_i \, \Delta\phi'_j}{\displaystyle\sum_{i,j} I_0 h_\lambda(\theta'_i) R^2 \sin\theta'_i \cos\theta'_i \, \Delta\theta'_i \, \Delta\phi'_j}, \tag{5.49}$$

where the sum is taken over the visible stellar surface, *i.e.*, $\theta' \in [0°, 90°]$, $\phi' \in [0°, 360°]$ and where we have assumed a constant Gaussian intrinsic profile and a non-variable surface normal for simplicity. Equation (5.49) essentially represents the line-profile computation suggested by Osaki (1971).

We show in Figs 5.13 and 5.14 sets of theoretically calculated profiles for $l = 2$ and $l = 6$ modes computed from Eq. (5.49). The profiles in Fig. 5.13 are prograde, those in Fig. 5.14 retrograde.

It is obvious that the pulsational broadening is easiest to unravel from the intrinsic broadening for the sharpest lines in the spectrum, provided that they are well resolved. Indeed, for sharp lines with narrow wings, the deformation of the line is detectable across the whole profile and not only in the line center. This is why we want to avoid hydrogen lines, which suffer heavily from Stark broadening in their wings, and helium lines for mode identification whenever possible. Nevertheless, Viskum *et al.* (1998) used the equivalent-width variations of Balmer and metal lines in low-resolution ($\mathrm{R} = 4\,000$) spectra to identify the dominant modes of FG Vir. They discriminated among different possibilities for l from a plot of the ratio of the amplitude of the equivalent-width variation of the Hα and an Fe I line versus the ratio of the amplitude for

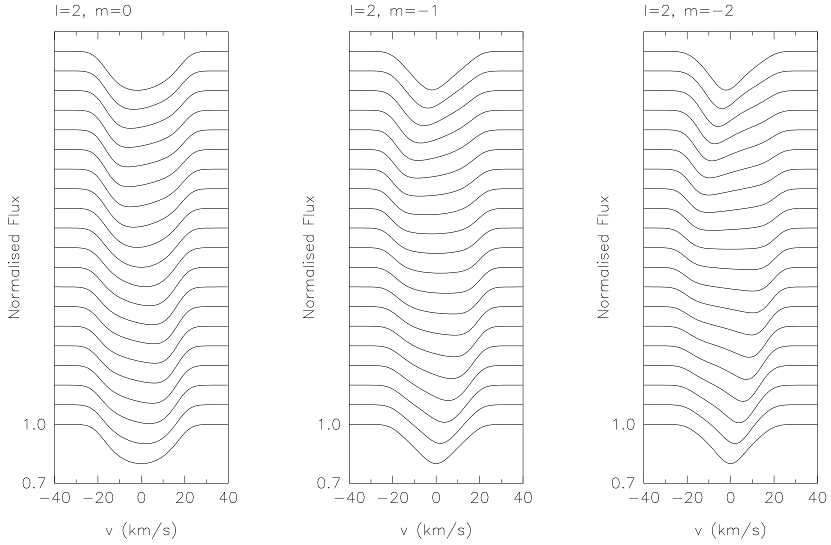

Figure 5.13: Theoretically determined line-profile variations calculated by means of the basic formalism described in the text considering an $l = 2$ mode and $m = 0$ (left panel), $m = -1$ (middle panel), and $m = -2$ (right panel) respectively. The other velocity parameters are: pulsation amplitude $v_{\rm p} = 5\,$km/s, projected rotational velocity $v \sin i = v_\omega = 30\,$km/s, thermal velocity $v_{\rm th} = 4\,$km/s, and inclination $i = 55°$. The line-of-sight velocity is given on the x-axis while the normalised flux (unitless, with values between 0.7 and 1.0) is drawn on the y-axis. The profiles are stacked according to increasing oscillation phase, from 0.00 (lowest profile) to 0.95 (uppermost profile) in steps of 0.05.

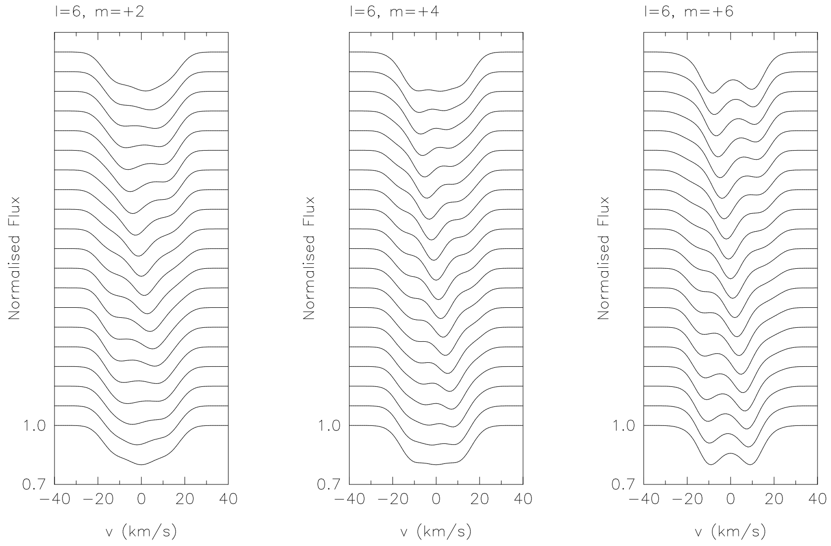

Figure 5.14: Same as in Figure 5.13, but for $l = 6$ with $m = +2$ (left panel), $m = +4$ (middle panel), and $m = +6$ (right panel).

Hα and an average photometric amplitude for the four Strömgren filters. In this way, they noticed "different observational regions" in their plot, similar to those used by Garrido *et al.* (1990) for multicolour photometry of δ Sct stars. The application by Viskum *et al.* (1998) concerned a purely observational diagram. In fact, the amplitude ratios in photometry are replaced here by amplitude ratios of the equivalent-width variations of lines that are strongly affected by $\delta T/T$. On this basis they identified l for the eight dominant modes; this identification was later confirmed by Breger *et al.* (1999) and Daszyńska-Daszkiewicz *et al.* (2005) (see Table 5.4 below). With the advent of high-resolution spectroscopy and the coupling between pulsation theory and observations in the quantitative methods outlined below, this Balmer-line application was not pursued for other stars.

As explained, the time dependence of the spectral line caused by the temperature eigenfunction δT may be important for the computation of the intrinsic line profile for lines that are sensitive to small temperature variations. This is particularly the case for metal lines with significant equivalent-width changes because the $\delta T/T$ is such that it brings the ion into a higher/lower ionization stage at compression/expansion compared with equilibrium. For this reason, one carefully selects the best spectral line for mode identification. It is advantageous to use an unblended, deep line which is insensitive to small temperature changes in the line-forming region in the atmosphere, so that one can avoid having to include $\delta T/T$ in the computations. This has been thoroughly investigated by De Ridder *et al.* (2002) for pulsating B stars. The choice of the best line depends, of course, on the effective temperature and gravity of the star. For β Cep stars, *e.g.*, the best line is the Si III 4560Å triplet (Aerts & De Cat 2003), while for slowly pulsating B stars the Si II 4130Å doublet is ideally suited (Aerts *et al.* 1999). For very fast B-type rotators, these multiplet lines are unfortunately blended and one has little choice but to consider the isolated He I 6678Å line (*e.g.*, Balona *et al.* 1997) or other helium lines (Rivinius *et al.* 2003). Temperature effects on line-profile variations of δ Sct and γ Dor stars have not been studied in the same detail as for B stars.

As discussed above, Eq. (5.49) for the computation of line-profile variations can be generalised in order to take into account the following additional time-dependent effects: a perturbed surface, a perturbed flux through non-adiabatic temperature and gravity variations, a time-dependent intrinsic profile. For fast rotators, Coriolis and centrifugal correction terms to the pulsation velocity expression should also be included. The most up-to-date line-profile generation codes take into account several of these effects, except those due to the centrifugal force. We refer the reader to Lee *et al.* (1992), Aerts & Waelkens (1993), Townsend (1997), Schrijvers *et al.* (1997), De Ridder *et al.* (2002), and Zima (2006) for a detailed description of such codes.

The complication due to the centrifugal force is not included in spectroscopic mode-identification methods at present. It would thus be necessary to adapt the methodology presented below in the case of oscillations in rapid rotators, *i.e.*, for stars that rotate at a considerable fraction of their critical velocity (say above 50%). In such a case, the expression for the velocity field in terms of one spherical harmonic as in Eq. (5.40) is inaccurate. It is clear that the applicability of the methodology breaks down in such a situation. As already emphasized in Chapter 3, we have no good theory of stellar oscillations for fast rotators. Thus, one cannot hope to build a good mode-identification method for such cases at present.

The improved stability of spectrographs, some of which have been developed for exoplanet searches since the beginning of this century, has allowed radial-velocity measurements with a precision of order $\mathrm{m\,s^{-1}}$. This led Hekker *et al.* (2006) to generalise the computation of line-profile variations to the case of solar-like damped oscillations. This revealed that line bisectors, as defined in Chapter 4, are not a good diagnostic to investigate such oscillations, as was also found independently by Dahl *et al.* (2006). Hekker *et al.* (2006) compared their simulations with the variations detected in the cross-correlation functions (CCF) of three red giants in which such damped oscillations were firmly established from radial-velocity measurements. This led to the surprising result that non-radial modes seem to explain the CCF far better than radial modes. This is at present not understood in terms of the theory outlined briefly in Chapter 3 and more thoroughly in Chapter 7.

5.2.2 Line profile fitting

It is clear that the velocity expression based on the non-radial oscillation theory contains many free parameters, even in the simple formulation in which rotational and non-adiabatic effects are neglected. The very large number of candidate modes is especially a problem when constructing identification techniques and it often keeps the predictive power low. This is particularly the case for the methods that are based on a trial-and-error principle. Quantitative methods are better to obtain a reliable mode identification. This need for quantitative methods has become apparent since more and more detailed spectroscopic analyses have revealed that multimode pulsations are more the rule than exception. Below, we treat two such methods, but first we mention trial-and-error line-profile fitting as a mode-identification method for historical reasons.

This rather subjective method was pioneered by M. Smith and his collaborators. They obtained for the first time high-resolution spectroscopic observations for various types of pulsating stars along the main sequence and implemented Osaki's (1971) scheme to compare these data with theoretical predictions (*e.g.*, Campos & Smith 1980; Smith 1983; Smith *et al.* 1984,1985a,b,c, 1986). The idea to identify modes is the following: one generates theoretical line profiles $(\lambda, p(\lambda))$ over the oscillation cycle from Eqs (5.45) and (5.49), or their more sophisticated version including temperature and Coriolis effects, and one compares them with the observed ones to select the best set of line-profile parameters. These are the velocity amplitude $v_{\rm p}$ of each of the modes, the projected rotation velocity v_Ω, the inclination angle i, and the intrinsic profile width $v_{\rm th}$. This selection of $(l, m, v_{\rm p}, i, v_\Omega, v_{\rm th})$ is either done by simple visual inspection (early days) or by defining a criterion that includes the deviation of the theoretical profiles from the observed ones in each wavelength pixel. In order to do this objectively, one must construct a fine grid of theoretical profiles for different values of (l, m) and for realistic ranges of the other line-profile parameters.

This method is relatively easy and straightforward to apply to a monoperiodic oscillator. Assume we have M observed normalised profiles of a spectral line $(\lambda_j, p_{\rm obs}(\lambda_j, t_k))$ with $j = 1, \ldots, N$ and $k = 1, \ldots, M$. We can then compute theoretical line profiles $(\lambda_j, p_{\rm theo}(\lambda_j, t_k))$ as explained above using Eq. (5.49) for different input parameters $v_{\rm p}, i, v_\Omega$ and $v_{\rm th}$. Subsequently, we derive the *line deviation parameter* based on the classical statistical technique of *standardised residuals* (*e.g.*, McCullagh & Nelder 1989):

$$\Sigma_l^m(v_{\rm p}, i, v_\Omega, v_{\rm th}) \equiv \sqrt{\frac{1}{(M \cdot N) - 1} \sum_{k=1}^{M} \sum_{j=1}^{N} \frac{\left[p_{\rm obs}(\lambda_j, t_k) - p_{\rm theo}(\lambda_j, t_k)\right]^2}{p_{\rm theo}(\lambda_j, t_k)[1 - p_{\rm theo}(\lambda_j, t_k)]}}. \tag{5.50}$$

The optimal choice of the continuous parameters $(v_{\rm p}, i, v_\Omega, v_{\rm th})$ leads to a minimum of Σ_l^m for each (l, m). By carefully screening a four-dimensional parameter space for each (l, m), and by subsequently comparing the Σ_l^m-values, one can thus identify the most likely mode.

Whenever more than one mode is present, however, the method becomes unrealistic in computation time because one cannot search a large enough parameter space. The latter has six dimensions for one mode and increases by 3 for any additional mode, in the approximation where one neglects temperature and Coriolis effects as well as mode coupling. Also, this method is sensitive to the neglect of low-amplitude modes that do affect the profiles slightly, because the time series of line profiles is used in an absolute sense. Quite often one constructs theoretical line profiles after the mode identification has been achieved with quantitative methods for direct comparison with the data. This is of course no longer line-profile fitting, but serves as an empirical goodness-of-fit test to check identifications resulting from other methods.

5.2.3 The moment method

To overcome the computational obstacle of line-profile fitting, and to make the identification more objective, quantitative mode-identification methods have been developed since the second part of the 1980s. With each of these, one replaces the observed line profiles by carefully studied diagnostics derived from the data. One such method is based on the moment variations of the spectral lines and was first introduced by Balona (1986a,b, 1987) and further developed by Aerts *et al.* (1992), De Pauw *et al.* (1993), Aerts (1996), Cugier & Daszyńska (2001) and Briquet & Aerts (2003). This method essentially relies on the statistical property that a line profile is fully characterised by all of its velocity moments. Given this, one derives information about the velocity of the non-radial oscillations from the time series of the moments of the line profiles. The moment method has meanwhile been applied to many different types of classical pulsators along the main sequence. It is very powerful for low-degree modes ($l \leq 4$) in slow rotators ($v \sin i \leq 50\,\mathrm{km\,s^{-1}}$). We discuss now the basic ingredients of this method and refer the reader to the papers listed above for details.

Definition of the moments

As discussed above, a line profile $p_{\mathrm{theo}}(v) \equiv (f * g)(v)$ is the convolution of an intrinsic profile denoted here as $g(v)$ for brevity, with the flux in the direction of the observer, denoted for convenience as $f(v)$, integrated over the visible stellar surface. The function $f(v)$ corresponds to the one defined in Eq. (5.44) while the velocity v is a function of the angular coordinates θ' and ϕ' and of time t: $v = v(R, \theta', \phi', t)$. The function $g(v)$ is a Gaussian with variance v_{th}^2.

We define the jth moment of the line profile as follows:

$$\langle v^j \rangle_{f*g} \equiv \frac{\int_{-\infty}^{+\infty} v^j p_{\mathrm{theo}}(v)\,\mathrm{d}v}{\int_{-\infty}^{+\infty} p_{\mathrm{theo}}(v)\,\mathrm{d}v} = \frac{\int_{-\infty}^{+\infty} v^j (f * g)(v)\,\mathrm{d}v}{\int_{-\infty}^{+\infty} (f * g)(v)\,\mathrm{d}v} \tag{5.51}$$

with v the component of the total (pulsation + rotation) velocity field in the line-of-sight.

All the information contained in the line profile can be reconstructed from the entire series of moments of order j. In practice, we consider the first three moments, *i.e.*, those for $j = 1, 2, 3$. There are several reasons for that, the major one being that each of these first three moments is connected to a specific property of the line profile:

1. the first moment $\langle v \rangle$ is the *centroid* of the line profile in a reference frame with origin at the stellar centre;
2. the second moment $\langle v^2 \rangle$ is a measure of the width of the line profile;
3. the third moment $\langle v^3 \rangle$ is a measure of the skewness of the line profile.

All higher-order moments can be written in terms of the first three moments for profiles whose wings do not deviate much from a Gaussian. For the practical application to observed line-profile variations one easily shows that the noise level in the observed moments increases with increasing moment order and that the noise is higher for even moments than for odd moments. Aerts *et al.* (1992) and Aerts (1996) showed that the use of the three lowest-order moments is the optimal balance between having a clear signal and adding independent information. Thus, each measured line profile is replaced by its first three normalised moments $\langle v \rangle$, $\langle v^2 \rangle$ and $\langle v^3 \rangle$.

Theoretical expression of the moments for a monoperiodic oscillation

In Eq. (5.51) we consider *normalised* moments, *i.e.*, each moment is divided by the *moment of order zero* M_0. The latter is the equivalent width of the line profile (see Chapter 4). The division by the equivalent width is very convenient because small temperature and flux variations during the oscillation are more or less averaged out in this way, as they occur in the same way in the numerator and denominator in the definition of the moments. De Pauw *et al.* (1993) tested the robustness of the mode identification against small equivalent-width variations and found the assumption of a constant M_0 to be acceptable up to equivalent-width changes of 5% in amplitude.

We subsequently make use of the property that the integral of a convolution equals the product of the integrals of the functions to be convolved. Hence it is straightforward to show that the first three moments can be written as:

$$\begin{aligned}
\langle v \rangle_{f*g} &= \langle v \rangle_f + \langle v \rangle_g, && (5.52)\\
\langle v^2 \rangle_{f*g} &= \langle v^2 \rangle_f + 2\langle v \rangle_f \langle v \rangle_g + \langle v^2 \rangle_g, && (5.53)\\
\langle v^3 \rangle_{f*g} &= 3\langle v^2 \rangle_f \langle v \rangle_g + 3\langle v \rangle_f \langle v^2 \rangle_g && (5.54)\\
&\quad + \langle v^3 \rangle_f + \langle v^3 \rangle_g.
\end{aligned}$$

The odd moments of a Gaussian with average 0 km/s and variance $v_{\rm th}^2$ are zero. The second moment of the intrinsic Gaussian equals $v_{\rm th}^2$. Thanks to these simple properties of a Gaussian, the convolution with the

Gaussian intrinsic profile can be written as follows:

$$\begin{aligned}
\langle v\rangle_{f*g} &= \langle v\rangle_f, && (5.55)\\
\langle v^2\rangle_{f*g} &= \langle v^2\rangle_f + v_{\rm th}^2, && (5.56)\\
\langle v^3\rangle_{f*g} &= \langle v^3\rangle_f + 3v_{\rm th}^2\langle v\rangle_f. && (5.57)
\end{aligned}$$

By considering the component of the total velocity vector $\vec{v} = \vec{v}_{\rm puls} + \vec{v}_{\rm rot}$ and by transforming the expression for $f(v)$ given by (5.44) to the reference frame (r, θ, ϕ) connected with the stellar rotation axis, we obtain the following expressions for the three normalised moments of a monoperiodic non-radial oscillator with infinite lifetime, after integration over the visible stellar surface:

$$\begin{aligned}
\langle v\rangle_{f*g} &= v_{\rm p}A(l,m,i)\sin(\omega t+\delta), && (5.58)\\
\langle v^2\rangle_{f*g} &= v_{\rm p}^2C(l,m,i)\sin(2\omega t+2\delta+3\pi/2) && (5.59)\\
&+ v_{\rm p}v_{\Omega}D(l,m,i)\sin(\omega t+\delta+3\pi/2)\\
&+ v_{\rm p}^2E(l,m,i)+v_{\rm th}^2+b_2v_{\Omega}^2\\
\langle v^3\rangle_{f*g} &= v_{\rm p}^3F(l,m,i)\sin(3\omega t+3\delta) && (5.60)\\
&+ v_{\rm p}^2v_{\Omega}G(l,m,i)\sin(2\omega t+2\delta+3\pi/2)\\
&+ \Big[v_{\rm p}^3R(l,m,i)+v_{\rm p}v_{\Omega}^2S(l,m,i)+v_{\rm p}v_{\rm th}^2T(l,m,i)\Big]\\
&\times \sin(\omega t+\delta).
\end{aligned}$$

In these expressions, δ is a phase constant depending on the chosen reference epoch and b_2 is a constant that depends only on the limb-darkening law. The functions $A, C, D, E, F, G, R, S, T$ depend on the (l, m) of the oscillation mode and on the inclination angle. Together with the pulsation velocity amplitude $v_{\rm p}$, these dimensionless and normalised functions contain the complete physical information connected with the theoretical expression of the non-radial oscillation mode. The derivation of the expressions for these (complicated) functions was presented by Aerts *et al.* (1992) to which we refer the reader for further information. We only consider the case of the first moment in somewhat more detail here. The function $A(l, m, i)$ can be decomposed as

$$A(l,m,i) = a_{l,m,0}(i)\cdot a(l,K,h_\lambda). \qquad (5.61)$$

An explicit expression for $a(l, K, h_\lambda)$ is available in Aerts *et al.* (1992) and in De Ridder *et al.* (2002) and is omitted here. From this decomposition, we encounter in a natural way again the same IACCs as for a photometric lightcurve, as the angles i for which $a_{l,m,0}(i) = 0$. Moreover, we can estimate the partial cancellation effect for spectroscopy from $a(l, K, h_\lambda)$. Some values are graphically depicted in Fig. 5.15 for two main-sequence stars with different spectral types (B and G) and for a typical p mode (upper panel) and g mode (lower panel). First of all, a comparison of Figs 5.5 and 5.15 shows at once that the partial cancellation effect is very different for a photometric time series compared with a spectroscopic one. While the decrease in detectability of modes with increasing l is apparent for photometry, this is not the case for spectroscopy. This explains why a larger variety of mode degrees is detected in spectroscopic data. It can be seen from Fig. 5.15 that, for p modes with the same intrinsic amplitude, those with $l = 2$ are easiest to detect in spectroscopy if we ignore the projection effect, particularly for hot stars. Modes with $l = 1$ and 3 have equal probability of being detected if they have the same intrinsic amplitude and similar projection effect. This explains why such modes have been derived from spectroscopy for some stars, while $l = 3$ modes are

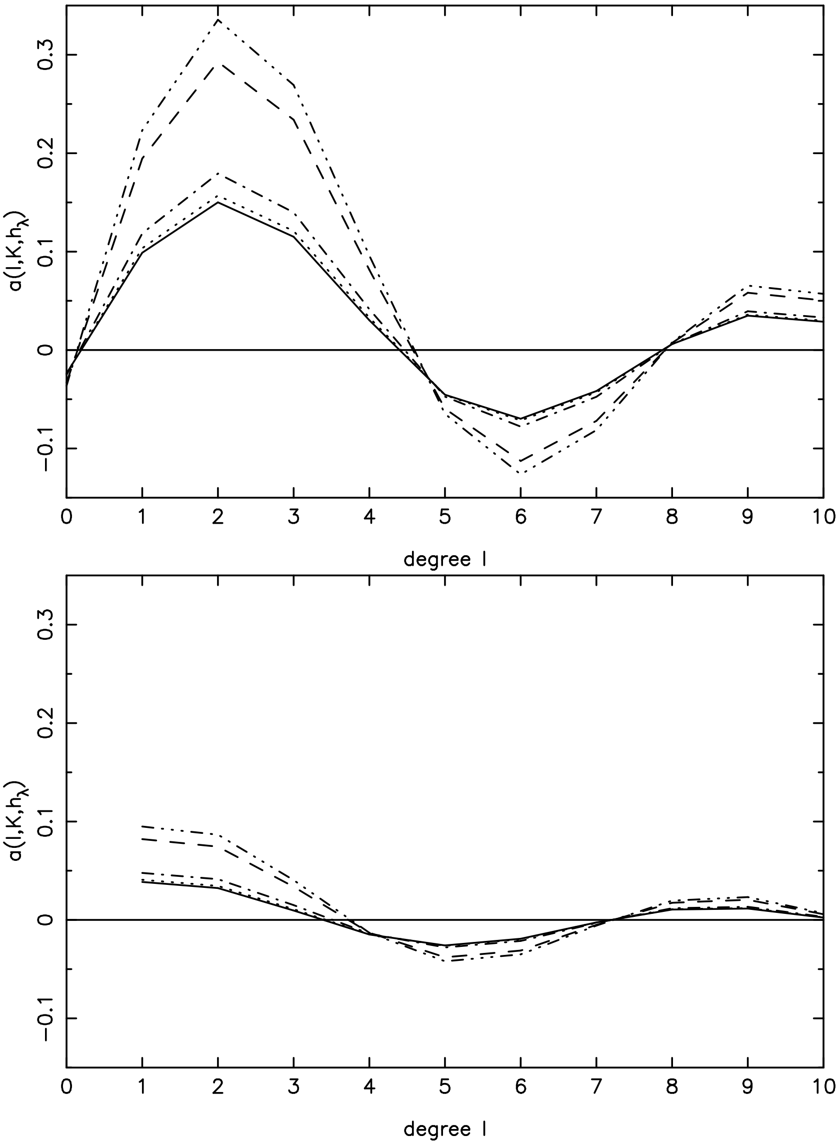

Figure 5.15: The function $a(l, K, h_\lambda)$ is shown for different mode degrees l for a linear limb-darkening law taken from Claret (2000). We considered a star of $T_{\rm eff} = 6000$ K and $\log g = 4.0$ at the wavelengts of the U (full line), B (dotted line) and V (dashed-dot line) filters, as well as a star of $T_{\rm eff} = 25000$ K and $\log g = 4.0$ at U and B (indistinguishable, shown as dashed line) and V (dashed-dot-dot-dot line) wavelengths. Upper panel: results for a typical p mode with $K = 0.1$; lower panel: results for a g mode with K=10.

usually absent in photometry (see, *e.g.*, the example of the β Cep star β Cru, Aerts *et al.* 1998). In general, the detected heat-driven p modes in individual target stars that have been studied do not follow the patterns predicted from Figs 5.5 and 5.15. This probably means that the intrinsic amplitudes of the excited p modes are clearly different, although the inclination effect may also partly be the cause of this.

The situation is quite different for g modes, which have, first of all, smaller $a(l,K,h_\lambda)$ values than p modes. They are thus harder to detect. In this case, the modes with $l=1$ and 2 are equally probable of being detected and the bottom panel of Fig. 5.15 shows that it is easier to achieve this for B stars than for G stars. Modes with higher degree are very hard to detect. This is fully compatible with the observations of g modes in SPBs (Townsend 2003, De Cat *et al.* 2005) and in γ Dor stars (Aerts *et al.* 2004, Dupret et al. 2005).

Computation of the observational moments

In practice we have sets of numbers (λ_i, F_i) with $i = 1, \ldots, N$ at our disposal for each measured line profile. Here, F_i stands for the normalised flux value measured at wavelength λ_i for pixel i. These profiles are considered to be barycentric, *i.e.*, their observation time and wavelengths have been shifted to the barycentre of the solar system in order to take into account the motion of the Earth around the Sun. The star under consideration exhibits an (*a priori* unknown) radial velocity with respect to the Sun caused by its space motion and any binary orbital motion. These space motions are not of interest to us here and are not contained in the theoretical expressions of the moments, which are valid for a reference frame connected to the stellar centre. We therefore have to correct the observed line profile (λ_i, F_i) for the radial velocity shift of this space motion, before we can study the intrinsic velocity due to the oscillation of the star as it occurs in the theoretical expressions (5.58), (5.59), (5.60) of the moments. This implies that we have to determine the observed moment variations in three different stages:

1. First we determine the *small unnormalised moments* as follows:

$$m_0 = \sum_{i=1}^{N}(1-F_i)\Delta x_i, \tag{5.62}$$

$$m_1 = \sum_{i=1}^{N}(1-F_i)x_i\Delta x_i, \tag{5.63}$$

$$m_2 = \sum_{i=1}^{N}(1-F_i)x_i^2\Delta x_i, \tag{5.64}$$

$$m_3 = \sum_{i=1}^{N}(1-F_i)x_i^3\Delta x_i, \tag{5.65}$$

with $\Delta x_i \equiv x_i - x_{i-1}$ where x_i is the velocity corresponding to λ_i with respect to the laboratory wavelength of the spectral line. One has to make a clever choice for the velocity (or wavelength) range $[x_1, x_N]$: not too narrow a range in order to have all the information in the line profile contained in the moment values and not too broad to limit the noise in the calculated higher-order moments.

2. The reduction of the small moments to average zero is achieved by correcting for the relative motion of the star with respect to the Sun. This motion is given by the average radial velocity of the star, which is the average value of m_1/m_0 (unit km s^{-1}). We denote this average by x_0. The *large unnormalised moments* are obtained by using x_0 as a reference value:

$$\begin{aligned} M_0 &= \sum_{i=1}^{N}(1-F_i)\Delta x_i, && (5.66)\\ M_1 &= \sum_{i=1}^{N}(1-F_i)(x_i-x_0)\Delta x_i, && (5.67)\\ M_2 &= \sum_{i=1}^{N}(1-F_i)(x_i-x_0)^2\Delta x_i, && (5.68)\\ M_3 &= \sum_{i=1}^{N}(1-F_i)(x_i-x_0)^3\Delta x_i. && (5.69)\end{aligned}$$

   This leads to odd moments with average zero.

3. Finally, we obtain the observed normalised moments $\langle v^j\rangle$ for $j=1,\ldots,3$ as M_j/M_0. These moments now have velocity units (km s^{-1})^j and can be compared with the theoretical expressions (5.58) – (5.60).

Interpretation of the moments

The periodograms of the three moments are immediately interpretable in terms of the oscillation frequencies of the detected modes. The variations of the moments $\langle v^j\rangle$ in time are thus a very suitable diagnostic that allows one to derive the temporal behaviour of the oscillations in full detail. It usually suffices to search the frequencies of the modes in the observed first moment variations, but some modes may show up easier in $\langle v^2\rangle$.

As soon as the oscillation frequencies have been derived, one is able to construct phase diagrams of the moment variations from a harmonic analysis as explained in Chapter 5. The results of such a harmonic analysis are observational values for the different amplitudes that occur in the theoretical expressions Eqs (5.58), (5.59), (5.60) of the moments. We are therefore able to derive information about the six oscillation parameters $(l, m, i, v_{\rm p}, v_\Omega, v_{\rm th})$. We explain how to do that, by means of an example.

In Figs 5.16 and 5.17 we show some observed profile variations and the three normalised moments of the δ Sct star ρ Puppis. The full lines in Fig. 5.17 correspond to the result of a harmonic analysis according to the Eqs (5.58), (5.59) and (5.60). The peak-to-peak value of the first moment gives an idea about the overall velocity range due to the oscillation with that particular frequency, although it is an integrated quantity. For linear oscillations (an assumption we adopted for the theoretical description of the moment method) we expect this range to be well below the sound speed in the line-forming region within the stellar atmosphere. If not, shock waves occur and the description of the modes in terms of a sine function is no longer valid.

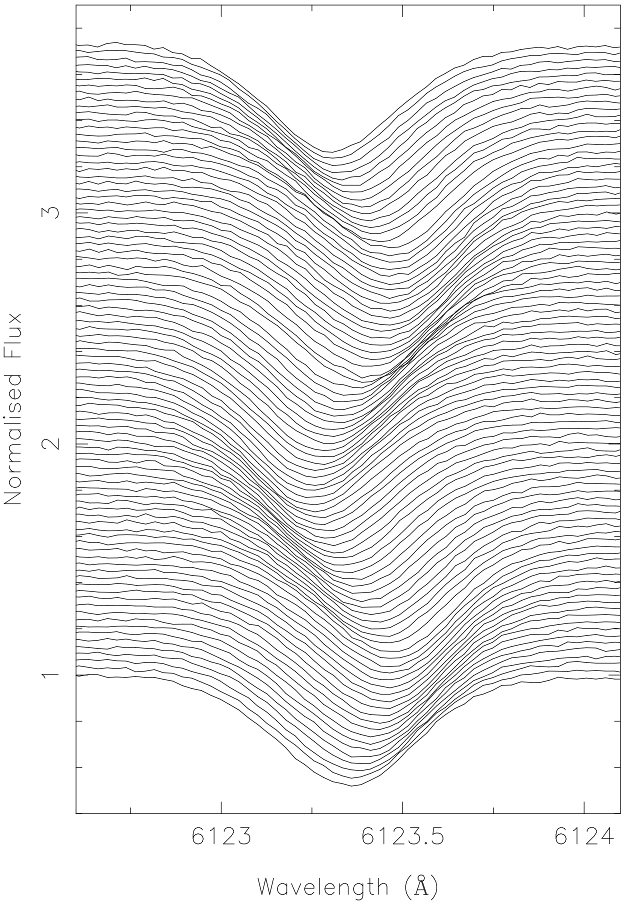

Figure 5.16: Some observed line-profile variations of the δ Sct star ρ Puppis obtained in 1995 with the Coudé Auxiliary Telescope of the European Southern Observatory in Chile phased with the dominant frequency of 7.098 d^{-1}. Data taken from Mathias *et al.* (1997).

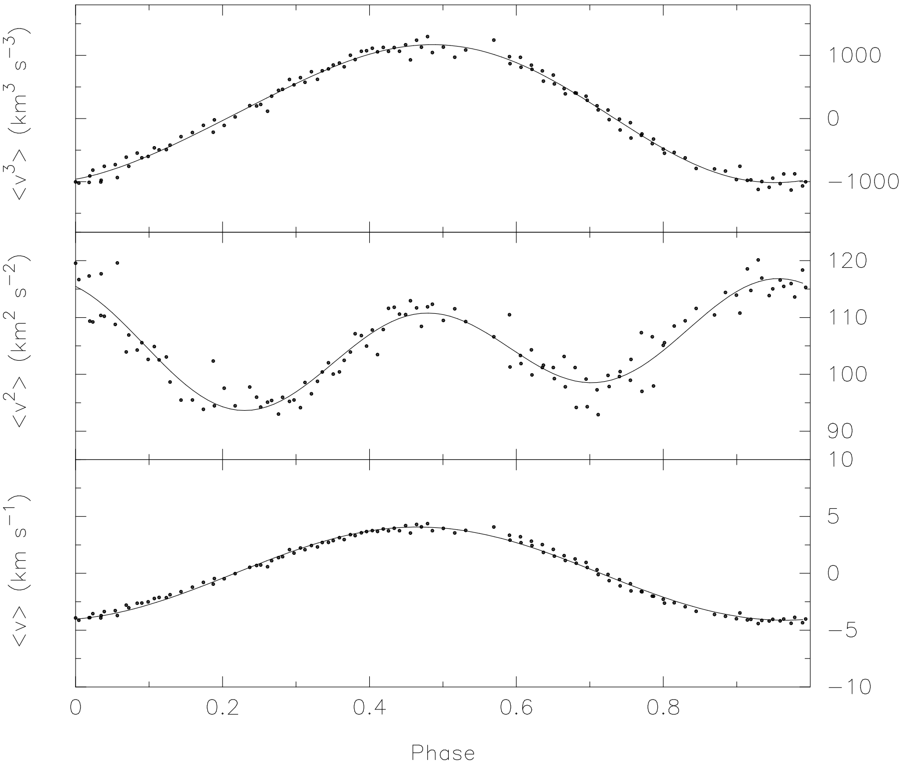

Figure 5.17: Phase diagrams of the normalised moments of the δ Sct star ρ Puppis for the dominant frequency 7.098 d^{-1}. The dots are the observations and the lines are the result of harmonic analyses according to expressions (5.58), (5.59) and (5.60). Data taken from Mathias *et al.* (1997). The analysis shows that this mode is radial. Part of the scatter in the diagrams arises from the presence of other, weaker modes.

For a linear oscillation, the first moment is expected to behave sinusoidally as is the case for ρ Puppis (see Figure 5.17).

The second moment turns out to be a very good diagnostic for the azimuthal number m. Indeed, as shown in Aerts *et al.* (1992), the function $D(l,m,i)$ equals zero for $m=0$. This allows us readily to distinguish between $m=0$ and $m\neq 0$ from a harmonic analysis of $\langle v^2\rangle$. Whenever the temporal behaviour of $\langle v^2\rangle$ can be described by a single sine function with frequency 2ω we are sure that $m=0$. The middle panel of Figure 5.17 therefore implies that it is likely that $m=0$ for the main mode of ρ Puppis, although there is clearly a small sinusoidal contribution with frequency ω since the shape of $\langle v^2\rangle$ is not fully symmetric. On the other hand, Aerts *et al.* (1992) have shown that $C(l,l,i)=0$. This implies that $\langle v^2\rangle$ will behave purely sinusoidally with frequency ω in the case of a sectoral mode. Any intermediate situation, *i.e.*, a second moment in which both a term with ω and one with 2ω occur with equal amplitudes, points towards a tesseral mode.

In order to obtain a complete identification of the mode from the three moments, one proceeds as follows. The idea is to compare the observed variations of the moments with their theoretical expectations and to select the most likely set of parameters $(l,m,i,v_{\rm p},v_\Omega,v_{\rm th})$. This comparison is done objectively by means of the calculation of the so-called *discriminant*. This is a function based on the observed amplitudes of the moments for all terms that occur in the moment variations, *i.e.*, one term in $\langle v\rangle$, three terms in $\langle v^2\rangle$ and three terms in $\langle v^3\rangle$. The discriminant is defined as follows:

$$\begin{aligned}\Gamma_l^m\quad &(v_{\rm p},i,v_\Omega,v_{\rm th})\equiv\Bigg[\Big|A_{\rm obs}-v_{\rm p}|A(l,m,i)|\Big|^2 f_A^2\\
&+\left(\Big|C_{\rm obs}-v_{\rm p}^2|C(l,m,i)|\Big|^{1/2} f_C\right)^2\\
&+\left(\Big|D_{\rm obs}-v_{\rm p}v_\Omega|D(l,m,i)|\Big|^{1/2} f_D\right)^2\\
&+\left(\Big|E_{\rm obs}-v_{\rm p}^2|E(l,m,i)|-v_{\rm th}^2-b_2v_\Omega^2\Big|^{1/2} f_E\right)^2\\
&+\left(\Big|F_{\rm obs}-v_{\rm p}^3|F(l,m,i)|\Big|^{1/3} f_F\right)^2\\
&+\left(\Big|G_{\rm obs}-v_{\rm p}^2v_\Omega|G(l,m,i)|\Big|^{1/3} f_G\right)^2\\
&+\Bigg(\Big|T_{\rm obs}-v_{\rm p}^3|R(l,m,i)|-v_{\rm p}v_\Omega^2|S(l,m,i)|\\
&\quad -v_{\rm p}v_{\rm th}^2|T(l,m,i)|\Big|^{1/3} f_T\Bigg)^2\Bigg]^{1/2}\end{aligned}\tag{5.70}$$

(Aerts 1996). Here $A_{\rm obs},C_{\rm obs},\ldots,T_{\rm obs}$ are the observed values of the functions $A(l,m,i),C(l,m,i),\ldots$ *etc.* occurring in Eqs (5.58), (5.59) and (5.60) of the theoretical predictions of the moments. These can be found from a harmonic least-squares fit to the observed moment time series. The quantities $f_A,\ldots,f_T$ are normalised weights that take into account the quality of such a fit to the observed moments. An amplitude that has a smaller standard error will receive a larger weight in the discrimination among the candidate l-values because it is more dominant in the discriminant Γ_l^m compared with an amplitude with a large standard error. The discriminant is constructed in such a way that it is expressed in $\mathrm{km\,s^{-1}}$. From its definition, it is unable to distinguish between positive and negative m. However, a greyscale representation of the observed line profiles or the phase behaviour across the line profile (see below) provides this additional information on the sign of m.

The adopted criterion for mode identification works as follows: the function $\Gamma_l^m(v_\mathrm{p}, i, v_\Omega, v_\mathrm{th})$ is minimized for each set (l, m):

$$\gamma_l^m \equiv \min_{v_\mathrm{p}, i, v_\Omega, v_\mathrm{th}} \Gamma_l^m(v_\mathrm{p}, i, v_\Omega, v_\mathrm{th}). \tag{5.71}$$

As "overall best solution" for l and m we retain the one with the lowest γ_l^m. This solution also provides us the most likely values for the continuous unknowns in the velocity expression, namely $v_\mathrm{p}, i, v_\Omega$ and v_th.

De Pauw *et al.* (1993) and Aerts (1996) each made an extensive simulation study to test the performance of the discriminant, taking into account realistic gapped time series with an appropriate noise level. In these papers, one also finds numerous examples of the behaviour of the three moments as a function of (l, m, i), and of the radial and horizontal amplitudes v_p and Kv_p. We advise a new user of the method to study these two simulation papers carefully and we refer to the paper by Aerts (1996) for more information on the performance of the discriminant defined in Eq. (5.70). In particular we warn the user not to accept solutions with i close to an IACC. Viewing in the direction of a nodal line of a mode is an easy way to get small amplitudes for the moment terms. Thus, stars with low moment amplitudes are easily explained by any (l, m) for inclinations equal to their IACC. The predictive power of the discriminant cannot be large in such a case. This must be kept in mind whenever interpreting the minima γ_l^m. An example of such a situation is discussed in detail in Sect. 5.2.3.

A robustness test was done by De Pauw *et al.* (1993) to assess the assumption of constant equivalent width despite the occurrence of $\delta T/T$. It turned out that the discriminant defined in Eq. (5.70) keeps performing well in identifying the correct input mode as long as the peak-to-peak variations of M_0 remain below 10% (De Pauw *et al.* 1993). This good performance occurs thanks to the use of normalised moments. It would not hold if we would work with M_1, M_2, M_3 without dividing them by M_0. Since most of the pulsating stars fulfil the criterion of having equivalent-width variations below 10% (see, *e.g.*, De Ridder *et al.* 2002 for B pulsators), it is indeed not necessary to include the consequences of $\delta T/T$ in the discriminant of the moment method, as already anticipated above. This is a very comforting situation, as we are thus not dependent on the details of the non-adiabatic oscillation theory in the outer atmosphere to identify the modes. All one relies on is the velocity expression in Eq. (5.40). *This is significant advantage over photometric mode identification.* Of course, the condition of the relative amplitude of M_0 being below 10% should be tested in any application of the discriminant.

The moment method as presented here is a good identification method, particularly for low-degree modes ($l \leq 4$). It is complementary to the Pixel-by-Pixel method outlined below. Modes with high degree $(l \geq 5)$ have very small moment amplitudes with large standard errors, which limits the application of the discriminant for such cases.

The application of the discriminant defined in Eq. (5.70) for the moments of ρ Puppis shown in Fig-

Table 5.2: The minima of the discriminant for the main mode of the δ Sct star ρ Puppis. γ_l^m, $v_{\rm p}$, $Kv_{\rm p}$, v_Ω and $v_{\rm th}$ are expressed in $\rm km\,s^{-1}$.

l	$\lvert m \rvert$	γ_l^m	$v_{\rm p}$	$Kv_{\rm p}$	i	v_Ω	$v_{\rm th}$
0	0	0.08	5.6	0.218	–	15.3	6.5
1	1	0.13	10.0	0.390	38°	14.8	5.9
2	1	0.17	12.1	0.472	64°	16.4	2.2
1	0	0.18	5.0	0.195	7°	19.6	1.7
2	2	0.23	15.0	0.585	53°	10.3	4.8
⋮	⋮	⋮	⋮	⋮	⋮	⋮	⋮

ure 5.17 is given in Table 5.2.

One finds a radial main mode for this star, as was already suggested by Campos & Smith (1980). The finding that $m = 0$ could be anticipated from the behaviour of $\langle v^2 \rangle$. The latter, however, does deviate from a pure double sine (see Fig. 5.17). Such a deviation is expected whenever additional modes, besides the dominant one, are present. Mathias *et al.* (1997) indeed found with two additional candidate low-amplitude modes in ρ Puppis. Due to their beating with the dominant mode, $\langle v^2 \rangle$ is not perfectly symmetric. The same situation occurs for the line-profile variations and their $\langle v^2 \rangle$ of the β Cep star δ Ceti (Aerts *et al.* 1992), whose low-amplitude modes were revealed in MOST space photometry (Aerts *et al.* 2006). The second moment is thus a suitable diagnostic to detect low-amplitude modes.

The largest shortcoming of the discriminant is that it lacks a statistical significance test. In other words, we have no means to decide if the mode with the lowest γ_l^m in the list of best candidates in Table 5.2 is truly better than the following solutions, or if it is acceptable to a certain significance level. This was elaborated upon by De Ridder *et al.* (2005), but the complexity of the theoretical expressions for the moments, and the mixture of discrete and continuous unknowns, prevented a solid goodness-of-fit test. The best procedure to adopt, as already mentioned above, is to generate theoretical line-profile variations for the top listed solutions and compare them with the data. In this way, one first eliminates a sufficient number of unlikely combinations of l, m, $v_{\rm p}$, i, v_Ω and $v_{\rm th}$ from the moment variations before starting a line-profile fitting method, fixing l and m combinations from a list like the one in Table 5.2 and allowing for slight changes in the continuous parameters to minimize the deviation between the observed and theoretically computed profiles. Even after such a test, it may still be impossible to discriminate among several (l, m) combinations and one should not do so in such a situation. In fact, confusion between different (l, m) is inherent to the mode-identification problem. A radial mode, *e.g.*, will resemble a $(1, 1)$ mode looked upon from the equator and is indistinguishable from a $(1, 0)$ mode viewed from the pole. There are several combinations of $(l, m, v_{\rm p}, i)$ that have closely resembling profiles, and thus moment variations. There are also cases where the profiles are not very similar, but the moment values are, because of the integration over the surface. Such cases can still be distinguished by applying the Pixel-by-Pixel method discussed in Sect. 5.2.4. To unravel similar profiles resulting from different combinations of $(l, m, v_{\rm p}, i)$, one needs a strong constraint on the inclination angle. Multiperiodicity helps in this respect, as will be shown below, but independent

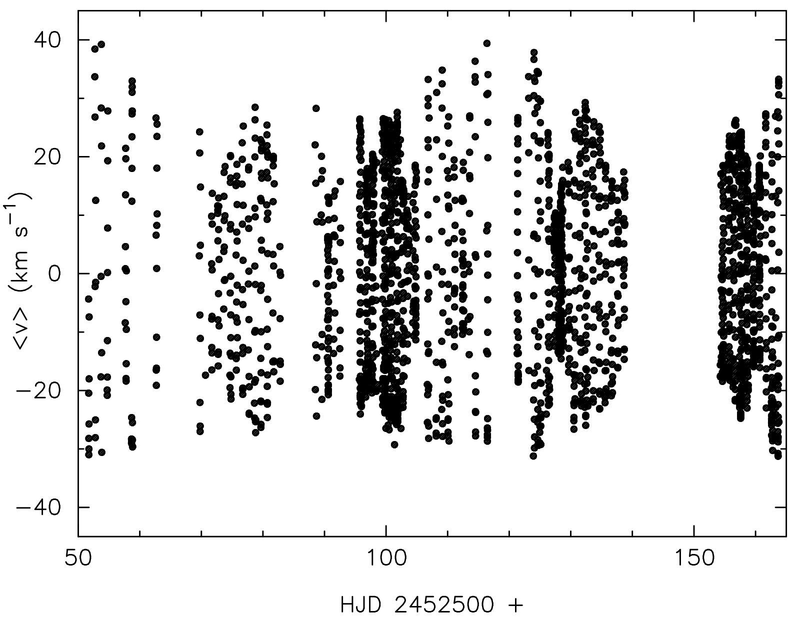

Figure 5.18: Time series of the first velocity moment of the multiperiodic β Cep star ν Eridani derived from a five-month dedicated multisite campaign (Aerts *et al.* 2004).

observational information is needed as well. This will be illustrated for the case of the δ Sct star 20 CVn in Sect. 5.2.3.

Generalisation to multiperiodic oscillations and to a numerical version of the discriminant

A generalization of the mode-identification method described above for a multiperiodic star was provided by Mathias *et al.* (1994). Whenever more than one mode is excited to measurable amplitude, the moment variations become more complicated. The first moment will simply consist of a linear superposition of all the separate modes. However, this is no longer the case for the second and third moments, as they will contain coupling terms from taking the square and the third power of the velocity expression in the integrand of Eq. (5.51). For example, a biperiodic oscillation with frequencies ω_1 and ω_2 will give rise to six frequencies in the second moment: ω_1, $2\omega_1$, ω_2, $2\omega_2$, $\omega_1 - \omega_2$ and $\omega_1 + \omega_2$. The third moment will in that case have to be fitted with twelve frequencies: those of $\langle v^2 \rangle$ and in addition $3\omega_1$, $3\omega_2$, $2\omega_1 + \omega_2$, $2\omega_1 - \omega_2$, $2\omega_2 + \omega_1$ and $2\omega_2 - \omega_1$. The number of frequencies occurring in the moment expressions increases very rapidly with the number of modes. *This is a disadvantage of this method.*

In order for the harmonic analysis to be accurate for a multiperiodic oscillation, *i.e.,* to lead to amplitudes with a small standard error as input for the discriminant, it is necessary to cover all the beat frequencies with line-profile observations. The sampling of the data also has to be of high temporal resolution in order to estimate the amplitudes of the sum frequencies in an accurate way. This fact implies large observational challenges. An example in which a beat phenomenon occurs in the time series of centroid velocities derived from spectra of the β Cep star ν Eri, which was the target of a multisite campaign, is shown in Fig. 5.18.

A beat pattern is clearly visible in this figure. Several other time series including beating phenomena were already shown in Chapter 2, such as in Figs 2.9, 2.13, 2.19, 2.21, 2.23, 2.50. The challenges are most prominent for stars with multiperiodic g-mode oscillations, such as slowly pulsating B stars, γ Doradus stars, pulsating Be stars and pulsating supergiants. In all of those, the beat periods can be of the order of months to years.

Solving the mode identification for multiperiodic oscillations is, of course, more complex than for a single mode. Three unknowns (l, m, v_p) are added for each additional oscillation mode. On the other hand, having more than one mode helps significantly to discriminate among almost equivalent solutions with different inclination angles i. From the very complicated analytical expressions for $\langle v^2\rangle$ and $\langle v^3\rangle$ available in Mathias *et al.* (1994), one sees that almost all of the terms contain couplings between different frequencies. As a consequence, identification of the modes is best performed simultaneously, and not mode by mode as was originally done by Mathias *et al.* (1994). With the advent of faster computers, the option of simultaneous identification of all detected frequencies in the moments was implemented by Briquet & Aerts (2003). With this technique, the authors did not used the analytical expressions of the moments to identify the modes as Aerts (1996) did. Instead, they computed line-profile variations for various combinations of the parameters, derived their moments numerically as in Sect. 5.2.3, and compared them with the corresponding values derived from the observations, in a similar way as in Eq. (5.70). Given that many of the factors occurring in the moments can be separated, one only needs to compute them once and stack them into huge tables. In that way, the moment method of Briquet & Aerts (2003) is more than a factor of ten faster than the version of Mathias *et al.* (1994).

Application to cross-correlation or least-squares-deconvolved profiles

The requirements on the quality of the spectra to apply the moment method successfully are stringent. The same is true for the Pixel-by-Pixel method, as will be discussed below. This limits the applicability of the methods to very bright stars (typically with $V < 6$ for telescopes with diameter below 4m) with not too short oscillation periods (typically longer than 15 min). One can overcome this obstacle, to a certain extent, by combining the information present in different spectral lines, such that fainter stars can be considered as well, or the integration times can be limited, or lower-amplitude modes can be searched for. Although of interest, one will seldom gain information on the correct (l, m) when repeating an analysis on additional different individual lines, because the best line will have been picked to start with in the first place.

While one can in principle combine the $\langle v\rangle$ values of different lines, this is certainly not true for $\langle v^2\rangle$ and $\langle v^3\rangle$. Indeed, each of the lines has its own thermal broadening, *i.e.*, its own value of v_th. This leads to a different constant term EE for $\langle v^2\rangle$ and different amplitudes for $\langle v^3\rangle$ for each of the lines, as can be seen from Eqs (5.59) and (5.60). One could still merge the second moments $\langle v^2\rangle$ of different lines, after shifting them to a common constant term $EE = 0$ and by avoiding using that term in Eq. (5.70) for the mode identification. However, the amplitudes are also different for different lines, because there is always some level of blending and this is different for different lines (see, *e.g.*, Mathias *et al.* (1994) for a thorough discussion and illustrations). *The conclusion is that a simple line-by-line treatment is not helpful, from the viewpoint of improving the mode identification.* Such an analysis is very useful, however, to detect small shock phenomena and details of wave propagation in the outer stellar atmosphere (*e.g.*, Crowe & Gillet

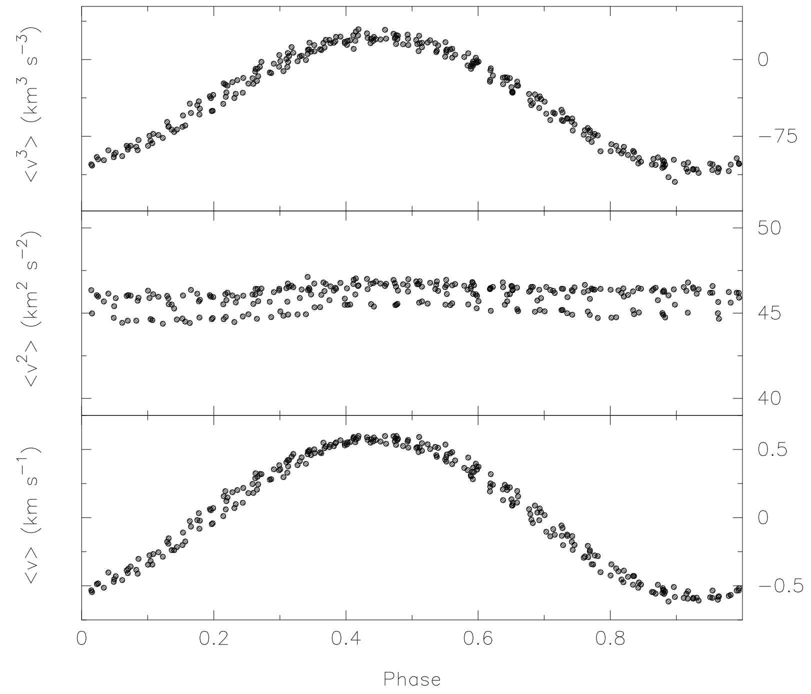

Figure 5.19: Phase diagrams of the observed normalised moments derived from cross-correlation functions of the δ Sct star 20 CVn for the frequency 8.2168 d^{-1} (Chadid *et al.* 2000).

1989; Mathias *et al.* 1991; Mathias & Gillet 1993).

We thus must search for a different way to combine the information in different spectral line variations. Whenever the different line-forming regions do not enclose nodal surfaces and are situated not too far from each other, one expects the moments to vary perfectly in phase with each other. This can easily be tested in practice. In that case, one may combine them to increase the S/N level. This can be done by computing a cross-correlation function (CCF) of each spectrum, or by least-squares deconvolution (LSD), as outlined in Chapter 4. One finds numerous examples of oscillation signatures in the CCFs of γ Dor stars in De Cat *et al.* (2006). It is very clear from that paper that the oscillations turn up in the CCFs. How to use them for mode identification, is, however, another issue to that of detecting the modes.

While computing the CCF or LSD, the same requirement as for the individual lines should be respected, *i.e.*, the study must be restricted to unblended thermally-broadened metal lines. This usually reduces the number of spectral lines considerably compared with the case where computation of the most accurate radial-velocity value is the goal. The S/N level in the CCF or LSD will increase by a factor $\sqrt{N}$, with N the number of lines used for the CCF or LSD, so even using only four lines for a mask to derive the CCF or for the computation of the LSD will imply doubling the S/N level.

One should not be fooled by thinking that the application of the moment method to such type of variations is exactly the same as for the individual spectral lines. This is not the case, because the second moment $\langle v^2\rangle$ of the CCF or LSD is again affected by the merging of lines with different $v_{\rm th}$ and by slight differences

Table 5.3: The minima of the discriminant according to Eq. (5.70) (left) and of the deviation parameter from line-profile fitting following Eq. (5.50) (right) for the monoperiodic δ Sct star 20 CVn (Chadid *et al.* 2000).

l	$\|m\|$	γ_l^m	$v_{\rm p}$	$Kv_{\rm p}$	i	v_Ω	$v_{\rm th}$	l	m	Σ_l^m	$v_{\rm p}$	$Kv_{\rm p}$	i	v_Ω	$v_{\rm th}$
3	2	0.09	4.50	0.27	75°	6	5.0	2	0	0.0022	2.50	0.15	45°	4.0	5.5
0	0	0.12	0.75	–	–	5	6.0	3	0	0.0022	2.00	0.12	25°	4.0	5.7
3	0	0.12	4.00	0.24	55°	6.0	4.0	0	0	0.0023	0.85	–	–	7.0	5.0
1	1	0.13	1.00	0.06	80°	6.0	5.0	3	+1	0.0024	2.50	0.15	85°	6.0	5.5
1	0	0.15	2.00	0.12	70°	6.0	5.0	4	+4	0.0026	1.50	0.09	70°	6.0	5.5
3	1	0.15	5.00	0.30	55°	5.0	5.0	3	+2	0.0026	3.00	0.18	15°	6.0	5.5
2	0	0.17	1.50	0.09	35°	7.0	5.5	3	-2	0.0027	3.00	0.18	15°	4.0	5.5
2	1	0.17	3.50	0.21	80°	4.0	5.5	2	+1	0.0029	2.00	0.12	90°	4.0	5.5
⋮	⋮	⋮	⋮	⋮	⋮	⋮	⋮	⋮	⋮	⋮	⋮	⋮	⋮	⋮	⋮

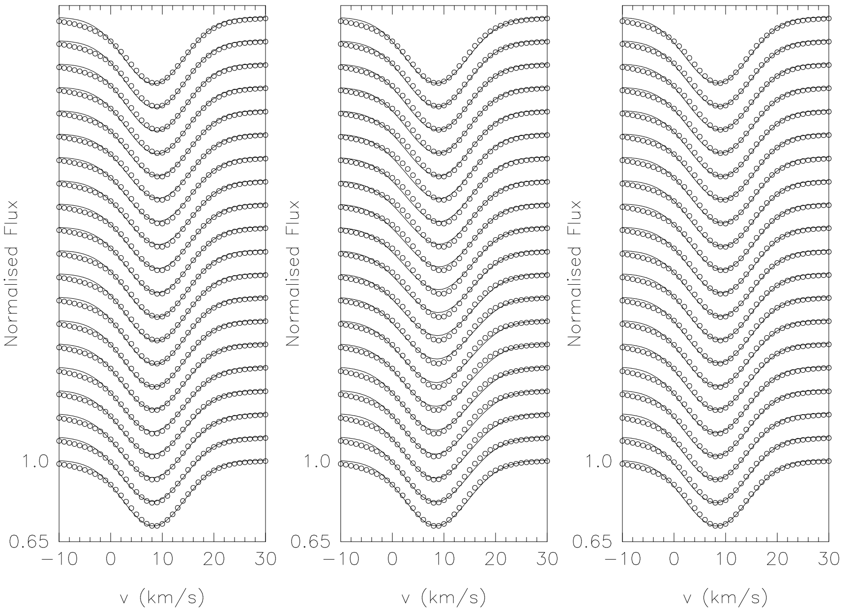

Figure 5.20: Theoretically determined line-profile variations (full lines) are compared with the observed cross-correlation functions (open circles) of the δ Sct star 20 CVn. The input modes are (l, m) equal to $(2, 0)$ (left), $(4, +4)$ (middle), $(0, 0)$ (right). The continuous input parameters are listed in the right part of Table 5.3 (Chadid *et al.* 2000).

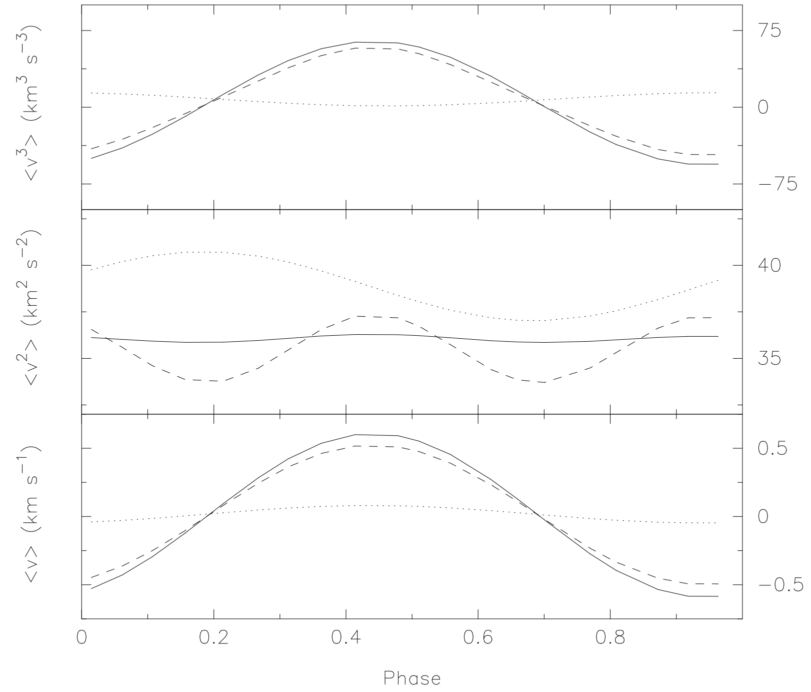

Figure 5.21: Theoretically determined moment variations for (l, m) equal to $(0, 0)$ (full line), $(2, 0)$ (dashed line) and $(4, +4)$ (dotted line) for the parameters listed in the right part of Table 5.3. These moments correspond to the theoretical line-profile variations shown in Fig. 5.20 and should be compared with the observed ones shown in Fig. 5.19.

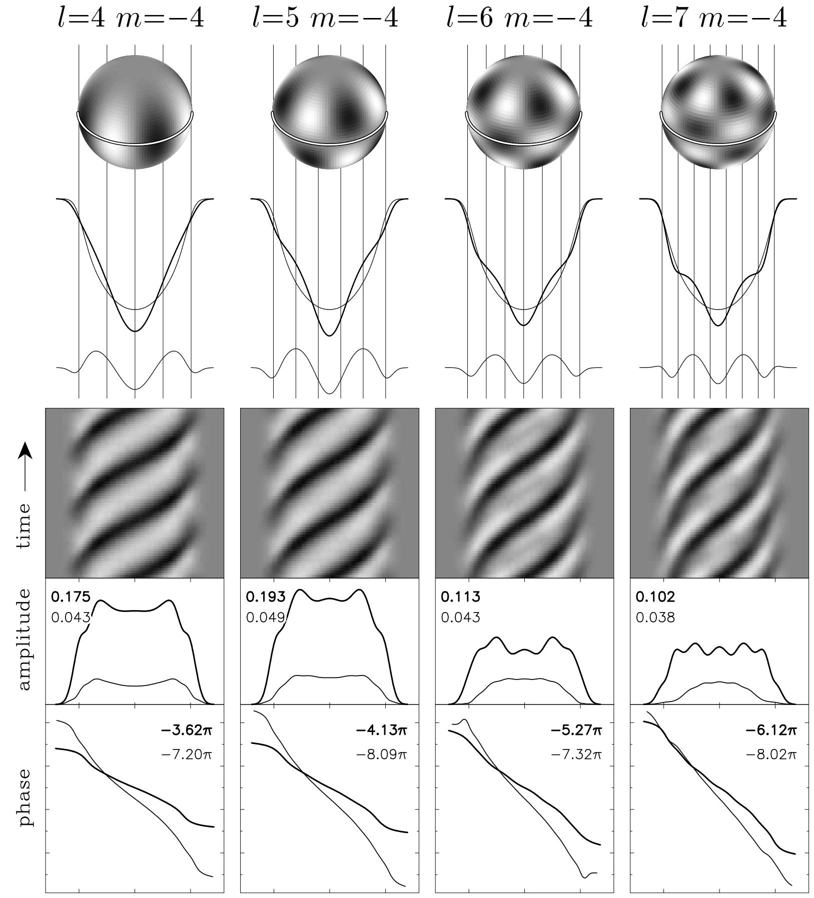

Figure 5.22: Simulated line-profile variations due to non-radial oscillations of different (l, m). From top to bottom we show: a representation of the real part of the radial component of the eigenfunction, the line profile due to the mode at a particular phase in the cycle in comparison with the profile without an oscillation, the difference between the two profiles, a grey-scale representation of the profiles with respect to the mean during three cycles, the distribution of the amplitude across the pulsation-induced line-profile variations (thick line) and its first harmonic (thin line) with the maximum values indicated, the distribution of the phase across the pulsation-induced line-profile variations (thick line) and its first harmonic (thin line) in units of π radians with the blue-to-red phase differences $\Delta\psi_0$ and $\Delta\psi_1$ used in Eqs (5.72) and (5.73) indicated. The projected equatorial rotation velocity is indicated by the outer vertical lines in the top panel. (From Telting & Schrijvers 1997.)

in the line blending of the different lines. The EE value is therefore affected, and, if computed without giving this thought, also the discriminant defined in Eq. (5.70).

A thorough discussion of such a situation is presented in Chadid *et al.* (2000) for the F3III monoperiodic δ Sct star 20 CVn. The purpose of their paper was to investigate the appropriateness of using CCF and the moment method to identify low-amplitude modes, because photometric mode-identification efforts for this star in the literature, before the one done by Daszyńska-Daszkiewicz *et al.* (2003) discussed above, led to a large discrepancy between the theoretical predictions and the observed values. We show in Fig. 5.19 the moment values derived from a CCF computed from a mask for an F-type star including some 2000 lines using the ELODIE spectrograph. The curves are phased according to the frequency 8.2168 d^{-1} known from photometric light curves. It can be seen that the second moment hardly varies, while the first and third moments have clear observed variations. This means that the constant term EE dominates in $\langle v^2\rangle$. This is a case where one has to be careful with the mode identification because solutions with i close to the IACC risk being favoured. The discriminant was subsequently computed, leaving out the constant terms of $\langle v^2\rangle$ and $\langle v^3\rangle$ following the careful analysis of all the terms occurring in the observed moments by Chadid *et al.* (2000). The values of this modified discriminant are provided in the left part of Table 5.3. It turns out that several solutions with i closer than 15° to an IACC occur (rows 1, 3, 6 and 8). These cannot be trusted. The minima γ_l^m are very close to each other, such that a unique solution cannot be derived without additional effort.

In order to check for the power of the modified discriminant for this monoperiodic star, the spectral deviation parameter in Eq. (5.50) through line-profile fitting was computed for all modes with $l \leq 4$. The results are listed in the right part of Table 5.3. It can be seen that the discriminating power of this method is lower than the one of the moment method for this star. Several solutions of almost equal quality occur. Three of those are compared with the observed CCFs in Fig. 5.20: one with an inclination angle close to an IACC (left), one with i far from an IACC (middle) and the radial mode. This is a clear case where line-profile fitting, even when using an objective deviation parameter, does not work, but where the addition of the moment variations allows the selection of one unique solution for (l, m). Indeed, a choice among the solutions in Table 5.3 can be made, by considering the theoretical moments belonging to the best solutions from Σ_l^m and comparing them with the observed ones shown in Fig. 5.19. These are plotted in Fig. 5.21. It is clear that only one set of $\langle v^2\rangle$ is in agreement with the observed ones and that 20 CVn is a radial oscillator. This is the second-best solution of the modified discriminant, the first one having $i \simeq$ IACC.

This example shows that, indeed, it is valid to work with CCFs in identifying modes, provided that one makes a very careful analysis. The moment method has not yet been tested on LSDs, but we expect similar performance. The performance of the Pixel-by-Pixel method, to which we turn next, has not yet been tested for CCFs or LSDs.

5.2.4 The Pixel-by-Pixel method

A second quantitative identification method was first introduced by Gies & Kullavanijaya (1988) and further developed by Kennelly & Walker (1996), Telting & Schrijvers (1997), Mantegazza (2000) and Zima (2006). Its use is illustrated and explained in Fig. 5.22. It is based on the properties of the amplitude and phase

Table 5.4: Comparison of the results for the mode identification of the thirteen dominant modes of the multiperiodic δ Sct star FG Vir, as available from the literature. Whenever more than one value for l or m is given in a column, discrimination among them was impossible.

Frequency	Viskum	Breger	Daszyńska-Daszkiewicz	Zima	
d^{-1}	*et al.* (1998)	*et al.* (1999)	*et al.* (2005)	*et al.* (2006)	
9.199	$l = 2$	$l = 2$	$l = 2$	$l = 1, 2, 3$	$m = +1$
9.656	$l = 2$	$l = 1, 2$	$l = 2$	$l = 0, 1, 2$	$m = 0$
12.154	$l = 0$	$l = 0$	$l = 0$	$l = 0, 1, 2$	$m = 0, +1$
12.716	$l = 1$	$l = 1$	$l = 1$	$l = 1$	$m = 0$
12.794	–	–	$l = 2, 1$	$l = 2, 3, 4$	$m = -2$
16.071	–	–	$l = 0$	–	–
19.227	–	–	$l = 2, 1, 0$	$l = 1, 2$	$m = +1$
19.867	$l = 2$	$l = 2$	$l = 2, 1$	$l = 0, 1, 2$	$m = 0$
20.287	–	–	$l = 0, 1$	$l = 1, 2, 3$	$m = -1$
20.834	–	–	–	$l = 2, 3, 4$	$m = +1$
21.051	$l = 2$	$l = 2$	$l = 1, 0$	$l = 0, 1, 2$	$m = 0$
23.403	$l = 0$	$l = 0, 1$	$l = 2, 1$	$l = 2$	$m = 0$
24.227	$l = 1$	$l = 1, 2$	$l = 1$	$l = 0, 1$	$m = 0$

distribution of each oscillation frequency and its first harmonic across the entire line profile. These properties are linked to the (l, m)-value of the mode, and to the inclination angle, as can be seen from Fig. 5.22.

The computation of the amplitude and phase behaviour across the profile is particularly suited to analyse line-profile variations in moderate to rapid rotators ($v \sin i \geq 50\,\mathrm{km\,s^{-1}}$), because we need a high resolving power within the lines to interpret small changes in the skewness of the line, and/or moving subfeatures. The method can also be applied to slow rotators with low-degree modes, however, when combined with the moment method (see Telting *et al.* 1997 for the first such application).

A particularly promising idea related to this method was to transform the line profile variations into 2D Fourier space, where power is sought for appropriate combinations of time and spatial frequency, in analogy to what had been done for the solar oscillations. This idea was put forward by Kennelly *et al.* (1992) and was further developed by Kennelly *et al.* (1998), who applied it to the δ Sct star τ Pegasi (see Fig. 5.24). In order to obtain the amplitude of the frequency as a function of l, however, one must perform a deconvolution of the original data into a time-dependent and a time-independent broadening function, and this relies on particular assumptions. Kennelly *et al.* (1998) assumed to be dealing with p modes having $K \simeq 0$, with profiles having a constant intrinsic width which can be disentangled from the constant rotationally broadened profile ignoring pulsational broadening, and with spectral lines which can all be well described by one and the same linear limb darkening law. Based on these assumptions, the authors developed a deconvolution scheme that connects the two-dimensional Fourier transform of the line profile with the time and spatial

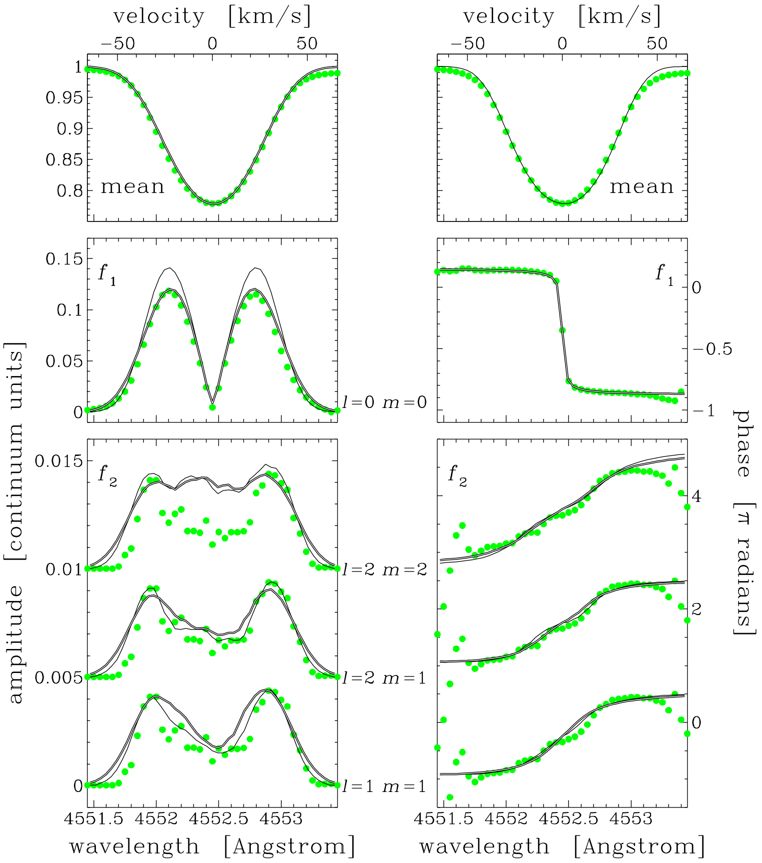

Figure 5.23: Line-profile computations (full lines) for two different biperiodic models are compared with data (dots) for the star β Cephei. The double full line has a slightly lower rotational velocity and amplitude for the radial mode (labelled as f_1), but a somewhat larger intrinsic width (differences of 2 km s^{-1}) than the single thin full line. The amplitude of the non-radial mode (labelled as f_2) was adopted to fit the observations after having fixed the parameters of the dominant radial mode, and varies between 1 and 2 km s^{-1}, depending on its (l, m) assignment. The top panel shows the average profile, the middle panels the amplitude and phase across the profile for the dominant radial mode and the lower panels the amplitude and phase of the three most likely identifications of the small-amplitude non-radial mode (f_2). Discrimination among these three possibilities is not possible. (From Telting *et al.* 1997.)

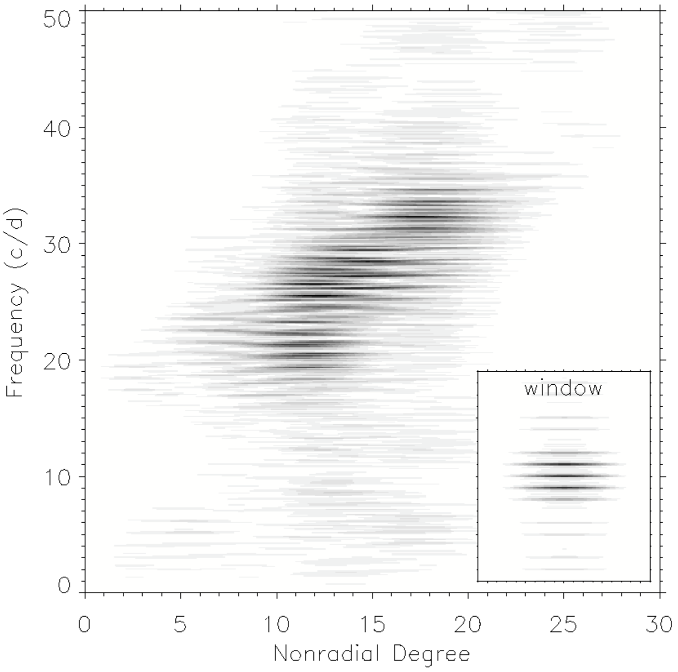

Figure 5.24: The observed line profile variations of the δ Sct star τ Pegasi were Fourier transformed and displayed as a function of the degree l by relying on particular assumptions (see text). The inset is the same transform representing the pattern due to the window function and gives an idea about the uncertainty in the identification of the mode degree due to the sampling. (From Kennelly *et al.* 1998.)

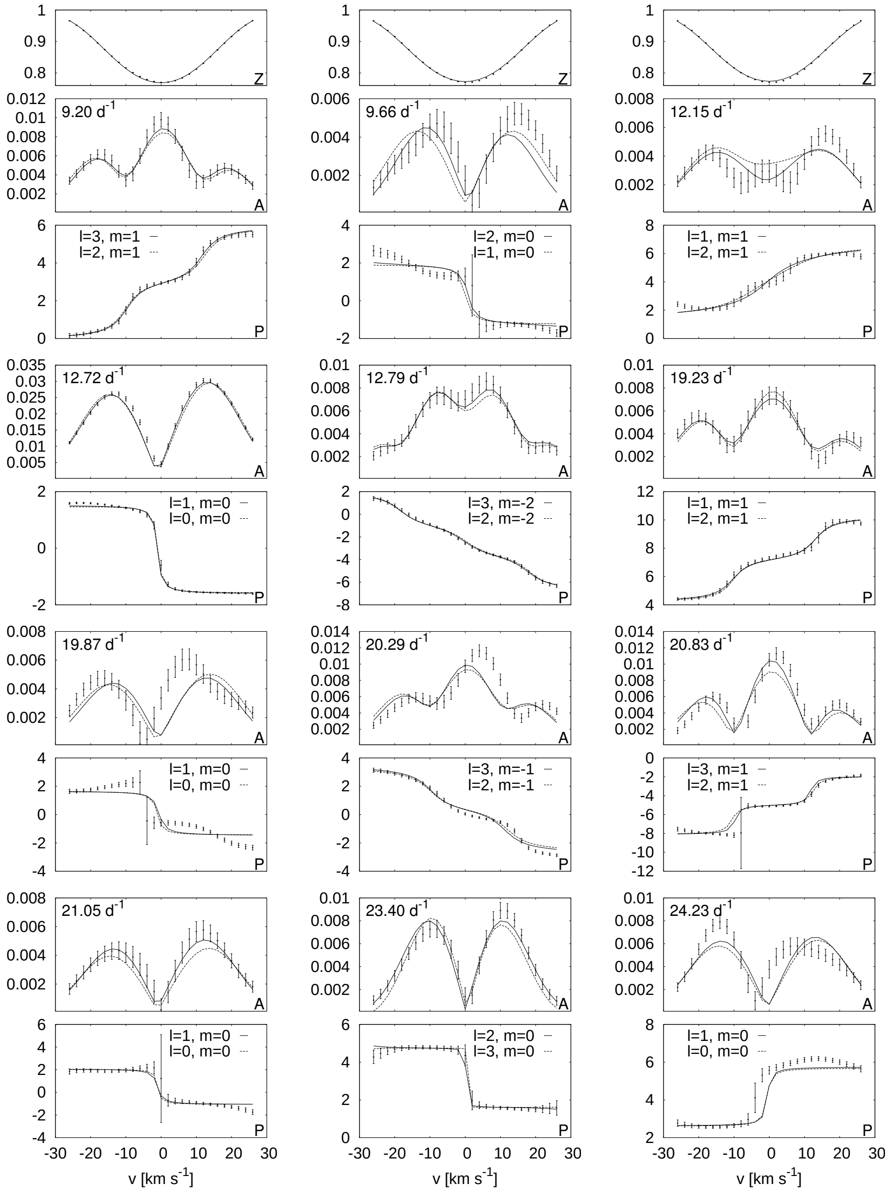

Figure 5.25: Fit of the amplitude and phase across the profile for the twelve dominant oscillation modes in the spectroscopy of the δ Sct star FG Vir. The top panels show the average, also termed zero profile (indicated as "Z"). For every single frequency, the observed amplitude (label "A") in units of the continuum and the phase distribution (label "P") in radians are shown together with the two best fitting models (Zima *et al.* 2006).

frequency, where the latter is assumed to be a particular measure of the mode degree l which is valid in the case of $K = 0$. The example shown in Fig. 5.24 shows this two-dimensional Fourier transform visually for τ Pegasi. While this idea was very attractive at first sight, the many assumptions underlying this method and the iterative manipulations of the data to end up with the result displayed in Fig. 5.24 leave a rather high level of uncertainty for the identification of the mode degree, in additional to the limitations of the predictive power introduced by the window function. This is due to the absence of a rigorous mathematical derivation of theoretical expressions for for the amplitude and phase variations across the profile, as a function of l and m. Hao (1998) tried to achieve such expressions, but did not succeed. This is thus the main difference between this method and the moment method, for which such expressions are readily available in Eqs (5.58), (5.59) and (5.60).

In order to remedy this situation and to understand the behaviour of the amplitude and phase variation across the profiles, without having to rely too much on assumptions and omitting deconvolution operations, Telting & Schrijvers (1997) performed an extensive simulation study to exploit the method visualised in Fig. 5.22 in terms of mode identification. Their simulations were restricted to p modes and low-order g modes, and included the effects of the Coriolis force in the velocity eigenfunctions. They computed more than 15 000 time series of line-profile variations for different combinations of $(l, m, v_{\rm p}, i, v_{\Omega}, v_{\rm th})$ considering $l \leq 15$ and all corresponding m-values $m \in [-l, l]$, realistic amplitudes for the modes, with or without the effects of the Coriolis force, with or without parameterised equivalent-width variations. For each of these time series, they subsequently computed the amplitude and phase across the profile for the input frequency and its first harmonic, in the way visualised in the lower panels of Fig. 5.22. The differences in phase between the bluest and reddest point in the line profile were then derived, for the frequency ($\Delta\psi_0$) and for its first harmonic ($\Delta\psi_1$). The authors then compared these values for $\Delta\psi_0$ and $\Delta\psi_1$ with the input values for (l, m) for all these simulated time series and reached the following conclusions:

- there exists a strong correlation between the phase difference $\Delta\psi_0$ at the blue and red edge of the profile for the oscillation frequency ω and the degree of the mode. A good estimate of l can be derived from the empirical relation

$$l \simeq (0.10 + 1.09\,|\Delta\psi_0|/\pi) \pm 1; \tag{5.72}$$

- there exists a clear, but less strong correlation between the phase difference $\Delta\psi_1$ from blue to red for the first harmonic of the oscillation frequency 2ω and the azimuthal number of the mode. A good estimate of m can be derived from the empirical relation

$$m \simeq (-1.33 + 0.54\,|\Delta\psi_1|/\pi) \pm 2. \tag{5.73}$$

The simulations of Telting & Schrijvers (1997) clearly showed that the original suggestion by Gies & Kullavanijaya (1988) to associate the phase differences $\Delta\psi_0$ with a measure of the m-value of the mode, assuming only sectoral modes to occur, is too limited for appropriate mode identification. This was also concluded by Kennelly *et al.* (1998). In a generalisation of their work, Schrijvers & Telting (1999) took into account the effects of intrinsic profile variations and equivalent width changes as well. This resulted in very similar fitting formulae than those given in Eqs (5.72) and (5.73). A similar simulation study to the one by Telting & Schrijvers (1997), but for stars with g modes, is not available.

The fitting formulae in Eqs (5.72) and (5.73) are easy to apply once the oscillation frequencies are determined. However, they provide only a crude estimate of the degree and azimuthal order with a large uncertainty, particularly for low-degree modes. It is therefore necessary to model the amplitude and phase across the profile in full detail to achieve a reliable identification. In order to do that, one computes theoretical line-profile variations from Eqs (5.45) and (5.49), derives their amplitude and phase across the profile as in Fig. 5.22 and compares them with those derived from the observations. The earliest such application was made for the star β Cep by Telting *et al.* (1997) and is depicted in Fig. 5.23 for a biperiodic model with a dominant radial mode and with the three best solutions for the identification of the second, low-amplitude mode.

Slightly different versions of the method by Telting & Schrijvers (1997) have been presented (*e.g.*, Mantegazza 2000). The most important and recent one is by Zima (2006), who introduced a statistical significance test into the method. In this way, he was able to discriminate more easily between different mode identification solutions. He tuned and applied his method, which he termed the *Pixel-by-Pixel Method* or PPM, after Mantegazza (2000), to observed line-profile variations of the δ Sct star FG Vir (Zima *et al.* 2006). Zima *et al.* (2006) found eleven modes in the line-profile variations in common with those detected with significant amplitude in the multicolour photometry. The fits to the amplitude and phase variation across FG Vir's profile for the best two identifications of the twelve dominant modes in spectroscopy, are shown in Fig. 5.25. This shows at once the big advantage of this method over the moment method: each mode can be treated separately without having to worry about coupling between the modes, at least in the linear approximation. The drawback, however, is that its discriminating power starts to fail whenever $v \sin i$ drops below, say typically, 20 km s^{-1}.

The spectroscopic mode identification for FG Vir is in good agreement with previous identifications. In particular, Fig. 5.25 illustrates the power to identify m from spectroscopy. In Table 5.4 we show the evolution of the ability to identify the dominant modes for this star from the literature. It can be seen that it is more difficult to find a unique l-value from the high-resolution spectroscopy. It is evident from this table that the ideal way to proceed with mode identification of multiperiodic stars is to use multicolour photometry to find the l-values, and line-profile variations to fix m. Depending on $v \sin i$, a moment or PPM analysis should be preferred, but there is no reason not to do both since they are complementary. This brings us in a natural way to the following section.

5.3 Mode identification from combined photometry and spectroscopy

Numerous applications of the mode-identification methods outlined above are available in the literature. The successful applications mainly concern p modes in β Cep or δ Sct stars, but also the dominant g modes in SPB stars (De Cat *et al.* 2005). Given the complementarity between the photometric and spectroscopic methods in terms of observational requirements and ability to derive l versus m, it is only natural to check whether consistency in the identifications is reached. This was already shown to be the case for the complex oscillations of FG Vir, besides the "simple" cases of 20 CVn and ρ Puppis, all δ Sct stars discussed above. Agreement between photometric and spectroscopic mode identifications was also achieved for the β Cep stars, such as for the dominant mode of δ Ceti (Aerts *et al.* 1992; Cugier *et al.* 1994), all three modes of

16 Lac (Cugier *et al.* 1994; Aerts *et al.* 2004), and most (but not all) of the modes of ν Eridani (De Ridder *et al.* 2004). There are, however, also cases with differences in the mode-identification results. One example is the famous β Cep star β Crucis, which was found to be a monoperiodic $l = 2$ pulsator from photometric data (Cugier *et al.* 1994), while Aerts *et al.* (1998) found it to have two low-amplitude modes of $l = 3$ or 4, besides a dominant $l = 1$ mode for the frequency detected in the photometry. The three modes found in the spectroscopy were later also detected in WIRE space white-light photometry (Cuypers *et al.* 2002). The misidentification from the multicolour photometry is probably due to the presence of the companion, which was ignored in that analysis but which is of similar spectral type to the oscillating component, and/or due to the neglect of the low-amplitude modes that are invisible in the ground-based photometry. Consistency was also reached between the most likely $l = 1$ mode identification of SPB stars as a group by Townsend (2002) and the mode identification from multicolour photometry and high-resolution spectroscopy of seven selected SPB stars by De Cat *et al.* (2005).

The case of β Crucis brings us to the fact that several β Cep stars and some SPB stars have modes that are invisible in ground-based photometry, while they are clearly present in the line-profile variations. The example of β Crucis shows that this may occur for slow rotators, but, most frequently, such finding is obtained for moderate to rapid rotators, *e.g.*, ω^1 Scorpii (Telting & Schrijvers 1998), λ Scorpii (Uytterhoeven *et al.* 2004), κ Scorpii (Uytterhoeven *et al.* 2005), β Centauri (Ausseloos *et al.* 2006) and numerous pulsating Be stars (Rivinius *et al.* 2003), all of which have $v \sin i$ above $60\,\mathrm{km\,s^{-1}}$. Of course, in such cases, one cannot rely on photometry to help in the mode identification, except that one can test *a posteriori* if the solutions found are compatible with the absence of photometric variations. The many B stars found to be oscillating from WIRE (Brunt *et al.* 2007) and MOST (Matthews *et al.* 2007) space photometry, while being essentially constant in ground-based photometry, prove that numerous low-amplitude modes are excited by the heat mechanism.

With the occurrence of low-amplitude modes in spectroscopy, only some of which are detectable in multicolour photometry in some cases, the idea arose to obtain simultaneous observations of these kinds. This is particularly the case for β Cep stars, for which extensive multisite, multi-technique campaigns were initiated by G. Handler from Vienna since 2002, as already outlined in Chapter 2. Cases where the multicolour photometry allowed the derivation of l, while the spectroscopy did not, occurred for the stars β Canis Majoris (Handler *et al.* 2005) and θ Ophiuchi (Shobbrook *et al.* 2006). The spectroscopists then were able to find the m-values, by fixing the photometric values for l and applying the moment method and evaluating the phase and amplitude across the profile for the best solutions as in Fig. 5.23 (Mazumdar *et al.* 2006, Briquet *et al.* 2005). We come back to these two β Cep stars in Chapter 10, where we discuss their seismic modelling based on the detected frequencies and the mode identification.

Whenever modes are detected in quasi-simultaneous multicolour photometry and high-resolution spectroscopy, one can do better than simply compare the mode identification results by exploiting the data simultaneously. This was first done by Daszyńska-Daszkiewicz *et al.* (2005) for the β Cep stars δ Ceti and ν Eridani. These authors added the amplitude and phase of the first moment to the multicolour amplitudes and phases, and upgraded the χ^2 criterion as in Eq. (5.37) accordingly. This led them to a much safer mode identification, and also an estimate of the parameter f_T, provided that the different types of data are not obtained too far apart in time to avoid different beat patterns to occur in the two types of data. From the derived f_T values for models with different opacities, the authors found a way to derive information on the most appropriate opacities to explain the modes. It is this combined method that also led to the identification of twelve modes for FG Vir discussed in the previous section and listed in Table 5.4. A natural extension of this method would be to include also the second and third moment variations to obtain an even more powerful discriminant, but this has not yet been done so far.

Finally, we point out that the empirical identification of the (l, m) values for the multiperiodic γ Dor stars remains problematic. There are hardly any simultaneous long-term multi-technique data sets available for such g-mode oscillators. The mode-identification results by De Cat *et al.* (2005) for some selected SPB stars show that the modes can be successfully identified, provided that one assembles multicolour photometry and high-resolution spectroscopy with a time span of a few years. Multicolour photometry with such a time span has been assembled from multisite campaigns dedicated to specific targets such as 9 Aurigae (Zerbi *et al.* 1997a), HD 164615 (Zerbi *et al.* 1997b), QW Puppis (Poretti *et al.* 1997), HR 8799 (Zerbi *et al.* 1999), and from single-site campaigns dedicated to samples of γ Dor stars (Henry & Fekel 2004, 2005; Cuypers *et al.* 2007). Long-term spectroscopic campaigns for large samples were also carried out (Mathias *et al.* 2005; De Cat *et al.* 2006). Unfortunately, these extensive data have not led to mode identification. The modes of only five γ Dor stars have been identified so far from multicolour photometry (Aerts *et al.* 2005b). This seems to point towards the excitation of only $l = 1$ modes, but this conclusion must be considered as preliminary. Very likely, ground-breaking results for g-mode oscillators will come from the CoRoT and Kepler photometry, in combination with ground-based spectroscopy.

5.4 Towards mode identification from combined interferometry and spectroscopy?

In an extensive review, Cunha *et al.* (2007) have discussed the synergies and cross-fertilisation between interferometry and asteroseismology. Interferometric measurements can help a lot in asteroseismic analyses in several different ways. Direct radius estimates with a relative precision better than a few percent, *e.g.*, can be obtained for several hundred stars in the solar neighbourhood with VLTI/AMBER. The masses of binary stars with a pulsating component can be derived independently from asteroseismology by interferometry, with precision of only a few percent. As far as mode identification is concerned, the combination of interferometric and spectroscopic data allows, in principle, the identification of the oscillation modes.

The PPM method described above exploits the amplitude and phase across the profile as a mode-identification diagnostic by relying, through Eqs (5.45) and (5.49), on the expression for the pulsational velocity in terms of l and m. The Doppler effect is considered to be the dominant source of information in identifying l and m from the variations through Eq. (5.49). A new interesting idea was put forward by Berdyugina *et al.* (2003a). They inverted a time series of line-profile variations, in this way turning the data into a stellar surface brightness distribution. This comes down to an image reconstruction method, also termed Doppler Imaging in the context of spotted stars. They applied this inversion without assuming any prior knowledge of the physical cause of the variations of the line profiles. After having performed the inversion, the authors assumed that the most important cause of the line-profile variations are surface brightness variations superposed onto a time-independent broadened Doppler profile. Rather than focusing on $v(R, \theta'_i, \phi'_j, t)$ in the interpretation through Eq. (5.49), they thus considered $\delta[F_\lambda(\theta', \phi')]$ to be the dominant information for the mode identification. Such a situation may occur for rapidly rotating stars, whose velocity perturbation due to the oscillations is very small compared with its rotational broadening. In such a case, the pulsation-induced intensity perturbations gain importance with respect to the velocity perturbations. Berdyugina *et al.* (2003b) applied their method to the β Cep star ω^1 Scorpii and found it to be capable of recovering l and m of the oscillation, which had been derived before from a PPM-like application by Telting & Schrijvers (1998). This brings us to the capability of combining surface brightness variations, *e.g.*, derived from interferometry, with surface velocity variations derived from high-resolution spectroscopy.

Long before the availability of appropriate instrumentation, Vakili (1992) had already suggested the study of surface variations due to non-radial oscillations of rapidly rotating stars from long-baseline differential interferometry (see Cunha *et al.* 2007 for the technicalities of how this can be achieved). As shown by Jankov *et al.* (2001), such a combined technique can be successful in identifying oscillation modes with $l > 2$ in rapid rotators, providing information on the modes that can perhaps not be obtained from each of the two types of observations, interferometry and spectroscopy, separately. The flux variations due to the non-radial modes introduce a complex pattern in the so-called interferometric $\mathcal{UV}$ plane (Cunha *et al.* 2007). This pattern can be disentangled by comparing the photocentre displacements in this plane due to the oscillations with predicted monochromatic intensity maps of a constant star. In practice, one simulates photocentre displacements as a function of (l, m, i). Such a simulation defines a kind of "spatial filter" for each (l, m, i). Applying one-by-one all these spatial filters to the data allows one to identify the true nature of the mode. This is illustrated in Fig. 5.26, in which the original signal in panel (a) is compared with a map (b) recovered from spectra alone with a method similar to the one of Berdyugina *et al.* (2003a), as well as with the map based on the photocentre shifts alone displayed in panel (c), and a combination of both shown in panel (d). The limitations of panels (b) and (c) are particularly apparent in the reconstruction of the features below the equator, where a loss of contrast occurs. A significant improvement with respect to these separate reconstructions is obtained using both spectra and photocentre shifts simultaneously, as in panel (d).

Domiciano de Souza *et al.* (2002, 2003) and Jankov *et al.* (2004) showed that measurements of the displacement of the photocentre across the stellar disk allows mapping of the surface brightness, but requires a minimum of three telescopes in an interferometric array in such a way that fringes are collected for all three baselines. The simulation study by Jankov *et al.* (2004) anticipates that the interferometric measurements are sufficiently sensitive to detect a mode of low (l, m). In general, however, numerous modes are simultaneously excited. In such more realistic cases, the photocentre displacements are 'washed out' by the averaging effect of the many (l, m)-values. In that case, one can still obtain identification for a fixed number of oscillation frequencies which have been derived from time series analysis of observables of any kind. When carrying out the interferometric measurements, a selected oscillation frequency is used to phase-lock the data to this frequency. In this way, all surface structures that are not associated with this frequency are assumed to be removed, greatly improving the signal strength for the frequency under consideration. Such frequency filtering can be done as a post-processing step by an appropriate weighting procedure. It is possible to design the appropriate weights for each of the measured oscillation frequencies separately, and use the same set of interferometric observations to constrain the identification of all the oscillation modes whose frequencies are known from other diagnostics.

Concrete applications of this promising mode-identification method are still awaited.

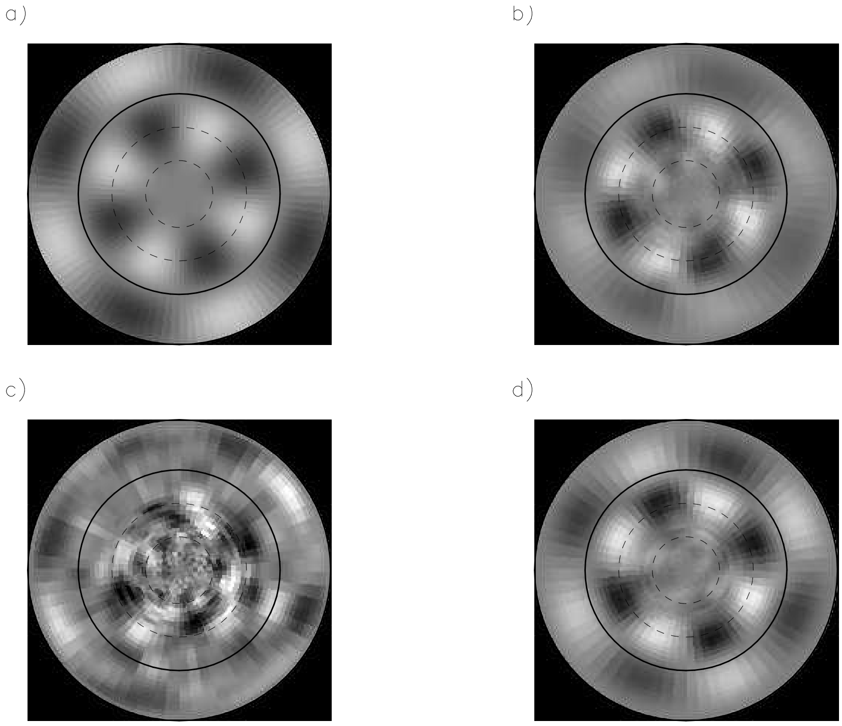

Figure 5.26: (a) Simulation of the pole-on projection of the stellar surface brightness perturbations due to an $l = 5, m = 4$ mode on a star with an inclination angle of $i = 45°$. The equator and the latitudes $30°$ and $60°$ are presented by full and dashed circles, respectively. Reconstruction based on (b) simulated flux spectra, (c) photocentre shifts, and (d) combined flux spectra and photocentre shifts. (From Jankov *et al.* 2001.)

5.5 Towards mode identification from eclipse mapping?

Unno *et al.* (1989, p.22) pointed out the possibility to observe phase shifts due to non-radial oscillations during the eclipse of a pulsating star by a companion, and to use this as a mode-identification method. No applications of this technique existed yet at the time they wrote the second edition of their monograph on non-radial oscillations of stars. Unno *et al.* (1989) realised that the earlier interpretation of phase jumps of 360° in the nova-like binary UX UMa in terms of non-radial oscillation modes of $l = 2$ by Nather & Robinson (1974) was premature, and that the observed phase phenomenon could be far better explained in terms of an oblique rotator model.

Current versions of the eclipse-mapping method for cataclysmic variables are based on the original development by Horne (1985). He introduced the method with the goal of mapping the surface brightness distributions in eclipsing cataclysmic variables. Eclipse mapping allows a test of accretion theory because the spatial structure of the disks can be derived from the light-curve behaviour. Moreover, the spot structure, including the hot spot originating from the collision of the stream of the donor onto the disk of the gainer, can be derived. For early applications to interacting binaries we refer to, *e.g.*, Rutten *et al.* (1993), Collier Cameron & Hilditch (1997) and Hilditch *et al.* (1998).

In the case of mode identification of a non-radially pulsating star in an eclipsing binary, one needs to reconstruct a time-dependent intensity map from the data, and subsequently infer the amplitude and phase behaviour of the pulsation mode. Nuspl & Bíró (2002) and Nuspl *et al.* (2004) modified Horne's method for mode identification from photometric data, as did Gamarova *et al.* (2003) who baptised their method the Spatial Filtration method. Unfortunately, these studies were only published in short proceedings papers and there is as yet no extensive simulation study of the methodology, highlighting its applicability to multiperiodic oscillations and an evaluation of the uniqueness of solutions.

While several δ Sct stars in eclipsing binaries are known (Pigulski 2006), the mode identifications performed for them are almost all based on the out-of-eclipse data, *e.g.*, RZ Cassiopeia (Ohshima *et al.* 2001; Rodríguez *et al.* 2004) and Y Cam (Kim *et al.* 2002). The next step towards application of mode identification through eclipse mapping was performed by Mkrtichian *et al.* (2004) for the Algol-type eclipsing binary star AS Eridani. They did not use the eclipse-mapping method, but they excluded the odd $l + m$ combinations of (l, m) from the fact that their disk-integrated amplitude disappears during the eclipse. Gamarova *et al.* (2004) made preliminary estimates of (l, m) for the Algol-type eclipsing binaries AB Cassiopeia and RZ Cassiopeia from Spatial Filtration. Rodríguez *et al.* (2004) also applied Spatial Filtration to AB Cassiopeia. Both studies provided a radial mode for the star, in agreement with the out-of-eclipse identification. This result was recently confirmed by Riazi & Abedi (2006), who considered only radial modes in their methodology. As far as we are aware, the case of AB Cassiopeia, a radial pulsator, is the only application they made so far.

By far the best documented version of mode identification from photometric data using eclipse mapping was provided by Reed *et al.* (2005). While their primary goal was to search for evidence of tidally tipped pulsation axes in close binaries, they also made simulations for the very specific case of eclipse mapping of pulsating subdwarf B star binaries, *i.e.*, assuming that the secondary has more or less the same size as the primary and does not contribute to the light. They assumed that the pulsation axis can take any value and is not necessarily aligned with the rotation or orbital axis. They investigated how the visibility of different types of modes varies between the out-of-eclipse and in-eclipse phase. In particular, they found that $l > 2$ modes become visible during an eclipse while they are essentially absent outside of eclipse. Their tools have so far only been applied to concrete cases of KPD 1930+2752 (Reed *et al.* 2006a) and of PG 1336-018 (Reed *et al.* 2006b; see also Fig. 2.59) but without clear results.

We must conclude that, still today, more than 30 years after the original idea of Nather & Robinson (1974), eclipse mapping has hardly been evaluated critically as a mode-identification method, nor has it been applied successfully in practice for binary stars that have been subjected to seismic modelling afterwards.

Part III

Applications of asteroseismology

In this part of the notes you find selected papers on applications of asteroseismology to different kinds of stars. Inevitably, this selection is a personal one by the lecturer and it is biased towards her own research interests. It is by no means the intention to give a complete overview of applications. Rather, the lecturer has opted to choose some specific papers which she finds well written and accessible to students while containing state-of-the-art seismic analyses and prominent results. Very likely, the choice of the papers will change during the forthcoming years as new analyses will become available in the international literature.

It is very important for the students to realise what the purpose of this last part of the course is: to provide them with a selection of papers from the modern literature on asteroseismology and to make them understand the role of asteroseismology in the general context of stellar astrophysics. The goal is that the students get a flavour of the major achievements of asteroseismology and, equally importantly, of what remains to be done in the future. As outlined in the Evaluation part of the notes, the material in this part of the course will be studied by the students themselves, now that they have received the basic introduction on stellar oscillations and tools to analyse data thereof as outlined in Parts I and II of these lecture notes. That preparation should suffice for them to understand large parts of the papers selected here and report on the results described in them.

The students must make a summary of the most important results in a (some of the) scientific paper(s) and present this summary to their fellow students, after considerable interaction with the lecturer. I stress that the goal cannot be for the students to understand all the details of all of those papers. In fact, the lecturer herself does not understand all these details. The purpose is that the students learn to select the highlights in these works and to place them in perspective into the global context of asteroseismology.

Chapter 6

Helioseismology and solar-like oscillators

6.1 Helioseismology

The oscillations discovered in the Sun in the early 1960s have provided astrophysicists with a unique opportunity to investigate the interior of a star with unprecedented precision. The Sun's oscillations have been observed extensively since their discovery up to the present day, both from ground-based networks and from space.

Many of the techniques used in asteroseismology have been developed in order to interprete the solar frequency spectrum in full detail. In this sense, helioseismology has clearly paved the road for applications of seismology to more distant stars with stochastically-excited modes. It is therefore evident that an overview of the results obtained from helioseismology cannot be omitted in the current course. A very extensive, recent review paper on helioseismology is available from

Christensen-Dalsgaard, J., 2002, Helioseismology,
Reviews of Modern Physics, Volume 74, pages 1073 – 1129.

Helioseismology is certainly not the specialisation of the lecturer. It is therefore evident that she would not have been able to provide so many details in such an excellent way, so we prefer to provide the students with the review paper mentioned above.

6.2 Solar-like oscillations in distant stars

In 2003, a review paper on solar-like oscillations in distant stars was published by two world-leading experts in this research field. We include it here instead of trying to make our own summary:

Bedding, T.R., Kjeldsen, H., 2003, Solar-like Oscillations,
Publications of the Astronomical Society of Australia, Volume 20, pages 203 – 212.

The discovery of solar-like oscillations in nearby stars is a domain that undergoes a real boom, so by the time you read these lecture notes new discoveries (among which in α Cen B!) will undoubtedly have occurred, as well as more refined observational studies of the stars mentioned in the review. Keep yourself informed and updated by checking the World Wide Web!

Chapter 7

Seismology of compact stars

7.1 White dwarf seismology

As already mentioned in the first introductory chapter of this course, the WET observing run of the white dwarf PG 1159-035 implied a real break-through in white-dwarf seismology. Although this result was obtained more than a decade ago, the same level of precision was reached for only a very limited number of stars so far. Moreover the paper on the WET run of PG 1159-035 is a very nice example of a good *end-to-end seismic analysis* in which one starts from the observations and ends with stringent constraints on the internal structure of the star. We therefore certainly include this important paper here:

Winget, D.E., Nather, R.E., Clemens, J.C., et al., 1991,
Asteroseismology of the DOV star PG 1159-035 with the Whole Earth Telescope,
The Astrophysical Journal, Volume 378, pages 326 – 346.

A recent interesting aspect of white dwarf seismology is the idea that it can constrain the nuclear reaction rate ^{12}C$(\alpha,\gamma)^{16}$O. This result is a very nice example of the implications asteroseismology could have for other fields in physics. However, there is no general consensus on this result in the international literature. We point out four papers in this respect:

Metcalfe, T.S., Salaris, M., Winget, D.E., 2002,
Measuring ^{12}C$(\alpha,\gamma)^{16}$O from white dwarf asteroseismology,
The Astrophysical Journal, Volume 573, pages 803 – 811.

Handler, G., Metcalfe, T.S., Wood, M.A., 2002,
The asteroseismological potential of the pulsating DB white dwarf stars
CBS 114 and PG 1456+103,
Monthly Notices of the Royal Astronomical Society, Volume 335, pages 698 – 706.

Fontaine, G., Brassard, P., 2002,
Can white dwarf asteroseismology really constrain the ^{12}C$(\alpha,\gamma)^{16}$O reaction rate?,
The Astrophysical Journal, Volume 581, pages L33 – L37.

Metcalfe, T.S., 2003,
White dwarf asteroseismology and the ^{12}C$(\alpha,\gamma)^{16}$O rate,
The Astrophysical Journal, Volume 587, pages L43 – L46.

7.2 Seismic studies of sdB stars

Ever since their discovery in 1997, the pulsating sdB stars, also termed EC 14026 or V 361 Hya stars, have been observed intensively. However, it took several years, even for the sdB stars with short-period pressure modes, before the observations reached the level of detail such that seismic inference could be achieved. The first such detailed seismic study is summarised in the paper:

Brassard, P., Fontaine, G., 2001,
Discovery and asteroseismological analysis of the pulsating sdB star PG 0014+067,
The Astrophysical Journal, Volume 563, pages 1013 – 1030,

which we regard to be a reference work in this area of asteroseismology. The need of modes with degree $l > 2$ to model the frequency spectrum of PG 0014+067 as explained in the paper is, however, not supported by all asteroseismologists. Therefore, the same star is the main target of a WET run and of a multicolour study with the instrument ULTRACAM attached to the William Herschel Telescope at La Palma in the second part of 2004. We will therefore hopefully be able to report on more detailed seismic results for this star in the version of these Lecture Notes next year.

In-depth seismic analyses are currently not yet possible for the much more recently discovered gravity-mode oscillators among the sdB stars. Many more observational efforts are needed to firmly establish numerous frequencies and mode identifications for the gravity modes in such objects.

Chapter 8

Seismology of massive stars

8.1 Delta Scuti star seismology

The first attempts to perform detailed seismic studies of stars more massive than the Sun, i.e. for stars with a considerable convective core, were made for selected δ Scuti stars which had been the targets of multisite campaigns (mainly organised by the Vienna team led by M. Breger). A reference work in this matter is:

Pamyatnykh, A.A., Dziembowski, W.A., Handler, G., Pikall, H., 1998,
Towards a seismic model of the δ Scuti star XX Pyxidis,
Astronomy & Astrophysics, Volume 333, pages 141 – 150.

While the conclusions from this study on the potential of δ Scuti star seismology were rather worrisome at the time of publication of that paper, a possible explanation for the limitations of the seismic modelling of XX Pyxidis was proposed recently:

Aerts, C., Handler, G., Arentoft, T., Vandenbussche, B., Medupe, R., Sterken, C., 2002,
The δ Scuti star XX Pyx is an ellipsoidal variable,
Monthly Notices of the Royal Astronomical Society, Volume 333, pages L35 – L39.

A second δ Scuti star in which many oscillation modes have been detected and that was therefore the subject of seismic modelling is FG Virginis. An example of such a study is:

Templeton, M., Basu, S., Demarque, P., 2001,
Asteroseismology of δ Scuti stars: a parameter study and application to seismology of FG Virginis,
The Astrophysical Journal, volume 563, pages 999 – 1012.

8.2 Seismic studies of roAp stars

A considerable amount of data of roAp stars has been gathered the past two decades. Frequency analyses of their light curves have yielded quite rich asteroseismic information in general, and in particular on the interaction of the oscillations with the magnetic field. However, many questions still remain unsolved today.

One of the best studied roAp stars is HR 1217, of which we list two recent remarkable and important publications:

Cunha, M.S., 2001, The sixth frequency of roAp star HR 1217,
Monthly Notices of the Royal Astronomical Society, Volume 325, pages 373 – 378.

Kurtz, D.W., Kawaler, S.D., Riddle, R.L., et al., 2002,
Discovery of the ‘missing’ mode in HR 1217 by the Whole Earth Telescope,
Monthly Notices of the Royal Astronomical Society, Volume 330, pages L57 – L61.

8.3 B-star seismology

It is always the privilige of the lecturer to put more emphasis on his/her favourite topic in lectures. While your lecturer's main research domain is asteroseismology of B stars, she has tried not to exaggerate and to limit to the most recent results also for this type of stars. As for the oscillating sdB stars, we are still awaiting the detection and mode identification of numerous gravity modes in the SPBs (up to some five modes have been detected in some stars).

At present, significant progress in the detailed seismic modelling of the p-mode oscillators among the B stars, i.e. the β Cep stars, is occurring. While attempts of such modelling already started in 1996 by our Polish colleagues W. Dziembowski and M. Jerzykiewicz for the stars 12 and 16 Lacertae, it was only in 2003 that a significant step forward has been achieved. One of the reasons for this is that we have finally obtained good mode identifications for the modes in some selected β Cep stars. This has led to inferences on internal properties of the convective core and the rotation profile in some cases. A second reason is that β Cep stars have become the targets of multisite campaigns lasting several months and involving dozens of instruments around the globe. The campaigns have been organised under the leadership of G. Handler from Vienna University. At the time of writing of these lecture notes, such a campaign has finished for the stars ν Eridani, 12 Lacertae, 16 Lacertae and V 2052 Ophiuchi. Interpretation of such network campaigns is a tedious job which takes a long time, even if tackled by a large team of researchers. In these notes, we include the final results of the campaign on ν Eridani, the analyses for the other targets are still ongoing and will be reported upon in the coming years.

The number of modes that are excited to detectable amplitudes in β Cep star is small, typically less than ten. The examples for the 6 stars studied below show the amazing power of asteroseismology, even with very few well-identified oscillation modes at hand:

Handler, G., Shobbrook, R.R., Vuthela, F.F., et al., 2003,
Asteroseismological studies of the three β Cephei stars: IL Vel, V 433 Car and KZ Mus,
Monthly Notices of the Royal Astronomical Society, Volume 341, pages 1005 – 1019.

Thoul, A., Aerts, C., Dupret, M.-A., et al., 2003,
Seismic modelling of the β Cephei star EN (16) Lacertae,
Astronomy & Astrophysics, Volume 406, pages 287 – 292.

Aerts, C., Waelkens, C., Daszyńska-Daszkiewicz, J., et al., 2003,
Asteroseismology of the β Cep star HD 129929.
I. Observations, oscillation frequencies and stellar parameters,
Astronomy & Astrophysics, Volume 415, pages 241 – 249.

Dupret, M.-A., Thoul, A., Scuflaire, R., et al., 2003,
Asteroseismology of the β Cep star HD 129929.
II. Seismic constraints on core overshooting, internal rotation and stellar parameters,
Astronomy & Astrophysics, Volume 415, pages 251 – 257.

Handler, G., Shobbrook, R.R., Jerzykiewicz, M., et al., 2004,
Asteroseismology of the β Cephei star ν Eridani
I. Photometric observations and pulsational frequency analysis,
Montly Notices of the Royal Astronomical Society, Volume 347, pages 454 – 462.

Aerts, C., De Cat, P., Handler, G., et al., 2004,
Asteroseismology of the β Cephei star ν Eridani
II. Spectroscopic observations and pulsational frequency analysis,
Montly Notices of the Royal Astronomical Society, Volume 347, pages 463 – 470.

De Ridder, J., Telting, J.H., Balona, L.A., et al., 2004,
Asteroseismology of the β Cephei star ν Eridani
III. Extended frequency analysis and mode identification,
Montly Notices of the Royal Astronomical Society, Volume 351, pages 324 – 332.

Pamyatnykh, A.A., Handler, G., Dziembowski, W.A., 2004,
Asteroseismology of the β Cephei star ν Eridani:
interpretation and applications of the oscillation spectrum,
Montly Notices of the Royal Astronomical Society, Volume 350, pages 1022 – 1028.

Ausseloos, M., Scuflaire, R., Thoul, A., Aerts, C., 2004,
Asteroseismology of the β Cephei star ν Eridani:
massive exploration of standard and non-standard stellar models to fit the oscillation data,
Montly Notices of the Royal Astronomical Society, Volume 355, 352 – 358.